

PROTOTYPING ELLIPTICALLY PROFILED INVERTED PENDULUM WALLS IN
CROSS-LAMINATED TIMBER (CLT) FOR PASSIVE SELF-CENTERING AND
SEISMIC RESILIENCY

by

Marco Lo Ricco

A Dissertation Submitted in
Partial Fulfillment of the
Requirements for the Degree of

Doctor of Philosophy

in Engineering

at

The University of Wisconsin-Milwaukee

August 2019

ABSTRACT

PROTOTYPING ELLIPTICALLY PROFILED INVERTED PENDULUM WALLS IN CROSS-LAMINATED TIMBER (CLT) FOR PASSIVE SELF-CENTERING AND SEISMIC RESILIENCY

by

Marco Lo Ricco

The University of Wisconsin-Milwaukee, 2019
Under the Supervision of Professor Al Ghorbanpoor

Cross-laminated timber (CLT) buildings garnered international attention, nearly a decade ago, for elevating wood construction to new heights on fully panelized assemblies of floors and walls. While highly regarded as a sustainable building material, use of CLT as a structural wall system depends on seismically resilient strategies like controlled rocking. This project prototyped elliptically profiled CLT panels and slotted-pin steel connections, at full-scale, to produce *rolling* and *slip-friction* inverted pendulum wall systems of one-story height and inspired by seismic isolation concepts. Digital fabrication realized elliptical profiles along the loadbearing edges of six 5-ply CLT panels and various customized slot shapes for accompanying steel connections. Pins traveling within V-shaped slots intended only to guide rolling as *displacement restraints*, in contrast with pins constrained within vertical slots that forced panels into *slip-friction* combinations of *rolling* and *sliding*. Six CLT panels and two versions of shear transfer connections yielded a total of 12 full-scale wall prototype configurations for cyclic lateral load-displacement testing that emulated standard quasi-static protocols for seismic isolation. The hysteresis plots generated by the tests confirmed that elliptical eccentricity predictably controlled effective lateral stiffness and displacement capacity, while providing inherent self-centering.

When configured to *roll* using traction along steel bearing surfaces as the primary mechanism of story shear transfer, CLT panels supported simulated gravity loads as high as 400 kN (90 kips) while achieving story drifts commonly exceeding 10 and even 20 percent. When configured to transfer shear primarily through a pin connection, however, CLT panels slid and sustained damage that limited gravity load capacity to 133 kN (30 kips). Connection constraint, therefore, dictated whether friction essentially transferred story shears transfer or dissipated energy. To help explain implications of friction, Digital Image Correlation (DIC), piezoelectric film pressure mapping, Finite Element Analysis, and fundamental free-body diagrams visualized the behavior of high-pressure contact between timber and steel. Despite the low damping exhibited by *rolling* and increased damage of *slip-friction rocking*, both models of elliptically profiled rocking walls can develop into viable options for isolation planes within multistory building schemes, based on the results of this study.

© Copyright by Marco Lo Ricco, 2019
All Rights Reserved

To those who encouraged and supported me—
especially my wife,
parents,
and
all who cared for my sons,
while I endeavored to build a more sustainable and resilient future.

TABLE OF CONTENTS

Abstract.....	ii
Table of Contents.....	vi
List of Figures.....	ix
List of Tables	xvi
Acknowledgements.....	xviii
Agency Sponsors	xviii
USDA/U.S. Forest Service, Forest Products Laboratory Contributors	xviii
UWM Affiliated or Invited Contributors.....	xix
College of Engineering and Applied Science	xix
Structural Engineering Laboratory.....	xix
Prototype Fabrication	xx
Computing Resources.....	xx
Faculty Committee Members	xx
Peer Review Consultants	xxi
Industry Partners in Digital Fabrication.....	xxi
I. Introduction	1
The Emergence of CLT as a Mass Timber Composite.....	2
The Rise of Cross-Laminated Timber.....	5
II. Literature Review	7
Mapping a Comprehensive Seismic Development Strategy.....	9
Inelastic Ductility: The Force-Based Approach	10
Controlled Rocking: An Evolving Displacement-Based Alternative	12
Mechanics of Inverted Pendulum Rocking.....	12
Evolution of Precast Concrete Panelized Systems.....	13
Timber Adaptations	14
Vertically Post-Tensioned Rocking Walls.....	15
Slip-Friction Hold-Downs	17
Ductile Anchorage	18
Isolation as a Path to Seismic Resiliency.....	19
General Considerations.....	20
III. Methodology	23
System Model	23
Elliptical Rolling Rod Isolation	24
No-Slip Traction Rolling	25
Slip-Friction Rocking.....	32
Principle of Virtual Work	36
Objectives and Hypotheses.....	36

Friction: Shear Transfer or Energy Dissipation?	38
Geometric Proportioning	38
Prototype Testing	40
Test Matrix	40
Prototype Connections	43
Simulating Boundary Conditions	45
Prototype Testing Protocol	46
Capabilities and Limitations	48
Imperfections	49
Data Collection	49
Scales of Study	51
IV. Results, Observations and Findings	52
Overview of Test Results	52
Hysteresis Plots	57
General Notes	57
Keyed Notes	58
Axis Scaling	58
Hysteresis Characteristics	58
No-Slip Traction Rolling	59
e = 0.63 Panel	59
e = 0.73 Panel	61
e = 0.82 Panel	65
e = 0.88 Panel	67
e = 0.91 Panel	71
e = 0.94 Panel	75
Slip-Friction Rocking	79
e = 0.63 Panel	79
e = 0.73 Panel	81
e = 0.82 Panel	84
e = 0.88 Panel	87
e = 0.91 Panel	90
e = 0.94 Panel	93
Hysteresis Characteristics	97
Stability	97
Stable Rolling through Variable Vertical Load	98
Slip-Friction Rocking Sensitivity to Vertical Loads	99
Out-of-Plane Stability	103
Restoring Forces	104
Predictability	105
Stiffness	105
Track and Roller Imperfections	107
Frictional Damping	107
Durability	108
Rolling Protection	109
Slip-Friction Rocking and Mixed Modes	109
Observed Damage	110

No-Slip Traction Rolling Effects on Laminations	111
Slip-Friction Rocking Effects on Laminations	114
Digital Image Correlation Comparisons	120
Timber Laminations	121
Steel Connections	127
Wind Restraint	130
V. Summary, Conclusions, and Recommendations	131
Summary Results Tables.....	132
Conclusions.....	138
Recommendations for Further Development.....	142
Use of the Hysteresis Models	144
Design Guidelines for Archetype Development	145
References.....	148
Appendix A: Principle of Virtual Work Models.....	158
Appendix B: Connection Details	165
Appendix C: Precursory Characterizations of Timber-to-Steel Contact	179
Finite Element Analysis.....	179
Piezoelectric Pressure Mapping.....	187
Digital Image Correlation	193
DIC Objectives.....	194
DIC Methodology	194
DIC Results.....	197
Timber Bearing Conditions	197
Conclusions of Precursory Phase.....	199
Curriculum Vitae	200

LIST OF FIGURES

Figure 1. Cross-Laminated Timber.....	2
Figure 2. Sections of Common CLT Layups	2
Figure 3. CLT panel assembly of Stadthaus on concrete podium	5
Figure 4. Construction of Brock Commons pairing timber with reinforced concrete	7
Figure 5. CLT platform structure on the E-Defense shake table, Japan	8
Figure 6. Project sequence patterned after the <i>Structural Research Drive</i>	9
Figure 7. Inelastic force-deformation curve.....	11
Figure 8. A rocking rigid block.....	12
Figure 9. Hysteretic behavior of various concrete walls.....	13
Figure 10. Free-body diagram of coupled CLT walls.....	16
Figure 11. Vertically post-tensioned (PT) CLT wall with UFPs	16
Figure 12. Simplified kinematics of wall with base anchorage	18
Figure 13. Classification of rocking wall developments in timber	20
Figure 14. Idealized lateral force-deflection relationships for isolation systems	22
Figure 15. Elevation view of 3 multistory building schemes	23
Figure 16. Shaping CLT panels for rocking response to earthquakes	23
Figure 17. Rigid superstructure isolated on elliptical rolling rods.....	25
Figure 18. Rolling elliptical pendulum model	25
Figure 19. Geometric parameters.....	28
Figure 20. Free-body diagram of rolling panel.....	30
Figure 21. Idealized hysteresis of $e = 0.73$ panel in No-Slip Traction Rolling	31
Figure 22. Slip-Friction elliptical pendulum model.....	33
Figure 23. Idealized hysteresis of $e = 0.73$ panel in Slip-Friction Rocking.....	35

Figure 24. Idealized stiffness comparisons of panels in No-Slip Traction Rolling	39
Figure 25. Idealized stiffness comparisons of panels in Slip-Friction Rocking	39
Figure 26. Test matrix.....	41
Figure 27. Effects of varying eccentricity of elliptical profiles	42
Figure 28. Exploded view of v-shaped slotted face plates for <i>No-Slip Traction Rolling</i>	44
Figure 29. Exploded view of vertically slotted face plates for <i>Slip-Friction Rocking</i>	44
Figure 30. Full-scale test apparatus.	45
Figure 31. Digital Image Correlation (DIC) setup.....	50
Figure 32. Prototype testing accomplished under low overburden of 133 kN (30 kips)	54
Figure 33. Prototype testing accomplished under medium overburden of 266 kN (60 kips).....	55
Figure 34. Prototype testing accomplished under high overburden of 400 kN (90 kips).....	56
Figure 35. No-Slip Traction Rolling of panel with e of 0.63 eccentricity	59
Figure 36. No-Slip Traction Rolling hysteresis plots of $e = 0.63$ panel under 3 overburden levels through $0.50D_M$	60
Figure 37. No-Slip Traction Rolling of panel with e of 0.73 eccentricity	61
Figure 38. No-Slip Traction Rolling hysteresis plots of $e = 0.73$ panel under 3 overburden levels through $0.50D_M$	62
Figure 39. No-Slip Traction Rolling hysteresis plots of $e = 0.73$ panel under 3 overburden levels through $0.75D_M$	63
Figure 40. No-Slip Traction Rolling hysteresis plots of $e = 0.73$ panel under 3 overburden levels through $1.00D_M$	64
Figure 41. No-Slip Traction Rolling of panel with e of 0.82 eccentricity	65
Figure 42. No-Slip Traction Rolling hysteresis plots of $e = 0.82$ panel under 3 overburden levels through $0.50D_M$	66
Figure 43. No-Slip Traction Rolling of panel with e of 0.88 eccentricity	67
Figure 44. No-Slip Traction Rolling hysteresis plots of $e = 0.88$ panel under 3 overburden levels through $0.50D_M$	68

Figure 45. No-Slip Traction Rolling hysteresis plots of $e = 0.88$ panel under 3 overburden levels through $0.75D_M$	69
Figure 46. No-Slip Traction Rolling hysteresis plots of $e = 0.88$ panel under 3 overburden levels through $1.00D_M$	70
Figure 47. No-Slip Traction Rolling of panel with e of 0.91 eccentricity	71
Figure 48. No-Slip Traction Rolling hysteresis plots of $e = 0.91$ panel under 3 overburden levels through $0.50D_M$	72
Figure 49. No-Slip Traction Rolling hysteresis plots of $e = 0.91$ panel under 3 overburden levels through $0.75D_M$	73
Figure 50. No-Slip Traction Rolling hysteresis plots of $e = 0.91$ panel under 3 overburden levels through $1.00D_M$	74
Figure 51. No-Slip Traction Rolling of panel with e of 0.94 eccentricity	75
Figure 52. No-Slip Traction Rolling hysteresis plots of $e = 0.94$ panel under 3 overburden levels through $0.50D_M$	76
Figure 53. No-Slip Traction Rolling hysteresis plots of $e = 0.94$ panel under 3 overburden levels through $0.75D_M$	77
Figure 54. No-Slip Traction Rolling hysteresis plots of $e = 0.94$ panel under 3 overburden levels through $1.00D_M$	78
Figure 55. Slip-Friction Rockling of panel with e of 0.63 eccentricity	79
Figure 56. Slip-Friction Rocking hysteresis plots of $e = 0.63$ panel under 3 overburden levels through $0.50D_M$	80
Figure 57. Slip-Friction Rockling of panel with e of 0.73 eccentricity	81
Figure 58. Slip-Friction Rocking hysteresis plots of $e = 0.73$ panel under 3 overburden levels through $0.50D_M$	82
Figure 59. Slip-Friction Rocking hysteresis plots of $e = 0.73$ panel under constant low overburden through $1.00D_M$	83
Figure 60. Slip-Friction Rockling of panel with e of 0.82 eccentricity	84
Figure 61. Slip-Friction Rocking hysteresis plots of $e = 0.82$ panel under constant low overburden through $0.75D_M$	85
Figure 62. Slip-Friction Rocking hysteresis plots of $e = 0.82$ panel under constant medium overburden through $0.75D_M$	86

Figure 63. Slip-Friction Rockling of panel with e of 0.88 eccentricity	87
Figure 64. Slip-Friction Rocking hysteresis plots of panel $e = 0.88$ under constant low overburden through $1.00D_M$	88
Figure 65. Slip-Friction Rocking hysteresis plots of $e = 0.88$ panel under constant medium overburden through $0.67D_M$	89
Figure 66. Slip-Friction Rockling of panel with e of 0.91 eccentricity.	90
Figure 67. Slip-Friction Rocking hysteresis plots of panel $e = 0.91$ under constant low overburden through $1.00D_M$	91
Figure 68. Slip-Friction Rocking hysteresis plots of panel $e = 0.91$ under constant medium overburden through $1.00D_M$	92
Figure 69. Slip-Friction Rockling of panel with e of 0.94 eccentricity	93
Figure 70. Slip-Friction Rocking hysteresis plots of $e = 0.94$ panel under 3 overburden levels through $0.50D_M$	94
Figure 71. Slip-Friction Rocking hysteresis plots of $e = 0.94$ panel under 3 overburden levels through $0.75D_M$	95
Figure 72. Slip-Friction Rocking hysteresis plots of $e = 0.94$ panel under 3 overburden levels through $1.00D_M$	96
Figure 73. No-Slip Traction Rolling hysteresis plots of $e = 0.94$ panel retest under high overburden through $1.00D_M$	99
Figure 74. Effective stiffness of $e = 0.63$ panel in Slip-friction Rocking	100
Figure 75. Shortening of ($e = 0.63$) panel at medium and high overburden loads during Slip- Friction Rocking	102
Figure 76. Free-body diagram of test setup exaggerating beam deflections	103
Figure 77. South elevation of panel ($e = 0.63$) in No-Slip Traction Rolling.....	111
Figure 78. Top load-bearing edges after initial steps of No-Slip Traction Rolling.	112
Figure 79. Free-Body-Diagrams of <i>No-Slip Traction Rolling</i> considering (a) top and (c) bottom contact points and (b) orientation of laminations	113
Figure 80. South elevation of panel ($e = 0.63$) in Slip-Friction Rocking	114
Figure 81. Damage to critical laminations of south elevation of panel ($e = 0.63$) after Slip- Friction Rocking.	115

Figure 82. Bottom load-bearing edges after initial round of Slip-Friction Rocking	116
Figure 83. Top corner of panel ($e = 0.73$) with opening gaps between and splits within south face laminations.	117
Figure 84. Typical damage in CLT face laminations surrounding pin hole.	118
Figure 85. Damage and elongation of hole around pipe bushing of ($e = 0.94$) panel.	118
Figure 86. Free-body-diagrams of forces on panel and severed lamination in Slip-Friction Rocking.....	119
Figure 87. Delamination and splitting of face board severed by pin connection.	119
Figure 88. Slip-Friction Rocking of $e = 0.63$ panel with (a) plot of equivalent elastic strains by FEA and (b) timber material displacements reported by DIC	121
Figure 89. DIC displacements (mm) of $e = 0.73$ CLT panel in No-Slip Traction Rolling at $1.00D_M$	122
Figure 90. DIC displacements (mm) of $e = 0.73$ CLT panel in Slip-Friction Rocking at: $1.00D_M$ for low overburden; $0.50D_M$ for medium and high overburden.	123
Figure 91. Splits at the tops of laminations in the $e = 0.73$ panel, adjacent to the vertically slotted connection	124
Figure 92. DIC displacements (mm) of $e = 0.94$ CLT panel in No-Slip Traction Rolling at $1.00D_M$	125
Figure 93. DIC displacements (mm) of $e = 0.94$ CLT panel in Slip-Friction Rocking at $1.00D_M$	126
Figure 94. Preliminary proof-test of vertically slotted connection (a) loaded to max shear and moment (b) yield lines at pin contact.....	128
Figure 95. Slip-Friction Rocking connection at $1.00DM$ of $e = 0.94$ panel (a) CLT hole elongation and DIC displacements (mm) of (b) D_x (c) D_y and (d) D_z	128
Figure 96. Wear of slotted shim edge for $e = 0.88$ panel in No-Slip Traction Rolling	130
Figure 97. Effects of various pin constraints on low-amplitude displacements	131
Figure 98. Stiffness comparison of idealized models to average linear fit of data.....	134
Figure 99. Sample rocking story arrangement supporting panelized superstructure.....	147
Figure 100. Normalized stiffness models for comparing Virtual Work and classical analyses of No-Slip Traction Rolling	160

Figure 101. Normalized stiffness models for comparing Virtual Work and classical analyses of Slip-Friction Rocking.....	164
Figure 102. Orthographic view of assembled prototype connection for No-Slip Traction Rolling.....	165
Figure 103. Main face plate enveloping slot shapes.....	166
Figure 104. Main baseplate.....	167
Figure 105. Slotted shim for ($e = 0.94$) panel.....	168
Figure 106. Slotted shim for ($e = 0.91$) panel.....	169
Figure 107. Slotted shim for ($e = 0.88$) panel.....	170
Figure 108. Slotted shim for ($e = 0.82$) panel.....	171
Figure 109. Slotted shim for ($e = 0.73$) panel.....	172
Figure 110. Slotted shim for ($e = 0.73$) panel.....	173
Figure 111. Wind restraint plate.....	174
Figure 112. Pipe bushing.....	175
Figure 113. Pin and cap assembly.....	176
Figure 114. Track shim.....	177
Figure 115. Continuous track surface.....	177
Figure 116. Exploded assembly list for No-Slip Traction Rolling steel connections.....	178
Figure 117. Equivalent elastic strain field of rotated 0.73 eccentricity panel (a) bounded by steel floor and ceiling beams and (b) viewing only CLT in elevation.....	180
Figure 118. Geometric assembly of 5-ply CLT panel laminations in FEA model.....	182
Figure 119. Laminations grouped as fully bonded (a) contact body and (b) target body of FEA model.....	183
Figure 120. (a) CLT elliptically profiled edge contact and (b) beam flange target bodies of Normal LaGrange FEA.....	183
Figure 121. Results of Normal LaGrange contact FEA model showing (a) contact status and (b) sliding along arc.....	185

Figure 122. Bearing contact stress distribution at curved edge of CLT plotted on (a) linear and (b) log color scales.....	186
Figure 123. Bearing contact stress distribution at hole in CLT plotted on (a) linear and (b) log color scales.	186
Figure 124. Pressure mapping film sensor, model 6300 by Tekscan	187
Figure 125. Piezoelectric pressure mapping (a) calibration and (b) sensor layout.	189
Figure 126. Precursory laboratory test of truncated panel with piezoelectric pressure mapping and DIC sensors.....	190
Figure 127. Contact bearing pressure map along 5-Ply CLT panel edge measured by piezoelectric sensors.....	191
Figure 128. Simplified contact pressure distribution of 5-ply CLT panel edge (a) concentrically loaded and (b) out-of-plumb.....	192
Figure 129. DIC speckle pattern comparison	196
Figure 130. DIC displacements (<i>mm</i>) of $e = 0.63$ CLT panel bearing 400 kN (90 kips) on steel (left) or neoprene (right) at top edge.....	198
Figure 131. Qualitative distribution of contact forces generated by neoprene	199

LIST OF TABLES

Table 1. Allowable Design Properties ^(a) for Lumber Laminations Used in Structurlam CrossLam CLT	4
Table 2. Allowable Design Capacities ^(a) for Structurlam CrossLam CLT produced with Table 1 Laminations	4
Table 3. Reduced Carbon Emissions Claims of Constructed Multistory CLT Buildings	6
Table 4. Performance expectations for Fixed-Base and Isolated buildings ^(a)	21
Table 5. Pros and cons of elliptical No-Slip Traction Rolling inverted pendulum.....	36
Table 6. Pros and cons of elliptical Slip-Friction inverted pendulum	37
Table 7. Cyclic prototype test protocol.....	47
Table 8. Overburden loads or simulated superstructure weight	48
Table 9. Geometric parameters for No-Slip Traction Rolling of $e = 0.63$ panel	59
Table 10. Test protocol for No-Slip Traction Rolling of $e = 0.63$ panel.....	59
Table 11. Geometric parameters for <i>No-Slip Traction Rolling</i> of $e = 0.73$ panel.....	61
Table 12. Test protocol for No-Slip Traction Rolling of $e = 0.73$ panel.....	61
Table 13. Geometric parameters for No-Slip Traction Rolling of $e = 0.82$ panel.....	65
Table 14. Test protocol for No-Slip Traction Rolling of $e = 0.82$ panel.....	65
Table 15. Geometric parameters for No-Slip Traction Rolling of $e = 0.88$ panel.....	67
Table 16. Test protocol for No-Slip Traction Rolling of $e = 0.88$ panel.....	67
Table 17. Geometric parameters for No-Slip Traction Rolling of $e = 0.91$ panel.....	71
Table 18. Test protocol for No-Slip Traction Rolling of $e = 0.91$ panel.....	71
Table 19. Geometric parameters for No-Slip Traction Rolling of $e = 0.94$ panel.....	75
Table 20. Test protocol for No-Slip Traction Rolling of $e = 0.94$ panel.....	75
Table 21. Geometric parameters for Slip-Friction Rocking of $e = 0.63$ panel.....	79
Table 22. Test protocol for Slip-Friction Rocking of $e = 0.63$ panel	79

Table 23. Geometric parameters for Slip-Friction Rocking of $e = 0.73$ panel.....	81
Table 24. Test protocol for Slip-Friction Rocking of $e = 0.73$ panel.....	81
Table 25. Geometric parameters for Slip-Friction Rocking of $e = 0.82$ panel.....	84
Table 26. Test protocol for Slip-Friction Rocking of $e = 0.82$ panel.....	84
Table 27. Geometric parameters for Slip-Friction Rocking of $e = 0.88$ panel.....	87
Table 28. Test protocol for panel with e of 0.88 eccentricity in Slip-Friction Rocking.....	87
Table 29. Geometric parameters for <i>Slip-Friction Rocking</i> of $e = 0.91$ panel.....	90
Table 30. Test protocol for Slip-Friction Rocking of $e = 0.91$ panel.....	90
Table 31. Geometric parameters for Slip-Friction Rocking of $e = 0.94$ panel.....	93
Table 32. Test protocol for Slip-Friction Rocking of $e = 0.94$ panel.....	93
Table 33. Stiffness comparisons of idealized model and fit to data through $0.5D_M$ of each panel configuration.....	133
Table 34. Average energy dissipated per cycle, E_{loop} , or area enclosed by hysteresis.....	135
Table 35. Orthotropic elasticity of fir laminations input in FEA models.....	181

ACKNOWLEDGEMENTS

Agency Sponsors

The work upon which this project is based was funded in major part through a grant awarded by the United States Department of Agriculture (USDA)/U.S. Forest Service, Wood Innovations, Federal Grant Number: 2016-DG-11420004-170, and cost-sharing investments by the University of Wisconsin – Milwaukee (UWM). The Engineering Mechanics and Remote Sensing Laboratory (EMRSL), located in Madison, Wisconsin, within the USDA Forest Products Laboratory (FPL), provided full-scale testing and additional support under a cooperator agreement with UWM. As a result of this work, the UWM Research Foundation, has filed provisional and non-provisional patent applications, in the interest of technology transfer. Laying the foundation for this work, a September 2014 Stage 1 IdeAdvance seed grant, awarded by the UW Extension and Center for Technology Commercialization, funded market discovery that enabled me to interview a diverse group of professionals seeking to develop mass timber buildings in Wisconsin and throughout the United States. Many representing USDA, UWM, and other academic or industry partners have inspired this project with their diverse skills and generous contributions.

USDA/U.S. Forest Service, Forest Products Laboratory Contributors

Douglas R. Rammer, Research General Engineer with FPL, made this research possible with guidance at critical points of the process. Steve Kalinosky, Project Leader with EMRSL, facilitated and coordinated all aspects of the full-scale tests, including safely executing hands-on tasks of specimen preparation, installation, and transport. Marshall Begel, General Engineer with EMRSL, designed details of the full-scale test apparatus and asked contemplative questions that led me to develop and compare two distinct connection prototypes. James Bridwell, General

Engineer with EMRSL, set up, programmed, performed, and documented all of the full-scale lateral-load displacement tests. Dr. Nathan J. Bechle, Computer and Electronics Engineer with EMRSL, instrumented strain gauging, linear variable displacement transducers LVDTs, and especially Digital Image Correlation (DIC) systems—sharing know-how and passion in all aspects of DIC setup and post-processing.

The dedication of several others, including Dwight McDonald and Will Kinney working in EMRSL and Joe Balczewski, Rick Beem, Joe Destree, Bruce Smith, and Randy Wruck working in fabrication shops of FPL, helped meet the fixturing and transport challenges of full-scale tests.

UWM Affiliated or Invited Contributors

College of Engineering and Applied Science

Structural Engineering Laboratory

Dr. Al Ghorbanpoor (Professor of Civil & Environmental Engineering and Director of the Structural Engineering Laboratory) mentored me throughout this project, my first experience involving full-scale structural testing. As Principal Investigator and Academic Advisor, Dr. Ghorbanpoor dedicated university resources, provided administrative and technical oversight, and envisioned the innovative analytical and experimental modeling techniques described in *Appendix C: Precursory Characterizations of Timber-to-Steel Contact* section of this work. In addition, Rahim Reshadi, Manager of the Structural Engineering Laboratory, coordinated and facilitated the prototyping and laboratory tests conducted at UWM in preparation of the full wall testing that took place at FPL. Rahim designed and built custom apparatus necessary to accomplish prerequisite testing with a combination of masterful planning and improvisation, based on decades of practical laboratory experience. Rahim, furthermore, installed strain gauges on the steel connections of the full wall system and managed safe handling and transport of the

full timber wall panels and steel components between UWM and FPL. Working under Rahim's supervision, Andrew A. Goff programmed load-displacement protocols of the prerequisite tests and assisted with prototype fabrication. Supplementing the Structural Engineering Laboratory, the Engineering Mechanics and Composites Research Laboratory furnished a DIC system used throughout precursory and full wall tests.

Prototype Fabrication

The Machine Shop made special fixtures and prototyped key components the rocking wall system, under the supervision of Mike Brown and with expertise of professional machinists John Condon and Robert Breske. Michael S. Powley provided essential digital fabrication, beginning with laser cutting components for a desktop model. Michael ultimately produced the critical steel connection components of the full-scale prototype connections with Computer Numerical Control (CNC) plasma cutting.

Computing Resources

Jason W. Bacon, Systems Manager of Research Computing Support, connected me with the high-performance computing networks and guided me through the shell scripting necessary to accomplish the Finite Element Analysis (FEA) component of this project.

Faculty Committee Members

Joining faculty advisor Al Ghorbanpoor in reviewing this work, the following committee members volunteered expertise:

- Dr. Rani Elhajjar, Associate Professor (UWM),
- Dr. Shiling Pei, Associate Professor (Colorado School of Mines),
- Dr. Nathan Salowitz, Assistant Professor (UWM),

- Dr. Konstantin Sobolev, Professor (UWM), and
- Dr. Habib Tabatabai, Associate Professor (UWM).

Peer Review Consultants

Reid B. Zimmerman, Associate Structural Engineer with KPFF Consulting Engineers in Portland, Oregon, assisted with planning, observing, and reviewing full-scale wall tests.

Industry Partners in Digital Fabrication

Shevonne Andersen, Principal of Andersen and Andersen Technical Services, LLC, of Elm Grove, Wisconsin, created Building Information Models (BIM) and Computer Aided Drafting (CAD) of steel connections and elliptical rolling diagrams providing the basis for many figures of this report.

Hank Wiedmeyer directed fabrication of the vertically slotted steel connection prototypes by Ace Iron & Steel Corporation of Milwaukee, Wisconsin.

Ryan Stock, Production Manager at Mattech, Inc., in Milwaukee, Wisconsin, provided precision drilling and tapping of larger scale parts.

Structurlam Mass Timber Corporation, formerly Structurlam LLP, provided the CLT panels and timber fabrication to digital design specifications.

I. Introduction

Sizable forest products economies of each populous world continent promise fertile ground for continued international growth of tall cross-laminated timber (CLT) panelized construction, but several wood industry hubs also bear the burden of significant earthquake risks. These regions expect dramatically better seismic response from CLT structures, in order to earn market share over earthquake-resisting systems currently listed in building codes. Evolution of seismic design in the precast concrete industry has blazed a trail leading panelized construction to outperform prevalent steel and cast-in-place concrete competitors in resiliency. This project emulates the progression pioneered by precast concrete with a new wood embodiment of an inverted pendulum system, shaped with a holistic vision focused on multistory CLT platform construction assembly. Curving the load-bearing edges of walls made from stock CLT panels induces kinematic rocking capable of:

- (1) Departing on large displacement excursions to effectively isolate superstructures from ground motions,
- (2) Tapping into potential energy to passively self-center and align through oscillatory damping, and
- (3) Averting material damage concentrated at the corners of conventional rectangular rocking wall panels.

Building upon theoretical precedents, this study developed practical details to show the implications of connection design and advance the concepts closer to engineering practice.

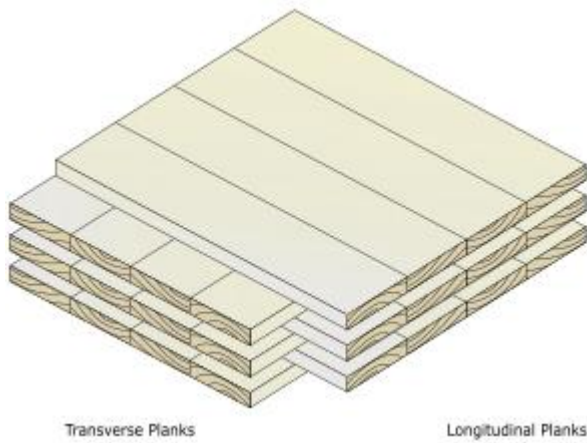


Figure 1. Cross-Laminated Timber
 Source: (Gagnon et al. 2013, p.4)



Figure 2. Sections of Common CLT Layups

The Emergence of CLT as a Mass Timber Composite

Cross-Laminated Timber (CLT) originated in Europe and took root in building construction, via collaborations between industry and academia, during the late twentieth century (M. Mohammad 2012). Comprising of adhesively bonded wood laminations, as arranged in Figure 1, the material composition of CLT, except for changes in adhesive type, generally resembles that of unidirectional glued laminated timber (glulam). The cross-ply layups, however, liken CLT to plywood. Figure 2 illustrates common CLT patterns made from three, five, seven, and nine layers of orthogonally stacked laminations (Gagnon et al. 2013). Panels produced by these two-dimensional configurations achieve composite strength that maximizes the structural capacity of individual sawn lumber boards with adhesive bonds that effectively provide continuous bracing.

Table 1 lists the assumed allowable structural design properties of visually graded softwood laminations that a North American manufacturer used to produce each lamella, or layer, of CLT panels tested in this study. Equal values in the longitudinal and cross-ply directions indicate laminations of the same strength throughout the panel. Table 2 lists the effective and allowable

laminated properties of the CLT panel, determined in accordance with North American production standards, and highlights values for the 5-ply layup of visually graded CLT used for this study (APA—The Engineered Wood Association 2015). Table 2 includes two rows of values for the 5-ply layup, because while this project was in progress, the manufacturer altered production practices to produce lamellae of constant thickness. CLT panels of Table 2 exhibit orthotropic properties because the odd number of lamellae orients the wood grain unequally, with respect to orthogonal directions. Each lamination, or individual wood board, moreover, behaves orthotropically and resists forces most efficiently when aligned parallel to grain. Compositely, CLT panels exhibit robust structural properties.

On the scale of individual laminations, the properties essentially match standards for species and grades used to design conventional timber structures. The specific gravity of laminations must meet or exceed 0.35, and moisture content of the laminations must not exceed 12%, according to North American Standards (ANSI/APA PRG 320 2012). Moisture meter probes into the first, second, and third laminations of the CLT supplied for this project reported moisture content of 9 to 9.5% in the face laminations and 10 to 10.5% in the central laminations at the time of testing.

Table 1. Allowable Design Properties^(a) for Lumber Laminations Used in Structurlam CrossLam CLT
(for use in the U.S.)

CLT Grade	Major Strength Direction						Minor Strength Direction					
	F _{b,0} (psi)	E ₀ (10 ⁶ psi)	F _{t,0} (psi)	F _{c,0} (psi)	F _{v,0} (psi)	F _{s,0} (psi)	F _{b,90} (psi)	E ₉₀ (10 ⁶ psi)	F _{t,90} (psi)	F _{c,90} (psi)	F _{v,90} (psi)	F _{s,90} (psi)
V2M1	875	1.4	450	1150	135	45	875	1.4	450	1150	135	45

For SI: 1 psi = 0.006895 MPa

(a) Tabulated values are allowable design values and not permitted to be increased for the lumber size adjustment factor in accordance with NDS. The design values shall be used in conjunction with the section properties provided by the CLT manufacturer based on the actual layout used in manufacturing the CLT panel.

Source: (APA—The Engineered Wood Association 2015)

Table 2. Allowable Design Capacities^(a) for Structurlam CrossLam CLT produced with Table 1 Laminations
(for use in the U.S.)

CLT Grade ^(b)	Layout #	Depth (in.)	Weight (psf)	Lamination Thickness (in.) in CLT layout									Major Strength Direction				Minor Strength Direction			
					⊥		⊥		⊥		⊥		F _b S _{eff,0} (lb _r -ft/ft)	E _I _{eff,0} (10 ⁶ lb _r -in. ² /ft)	GA _{eff,0} (10 ⁶ lb _r /ft)	V _{r,0} (lb/ft)	F _b S _{eff,90} (lb _r -ft/ft)	E _I _{eff,90} (10 ⁶ lb _r -in. ² /ft)	GA _{eff,90} (10 ⁶ lb _r /ft)	V _{r,90} (lb/ft)
V2M1 V2M1.1	SLT3	3.90	10.5	1.26	1.38	1.26							1,800	79	0.49	1,340	280	3.7	0.52	495
	SLT5	6.66	17.0	1.26	1.38	1.38	1.38	1.26					4275	321	1.0	1860	2410	96	1.0	1440
	175V	6.88	15.0	1.38	1.38	1.38	1.38	1.36					4701	366	1.1	1980	2403	96	1.1	1440
	SLT7	9.42	25.0	1.26	1.38	1.38	1.38	1.38	1.38	1.26			7700	818	1.5	2370	5500	364	1.6	1970
	SLT9	12.1 8	32.0	1.26	1.38	1.38	1.38	1.38	1.38	1.38	1.38	1.26		12,075	1662	2.1	2875	9675	898	2.1

For SI: 1 in. = 25.4 mm; 1 ft = 304.8 mm; 1 lb_r = 4.448 N

(a) Tabulated values are allowable design values and not permitted to be increased for the lumber size adjustment factor in accordance with the NDS.

(b) The CLT grades are developed based on ANSI/APA PRG 320, as permitted by the standard, using visually graded No. 2 SPF lumber in both major and minor strength directions. 5-Layer CLT values are highlighted, for CLT grades V2M1 and V2M1.1 only, because pendulum isolator prototypes, for this project, were produced from this material.

Source: (APA—The Engineered Wood Association 2015)

The Rise of Cross-Laminated Timber

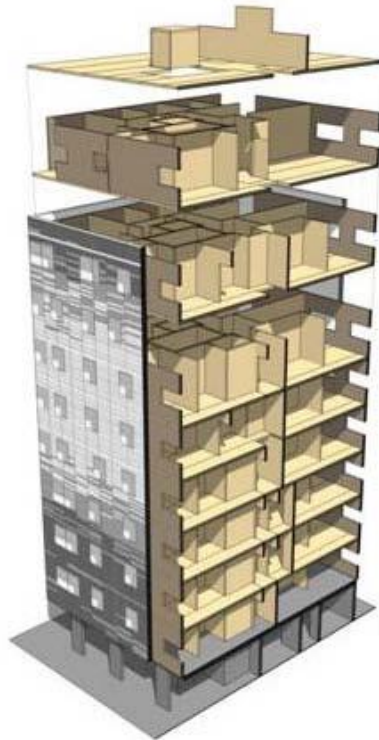


Figure 3. CLT panel assembly of Stadthaus on concrete podium
Source: (Waugh et al. 2010)

Completion of a nine-story London apartment building (Stadthaus illustrated in Figure 3) and a ten-story Melbourne apartment building (Forté) piqued global interest in panelized cross-laminated timber (CLT) construction circa 2012 (Waugh et al. 2010, Gröndahl 2012, Lend Lease 2012, Risen 2014). These fully panelized structures rose far above the 5 or 6-story limits of conventional timber framing with assemblies of walls and floors that featured the versatility of CLT. Largely leveraging newfound composite strength, advantages of prefabrication, and sustainability of renewable timber—a burgeoning international portfolio of tall twenty-first century CLT structures ensued (Perkins + Will 2014).

Table 3. Reduced Carbon Emissions Claims of Constructed Multistory CLT Buildings

Project Name	Country	Timber Stories (Qty.)	Structure Type	Carbon Sequestration (tons CO ₂)	Avoided Carbon (tons CO ₂)	Net Carbon Savings (tons CO ₂)	Ref.
Stadthaus, Murray Grove	United Kingdom	8	Panelized CLT	186	137	323	(Vaughan et al. 2010)
Forté Tower	Australia	9	Panelized CLT	700	700	1400	(Johnson 2014)

Tons of CO₂ are metric system units. One metric ton approximately equals 1.102 U.S. ton.

In addition to heights, tall CLT buildings boast compelling eco benefits. Timber sequesters carbon and saves additional carbon emissions, by displacing steel and concrete materials that require much more energy to produce (Sathre and O’Connor 2010). The multistory archetype, furthermore, efficiently meets the housing needs of growing populations trending toward urbanization (Green and Karsh 2012, Lehmann 2013, Skidmore 2014). Table 3 summarizes the claims of net carbon saved by Stadthaus and Forte, itemized in terms of carbon sequestered by the wood and carbon avoided by displacing steel and concrete with wood. CLT production, furthermore, promises to reinvigorate forest products economies (Ritter et al. 2011).

Despite the obvious boons of sustainability, few fully panelized CLT towers have been replicated in recent years. Instead, a multitude of multistory building archetypes that combine wood with other structural materials emerged and prompted categorization of tall timber construction (Foster et al. 2016). Current tall wood building trends favor hybrid structural schemes, over fully panelized CLT systems. For example, the recently constructed 18-story Brock Commons, pictured in Figure 4 on the campus University of British Columbia campus, expedited approval of the lateral force-resisting system by pairing the timber gravity system with prequalified reinforced concrete cores (Fast and Jackson 2017). Development of a 21-story building based on a similar timber frame and reinforced concrete core archetype is underway in Milwaukee, Wisconsin (Daykin 2019). While hybrid construction practices prevail throughout the

construction industry, many of the options relegate CLT to floor and roof decks and signal that the industry awaits technological advances in wall systems.



Figure 4. Construction of Brock Commons pairing timber with reinforced concrete
Source: (Aston Ostry, UBC Media Relations)

II. Literature Review

During the first decade of the 21st century, the SOFIE research project culminated a seismic testing program with full-scale 3D shake-table tests of two buildings, 3 and 7 stories tall (Ceccotti and Follesa 2006, Ceccotti et al. 2013). Though few official standards of CLT construction had yet been set, the SOFIE test structures exemplified conventions emerging from a rapidly growing European CLT industry. Both structures assembled panels in platform-style arrangements, sandwiching floor panels between the bearing ends of wall panels and stacking

stories similarly to conventionally framed timber construction. Each building, furthermore, used commercially available hold-down anchorages, shear transfer angles, and standard dowel fasteners to attach floors, walls, and foundations. Laminated veneer lumber (LVL) splined panels in plane. Though the test structures generally survived intense shaking, nails pulling out at the base connections prompted interventions between tests. Less conspicuously, peak accelerations exceeding 3 and a half times gravitational acceleration at the top floor level of the 7-story structure, pictured in Figure 5, added to performance concerns (Ceccotti et al. 2013). The tests pioneered by the SOFIE project, therefore, revealed a need to develop seismic design approaches to better suit the inherent rigidity of CLT.

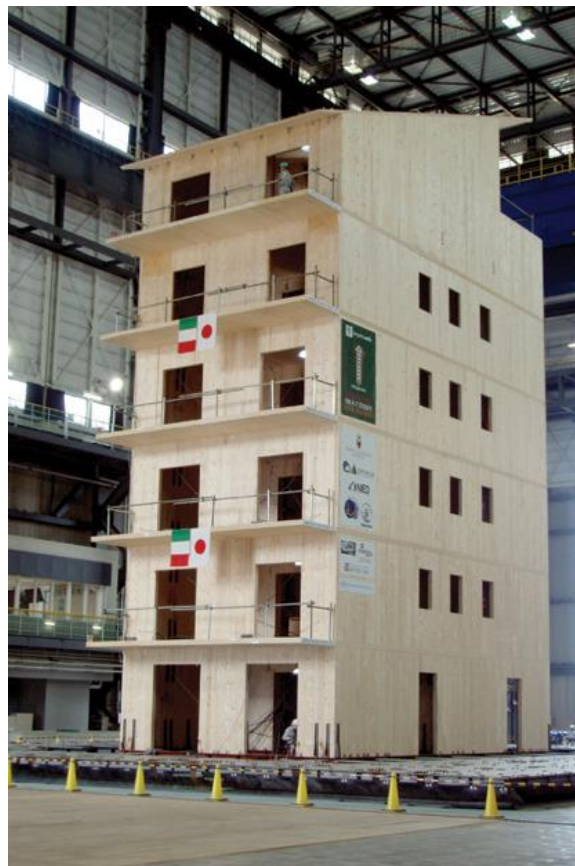


Figure 5. CLT platform structure on the E-Defense shake table, Japan
Source: (van de Lindt et al. 2013)

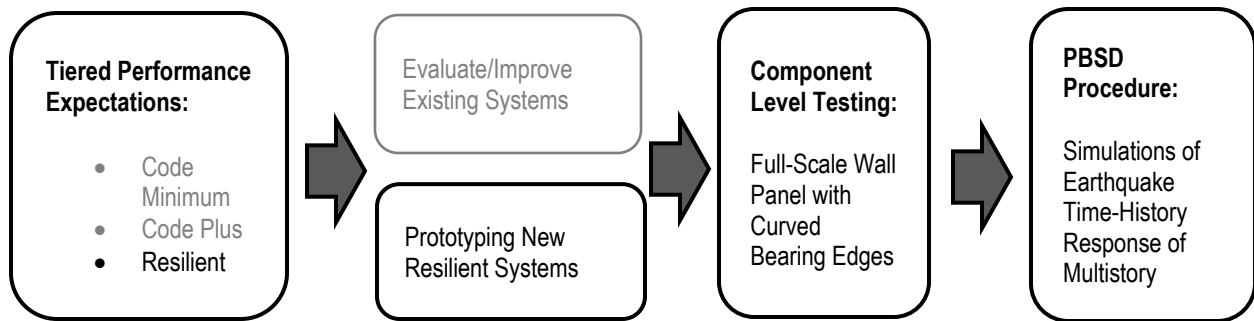


Figure 6. Project sequence patterned after the *Structural Research Drive* (Pei et al. 2016)

Mapping a Comprehensive Seismic Development Strategy

The “Structural Research Drive” maps a comprehensive strategy for developing various CLT lateral systems, based on *code minimum*, *code plus*, and *resilient* tiers of seismic performance expectations (Pei et al. 2014, Pei et al. 2016). Figure 6 patterns the “Structural Research Drive” to emphasize the *resilient* objectives central to this project. “Code Minimum” approaches refer to the most widely applied seismic design parameters, which rank among the most highly anticipated developments for CLT wall systems. Though standard seismic design parameters for CLT are essential, the “Structural Research Drive” asserts that CLT should target resilient objectives for more competitive inroads (Pei et al. 2016). Western United States, for example, support a sizable forest products economy, sensitive to market downturns in low-rise housing (Keegan et al. 2011). At the same time, the West Coast bears the burden of over \$4.5 billion in estimated annualized losses from earthquakes (Federal Emergency Management Agency (FEMA) 2017). CLT construction, therefore, promises multifaceted revitalization for the western United States, by aiming for sustainable and resilient structural solutions.

Inelastic Ductility: The Force-Based Approach

Code minimum objectives refer to the most commonly applied seismic design provisions of the building code. In the United States, most engineering practitioners reference “Chapter 12” of the *ASCE 7* structural engineering standard early and often during the design of seismic force-resisting systems (ASCE/SEI 7 2017). “Table 12.2-1” of *ASCE 7* lists design coefficients and factors, height restrictions, and detailing requirements, for prequalified seismic force-resisting systems. Efforts to add CLT systems to this list of prequalified seismic force-resisting systems are currently in progress and proposing parameters for future editions of structural design standards (Amini et al. 2014).

Figure 7 plots the general methodology behind the most commonly applied, force-based seismic design provisions (Building Seismic Safety Council 2015). Designing structures for completely elastic response, at the V_E level, to an earthquake will produce uneconomical or even infeasible results for most structures. Elastic designs, furthermore, generally lead to high floor accelerations. To reduce seismic design forces and facilitate design procedures, such as Equivalent Lateral Force analysis, structures are designed at elastic load levels, V_s , anticipating that the structure will respond inelastically, well before and even after, the structure reaches its maximum yield strength, at the V_y level. According to best practices, designers should consider the formation and sequence of plastic hinge formation, but prescriptive provisions of the code can mask these concepts that become more explicit in performance-based design methodology (Applied Technology Council (ATC) et al. 2006).

Determining values for Response Modification Factor, R , Overstrength Factor, Ω_o , and Deflection Amplification Factor, C_d , requires rigorous design, analysis, testing, and statistical

procedures outlined in recently developed FEMA P-695 protocols (Applied Building Technology Council 2009). Fulfilling the requirements of FEMA P-695 and achieving code prequalification lays a foundational tier of seismic performance for CLT structures. As Figure 7 demonstrates, however, inelastic response invites material damage and amplified residual displacements, to dissipate energy and protect occupants. Baseline seismic performance defined by building codes seeks only to prevent collapses, so that building occupants may evacuate safely. As automobiles use crumple zones to dissipate energy and protect the integrity of the driver and passenger compartments in collisions, buildings sacrifice plastic hinges to maintain integrity of the story spaces in earthquakes. Plastic hinging and residual displacements that render buildings uninhabitable after intense ground shaking, therefore, should come as no surprise.

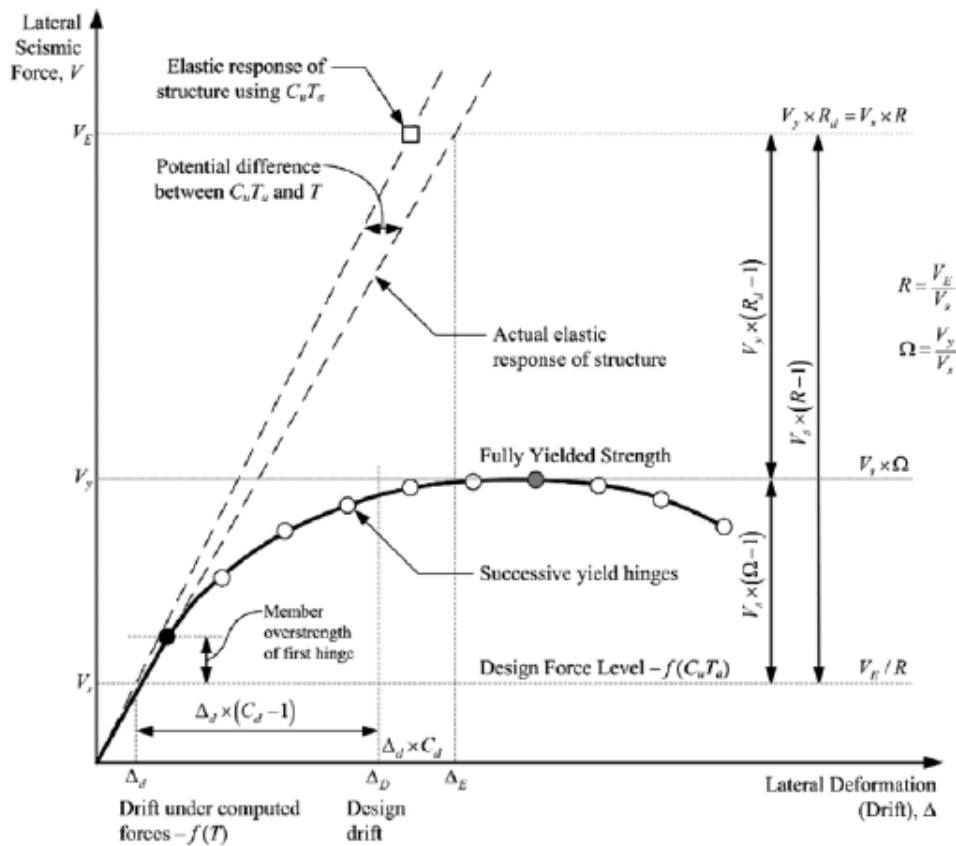


Figure 7. Inelastic force-deformation curve
 Source: (Building Seismic Safety Council 2015)

Controlled Rocking: An Evolving Displacement-Based Alternative

The rigidity of CLT poses a mismatch with more inherently ductile materials such as steel or reinforced concrete. While many perceive a lack of ductility disadvantageous, alternative approaches in precast concrete, mass timber, and seismic isolation systems have demonstrated that rigidity presents its own benefits. Rocking offers a potentially resilient approach that has been pioneered by the precast industry and recently adapted with signs of promise in timber. The following sections review a progression of rocking concepts that have been applied to wall systems for seismic mitigation.

Mechanics of Inverted Pendulum Rocking

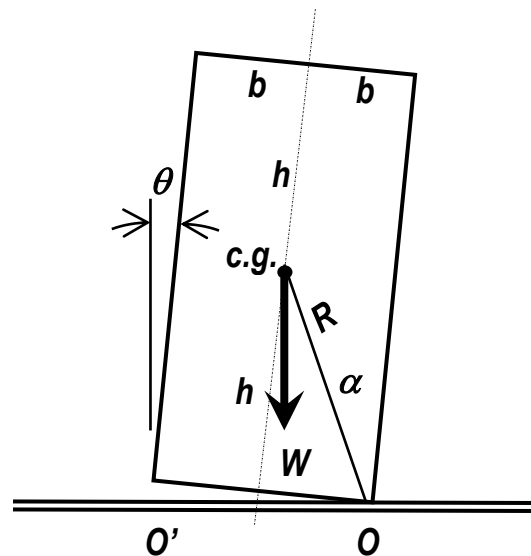


Figure 8. A rocking rigid block
Source: (Housner 1963, p. 404)

Parametric analysis of the rigid rectangular block of Figure 8, set to rocking by dynamic excitations, helped explain why slender and seemingly unstable structures had survived devastating earthquakes (Housner 1963). Housner assessed rocking stability by equating square, sinusoidal, and earthquake pulse energy with the energy required to overturn the block. For three

dynamic pulse types, Housner presented equations expressing the block width required to resist overturning as a function of height and accelerations. Evaluating the equations across a range of rectangular proportions revealed “an unexpected scale effect which makes the larger of two geometrically similar blocks more stable than the smaller block” (Housner 1963, p. 415). Applying inverted pendulum mechanics of the rigid block to an elevated water tank, Housner estimated overturning resistance of the tank at greater than 50% probability, but cautioned, “At present it is not known how to design a rocking structure to have a specified small probability of failure” (1963, p.417). Dynamic analyses of the inverted pendulum block, thus, revealed an analytical limitation of static-force analysis and a practical limitation of overturning. The scale effect revealed by Housner also explains why blocks must be slender to preclude sliding and induce rocking.

Evolution of Precast Concrete Panelized Systems

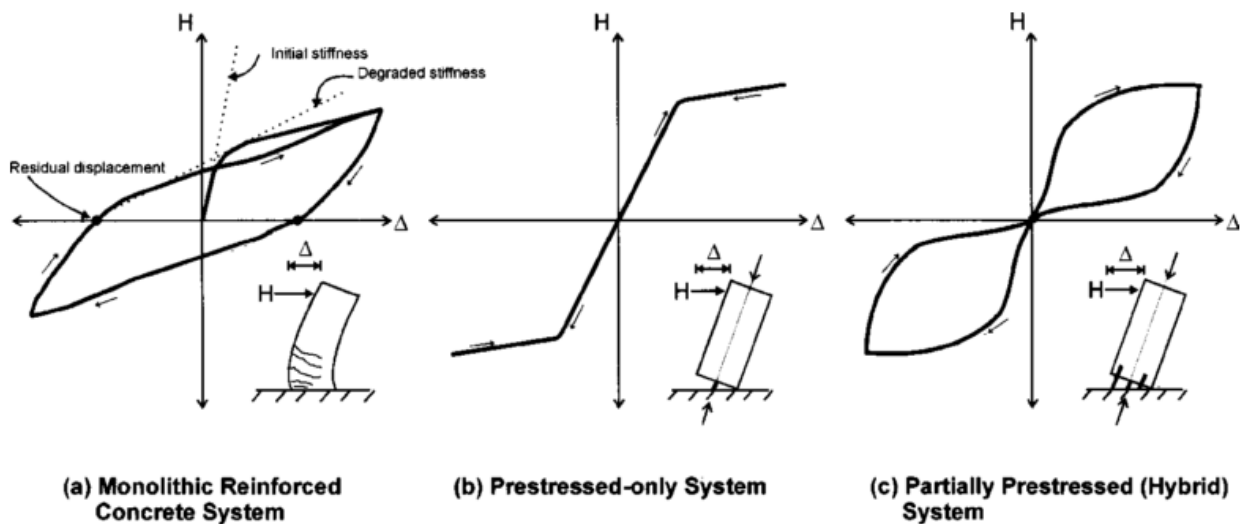


Figure 9. Hysteretic behavior of various concrete walls
 Source: (Holden et al. 2003, p. 287)

Several decades after Housner’s seminal paper relating inverted pendulum mechanics to the seismic response of structures, the precast concrete industry availed the benefits of rocking by

safeguarding overturning with vertically unbonded post-tensioning (PT). Controlled rocking transformed the rigidity of precast concrete wall panels from a seismic performance liability into an asset. Rather than rock monolithically, precast panelized shear walls evolved to make use of joints, or “separation gaps” (Restrepo and Rahman 2007, p. 1561). Kurama et al. controlled the lateral flexibility of horizontally jointed shear walls with vertical unbonded PT (Kurama et al. 1999). Several precast concrete projects later developed *hybrid* or *partially post-tensioned* walls, across horizontal joint interfaces, to combine the *energy dissipation* of yielding mild steel with the *self-centering* benefits of rocking restrained by vertically unbonded PT (Kurama 2002, Holden et al. 2003, Kurama 2005, Restrepo and Rahman 2007). Perez et al. similarly developed schemes to add energy dissipation with ductile connectors along vertical joint interfaces between rocking panels (Perez et al. 2004). The U-shaped Flexural Plate (UFP) connector, which had previously demonstrated stable and predictable hysteretic performance, continues to serve as an energy dissipater of choice for vertically jointed panel systems (Schultz and Magaña 1996). Figure 9 summarized the evolution of concrete rocking walls (Holden et al. 2003) . Monolithic reinforced concrete systems dissipated a lot of energy but degraded in stiffness and permanently deformed, leaving residual displacements. Rocking walls re-centered and avoided significant damage but offered virtually no energy dissipation, so a variety of components placed at joint interfaces reintroduced ductility to produce the characteristic “*flag-shape*” hysteresis (Sarti et al. 2015).

Timber Adaptations

Timber adaptations of the rocking mechanism generally fall into one of three categories. A leading category of Vertically Post-Tensioned Rocking Walls is rapidly approaching final stages of development for CLT, which will culminate with full-scale shake-table testing. A second

category of Slip-Friction Anchored Rocking Walls relies on fastener pre-tension to allow frictional sliding when overloaded and restore the system to self-centering equilibrium. A third category of Ductile-Anchorage Walls yields connections to dissipate energy but seeks to induce rocking as the preferred kinematic mechanism over sliding.

Vertically Post-Tensioned Rocking Walls

Several timber rocking shear walls have recently adapted technologies pioneered in precast concrete. Researchers in New Zealand tested three-dimensional assemblies of cross-laminated timber shearwall cores, at half scale, including a high-performance seismic option using vertical PT and UFP connectors (Dunbar et al. 2014). Another similar adaptation tested laminated veneer lumber (LVL) hybrid PT walls, at two-thirds scale, with energy-dissipating bars crossing the horizontal interface with a concrete foundation (Sarti et al. 2015). Researchers in the United States tested several vertically post-tensioned CLT rocking shear walls, including multiple specimens rocking on a steel beam base, one specimen rocking on a CLT floor panel base, and a pair of rocking walls coupled by UFP connectors, as illustrated in the free-body diagram of Figure 10 (Ganey et al. 2017). Ganey et al. added deformation effects at panel base corners, upon which the rectangular panels pivot, to calculate the static equilibrium forces. Toe crushing typically controlled capacity of the rocking walls in the experiments, but Ganey et al. observed floor failures when CLT walls rocked on CLT slabs.

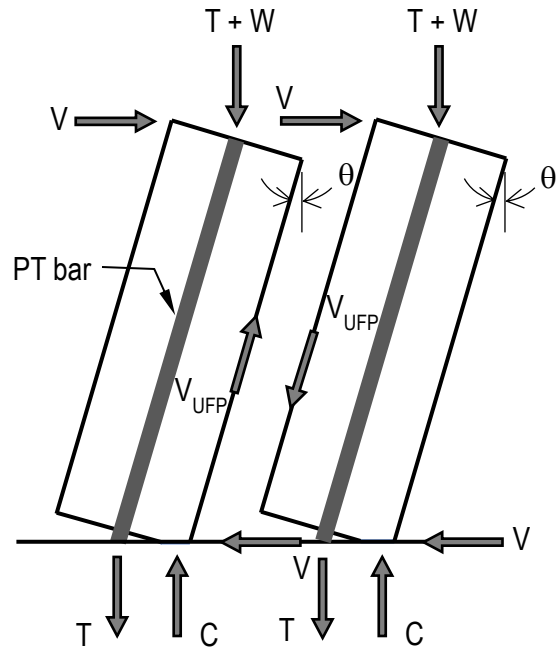


Figure 10. Free-body diagram of coupled CLT walls
 Source: (Ganey et al. 2017).



Figure 11. Vertically post-tensioned (PT) CLT wall with UFPs
 Viewed at (a) ground floor and (b) top of wall PT anchorage.
 Peavy Hall, Oregon State University

Figure 11 photographs a vertically post-tensioned CLT wall system with UFP connectors to boundary columns, installed on the campus of Oregon State University. The installation is

among the first U.S. applications, and several researchers are advancing development of similar systems. Shake-table tests of a 2-story timber structure of vertically post-tensioned walls, diaphragms, and glulam framing, demonstrated resiliency with a construction assembly that exhibited very little damage after intense replicated earthquakes (Pei, Blomgren, et al. 2018, Pei, van de Lindt, et al. 2018). Future shake-table tests will soon examine 10-story timber archetypes featuring various vertically post-tensioned CLT walls (Pei, Berman, et al. 2018). Vertically post-tensioned walls, therefore, generally show promise for balloon-type construction assemblies, where the CLT rocking walls generally act as one monolithic wall along the full height of the building and span past each floor level.

Slip-Friction Hold-Downs

For alternatives to vertical post-tensioning, precast concrete engineering has explored slip-friction, energy-dissipation devices to hold-down pivoting base corners of rocking rectangular panels (Bora et al. 2007). Brass shims between steel plates have proven reliability in frictional energy dissipation and applicability to a variety of structures (Grigorian et al. 1993). Timber adaptations generally implement slip-friction concepts with innovative hold-down connections in recent tests of both LVL and CLT panel specimens (Loo et al. 2012, Loo et al. 2014, Hashemi et al. 2017). Slip-friction hold-down anchorages rely on pre-compressed Bellville washers or disc springs to generate consistent friction and normal forces on planes of the connection faying surfaces to re-center the system. Hashemi et al. presented inclined faying surfaces that facilitate re-centering. Laboratory tests of slip-friction hold-down connections show consistent and predictable energy dissipation and potential for resilient performance. Pre-stressing of fasteners in the anchorage connections replaces the function of unbonded vertical post-tensioning and adds frictional energy dissipation.

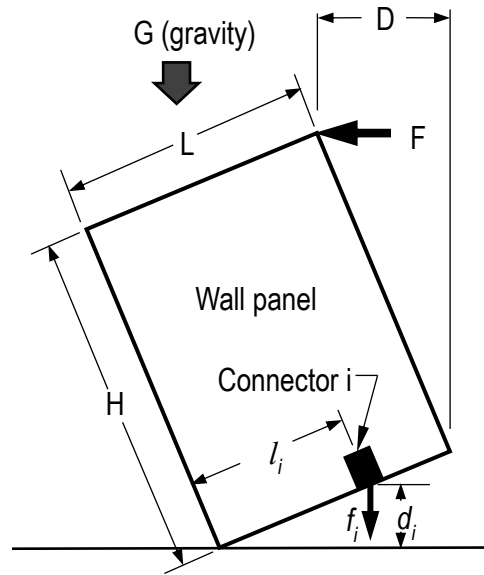


Figure 12. Simplified kinematics of wall with base anchorage
Source: (Pei 2013)

Ductile Anchorage

Conventional hold-down and shear connectors have achieved a wide range of performance in cross-laminated timber. Early in development, researchers in Europe identified boundary conditions that determined whether CLT wall panels would respond to lateral forces by racking, sliding, or rocking (Dujic et al. 2004, Dujic et al. 2005, Dujic et al. 2006). Similar concepts tracking displacements from various response modes extended to coupled wall panels (Gavric et al. 2015). Numerous models of pinched hysteresis behavior have been developed via tests for analytical modeling of these systems (Pei 2013, Rinaldin et al. 2013, Shen et al. 2013, Schneider et al. 2014, Schneider et al. 2015). Figure 12 presents a widely cited simplified kinematic model for base-connected CLT walls. Though not entirely resilient, because hold-downs intend to yield, rocking provides a stable mechanism for engaging base connections and mitigating excessive sliding.

Isolation as a Path to Seismic Resiliency

Seismic isolation of structures has developed over decades into a high-performance seismic mitigation option, adaptable to a wide variety of rigid construction, including CLT. Slip-friction pendulum isolators rank highly among isolation system components for the ability to provide two main desirable features: re-centering and energy dissipation. Complexity of slip-friction isolators varies from simple, single-stage mechanisms to intricate multi-stage pendulum instruments that can effectively isolate a broader spectrum, including near-fault ground motions (Morgan and Mahin 2011). Numerical experiments of single-stage slip-friction pendulum isolators demonstrated the potential isolation benefits for multistory wood-framed structures and developed procedures for selecting an effective pendulum radius (van de Lindt and Jiang 2014). While the majority of seismic isolation uses base-isolated building configurations, another numerical study demonstrated that CLT buildings could be designed using inter-story isolation to distribute displacements along the height of the building, which makes implementation of the isolation scheme more practical (Bolvardi et al. 2018). Isolation schemes in the literature typically investigate spring and damper devices placed beneath wood structures, but this project explores whether CLT wall panels, themselves, can act like seismic isolation. Figure 13 shows where elliptically profiled rolling walls fit into the overall context of rocking wall development.

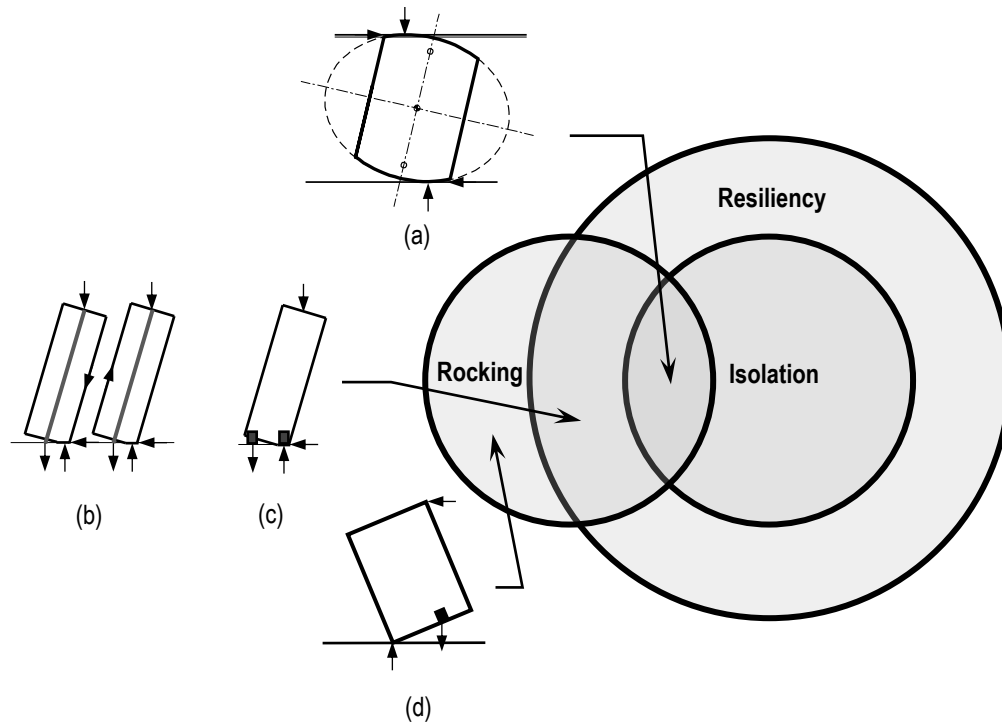


Figure 13. Classification of rocking wall developments in timber

- (a) new elliptically profiled rolling walls,
- (b) vertically post-tensioned rectangular walls with ductile coupling,
- (c) slip-friction anchorage of rectangular walls, and
- (d) ductile anchorage of rectangular rocking walls.

General Considerations

Within the framework of the *ASCE 7* structural building code, “Chapter 17” performance standards for seismically isolated structures provide a clear path to resiliency (*ASCE/SEI 7 2017*). Table 4, adapted from *ASCE 7* “Table C17.2-1,” shows that seismically isolated structures expect to outperform conventional fixed-based buildings in moderate to major earthquakes (*ASCE/SEI 7 2017*). Fixed-based schemes rely on ductility to survive earthquakes, but isolated schemes generally displace to reduce earthquake-induced forces.

Table 4. Performance expectations for Fixed-Base and Isolated buildings^(a)

Performance Measure	Earthquake Ground Motion Level		
	Minor	Moderate	Major
Life safety: loss of life or serious injury is not expected	F, I	F, I	F, I
Structural damage: significant structural damage is not expected	F, I	F, I	I
Nonstructural damage: significant nonstructural or contents damage is not expected	F, I	I	I

(a) "F" indicates fixed base; "I" indicates isolated.
Adapted from Commentary Chapter C17: (ASCE/SEI 7 2017)

Rather than prescribe specifics regarding isolators, the recently revamped seismic isolation provisions of *ASCE 7* specify performance requirements (ASCE/SEI 7 2017). The seismic isolation commentary chapter of *ASCE 7* defines acceptable seismic isolation systems with four fundamental features:

1. Horizontal and vertical stability when subjected to design displacements,
2. Inherent restoring forces that increase with increasing lateral displacement,
3. Durability without significant degradation under repeated cycles, and
4. Quantifiable engineering parameters (namely stiffness and damping).

Isolation systems, therefore, provide the basic attributes of a seismically resilient system. Figure 14, moreover, demonstrates that various modes of isolator behavior can accomplish the overarching goals of seismic isolation (Building Seismic Safety Council 2015).

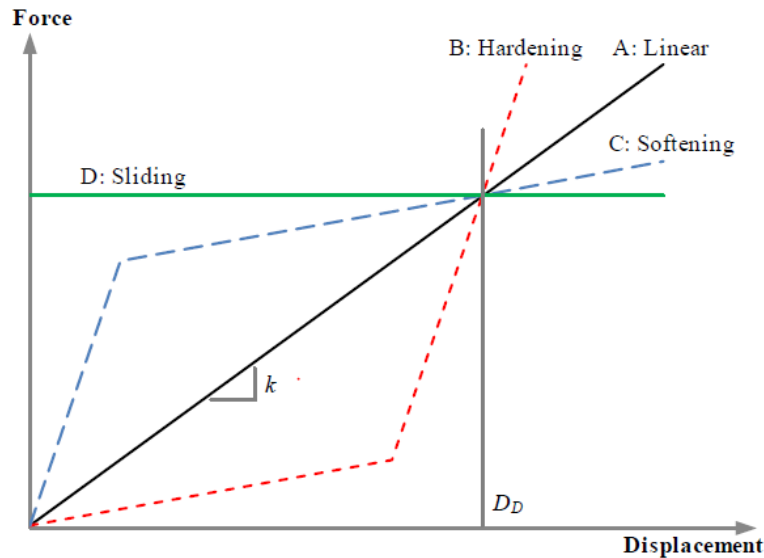


Figure 14. Idealized lateral force-deflection relationships for isolation systems
 Stiffness effects of sacrificial wind-restraint systems not shown for clarity
 Source: (Building Seismic Safety Council 2015)

Using isolation standards as a guide, this project prototypes an inverted pendulum wall system that can provide soft-story isolation as schematically illustrated in Figure 15. As depicted, rocking soft stories isolate superstructures by displacing. While current design practice discourages soft stories, as a vertical irregularity, an intentional rocking soft story mechanism poses several advantages apt for CLT archetypes (Pei et al. 2014). Rocking soft stories occupy space that can act as mechanical level transitions between foundation or podium structures and the superstructure. Rocking soft stories take up most of the lateral displacements, which allows superstructures to remain rigid. Any rigid construction scheme, including platform assemblies, can be built between rocking soft stories. Rocking soft-stories, furthermore, can leverage superstructure weight to re-center the pendulum mechanism.

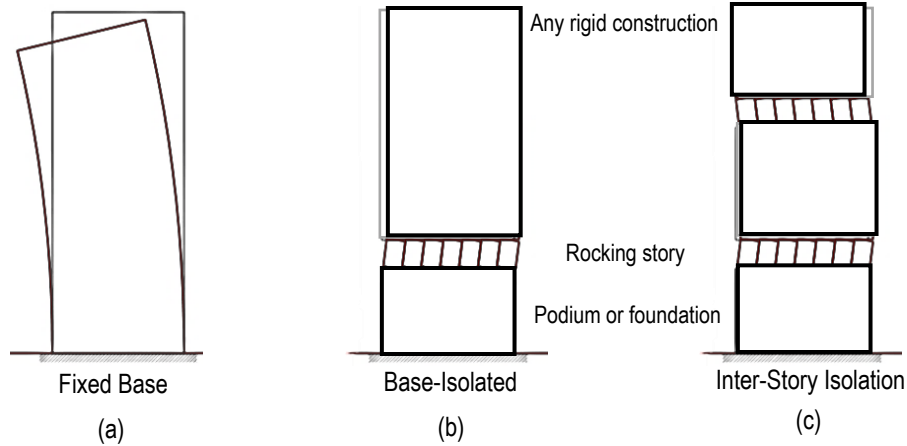


Figure 15. Elevation view of 3 multistory building schemes
Source: (Lo Ricco et al. 2018)

III. Methodology

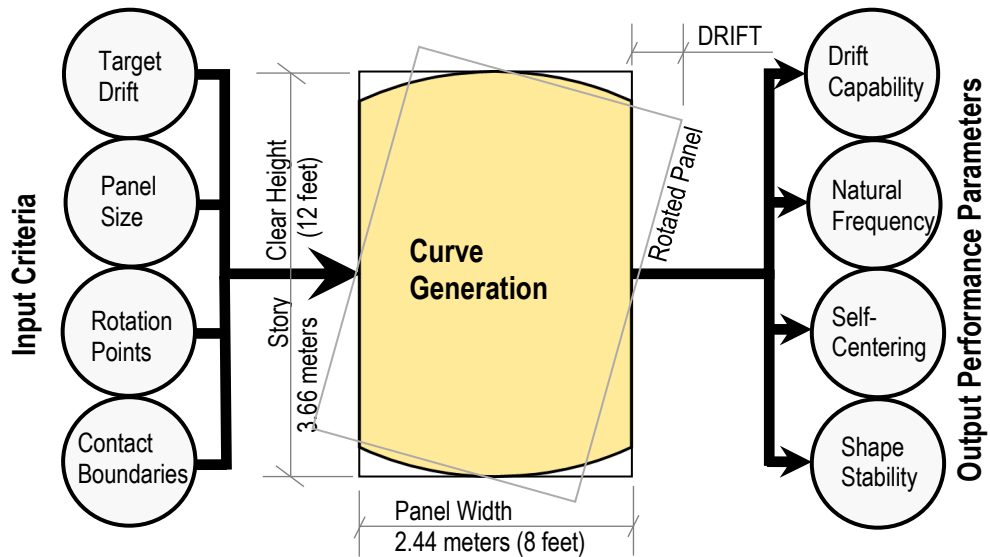


Figure 16. Shaping CLT panels for rocking response to earthquakes
Source: (Lo Ricco et al. 2018)

System Model

The story of development began with a simple question. Would rocking along a curve accomplish a smooth self-centering response to earthquakes? Curve geometry makes it possible to achieve a cost-effective and resilient rocking wall system that:

- Leverages digital fabrication techniques already prevalent in the CLT industry,

- Integrates with any type of rigid superstructure, including platform construction assemblies,
- Isolates superstructures by reliably displacing to a high capacity, and
- Passively re-centers under superstructure weight without reliance on post-tensioning.

Figure 16 organizes the initial concepts of curve generation that drive the CLT rocking wall system. This project began with the hypothesis that curvilinear cuts to the top and bottom loadbearing edges of a CLT panel could facilitate rocking response to earthquakes. Research of rocking half disks with circular, elliptical, and parabolic boundary profiles showed that geometric proportions controlled natural frequency and stability of the pendulum action (Mazzoleni et al. 2015).

Elliptical Rolling Rod Isolation

Among curved geometric options, the ellipse had previously demonstrated ability to isolate superstructures from ground motions (Jangid and Londhe 1998, Londhe and Jangid 1999). Jangid and Londhe showed the effectiveness of elliptical rolling rods as isolation with numerical models of a rigid-frame superstructure placed atop the rods, as shown in Figure 17. As the elliptical rods roll, geometric eccentricity provides inherent self-centering. Rolling pendulum isolation concepts have a long history but lack practical development (Harvey Jr. and Kelly 2016). This project invented steel connection details to reduce the concept of elliptical rolling isolation to practice with CLT panels. The following analysis details mechanics of elliptical rolling isolation, with practical enhancements, and introduces a new slip-friction inverted pendulum system.

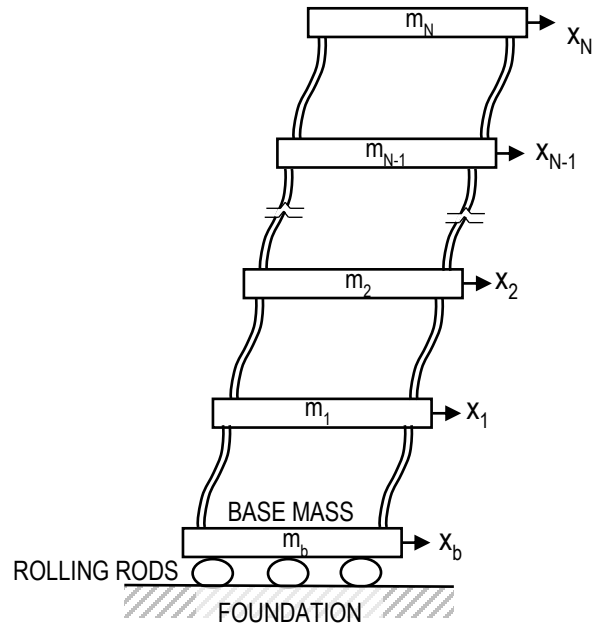


Figure 17. Rigid superstructure isolated on elliptical rolling rods
 Source: (Jangid and Londhe 1998)

No-Slip Traction Rolling

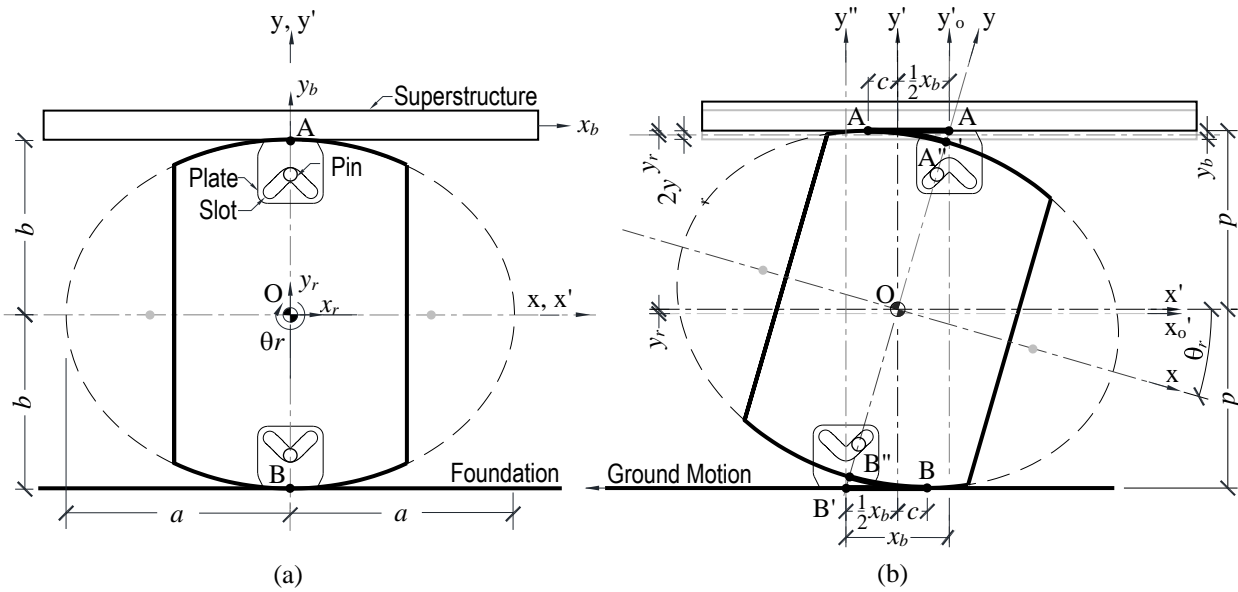


Figure 18. Rolling elliptical pendulum model

(a) vertically plumb position,

(b) rotated position.

Adapted from: (Jangid and Londhe 1998);

Source: (Lo Ricco et al. 2018)

Figure 18 adapts elliptical rolling rod concepts to CLT panels and preserves the original mathematical model that characterizes the rolling isolation system, with a few notable differences (Jangid and Londhe 1998, Londhe and Jangid 1999, Lo Ricco et al. 2018). First, CLT panels need only to fill the middle portion of the elliptical profile to be effective. Second, displacement restraints (in the form of pins and plates with V-shaped slots) guide rolling of the system and safeguard slip, which threatens to leave residual displacements. For numerical analysis, Londhe and Jangid offered an expression to determine whether a superstructure would slide over rods but assumed high values of frictional traction to engage the ellipses in rolling, without offering further details. The V-shaped slots of Figure 18 trace the *cycloids* of a rolling ellipse centered at the pins through a partial revolution limited by maximum displacement, D_M (Stephens 2011). Shaping slots in this manner minimizes connection constraint, while keeping rolling on track. Pin connections developed for rectangular rocking walls have followed a similar V-shaped path to transfer shear and reported altered effects on the rocking (Loo et al. 2014). The rolling pendulum connections strive to avoid altering rocking, altogether, by guiding rolling rather than transferring shear.

View (a) of Figure 18 illustrates the degrees of freedom and ellipse parameters, according to the original elliptical rolling rod model (Jangid and Londhe 1998, Londhe and Jangid 1999, Lo Ricco et al. 2018). With subscript “ r ”, the model denotes three degrees of freedom (x_r , y_r , and θ_r) to describe center-of-gravity translations, x_r and y_r , and panel rotations, θ_r , for the “rolling rod” respective to global x' and y' axes. Two translation degrees of freedom, x_b and y_b subscripted to denote the “base mass” of the superstructure, depend on motion of the panel. The system omits rotation of the base mass and stipulates that superstructure design and rocking story layout fully resolve overturning effects so that the base mass moves upward in level fashion, as illustrated in

View (b) of Figure 18. Local x and y axes respectively align with major and minor ellipse axes of length $2a$ and $2b$. In the vertically plumb position of Figure 18 (a), clear height of the story matches minor-axis height of the ellipse, but clear height of the rocking story grows according to the dimensioned parameters of Figure 18 (b) as the ellipse rolls.

Figure 18 (b) also illustrates travel of top and bottom contact points A and B , the distinctive feature of the elliptical rolling system. Unlike rectangular rocking panel systems which pivot exclusively on the base corners, elliptical panels disperse high-pressure contact stresses to changing points along the loadbearing edges. Figure 18 (b) highlights the essential paths of contact point travel with bold lines at the floor and ceiling. Along the foundation, for example, the contact point simultaneously travels the elliptical arc length $\widehat{BB''}$ along the panel edge and straight-line distance $\overline{BB'}$ across the floor. The horizontally dimensioned parameters of Figure 18 (b) show arc and straight-line distances, each equating to the sum of one-half the:

- Lateral story translation x_b and
- Force-couple distance $2c$ between contact points.

The assumptions equating elliptical arc length to straight-line travel across the ceiling or floor imply constant contact between the ellipse and bounding horizontal planes. While not necessarily the case, no slip should be allowed to occur. Geometric eccentricity of the ellipse only provides a way to self-center rotations generated via traction, not sliding translations. Traction, therefore, provides essential story shear transfer between the wall panel and bearing contact points at the floor and ceiling. Slip of the superstructure across the panel, or panel sliding on the foundation, could produce significant residual displacements and negate benefits of the rolling pendulum. For this reason, *No-Slip Traction Rolling* aptly names the original elliptical rolling rod model.

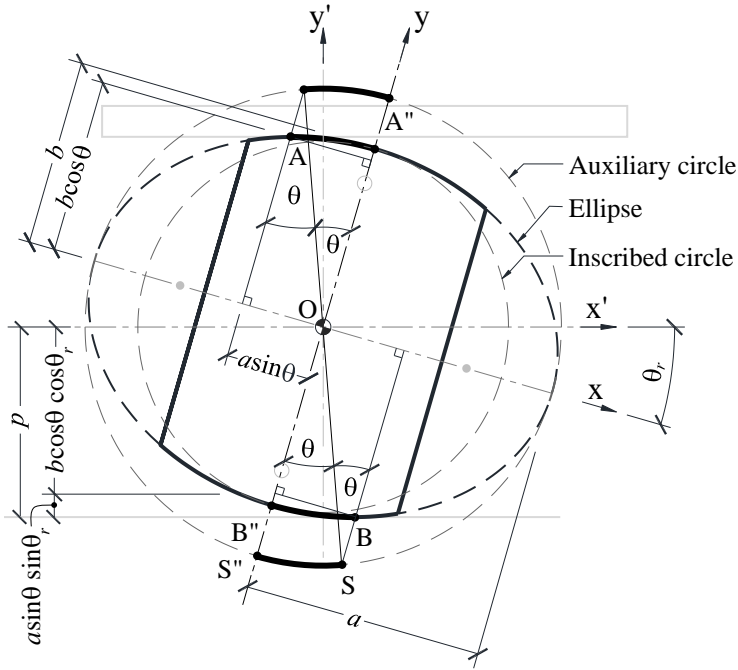


Figure 19. Geometric parameters
Adapted from (Londhe and Jangid 1999)

Figure 19 diagrams the geometry that Londhe and Jangid used to calculate elliptical arc length, based on a centuries old method of constructing an ellipse from concentric circles (de La Hire 1685, Weiss 2015). Rotations, of auxiliary circle through θ and ellipse through θ_r , relate the angles according to the expression provided by Jangid and Londhe:

$$\theta_r = \tan^{-1} \left(\frac{b}{a} \tan \theta \right) \quad \text{Equation (1),}$$

where a and b are semi major and minor axis lengths, respectively, or radii of the auxiliary and inscribed circles. The relation between angles leads to an expression of, p , the instantaneous half clear height of the story diagramed in Figure 19:

$$p = a \sin \theta \sin \theta_r + b \cos \theta \cos \theta_r \quad \text{Equation (2) .}$$

Eccentricity, or out-of-roundness with respect to a circle that exhibits zero eccentricity by definition, drives the self-centering mechanism with geometry. Proportioning minor and major axes expresses ellipse eccentricity, e , as:

$$e = \sqrt{1 - \frac{b^2}{a^2}} \quad \text{Equation (3) .}$$

Jangid and Londhe equated elliptical arcs and straight-line lengths to yield:

$$\frac{x_b}{2} + c = a \int_0^\theta \sqrt{1 - e^2 \sin^2 \phi} \, d\phi \quad \text{Equation (4),}$$

where c is horizontal travel of the contact point relative to panel centerline; a is semi-major axis length, and e is ellipse *eccentricity*. The incomplete elliptic integral of the second kind, appearing in the right half of the equation, makes estimation of elliptic arc length possible with tabulated numerical solutions of the integral or math software with elliptic functions (Beliakov et al. 1965, Jangid and Londhe 1998, Londhe and Jangid 1999). Calculating the arc length of the auxiliary circle, highlighted in Figure 19, approximates the elliptic integral in the right half of Equation (4).

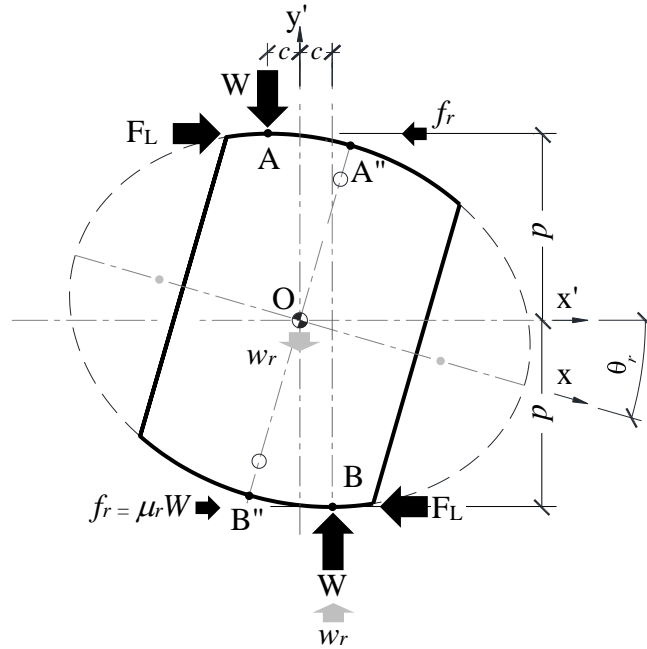


Figure 20. Free-body diagram of rolling panel
(not showing inertial forces for clarity)
Source: (Lo Ricco et al. 2018)

Figure 20 presents a simplified free-body diagram of a rolling elliptical panel. The diagram omits inertial effects, not generated during quasi-static testing, and deemphasizes w_r , because weight of the panel amounts to 5% or less of W , the total applied vertical load. The following equation, derived by Jangid and Londhe, estimates the lateral force-displacement relationship of rolling elliptical isolation:

$$F_L = W \left(\mu_r \operatorname{sgn}(\dot{x}_b) + \frac{c}{p} \right) \quad \text{Equation (5).}$$

where W is the superstructure weight transferred through the directly supported mass; μ_r is a rolling friction coefficient; the *signum function* specifies the direction of horizontal frictional traction forces, and dimensions c and p respectively indicate half the moment arm distance of the vertical restoring moment and horizontal overturning moment induced by traction. Figure 21

plots an idealized lateral load-displacement hysteresis for an ellipse with an eccentricity parameter, e , equal to 0.73, based on Equation (5). Figure 21 normalizes the lateral force by dividing each side of Equation (5) by superstructure weight, W . Figure 21, furthermore, expresses lateral drift as a ratio of displacement and the original clear height of the story, $2b$. Slope of the hysteresis function changes with ellipse proportions, growing steeper as ellipses widen (i.e. as eccentricity, e , approaches unity). Rolling friction coefficient, $\mu_r = 0.01$ as pictured, dictates spacing between the line segments of the hysteresis. The idealized model of Figure 21 does not distinguish damping attributable to material damage versus friction, anticipating that the energy dissipated by minor wear could be neglected. With low damping, the system would have to rely on external damping devices for additional energy dissipation. Traction, or assumptions of no slip, furthermore, introduced uncertainty that prompted the development of an alternative means of lateral force transfer.

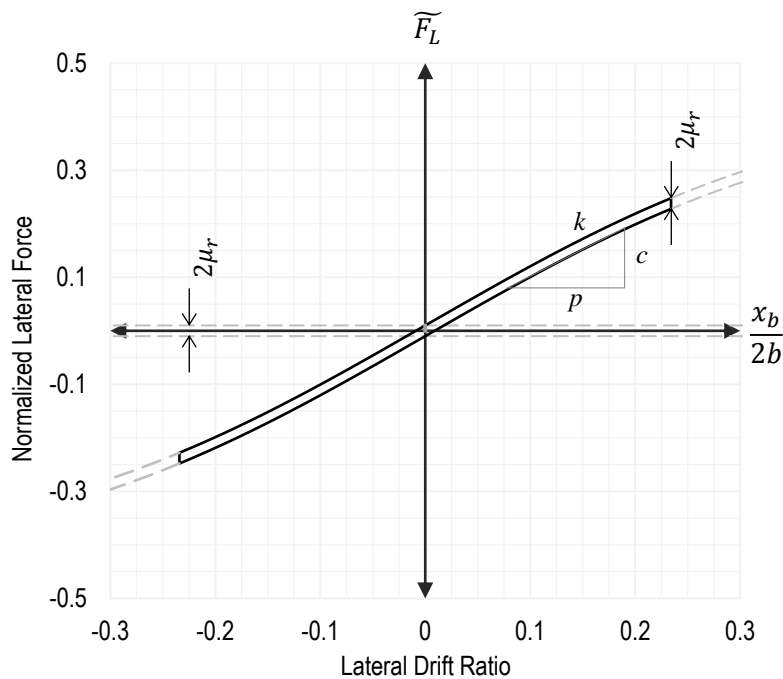
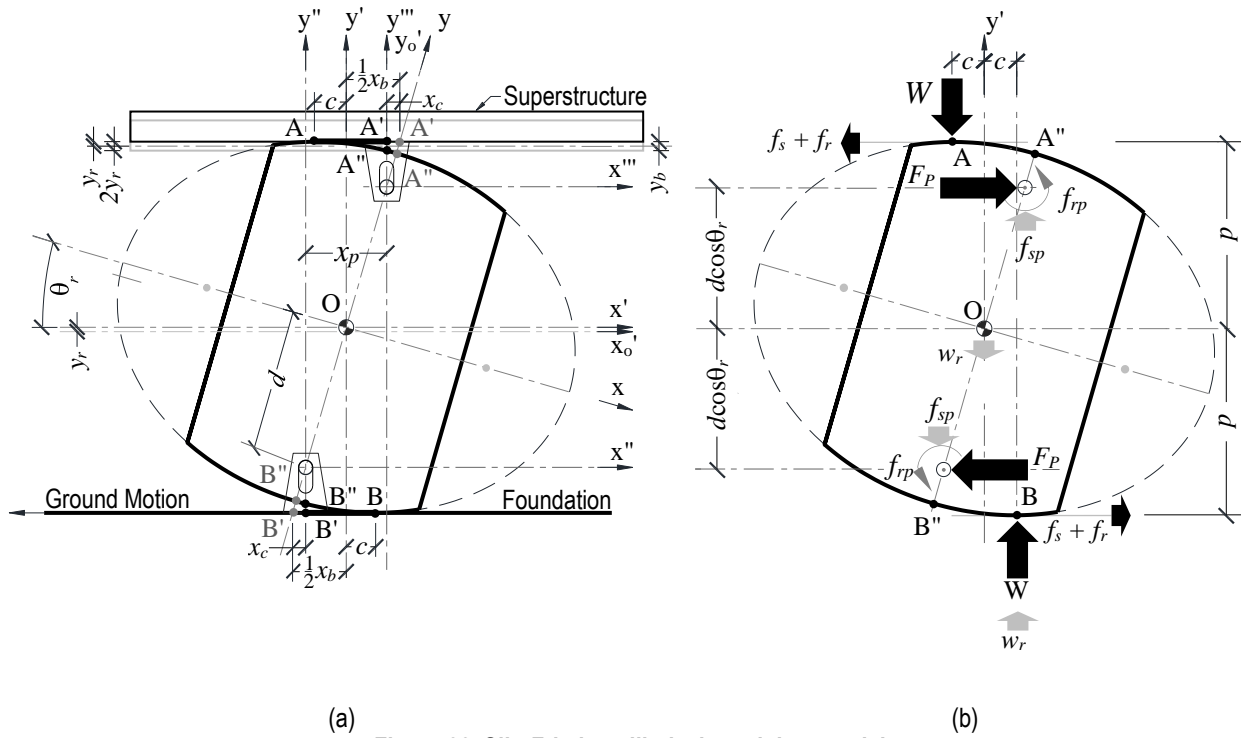


Figure 21. Idealized hysteresis of $e = 0.73$ panel in No-Slip Traction Rolling
 Source: (Lo Ricco et al. 2018)

Slip-Friction Rocking

Figure 22 presents a more proactive approach to shear transfer, in the form of vertically slotted connection plates that establish a *slip-friction* pendulum. As dimensioned in view (a), the vertical slots constrain horizontal movement of each pin a distance denoted x_c during rocking motion. As a result, the pins rotate and force the CLT panel to slide simultaneously to rolling. Figure 22 (b) shows the main forces at play in *Slip-Friction Rocking*. In the free-body-diagram for the slip-friction case, pins primarily transfer story shears and counteract friction. Figure 22 (b) grays out the frictional pin sliding force, f_{sp} , and frictional pin rotation force, f_{rp} , because this model assumes that the pins contribute only a small percentage of total friction in the system. Sliding friction, f_s , between the panel edges and horizontal planes dominates the system. Because friction, f_s , opposes the pin force F_P now the primary means of story-shear force transfer, sliding friction adds energy dissipation to the *Slip-Friction Rocking* scheme. Globally, the model does not consider the force couple produced by f_{sp} as restorative but aggregates sources of frictional damping into a sum of rolling and sliding, μ_r and μ_s , coefficients.



(a) **Figure 22. Slip-Friction elliptical pendulum model**
Source: (Lo Ricco et al. 2018)

Lateral displacement of the newly constrained configuration, x_p dimensioned in Figure 22, relates to the previous rolling mechanism via:

$$x_p = x_b - 2x_c \quad \text{Equation (6) .}$$

Though the net lateral displacement of x_p is less than x_b , for a given panel rotation θ_r , the path effectively traveled by the constrained system measures $2x_c$ greater than x_b . Proportioning similar triangles expresses the cumulative path of travel as:

$$x_b + 2x_c = \left(\frac{2p}{d \cos \theta_r} - 1 \right) x_p \quad \text{Equation (7) .}$$

Pushing panels with greater force through the same rotation, θ_r , but with less translation, increases effective lateral stiffness.

Figure 23 estimates the added friction from sliding, μ_s at 9%, relative to the *No-Slip Traction Rolling* case. In addition to enhanced energy dissipation, the hysteresis for *Slip-Friction Rocking* predicts increased effective stiffness resulting from connection constraint. Equation (8) models both effects of sliding friction and horizontal constraints as a function of x_p :

$$F_P = W \left((\mu_r + \mu_s) \operatorname{sgn}(\dot{x}_p) + \frac{c}{d \cos \theta_r} \left(\frac{2p}{d \cos \theta_r} - 1 \right) \right) \quad \text{Equation (8) ,}$$

where μ_s adds a sliding friction coefficient, presumably greater than rolling friction coefficient μ_r , and d dimensions the pin from panel center, as diagrammed in Figure 22 (Lo Ricco et al. 2018). The moment arm between pin horizontal forces F_P replaces the parameter p , in the previous *No-Slip Traction Rolling* model of Equation (5), with the lesser term $d \cos \theta_r$, making F_P greater than F_L of Equation (5). The ratio of displacements, based on constraints that Equation (7) relates, further increases the lateral force F_P , of the slip-friction system relative to F_L of the plainly rolling system.

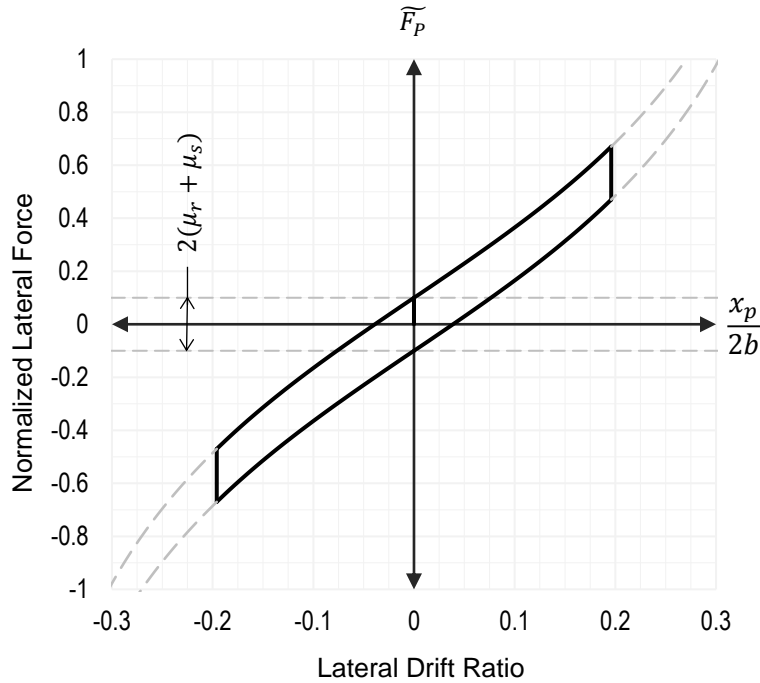


Figure 23. Idealized hysteresis of $e = 0.73$ panel in Slip-Friction Rocking.
Source: (Lo Ricco et al. 2018)

Figure 23 plots an idealized hysteresis model of the *Slip-Friction Rocking* configuration of a panel with 0.73 eccentricity (Lo Ricco et al. 2018). The slip-friction hysteresis divides Equation (8) pin forces by superstructure weight, W , to normalize lateral pin forces and expresses lateral drift as a ratio of constrained displacements x_p over $2b$ story height. The slip-friction model of Figure 23, in comparison with Figure 21 for *No-Slip Traction Rolling*, exhibits steeper slopes (increased stiffness) and greater spacing between branches of the hysteresis loop (increased frictional energy dissipation). As shown, the hysteresis function of Figure 23 assumes a coefficient of sliding friction μ_s equal to 0.09, that yields a total frictional coefficient of 0.10 by adding both rolling and sliding coefficients. Equation (9) makes a simple, but important, distinction between the friction modes:

$$\mu = \mu_r + \mu_s \quad \text{Equation (9).}$$

Principle of Virtual Work

The previous model of *Slip-Friction Rocking* used an equivalent system approach to derive Equation (8). The rolling model laid the groundwork, and effects of connection constraint led to a slip-friction version. As a check on the two system models presented in Equations 5 and 8, *Appendix A: Principle of Virtual Work Models* compares alternative approaches. Virtual work methods offer an explicit way to feature the potential energy intrinsic to the self-centering of the pendulum system. Modeling friction using the energy approach, however, presents complications, particularly at small lateral displacements. Even though friction may be present as a constant force in the system, friction only performs work when the system moves either virtually or in actuality. Initial boundary conditions, therefore, must be carefully developed for the virtual work methods to offer accuracy. For practicality, this study opted for the *No-Slip Traction Rolling* model of Equation (5) and the *Slip-Friction Rocking* model of Equation (8), because simple but effective Coulomb friction models form the basis of each system.

Objectives and Hypotheses

Table 5. Pros and cons of elliptical No-Slip Traction Rolling inverted pendulum

Advantages (+)	Disadvantages (-)
Isolates most effectively.	Undergoes high lateral displacements.
Imposes the least constraint on rocking.	Requires supplementary wind restraint.
Leverages contact forces at load-bearing panel edges.	Requires sufficient traction to transfer story shear.
Minimizes energy input and damage of CLT panels.	Offers only light inherent damping ($\alpha \leq 5\%$ of critical).
Eliminates residual displacements with ellipse eccentricity and rolling under ideal <i>no-slip</i> conditions.	Requires complexly slotted connections to safeguard against slip.

Each version of the elliptical inverted pendulum, *No-Slip Traction Rolling* and *Slip-Friction Rocking*, presents a series of advantages and disadvantages. Tables 5 and 6 respectively summarize the pros and cons of *No-Slip Traction Rolling* and *Slip-Friction* configurations, based on the preceding system models. With lesser lateral stiffness, *No-Slip Traction Rolling* isolates

more effectively and lessens risks of damage, because the connections guide rocking with minimal constraint and transfer only incidental contact forces. Rolling generates low frictional resistance that makes rocking easier, but not without drawbacks. With low inherent damping, *No-Slip Traction Rolling* requires a *wind restraint system*, typically *sacrificial* to prevent rocking in everyday service yet concede to pendulum earthquake response. Relying on traction as the primary means of shear transfer, furthermore, exposes the rolling system to residual displacements. V-slotted *displacement restraints* alleviate concerns, but slot shape must accurately anticipate the rolling paths at the connection points of each panel with enough tolerance for assembly yet precision for minimizing slippage.

Slip-Friction Rocking primarily transfers story shears through universally applicable pin connections, horizontally constrained in vertical slots, that practically eliminate residual displacements, add inherent damping with sliding friction, and increase the threshold of rocking. The concentration of forces around pins and energy dissipated by sliding, however, risk more damage to CLT panels. Too much friction could cause the vertically slotted pin connections to overload CLT laminations around the pinhole bushing and wear out the loadbearing edges of the CLT panel.

Table 6. Pros and cons of elliptical Slip-Friction inverted pendulum

Advantages (+)	Disadvantages (-)
Adds inherent frictional damping for less displacement.	Compromises isolation with increased stiffness.
Sliding friction raises threshold of rocking.	Vibrations at low wind drift levels may still result.
Story shears pass through a redundant pin connection.	High frictional forces overstress CLT around pin.
Significantly increases energy dissipation.	CLT suffers damage from energy dissipation.
Eliminates residual lateral displacements with simple vertically slotted pin connections.	Wear to CLT load-bearing edges shortens panels, resulting in vertical residual displacement.

Friction: Shear Transfer or Energy Dissipation?

No-Slip Traction Rolling and *Slip-Friction* pendulum systems both present viable options for rocking and passive self-centering, under superstructure weight. Friction, however, will predominantly determine resiliency of each system. A number of studies have characterized frictional contact between wood and steel (McKenzie and Karpovich 1968, Guan et al. 1983, Murase 1984, Seki et al. 2013). According to consensus, frictional contact varies with wood species, moisture content, fiber orientation, surface roughness of steel, pressure, and speed of sliding, yet discerning a coefficient of sliding friction for structural applications remains inconclusive when comparing the literature. Though challenging to determine directly, Figures 21 and 23 presume that depth of the hysteresis loops estimates the overall friction of each system. Lateral load-displacement data from full-scale prototype tests, therefore, should provide estimates of friction coefficients and validate other critical aspects of the system models.

Geometric Proportioning

In addition to friction generated by connection constraint, ellipse eccentricity factors into the performance of each pendulum system. Figures 24 and 25 plot the top right segments of idealized lateral-load displacement relationships, for comparing the variable effects of eccentricity and connection constraint. Both charts show that lateral stiffness increases proportionally to ellipse eccentricity, e determined by Equation (3). The nonlinear functions plotted in Figure 24 for *No-Slip Traction Rolling* show a softening effect, most pronounced in the theoretical ranges plotted by dashed lines. If allowed to complete full revolutions, ellipses would exhibit steep downturns in stiffness when rolling from a stable, oblate position to an unstable, prolate state. Displacement restraints, however, should limit the system to practical ranges plotted by the solid lines.

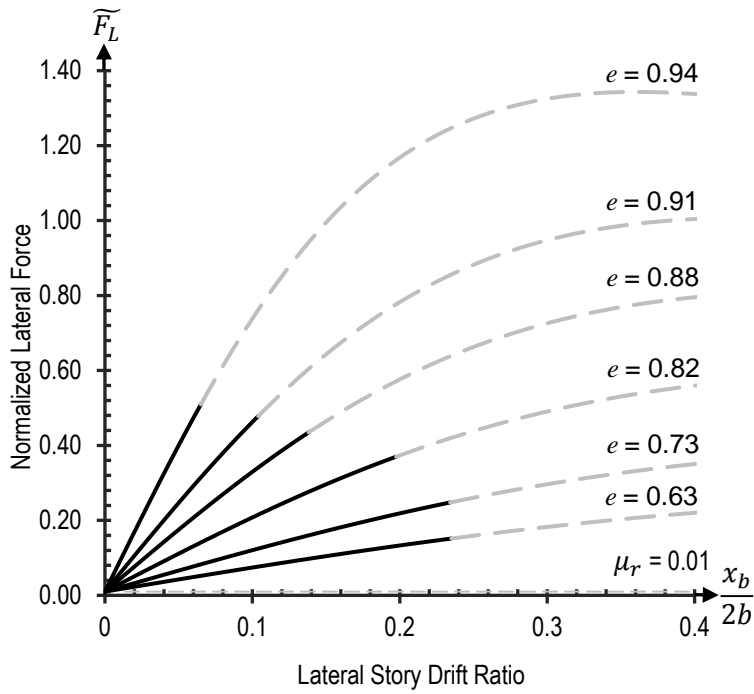


Figure 24. Idealized stiffness comparisons of panels in No-Slip Traction Rolling

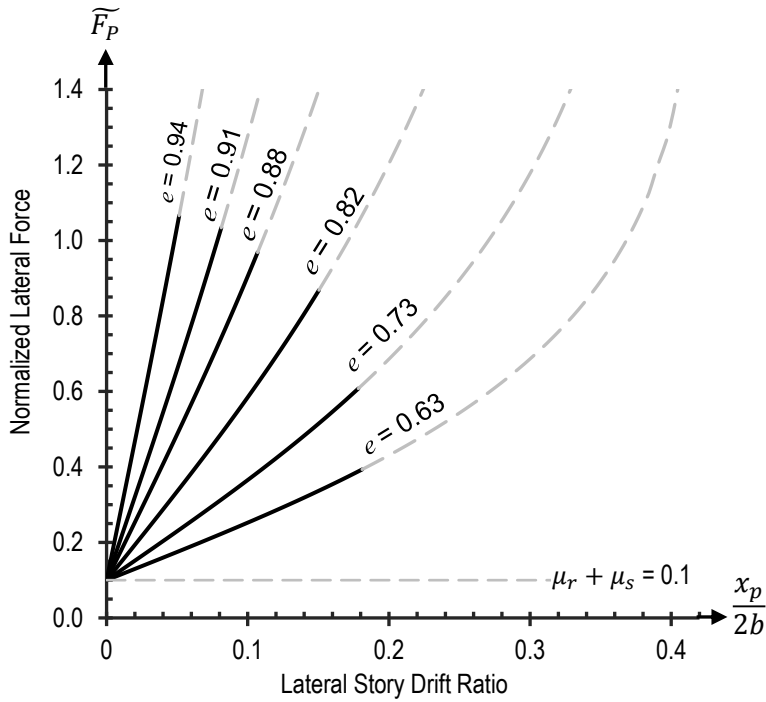


Figure 25. Idealized stiffness comparisons of panels in Slip-Friction Rocking

Corner contact of the truncated ellipse typically determines the transitions from practical to theoretical ranges shown in these graphs. Changing geometry of both panels and connections,

however, can customize the practical range to other desired drift limits. Figure 25 plotting *Slip-Friction Rocking* shows an opposite nonlinear stiffening effect most pronounced in hypothetical ranges represented by dashed lines. Within the practical ranges indicated by solid lines, both systems essentially behave linearly.

Prototype Testing

Test Matrix

To validate idealized models of each configuration, the test matrix of Figure 26 organized six panel specimens in rows of eccentricity and columns of connection type. Overall panel heights, or minor-axis lengths $2b$ of the ellipses, remained constant at 3.66 meters (12 feet) each throughout the sampling to match typical story clear height. In keeping with height, dimension d of Figure 22 from center of panel to center of pin hole consistently measured 1473 mm (58 in.) for all specimens. Panel widths also held constant at 2.44 meters (8 feet), but major-axis lengths $2a$ of the elliptical profiles varied from wide to narrow with respect to the top and bottom rows of the matrix. The matrix lists values and units for semi-major axis length a and gives a unitless eccentricity parameter e , computed by Equation (3), for each specimen. Each specimen comprised of 5-ply CLT, but panel depths d_1 (169 mm or 6 $\frac{5}{8}$ in.) and d_2 (175 mm or 6 $\frac{7}{8}$ in.) labeled in the test matrix varied because of a change in production practice from “SLT5” to “175V” layup referenced in Table 2. The wood species and grade of laminations remained constant through two different production runs by the same manufacturer, with structural values that correspond to Table 1. Computer Numerical Control (CNC) fabrication by the CLT producer realized geometry of the test matrix.

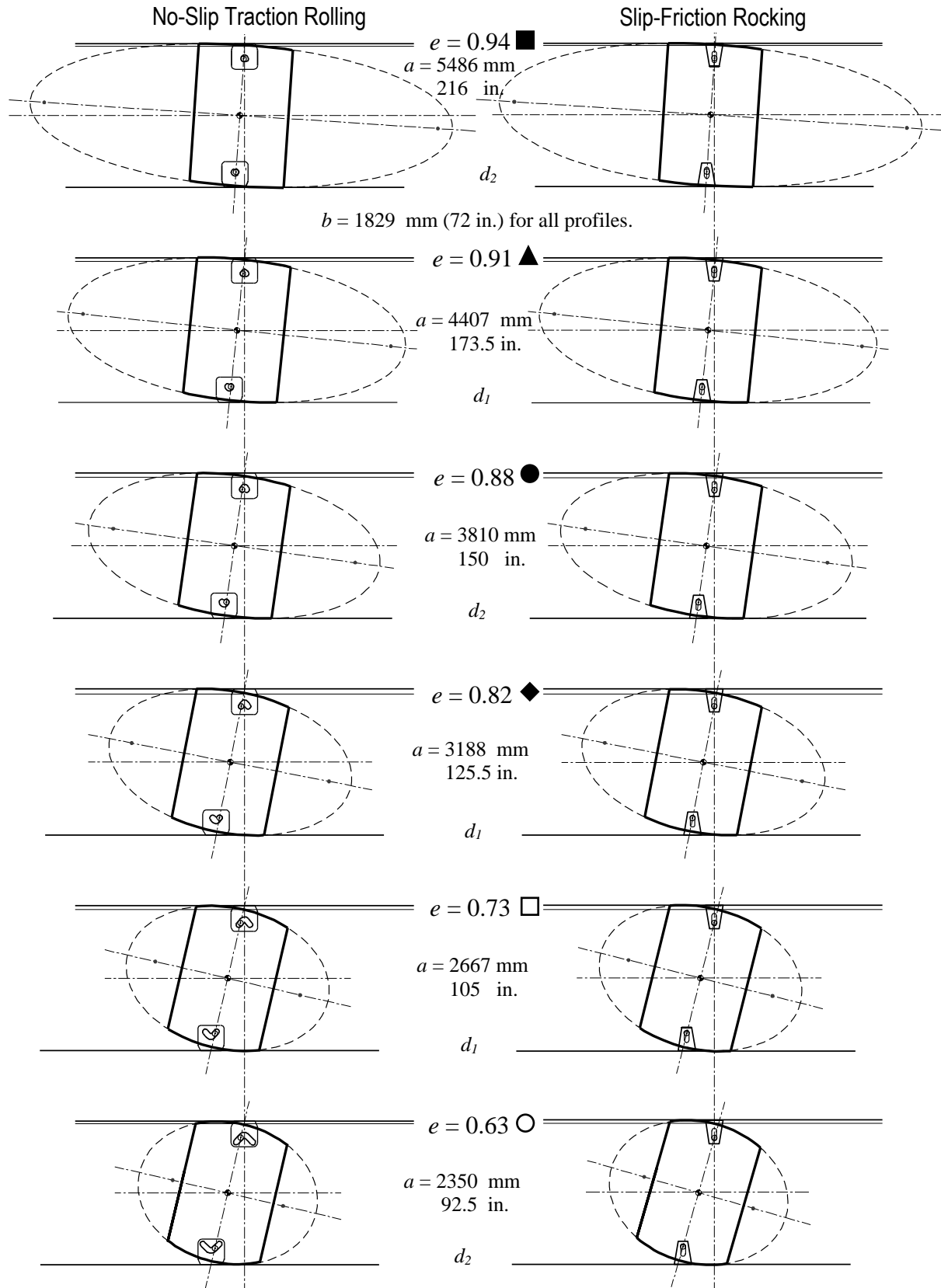


Figure 26. Test matrix

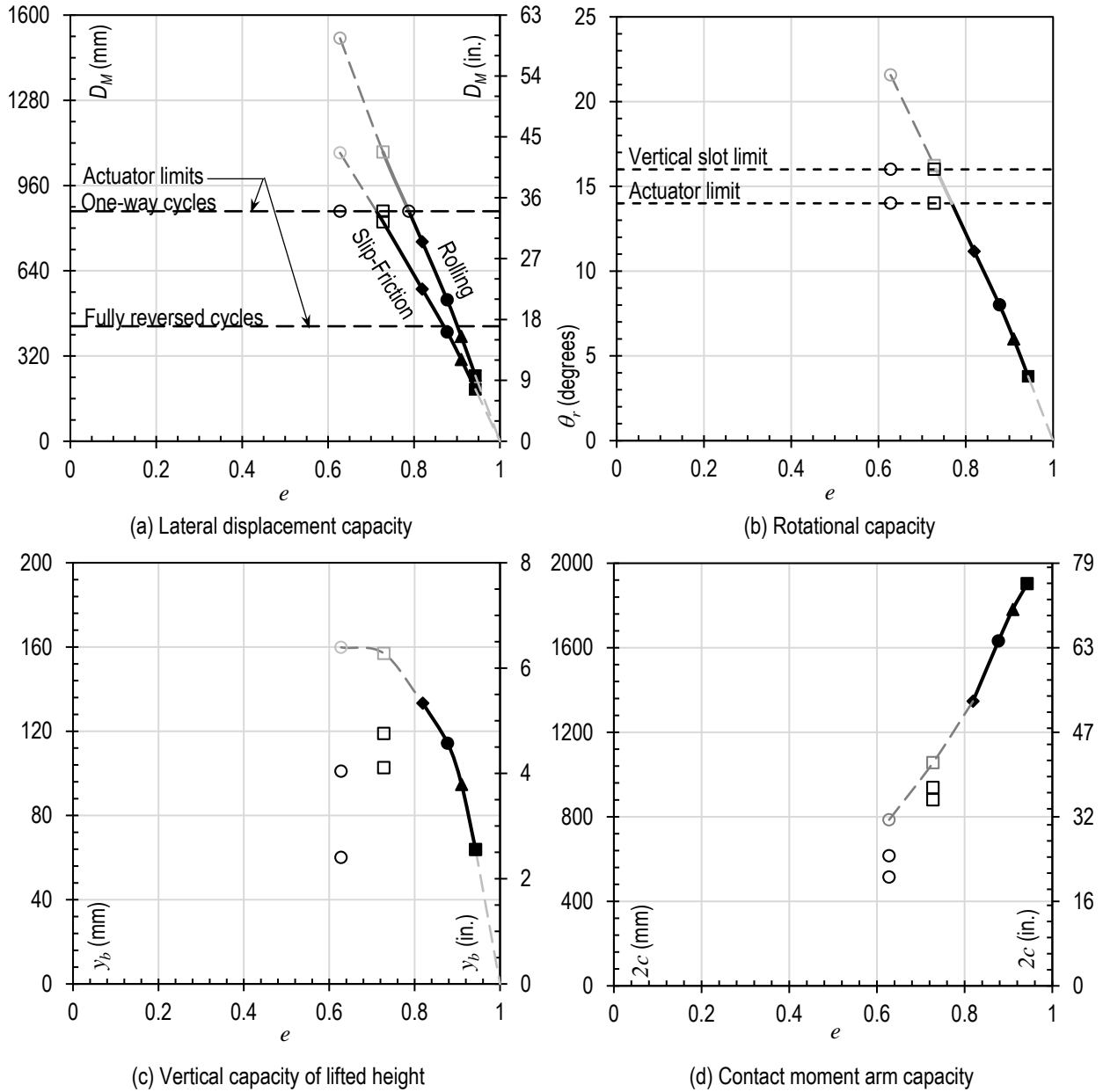


Figure 27. Effects of varying eccentricity of elliptical profiles

Symbols key the eccentricities of the test matrix to the Figure 27 plots that show key features of the rolling pendulums in terms of eccentricity. The test matrix and Figure 27 (a) define lateral displacement capacity, D_M , of each specimen as the limit when panel corners come into contact. No-Slip Traction Rolling and Slip-Friction Rocking diverge in terms of lateral displacement capacity, but graphs (b) through (d) show only one plotted series, because the two configurations

share identical rotational, vertical and moment arm capacities. Exceeding the D_M limits ventures beyond the scope of the test matrix prototypes and into truncated end regions of the ellipses. The six initial prototypes selectively truncated ellipses, based on typical construction module dimensions, but customization could model a greater portion, if not all, of each elliptical profile. Narrowing ellipses increases lateral displacement capacity (D_M), rotational capacity (θ_r), and lifting of the superstructure (y_b), as the inversely proportional relations of plots (a) through (c) show. The two panels of least eccentricity do not reach charted limits, because the limits exceed either maximum lateral actuator stroke or extents of the vertically slotted connections. Plots (d) and (e), however, show narrowing ellipse eccentricity directly proportional to diminishing both lifting height and moment arm distance between the contact points. Widening ellipses conversely generates more potential energy and restoring moment that drive re-centering. Ellipse proportioning, therefore, balances lateral stiffness with reliable self-centering.

Prototype Connections

The test matrix of Figure 26 illustrates various slot shapes of *No-Slip Traction Rolling* that traced cycloids, or roulettes, of each ellipse as the system model described. Rather than produce a dozen specific connections, a pair of main connections, (a) illustrated in Figure 28 with interchangeable slotted plates (b), facilitated changing specimens. Each V-shaped slot matched a specific elliptical profile. Some trials of *No-Slip Traction Rolling* included straps (c) bolted outboard the main connection assembly with notched dowels as sacrificial wind restraint. Steel pins (d) through the V-shaped slots and pipe bushings (e) embedded in the CLT panels connected the entire assembly of steel and timber. The vertically slotted connection, illustrated in Figure 29, universally applied to all *Slip-Friction Rocking* tests. CNC plasma cutting of steel plates realized

each set of slots. *Appendix B: Connection Details* provides further specifications of the steel connections.

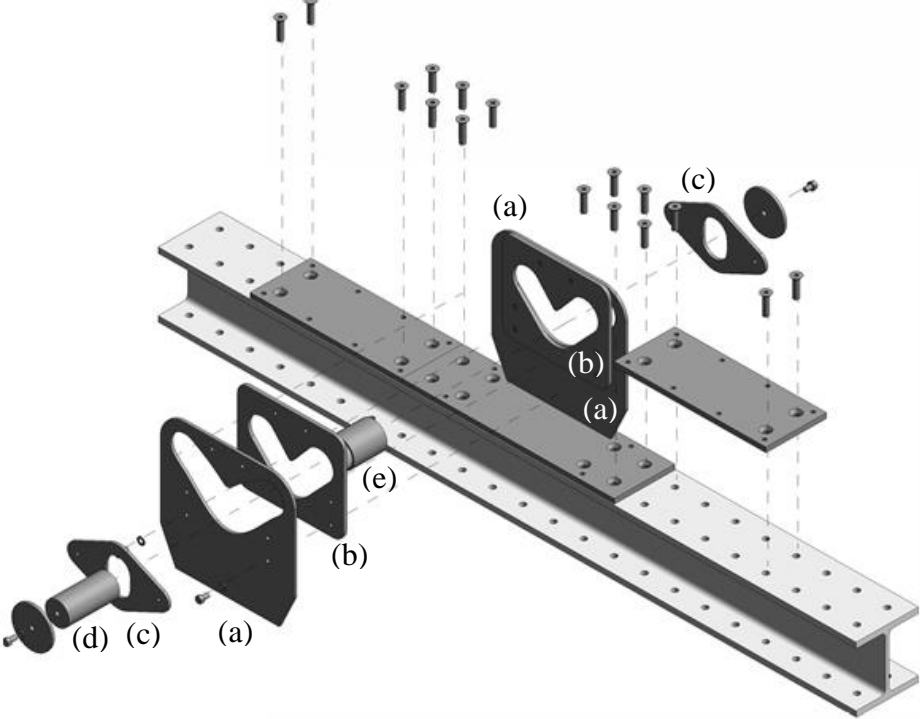


Figure 28. Exploded view of v-shaped slotted face plates for *No-Slip Traction Rolling*.

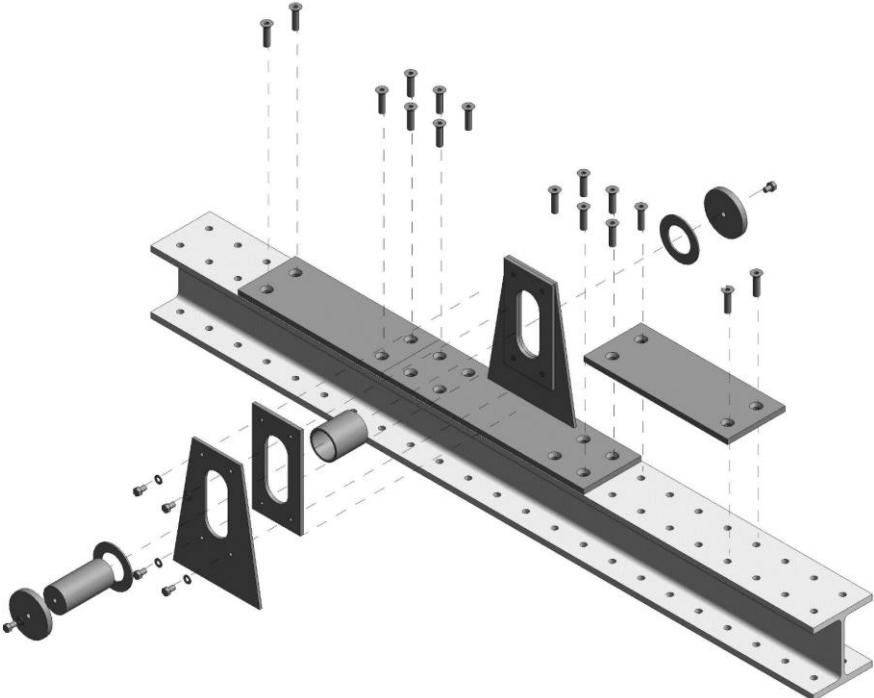


Figure 29. Exploded view of vertically slotted face plates for *Slip-Friction Rocking*.

Simulating Boundary Conditions

Figure 30 illustrates the full-scale test apparatus used to validate the elliptical pendulum concepts with CLT. The test panel (a) stood one-story tall within a frame made primarily of steel. To replicate boundary conditions of platform construction, the steel test frame of Figure 30 combined stationary and moving parts (Lo Ricco et al. 2018). A pair of horizontally oriented actuators (b), linked in series, powered translation of the bottom beam (c) and achieved strokes up to (± 17 in.) in fully reversed cycles and 863 mm (34 in.) in half cycles that pushed only in one direction and returned to a plumb, original position. The bottom steel wideflange beam glided on 2 industrial chain rollers (d), each rated for 34 metric ton (37.5 U.S. ton) capacity and confined within a steel channel track bolted to the floor. Vertically oriented actuators (e) simulated superstructure weight through a feedback loop that kept the main top beam (f) level and in direct contact with the panel under a constant sum of load, up to 400 kN (90 kips) while simultaneously adjusting to the moving panel contact point. (i) is the concrete wall, (h) is the diagonal bracing, and (k) is the base plate.

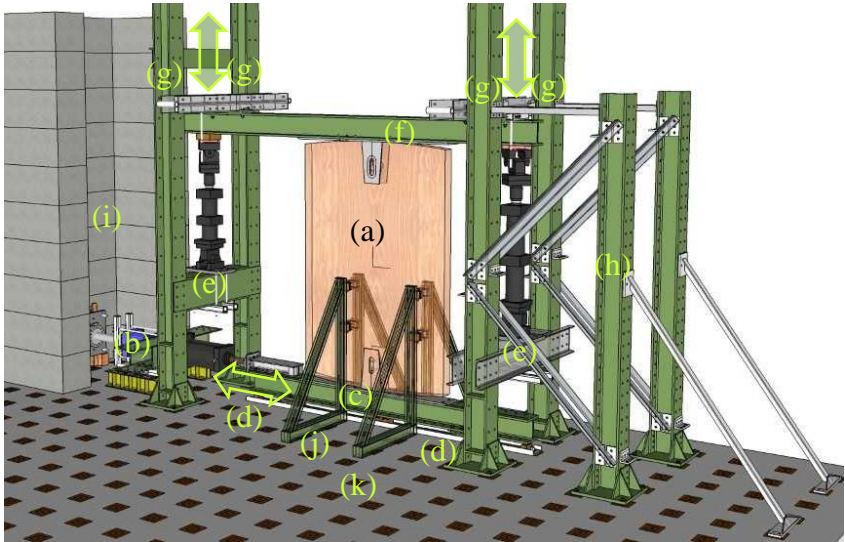


Figure 30. Full-scale test apparatus.
Rendering by Marshall Begel.

Secondary top beams (g), pictured in gray, laterally braced the main beam in each direction transverse to the wall plane. In the plane of the CLT wall, the gray beams transferred lateral story shear loads to columns of the test frame while gliding up and down, using heavy-duty spherical polytetrafluoroethylene (PTFE) bearings that rolled on plates fastened to the faces of the column flanges. Lateral story shear force, in-plane of the wall at the ceiling beam level, only engaged two columns in compression bearing contact at any given time. For stability transverse to the CLT wall plane, the gray beams used PTFE glide bearing strips, glued to stiff steel angles, to slide along the column flange tips. Ultimately, story shears transferred from the CLT wall to the braced steel frame (h) pictured right of the panel or the concrete strong-wall (i) shown left of the panel. Precautionary out-of-plane wall bracing (j), triangular brackets mounted to the strong-floor (k), typically did not engage, because panels rolled stably within tolerances set by gaps between braces and CLT faces.

Prototype Testing Protocol

Rather than offer ductile resistance to lateral loads, elliptical pendulums effectively isolate superstructures by undergoing large lateral displacements. Test protocols of the elliptical rocking walls, therefore, emulated quasi-static prototyping procedures for seismic isolation (ASCE/SEI 7 2017). The test protocol of Table 7 generally followed code provisions but required simplifying assumptions for first-iteration prototypes (Lo Ricco et al. 2018). The first displacement step estimated a reasonable wind drift limit to gauge lateral stiffness at the onset of rocking. The remaining displacement steps represented seismic demands with fractions of the maximum lateral planar displacement of the CLT wall, D_M . ASCE 7 defines D_M as the maximum displacement of an isolation system at the center of rigidity with respect to the direction under consideration (ASCE/SEI 7 2017). For generalized application of the wall system, however, the

test matrix interpreted D_M as the maximum displacement capacity of each individual CLT panel in-plane of the elliptical profiles.

The last displacement step of Table 7 tests seismic durability with a higher number of cycles. Determining the ultimate number of cycles requires spectral acceleration parameters, largely dependent on geographic location, soil properties, and an estimation of damping (ASCE/SEI 7 2017). For versatility, the test protocol included values of D_M , up to 864 mm (34 in.), and set the number of final cycles sufficiently greater than the minimum of 10. To maximize value of the test specimens, most CLT panels sustained multiple cyclic protocols that demonstrated durability in excess of minimum requirements.

Table 7. Cyclic prototype test protocol

Displacement Step	Number of Cycles
$0.0025h_s$	20
$0.25D_M$	3
$0.50D_M$	3
$0.67D_M$	3
$1.00D_M$	6
$0.75D_M$	$\frac{30S_{M1}}{S_{MS}B_M} = 18 \geq 10$

h_s = story clear height = 3.66 m (12 ft)

D_M = in-plane maximum lateral displacement, limited by panel geometry or external connection limits.

S_{M1} = the MCE_R , 5% damped, spectral response acceleration parameter at a period of 1s adjusted for site class effects

S_{MS} = the MCE_R , 5% damped, spectral response acceleration parameter at short periods adjusted for site class effects

B_M = Numerical coefficient depending on effective damping, β_M , percentage of critical.

Adapted from: Chapter 17 of ASCE/SEI 7-16

Table 8. Overburden loads or simulated superstructure weight

Intensity	(kN)	(kips)
Low	166	30
Medium	233	60
High	400	90

Standards require prototype testing under varied high, medium, and low levels of load, to demonstrate stability and predictability of the engineering parameters. *ASCE 7* isolation provisions specify load combinations appropriate for building design. Table 8, however, provides loads at regular intervals for clearer statistical determination of whether superstructure weight influences applicability of the system models or wall performance. Two vertical actuators, labeled (e) in Figure 30, applied the Table 8 loads during test trials. Each cell of the Figure 26 test matrix, therefore, called for three trials or one protocol at each level of overburden load. A limited supply of six full-scale CLT panels slated a total of 6 test protocols for each specimen, at 3 levels of simulated gravity loads times 2 connection configurations. Completion of planned protocols would have yielded a total of 36 trials.

Capabilities and Limitations

Though relatively sophisticated with the synchronization of moving parts and impressive in scale, the test apparatus of Figure 30 imposed limitations on realism and sequencing of the prototype trials. The hydraulic actuator setup, for example, lacked the power to generate dynamic excitations at high magnitudes of displacement. The quasi-static, cyclic displacement step protocol of Table 7 includes more cycles than dynamic procedures to make up for the inability to match the frequencies of earthquake histories (*ASCE/SEI 7 2017*). Lateral actuators stroked in series, which achieved high displacements but at slow speeds. Translating panels beyond 432 mm (17 in.) of displacement required repositioning of both CLT walls and the slotted pin connections. The adjusted position limited the rotational and translational motion to one

direction with respect to the vertical plumb position. For repositioning and other logistics, such as data collection, testing often paused between displacement steps of Table 7. Because *prototype* testing aimed to understand systems behavior, logical interruptions in the test sequence provided opportunities for adjustments with little consequence. To meet objectives of *qualification* testing, however, full protocols may have to run continuously.

Imperfections

Geometric imperfections of the structural steel test frame placed panels into certain misalignment. The misalignment, however, resulted from construction tolerances that could arguably represent typical structural steel framing. Additionally, damping of the test apparatus was not readily distinguished from damping inherent to the CLT panel and shear transfer connections. Friction and even yielding of steel under high-pressure contact with multiple rollers and bearings likely introduced damping external to the CLT system. Reasonable efforts to align apparatus and minimize friction assured that tests would capture specimen behavior within most of the cyclic range. At outer reaches of the actuators, however, friction and flexibility of the test apparatus likely introduced a slightly increased degree of uncertainty in the results.

Data Collection

Synchronized load cells and displacement transducers of the hydraulic actuator system supplied the primary load-displacement data. Processing this data determined the lateral load-displacement hysteresis characteristics of the rocking wall systems and fulfilled the prime objectives of the test program. The program, however, anticipated that supplemental data would lead to deeper understanding of steel and timber materials of the system. Wherever practical, additional sensors were added. Strain gauges, for example, measured the fixed, vertically slotted steel connections. Linear Variable Differential Transducer (LVDT) devices tracked motion of the

bottom pin in the horizontally constrained connection, where pin motion could be assumed vertical within the slot.

Because wall movement of the elliptical pendulum systems exceeds displacement of conventional shear walls, Digital Image Correlation (DIC) proved useful. Cameras collected ample data, in the full field of view, with relatively less effort and no physical contact with the specimen. Figure 31 shows a photo of the scaffold setup that enabled one pair of DIC cameras to focus on the steel connection and another pair to capture the moving contact zone between timber and steel, at the edge of the rocking panel. Other cameras, on opposite face of the panel, tracked the overall elevation of each panel specimen. Digital Image Correlation captured various fields of view with multiple cameras. Though capable of capturing a broader field of view than traditional sensors, DIC remains limited to only capturing what is in the field of view.

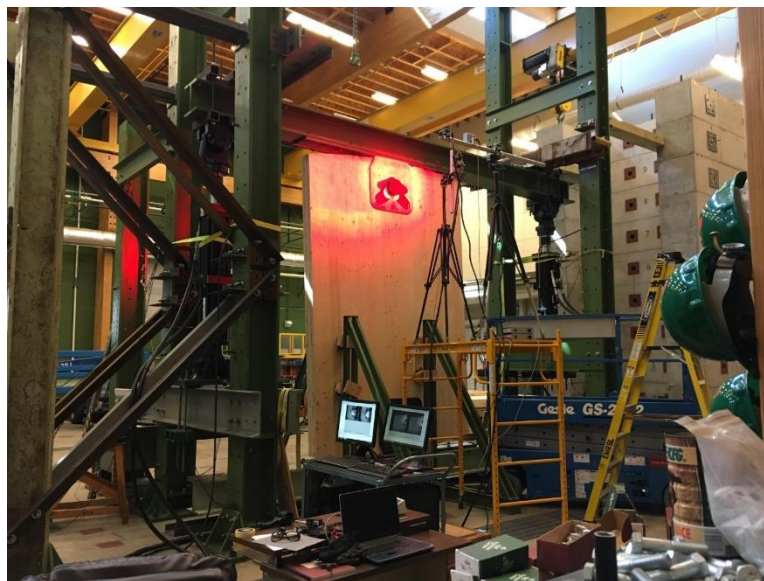


Figure 31. Digital Image Correlation (DIC) setup.
No-Slip Traction Rolling configuration shown.

Contact bearing pressures through the thickness of the panel vary greatly, because of the orthotropic nature of wood and layup of the panel. Experimental designs had considered

measuring these bearing contact pressures with an array of load cells or piezoelectric film sensors. Load cell arrays, however, typically require considerable effort to assemble, provide low resolution of the bearing contact area, and might interfere with the contact conditions, rather than gauge realistic behavior. Piezoelectric film sensors provide better resolution of the contact area but are too fragile to withstand the shears generated by either traction rolling or frictional sliding. This study, therefore, conducted precursory Finite Element Analysis (FEA) and static tests of 1.22 meter (4 ft) square portions of 5-ply panels, to gain understanding of force-displacement distribution within critical CLT regions, around the pin hole and compression bearing edge. *Appendix C: Precursory Characterizations of Timber-to-Steel Contact* provides additional details of the FEA, pressure-mapping, and DIC program leading into full prototype tests.

Scales of Study

Because CLT panels behave rigidly, relative to other forms of wood construction, this study developed elliptical inverted pendulums on assumptions of rigid-body mechanics. Unknowns regarding the orthotropic behavior of timber in zones of high-pressure bearing contact, therefore, challenged principles of the rocking wall system. General hypotheses presumed that local material damage could occur at the contact edge, but that multiple plies of the CLT panel would rapidly dissipate force concentrations. Despite local crushing and splitting of wood fibers along the edges of panels, the program expected that elastic material deformations would prevail throughout the system, including connections. DIC data, though limited to observing only face laminations, provided visualization and measurements of the timber contact zone that helped assess whether small material deformations had appreciable effects on overall system function of the wall pendulums.

IV. Results, Observations and Findings

The data collected during validation testing of the *No-Slip Traction Rolling* and *Slip-Friction Rocking* configurations captured two viewpoints. At a system level, hysteresis data defined behavior of the rocking wall system. Lateral force-displacement plots gauged stiffness, damping, and durability, for comparison with the idealized system models. At a localized level, DIC displacement measurements defined the contact zone behavior. The hysteresis data generally shows that elliptical rocking walls achieved lateral displacements, sometimes exceeding 10 or 20 percent lateral drift, with minimal degradation of stiffness.

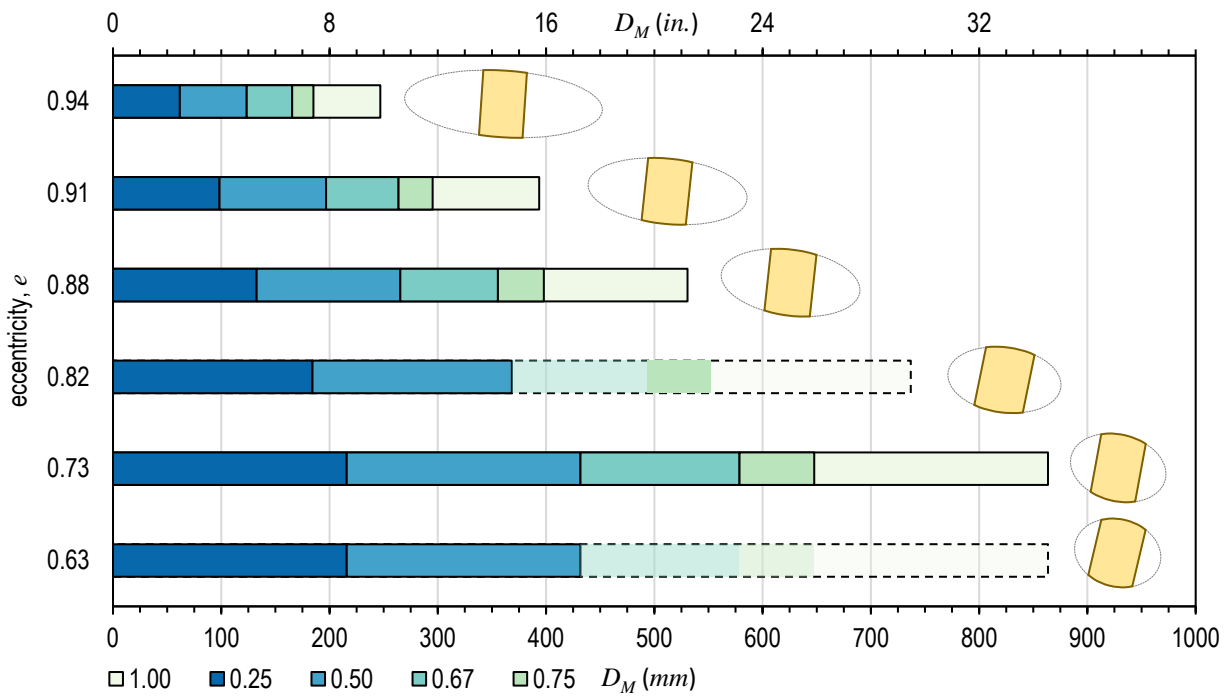
Overview of Test Results

The test program originally sequenced *No-Slip Traction Rolling* and panels with the narrowest elliptical profiles, first, and intended to preserve specimens for later testing in *Slip-Friction Rocking*. Stroke limitations of the lateral actuators, however, prompted a logistical compromise. Sequencing tests based on the 430-mm (17-in.) reach of the lateral actuators in fully reversed cycles saved the number of times apparatus had to be reconfigured. Actuator stroke limitations, therefore, prompted interruptions in displacement protocols of both *No-Slip Traction Rolling* and *Slip-Friction Rocking*. Changing the original order of tests procedures proved consequential, primarily because of the damaging effects of *Slip-Friction Rocking* at medium and high levels of overburden. The next paragraphs discuss which specimens were damaged, and *Observed Damage* provides specifics later in this chapter.

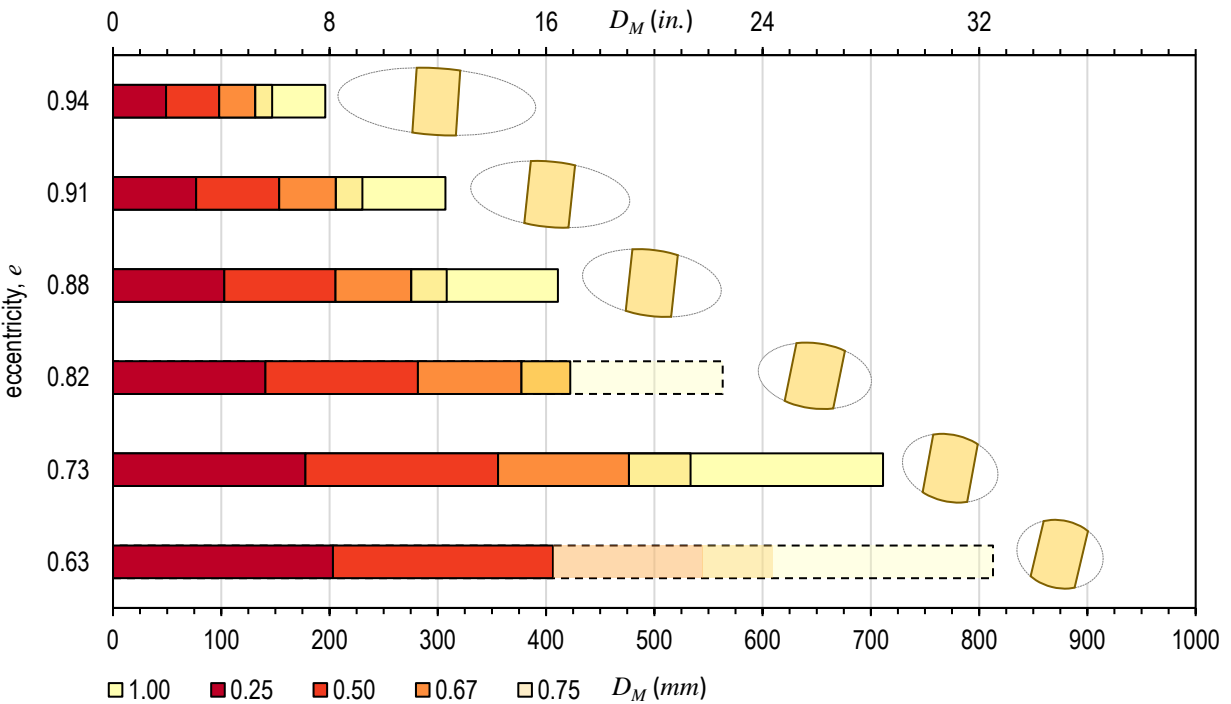
Figures 32 through 34 illustrate the ranges of displacement steps for each panel. The (a) graphs represent *No-Slip Traction Rolling*, and (b) graphs represent *Slip-Friction Rocking*. High, medium, and low levels of overburden generated three graphs of each configuration.

Comparisons of (a) and (b) show significant constraints imposed by *Slip-Friction Rocking*, relative to *No-Slip Traction Rolling*. Within each configuration, the graphs clearly show progressively shorter bars as eccentricity of the elliptical profiles grew wider. The displacement capacity, D_M , varied for each panel, because ellipse proportion and truncation determined the ratio between lateral displacement and corner contact.

Dashed bars of Figures 32 through 34 indicate unfulfilled displacement steps. The only two panels that did not complete displacement steps slated for *No-Slip Traction Rolling* had been tested out of sequence. Based on the trends observed in the other four specimens, the dashed bars of (a) in Figures 32 through 34 would have been solid had the specimens been tested in *No-Slip Traction Rolling* prior to any exposure in *Slip-Friction Rocking*. Under low overburden, most of *Slip-Friction Rocking* tests achieved completion, as indicated in Figure 32 (b). Again because of discontinuities in test sequencing, *Slip-Friction Rocking* capacities of the same two panels remains unknown for displacement steps beyond the reach of the lateral actuators in fully reversed cycles. The panel with e of 0.82 sustained damage near the end of the medium overburden cycles charted in Figure 33 (b), and the panel with e of 0.63 sustained damaged near the end of the high overburden cycles charted in Figure 34 (b). Had panels completed displacement steps at the low overburden level of 133 kN (30 kips) before ratcheting up the loads, all bars of Figure 33 (a) and perhaps more bars of Figure 33 (b) might have been accomplished. Fewer tests completed all displacement steps at the medium overburden level charted in Figure 34 (b). All specimens sustained some damage before rocking through cycles under high overburden, leaving Figure 34 (b) mostly faded. The bar charts summarize results that confirm the overall hypothesis that *Slip-Friction Rocking* demanded more of CLT connections than *No-Slip Traction Rolling*.

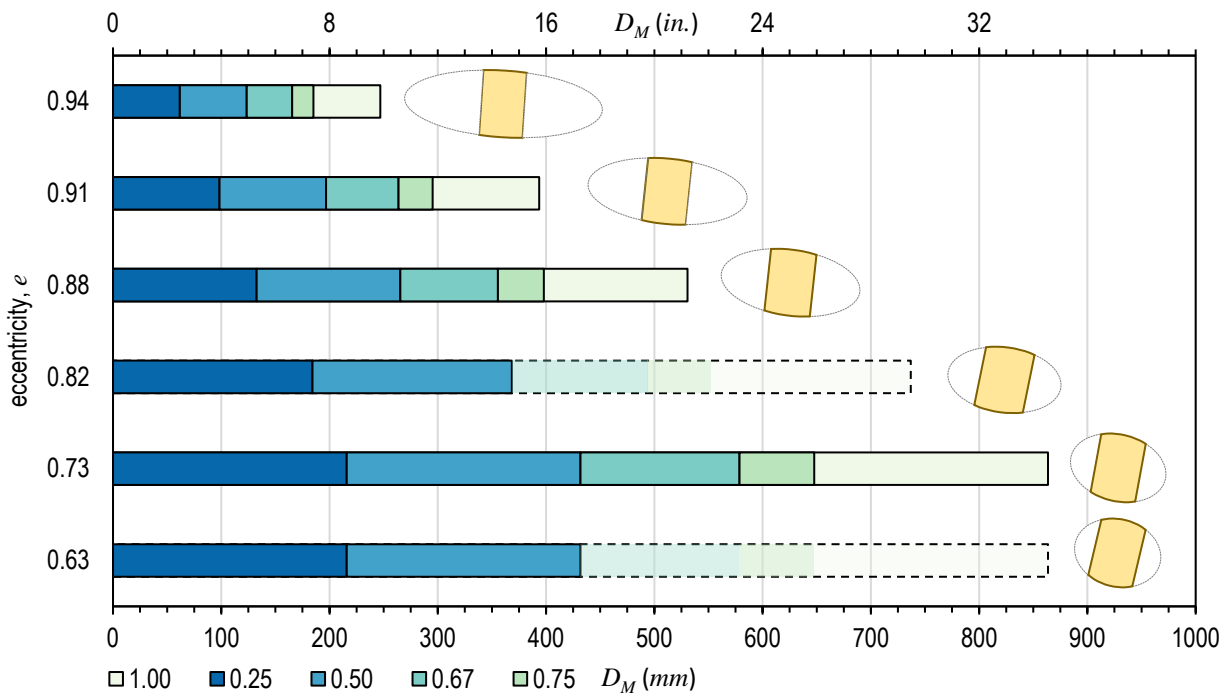


(a) Displacement steps for No-Slip Traction Rolling

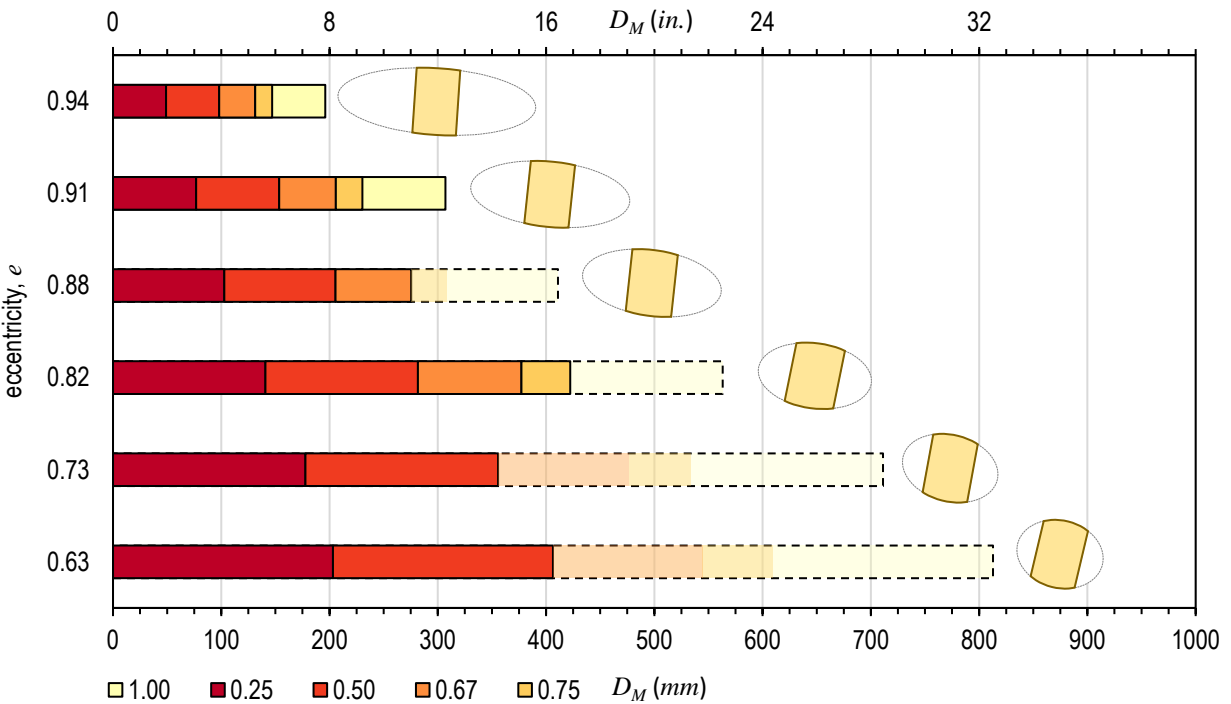


(b) Displacement steps for Slip-Friction Rocking

Figure 32. Prototype testing accomplished under low overburden of 133 kN (30 kips)

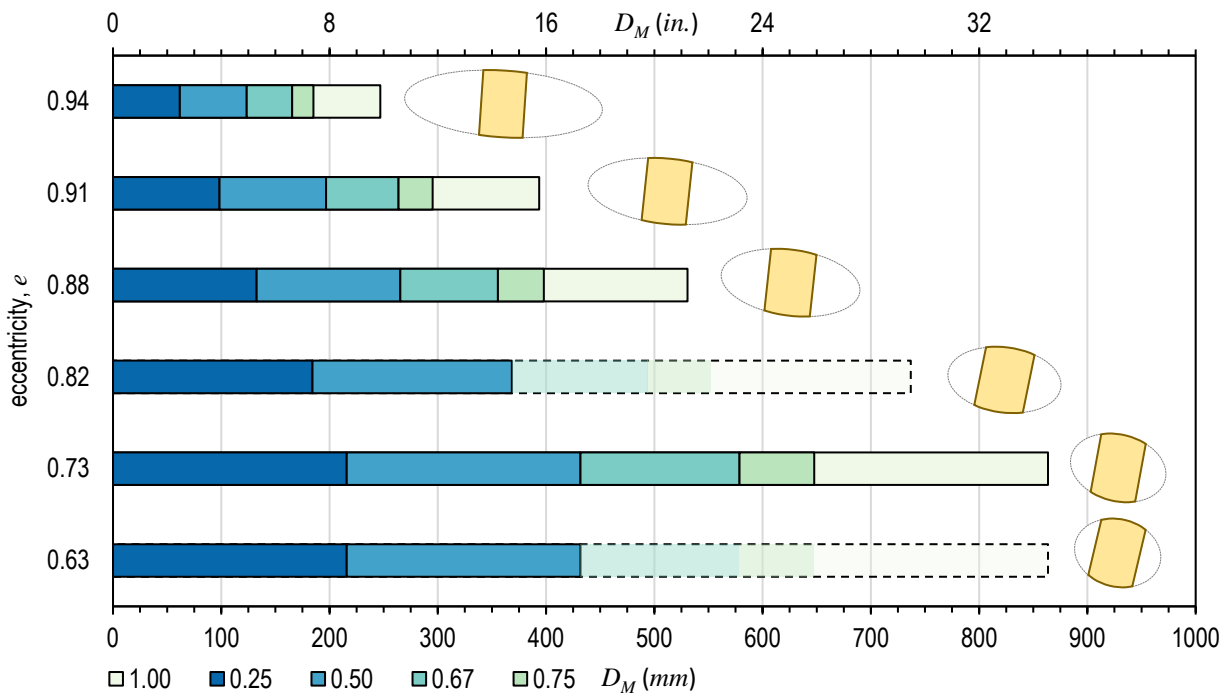


(a) Displacement steps for No-Slip Traction Rolling

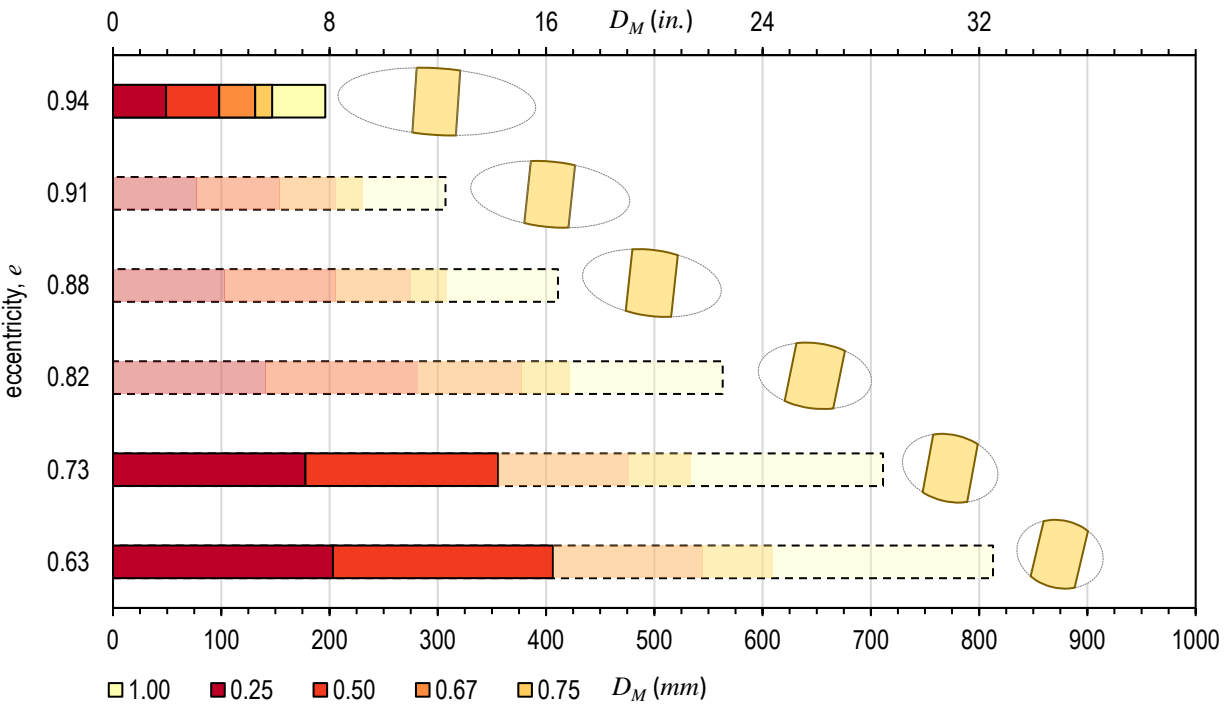


(b) Displacement steps for Slip-Friction Rocking

Figure 33. Prototype testing accomplished under medium overburden of 266 kN (60 kips)



(a) Displacement steps for No-Slip Traction Rolling



(b) Displacement steps for Slip-Friction Rocking

Figure 34. Prototype testing accomplished under high overburden of 400 kN (90 kips)

Hysteresis Plots

General Notes

- A page that diagrams and tabulates geometry and test protocol for each specimen precedes corresponding hysteresis plots.
- Each figure of hysteresis plots organizes multiple steps of the lateral load-displacement protocols.
- Figure captions at the bottom of each page name connection configuration, panel eccentricity, overburden conditions (varying or constant), and maximum displacement step.
- The middle column of each figure lists overburden, or simulated gravity, loads.
- Hysteresis charts for *No-Slip Traction Rolling* superpose idealized models derived from Equation (5).
- Idealized models assume rolling friction coefficient, μ_r , equals 0.01, or 1 percent of the overburden weight.
- Hysteresis charts for *Slip-Friction Rocking* superpose idealized models derived from Equation (8).
- Idealized models assume rolling friction coefficient, μ_s , equals 0.09, or 9 percent of the overburden weight.
- In cases exhibiting mixed mode behavior, results for *Slip-Friction Rocking* include overlays of the *No-Slip Traction Rolling* model.
- Labels below each plot provide the number of cycles and displacement step, as a fraction of the maximum displacement D_M , for isolated views.

- Superposed views overlay the cumulative displacement steps completed for a given panel eccentricity and overburden.
- Conversion from metric to U.S. customary units approximate, providing *soft* conversions, to align axes.
- Wherever practical, plots display the same scales of axes to facilitate comparisons.

Keyed Notes

Axis Scaling

- A. Horizontal axes rescaled to the range of superposed displacement steps.
- B. Vertical axes rescaled to peak loads.

Hysteresis Characteristics

- C. Blips or dips because of local and regular floor track imperfections.
- D. Widening of hysteresis loops.
- E. Slope increase of hysteresis loading segments.
- F. Slope decrease of hysteresis unloading segments.
- G. Local irregularity corresponding to audible slip or split of laminations.
- H. Global slip of panel.
- I. Deflation of hysteresis and potential indicator of damage.
- J. Stick-slip friction.
- K. Pinching of hysteresis along loading branches.

Boxed callouts identify hysteresis characteristics C through K on superposed plots of cumulative panel tests. For panels that did not fulfill complete load-displacement protocols, boxed callouts appear in plots of individual displacement step. Boxed callouts followed by “TYP.” typically apply to subsequent displacement steps of tests of the same panel and connection configuration.

No-Slip Traction Rolling

$e = 0.63$ Panel

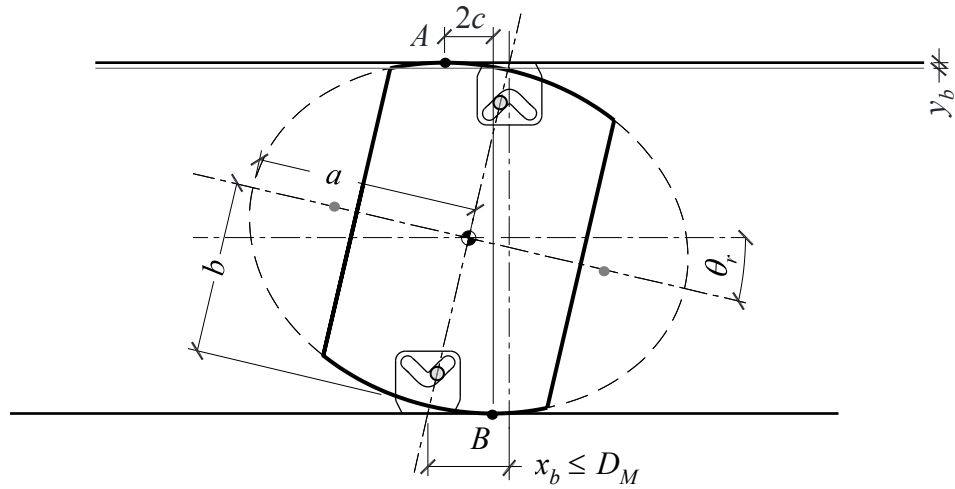


Figure 35. No-Slip Traction Rolling of panel with e of 0.63 eccentricity

Table 9. Geometric parameters for No-Slip Traction Rolling of $e = 0.63$ panel

a		b		e	D_M		Max θ_r		Max y_b		Max $2c$	
(mm)	(in.)	(mm)	(in.)		(mm)	(in.)	(deg.)	(rad.)	(mm)	(in.)	(mm)	(in.)
2350	92.5	1829	72.00	0.63	864	34.00	13	0.23	61	2.40	514	20.25

Table 10. Test protocol for No-Slip Traction Rolling of $e = 0.63$ panel

Displacement step	No. of Cycles	Drift		
		(mm)	(in.)	(%)
0.0025 h_s	20	9	0.36	0.25
0.25 D_M	3	216	8.50	5.90
0.50 D_M	3	432	17.00	11.81
0.67 D_M	3	579	22.78	15.82
1.00 D_M	6	864	34.00	23.61
0.75 D_M	18	648	25.50	17.71

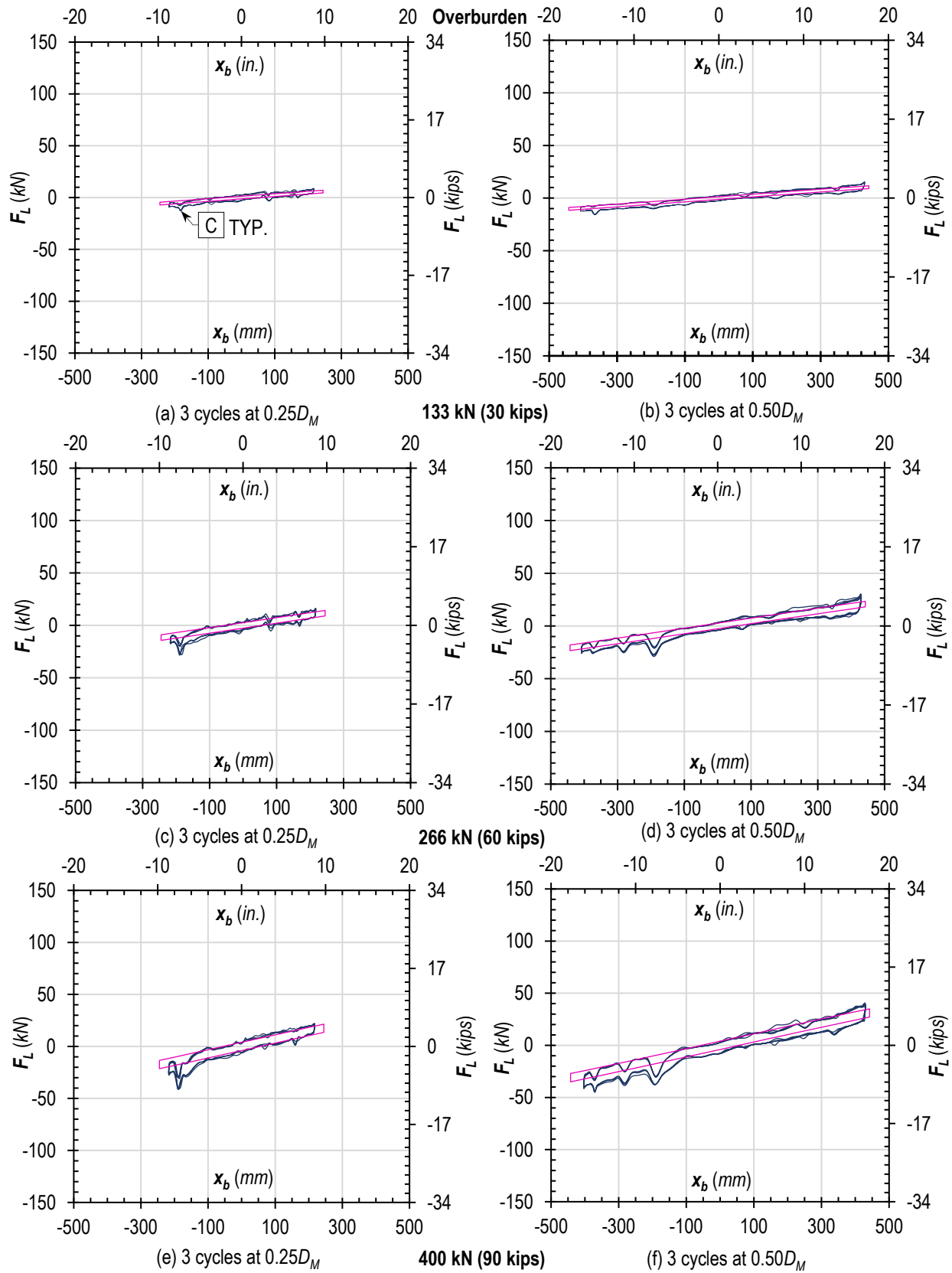


Figure 36. No-Slip Traction Rolling hysteresis plots of $e = 0.63$ panel under 3 overburden levels through $0.50D_M$

$e = 0.73$ Panel

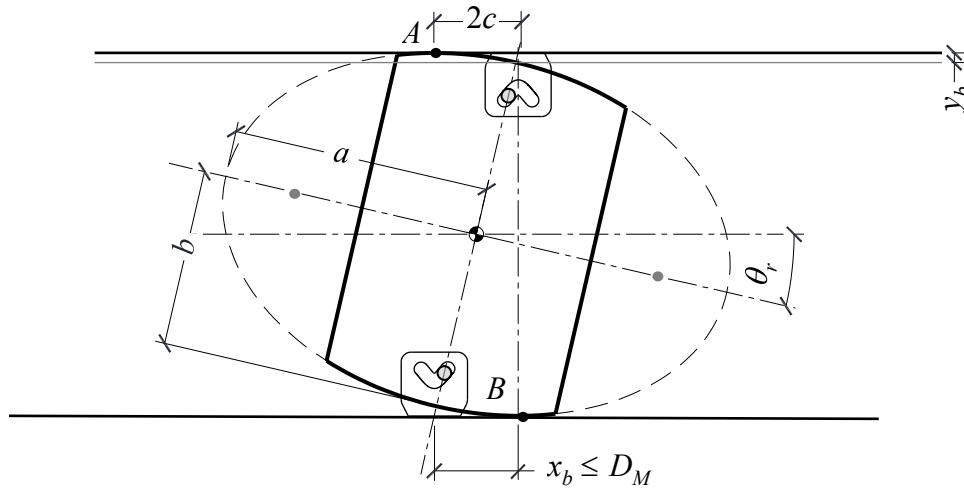


Figure 37. No-Slip Traction Rolling of panel with e of 0.73 eccentricity

Table 11. Geometric parameters for No-Slip Traction Rolling of $e = 0.73$ panel

a		b		e	D_M		Max θ		Max y_b		Max $2c$	
(mm)	(in.)	(mm)	(in.)		(mm)	(in.)	(deg.)	(rad.)	(mm)	(in.)	(mm)	(in.)
2667	105	1829	72.00	0.73	864	34.00	13	0.23	103	4.04	880	34.64

Table 12. Test protocol for No-Slip Traction Rolling of $e = 0.73$ panel

Displacement step	No. of Cycles	Drift		
		(mm)	(in.)	(%)
0.0025 h_s	20	9	0.36	0.25
0.25 D_M	3	216	8.50	5.90
0.50 D_M	3	432	17.00	11.81
0.67 D_M	3	579	22.78	15.82
1.00 D_M	6	864	34.00	23.61
0.75 D_M	18	648	25.50	17.71

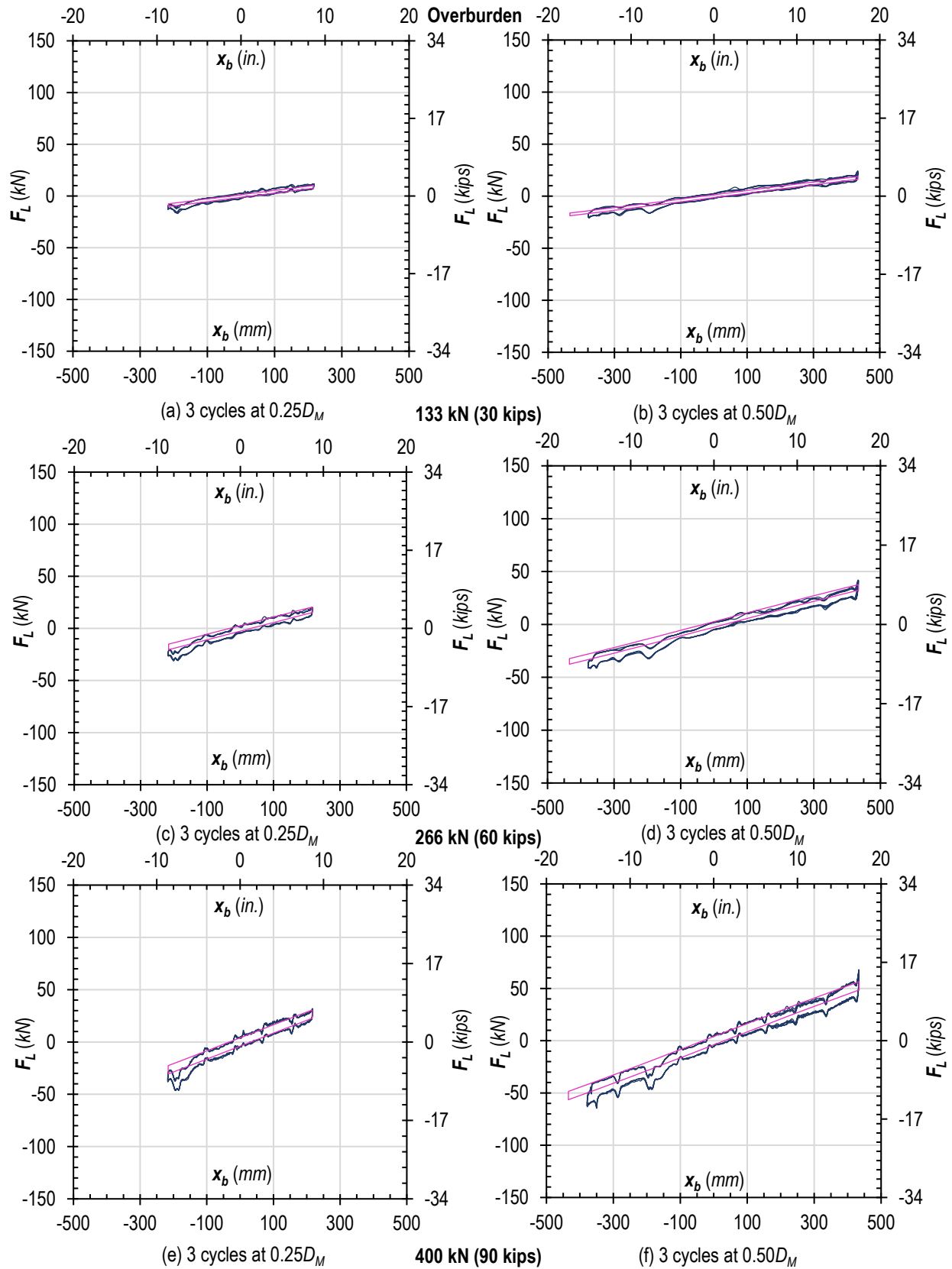


Figure 38. No-Slip Traction Rolling hysteresis plots of $e = 0.73$ panel under 3 overburden levels through $0.50D_M$

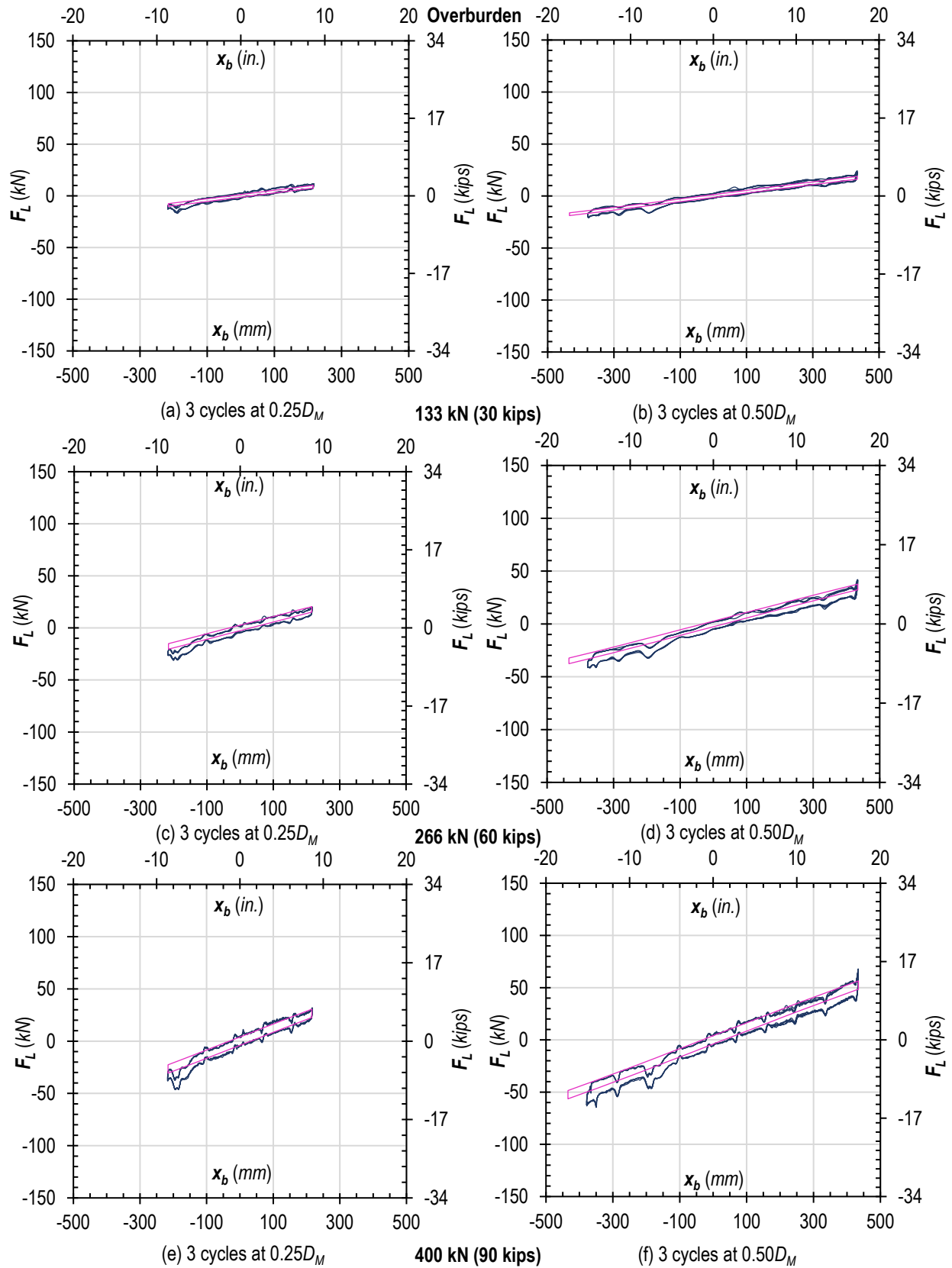


Figure 39. No-Slip Traction Rolling hysteresis plots of $e = 0.73$ panel under 3 overburden levels through $0.75D_M$

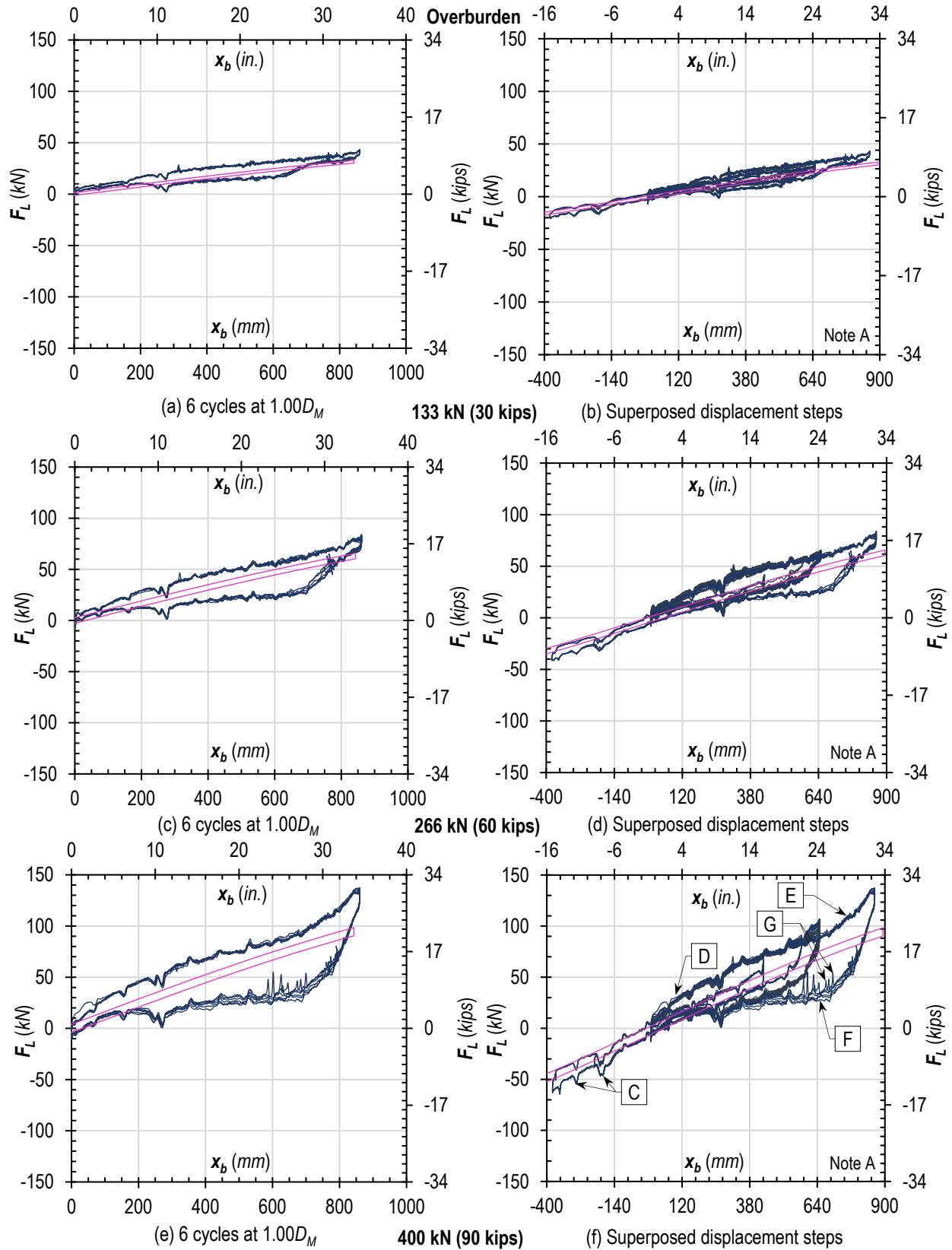


Figure 40. No-Slip Traction Rolling hysteresis plots of $e = 0.73$ panel under 3 overburden levels through $1.00D_M$

$e = 0.82$ Panel

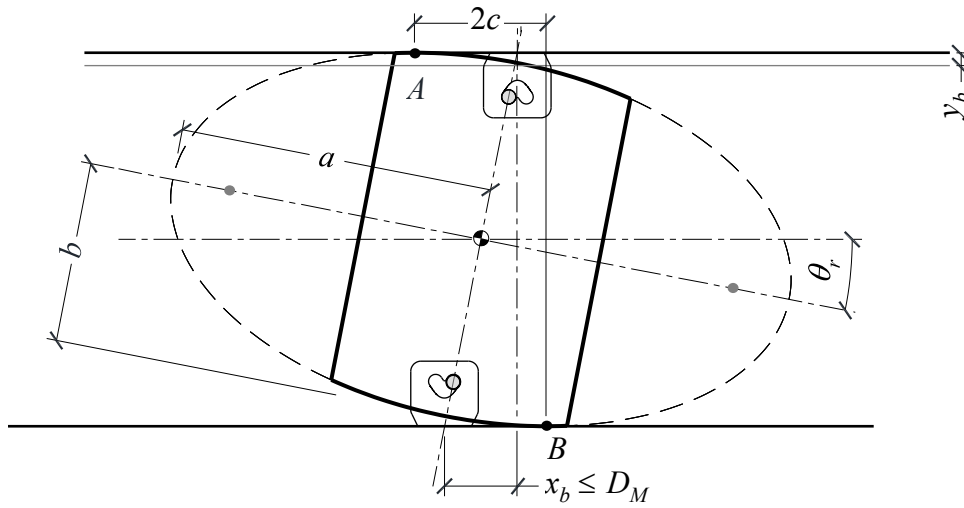


Figure 41. No-Slip Traction Rolling of panel with e of 0.82 eccentricity

Table 13. Geometric parameters for No-Slip Traction Rolling of $e = 0.82$ panel

a		b		e	D_M		Max θ_r		Max y_b		Max $2c$	
(mm)	(in.)	(mm)	(in.)		(mm)	(in.)	(deg.)	(rad.)	(mm)	(in.)	(mm)	(in.)
3188	125.5	1829	72.00	0.82	737	29.00	11	0.19	133	5.25	1347	53.04

Table 14. Test protocol for No-Slip Traction Rolling of $e = 0.82$ panel

Displacement step	No. of Cycles	Drift		
		(mm)	(in.)	(%)
0.0025 h_s	20	9	0.36	0.25
0.25 D_M	3	184	7.25	5.03
0.50 D_M	3	368	14.50	10.07
0.67 D_M	3	494	19.43	13.49
1.00 D_M	6	737	29.00	20.14
0.75 D_M	18	552	21.75	15.10

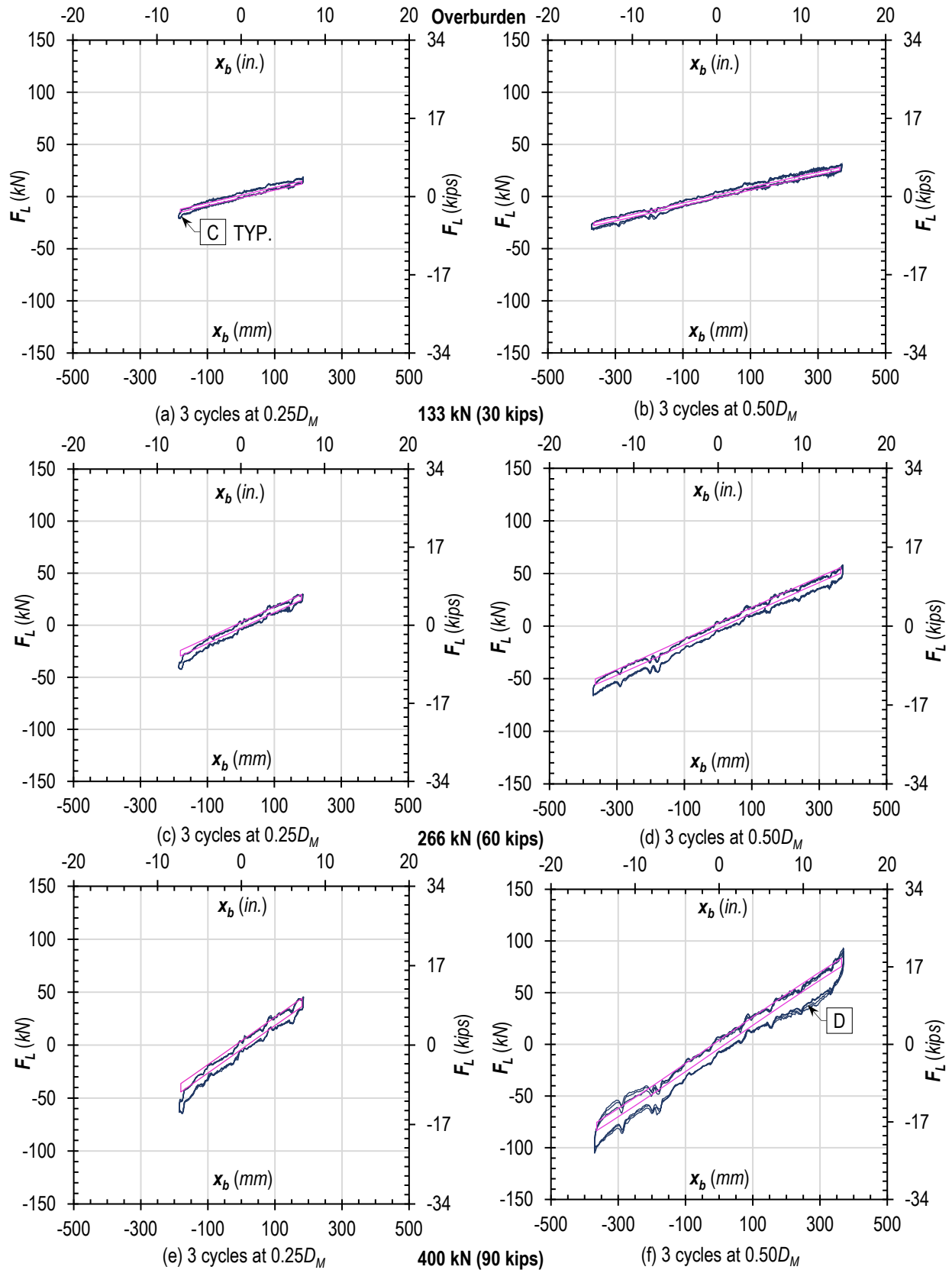


Figure 42. No-Slip Traction Rolling hysteresis plots of $e = 0.82$ panel under 3 overburden levels through $0.50D_M$

$e = 0.88$ Panel

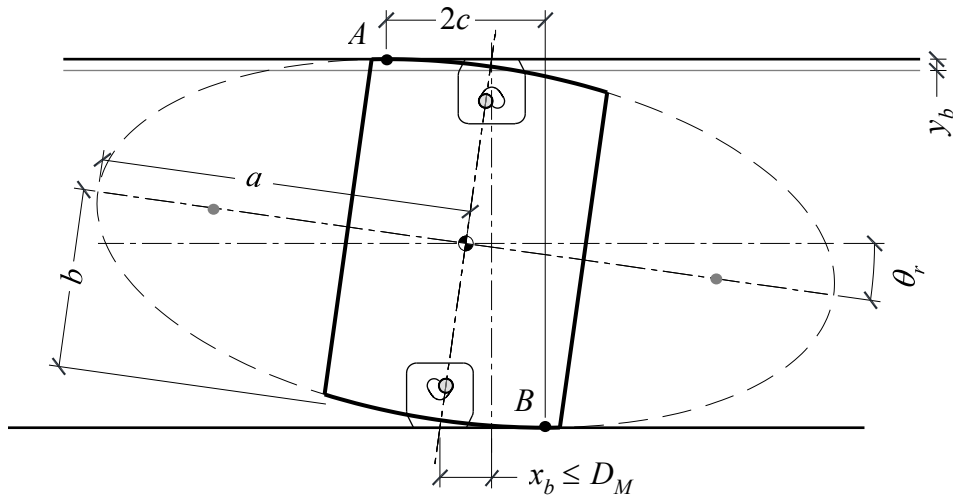


Figure 43. No-Slip Traction Rolling of panel with e of 0.88 eccentricity

Table 15. Geometric parameters for No-Slip Traction Rolling of $e = 0.88$ panel

a		b		e	D_M		Max θ_r		Max y_b		Max $2c$	
(mm)	(in.)	(mm)	(in.)		(mm)	(in.)	(deg.)	(rad.)	(mm)	(in.)	(mm)	(in.)
3810	150	1829	72.00	0.88	531	20.89	8	0.14	116	4.58	1632	64.25

Table 16. Test protocol for No-Slip Traction Rolling of $e = 0.88$ panel

Displacement step	No. of Cycles	Drift (mm)	Drift (in.)	Drift (%)
0.0025 h_s	20	9	0.36	0.25
0.25 D_M	3	133	5.22	3.63
0.50 D_M	3	265	10.45	7.25
0.67 D_M	3	356	14.00	9.72
1.00 D_M	6	531	20.89	14.51
0.75 D_M	18	398	15.67	10.88

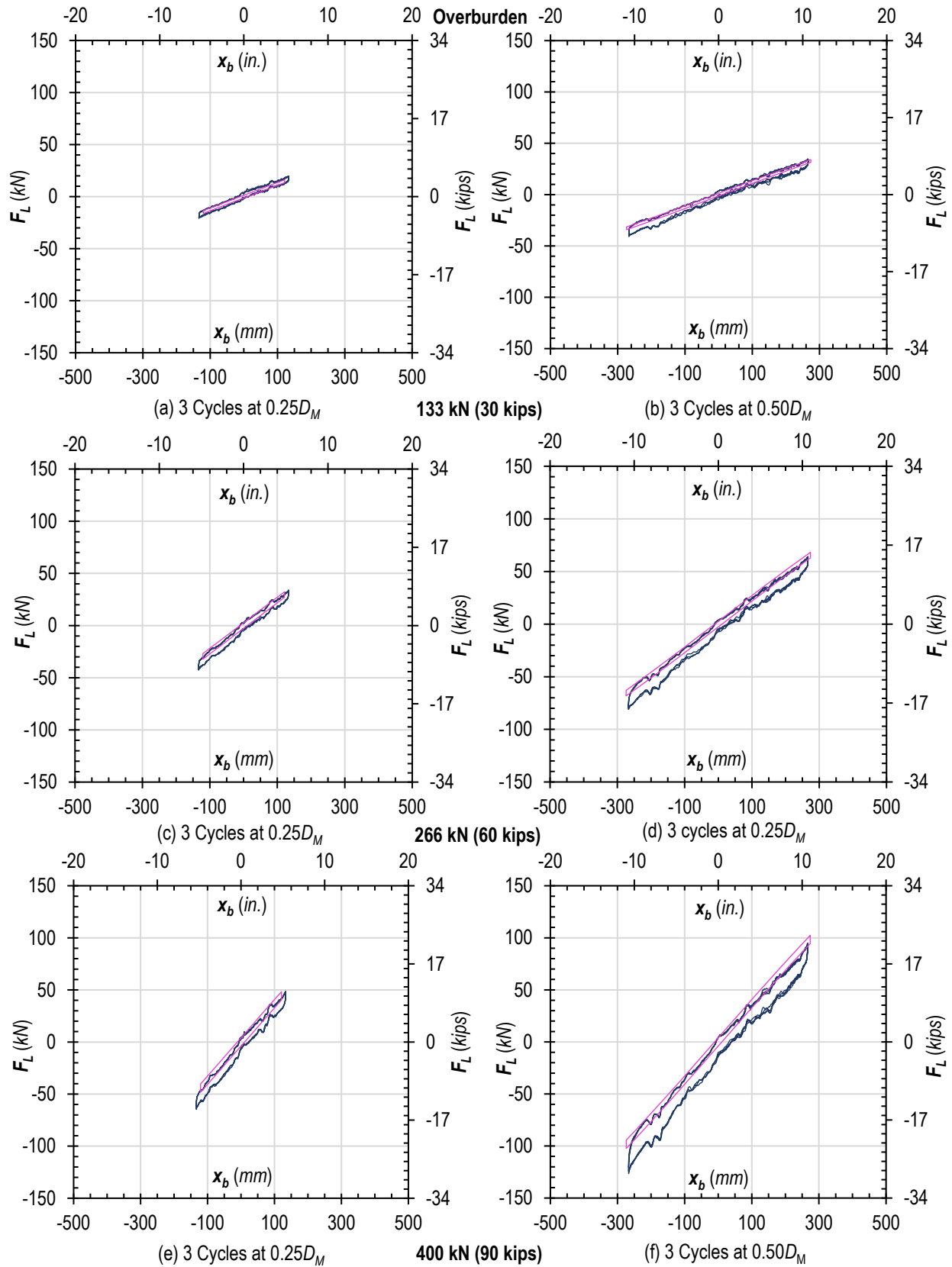


Figure 44. No-Slip Traction Rolling hysteresis plots of $e = 0.88$ panel under 3 overburden levels through $0.50D_M$

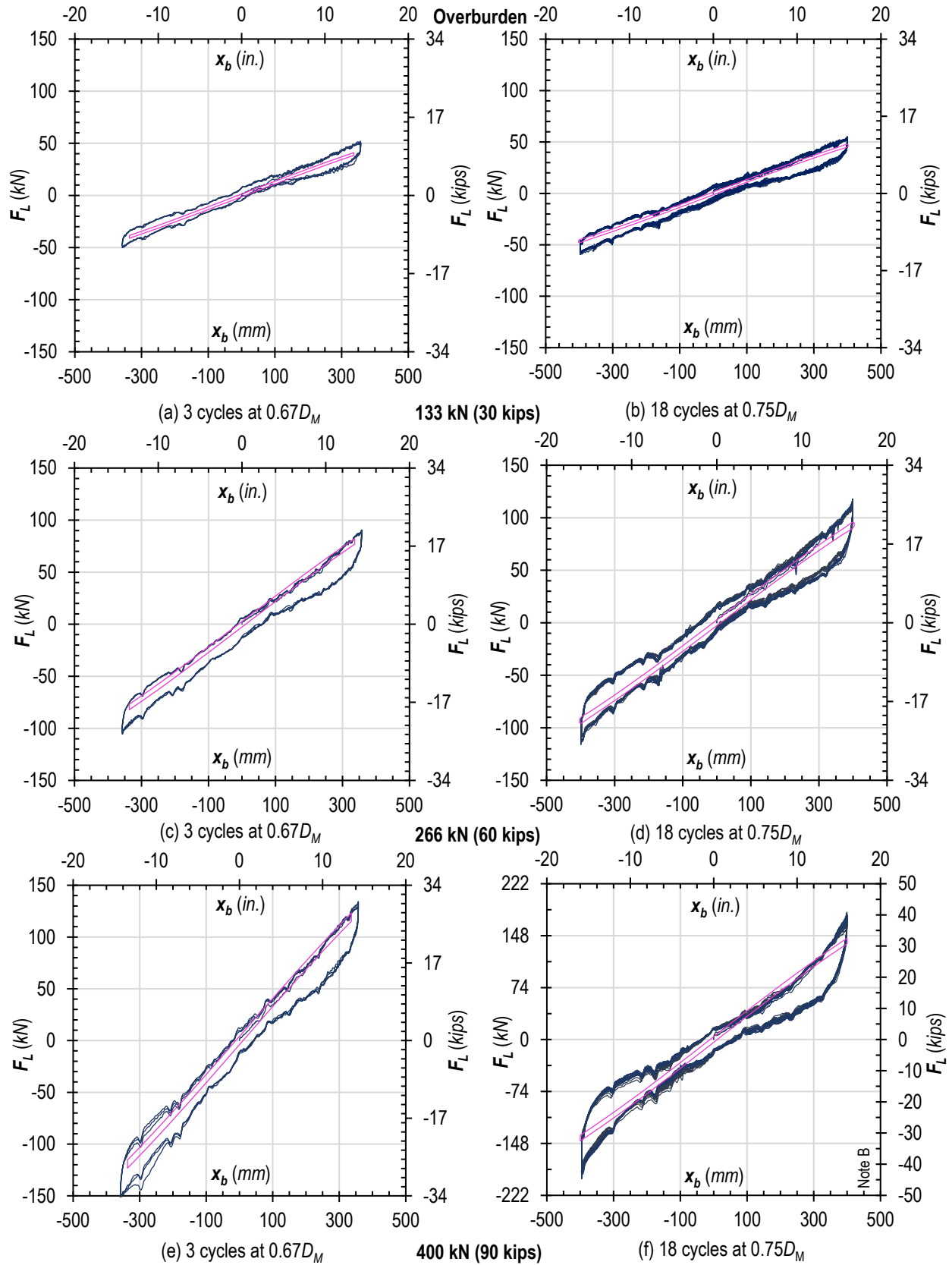


Figure 45. No-Slip Traction Rolling hysteresis plots of $e = 0.88$ panel under 3 overburden levels through $0.75D_M$

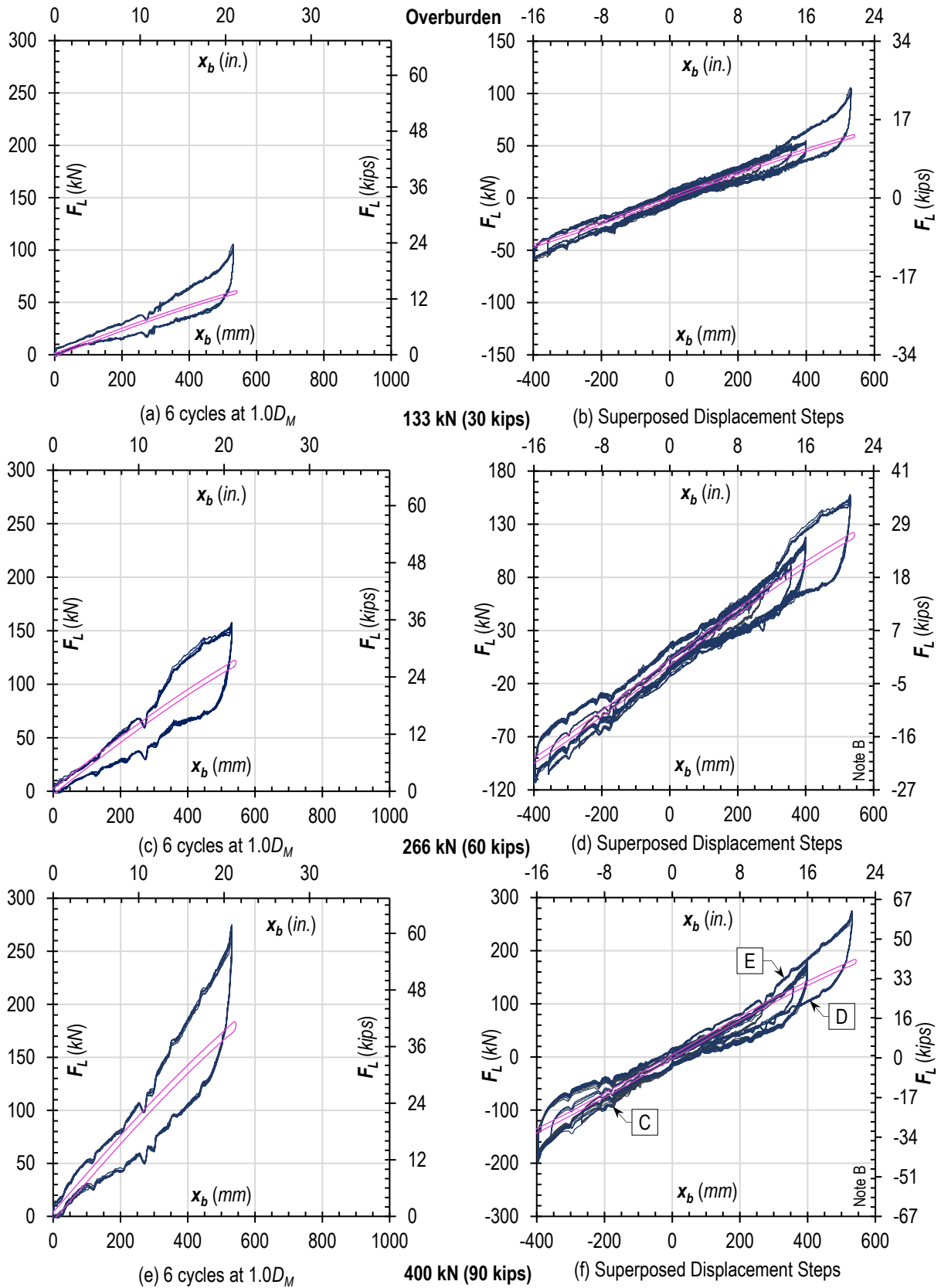


Figure 46. No-Slip Traction Rolling hysteresis plots of $e = 0.88$ panel under 3 overburden levels through $1.0D_M$

$e = 0.91$ Panel

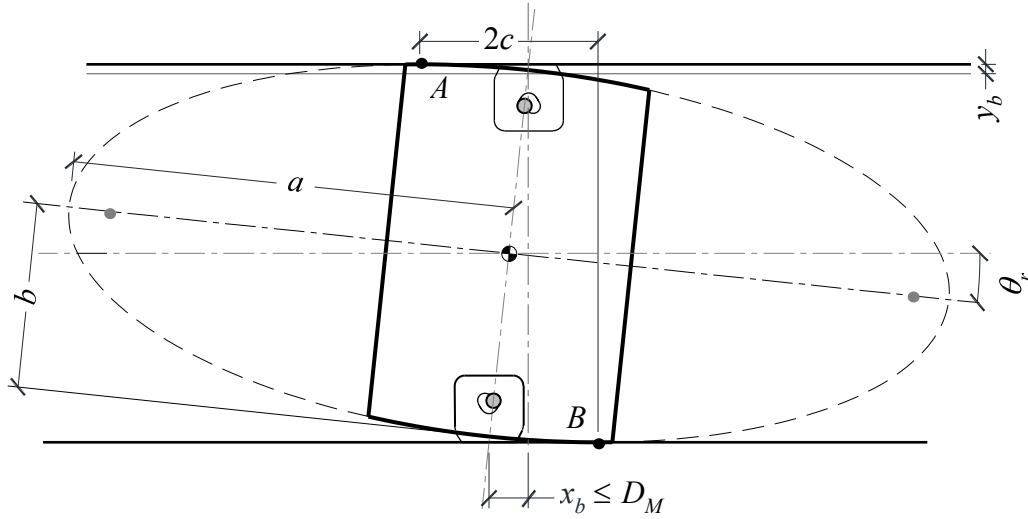


Figure 47. No-Slip Traction Rolling of panel with e of 0.91 eccentricity

Table 17. Geometric parameters for No-Slip Traction Rolling of $e = 0.91$ panel

a		b		e	D_M		Max θ_r		Max y_b		Max $2c$	
(mm)	(in.)	(mm)	(in.)		(mm)	(in.)	(deg.)	(rad.)	(mm)	(in.)	(mm)	(in.)
4407	173.5	1829	72.00	0.91	394	15.50	6	0.10	95	3.73	1782	70.14

Table 18. Test protocol for No-Slip Traction Rolling of $e = 0.91$ panel

Displacement step	No. of Cycles	Drift		
		(mm)	(in.)	(%)
0.0025 h_s	20	9	0.36	0.25
0.25 D_M	3	98	3.88	2.69
0.50 D_M	3	197	7.75	5.38
0.67 D_M	3	264	10.39	7.21
1.00 D_M	6	394	15.50	10.76
0.75 D_M	18	295	11.63	8.07

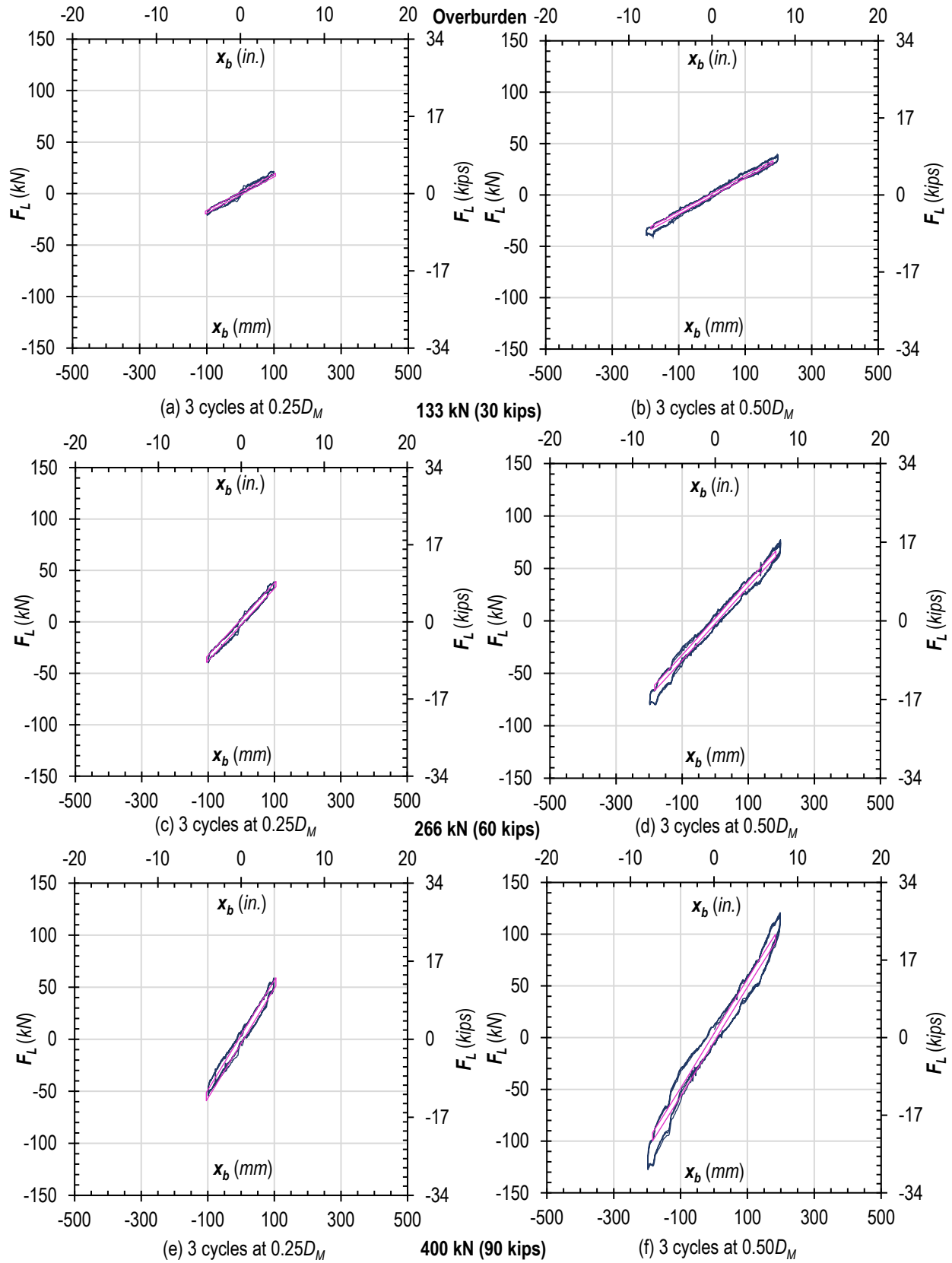


Figure 48. No-Slip Traction Rolling hysteresis plots of $e = 0.91$ panel under 3 overburden levels through $0.50D_M$

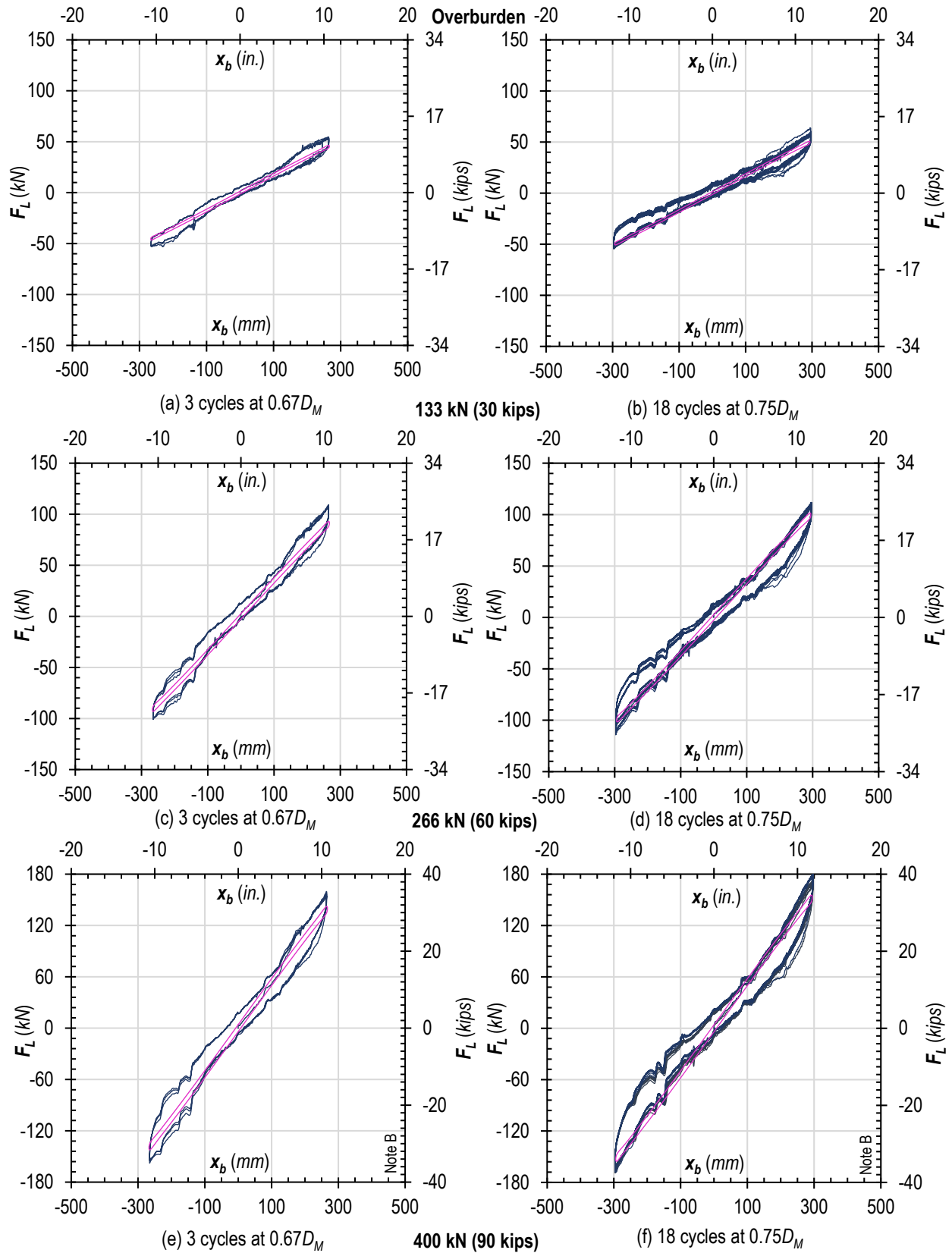


Figure 49. No-Slip Traction Rolling hysteresis plots of $e = 0.91$ panel under 3 overburden levels through $0.75D_M$

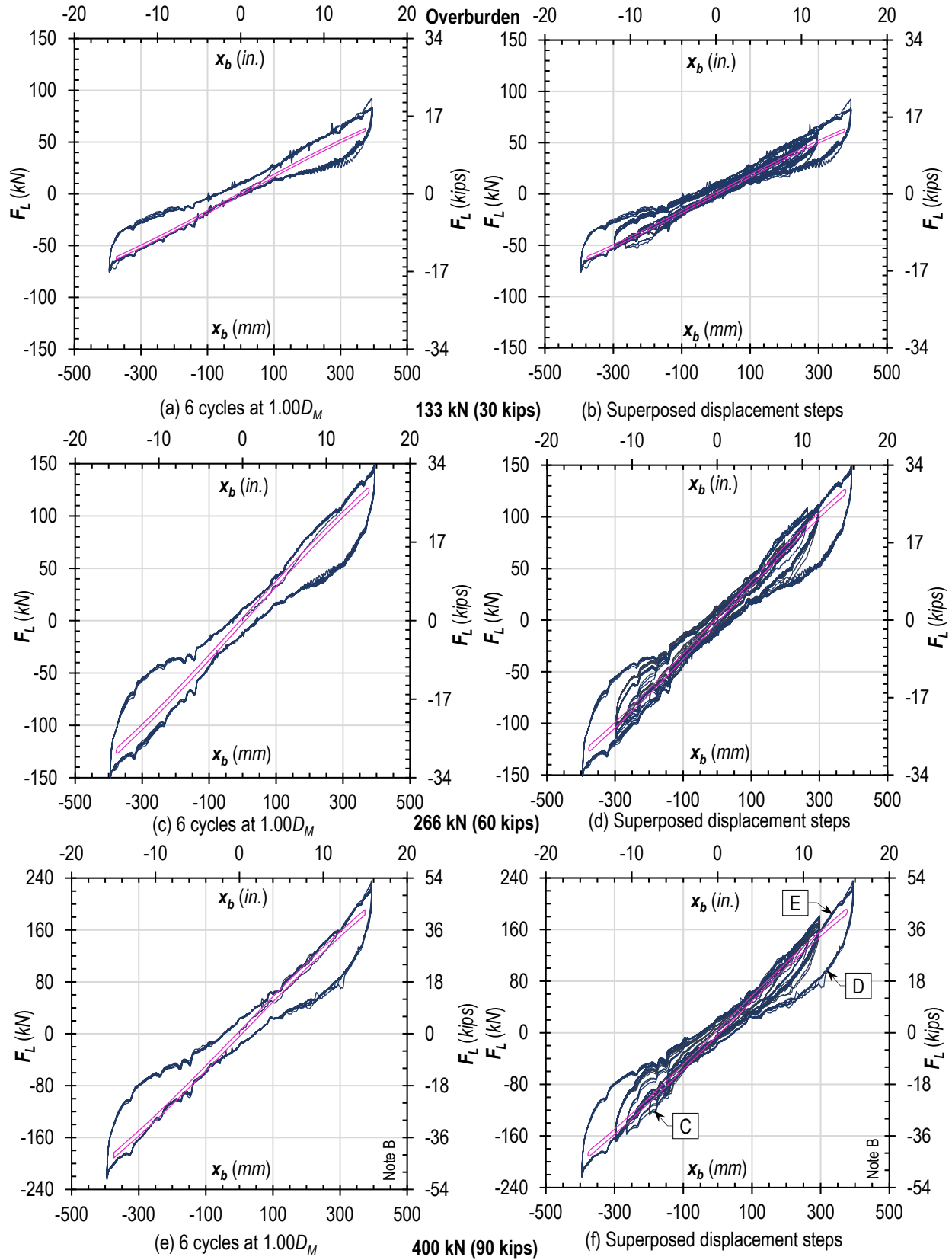


Figure 50. No-Slip Traction Rolling hysteresis plots of $e = 0.91$ panel under 3 overburden levels through $1.00D_M$

$e = 0.94$ Panel

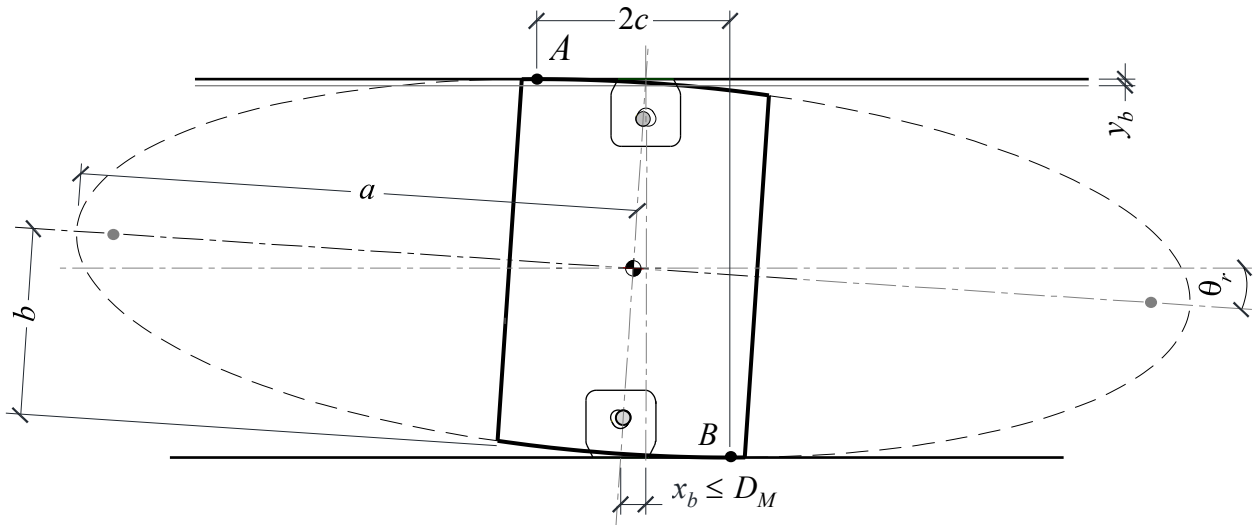


Figure 51. No-Slip Traction Rolling of panel with e of 0.94 eccentricity

Table 19. Geometric parameters for No-Slip Traction Rolling of $e = 0.94$ panel

a		b		e	D_M		Max θ_r		Max y_b		Max $2c$	
(mm)	(in.)	(mm)	(in.)		(mm)	(in.)	(deg.)	(rad.)	(mm)	(in.)	(mm)	(in.)
5486	216	1829	72.00	0.94	247	9.72	4	0.07	64	2.51	1903	74.92

Table 20. Test protocol for No-Slip Traction Rolling of $e = 0.94$ panel

Displacement step	No. of Cycles	Drift		
		(mm)	(in.)	(%)
0.0025 h_s	20	9	0.36	0.25
0.25 D_M	3	62	2.43	1.69
0.50 D_M	3	123	4.86	3.38
0.67 D_M	3	165	6.51	4.52
1.00 D_M	6	247	9.72	6.75
0.75 D_M	18	185	7.29	5.06

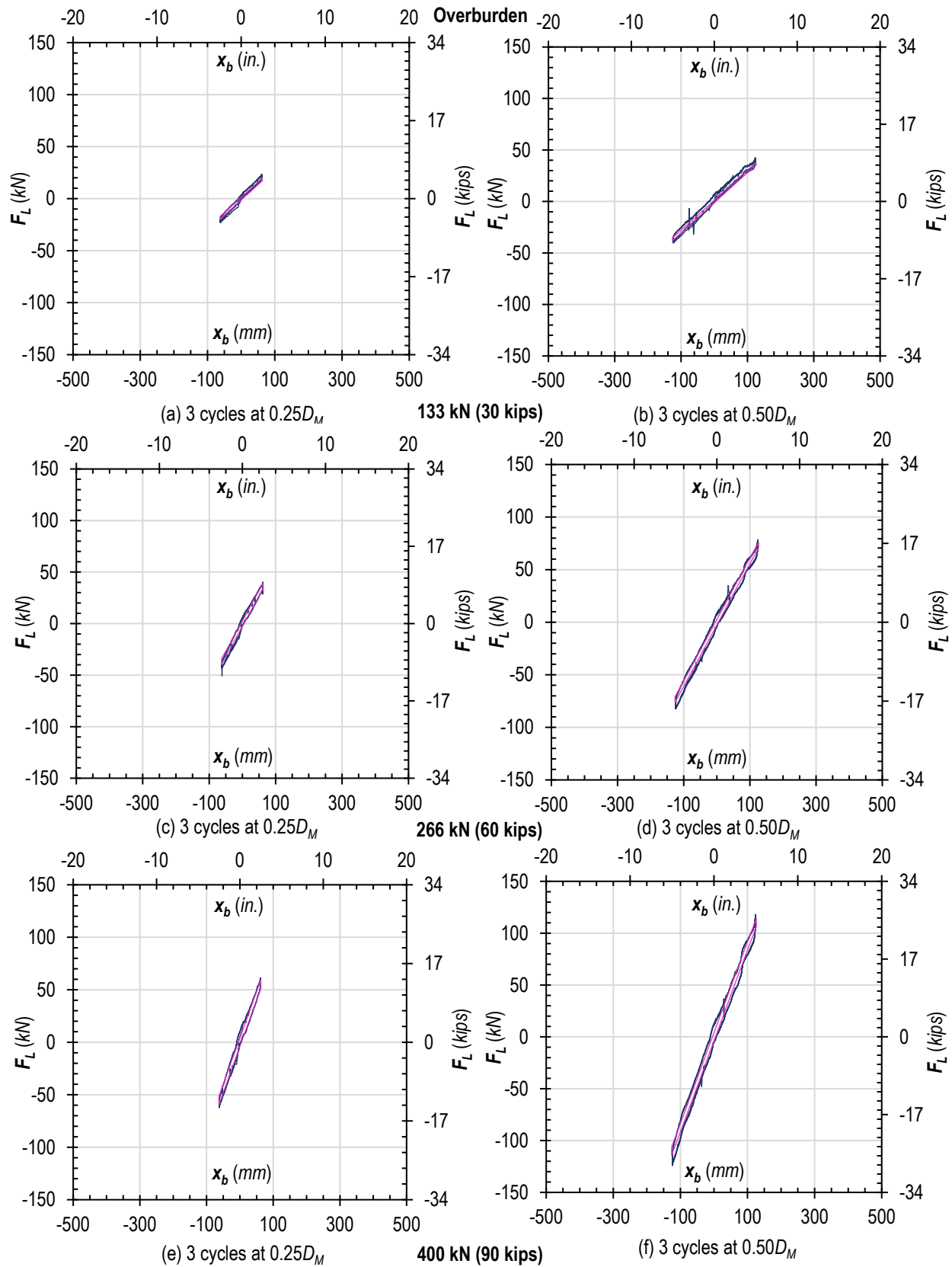


Figure 52. No-Slip Traction Rolling hysteresis plots of $e = 0.94$ panel under 3 overburden levels through $0.50D_M$

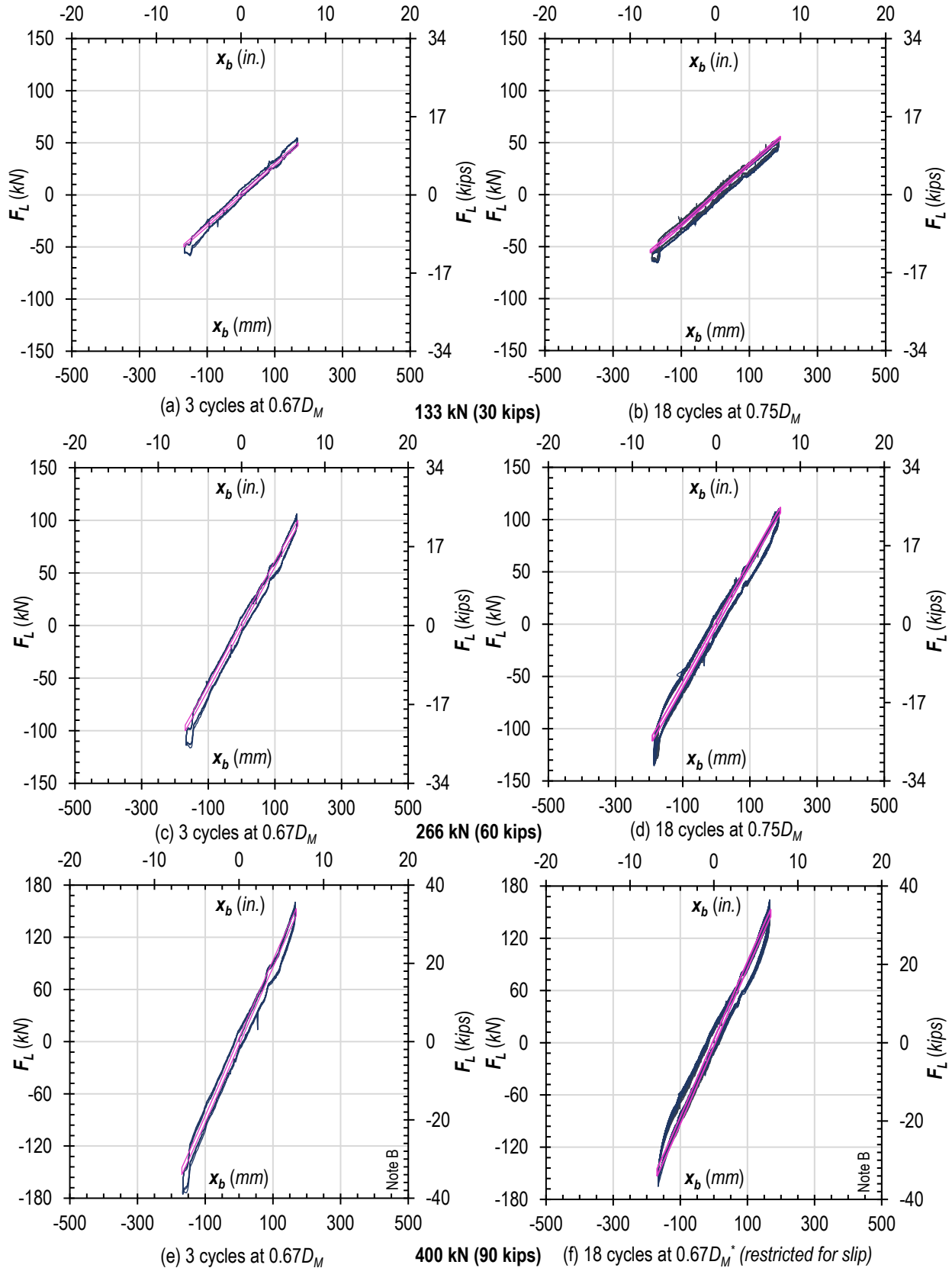


Figure 53. No-Slip Traction Rolling hysteresis plots of $e = 0.94$ panel under 3 overburden levels through $0.75D_M$

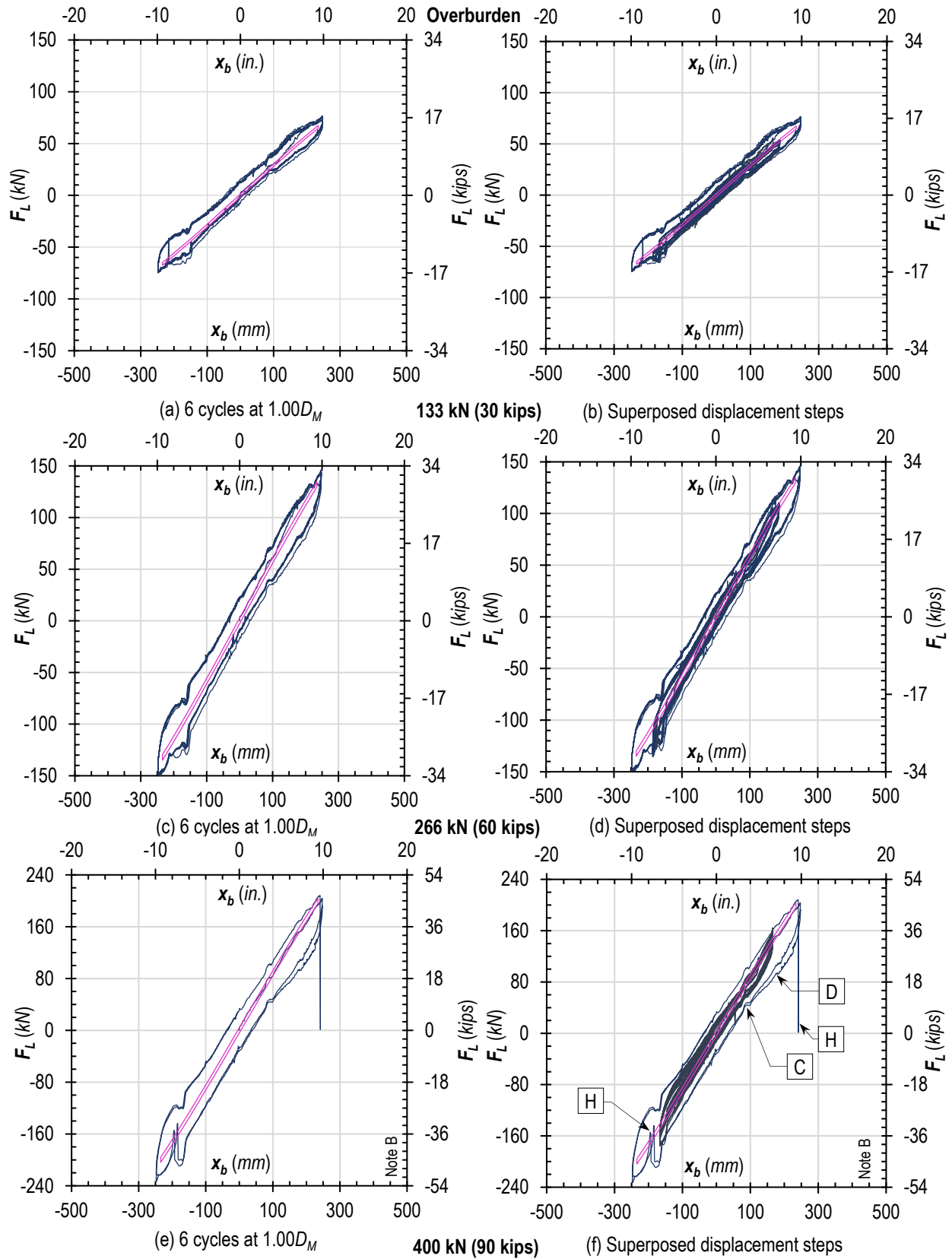


Figure 54. No-Slip Traction Rolling hysteresis plots of $e = 0.94$ panel under 3 overburden levels through $1.00D_M$

Slip-Friction Rocking

$e = 0.63$ Panel

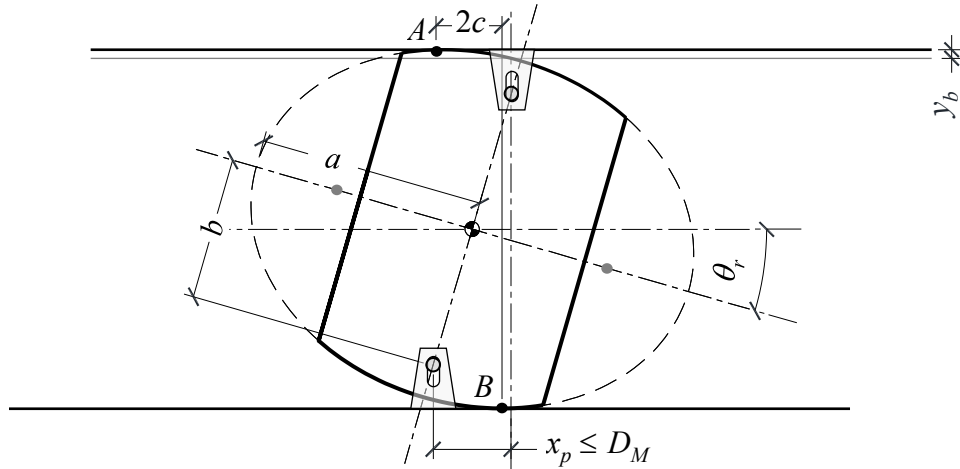


Figure 55. Slip-Friction Rocking of panel with e of 0.63 eccentricity

Table 21. Geometric parameters for Slip-Friction Rocking of $e = 0.63$ panel

a		b		e	D_M		Max θ_r		Max y_b		Max $2c$	
(mm)	(in.)	(mm)	(in.)		(mm)	(in.)	(deg.)	(rad.)	(mm)	(in.)	(mm)	(in.)
2350	92.5	1829	72.00	0.63	813	32.00	16	0.28	90	3.56	616	24.25

Table 22. Test protocol for Slip-Friction Rocking of $e = 0.63$ panel

Displacement step		No. of Cycles		Drift	
			(mm)	(in.)	(%)
0.0025	h_s	20	9	0.36	0.25
0.25	D_M	3	203	8.00	5.56
0.50	D_M	3	406	16.00	11.11
0.67	D_M	3	545	21.44	14.89
1.00	D_M	6	813	32.00	22.22
0.75	D_M	18	610	24.00	16.67

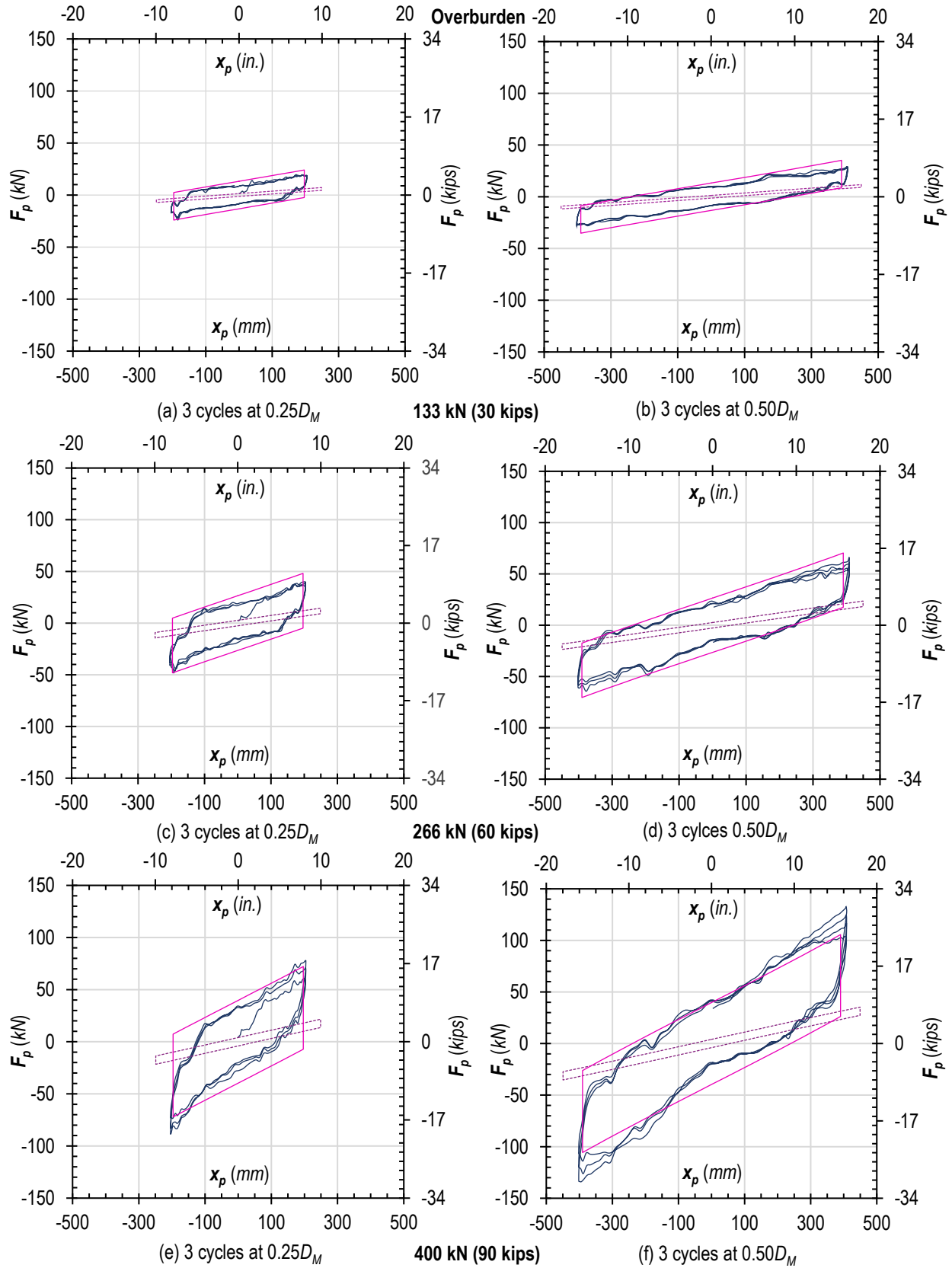


Figure 56. Slip-Friction Rocking hysteresis plots of $e = 0.63$ panel under 3 overburden levels through $0.50D_M$

$e = 0.73$ Panel

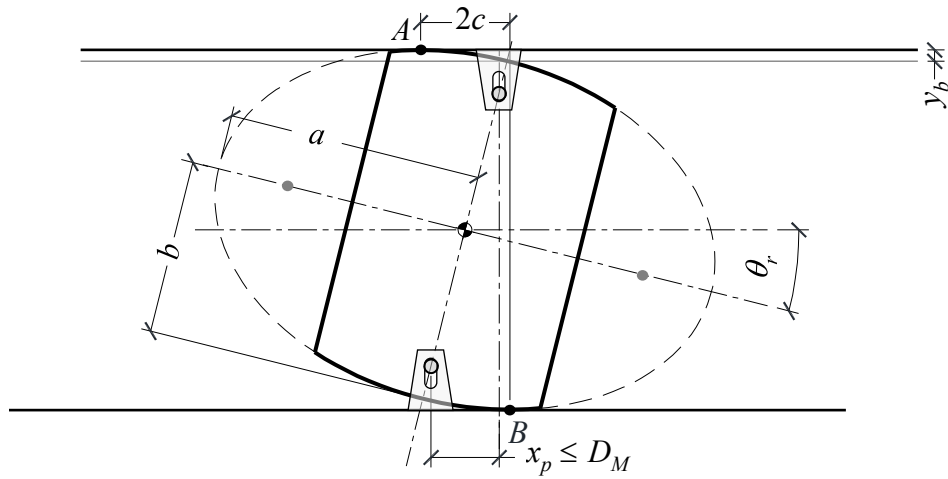


Figure 57. Slip-Friction Rocking of panel with e of 0.73 eccentricity

Table 23. Geometric parameters for Slip-Friction Rocking of $e = 0.73$ panel

a		b		e	D_M		Max θ_r		Max y_b		Max $2c$	
(mm)	(in.)	(mm)	(in.)		(mm)	(in.)	(deg.)	(rad.)	(mm)	(in.)	(mm)	(in.)
2667	105	1829	72.00	0.73	711	28.00	14	0.24	119	4.68	938	36.93

Table 24. Test protocol for Slip-Friction Rocking of $e = 0.73$ panel

Displacement step	No. of Cycles	Drift		
		(mm)	(in.)	(%)
0.0025 h_s	20	9	0.36	0.25
0.25 D_M	3	178	7.00	4.86
0.50 D_M	3	356	14.00	9.72
0.67 D_M	3	477	18.76	13.03
1.00 D_M	6	711	28.00	19.44
0.75 D_M	18	533	21.00	14.58

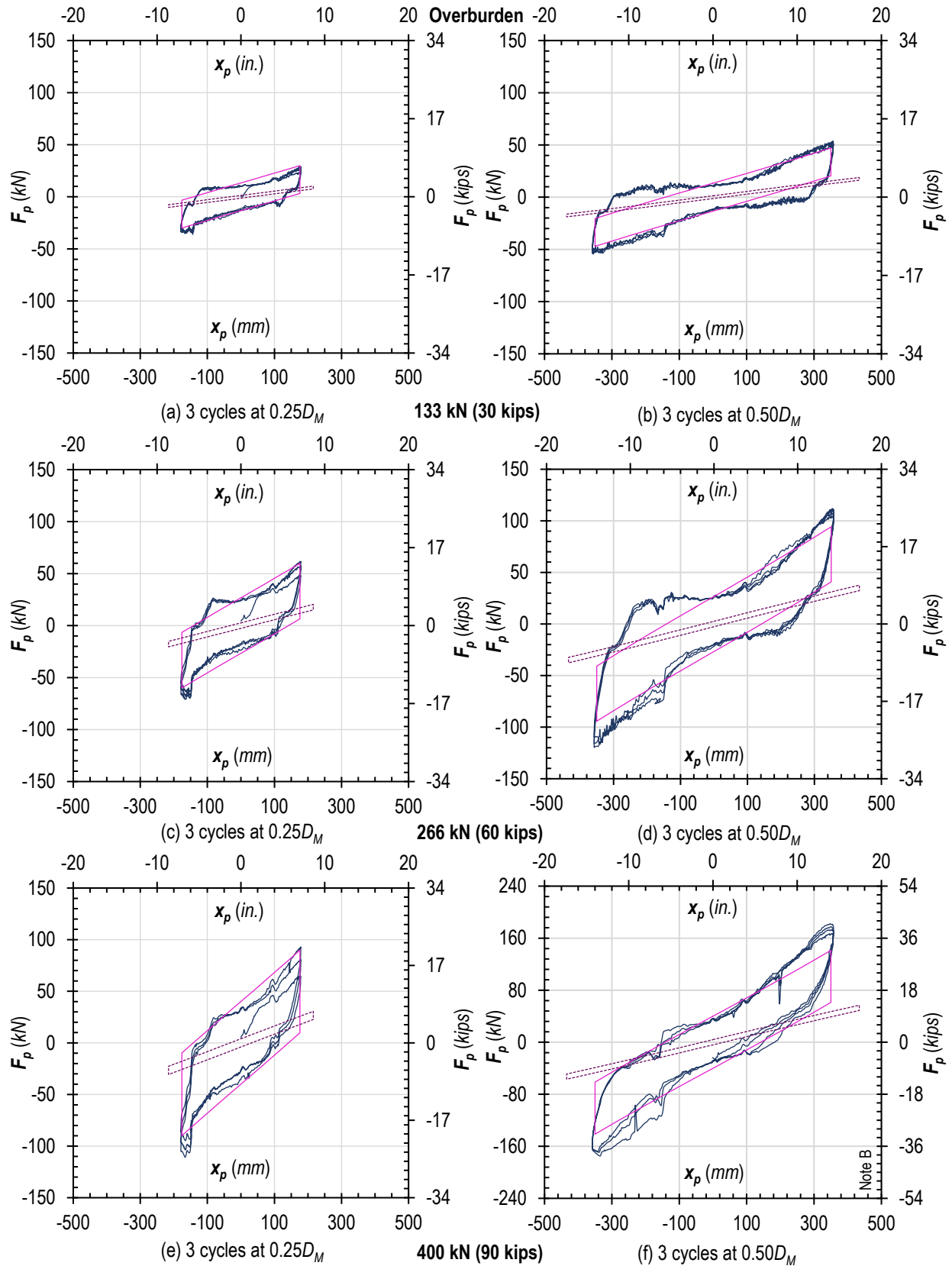


Figure 58. Slip-Friction Rocking hysteresis plots of $e = 0.73$ panel under 3 overburden levels through $0.50D_M$

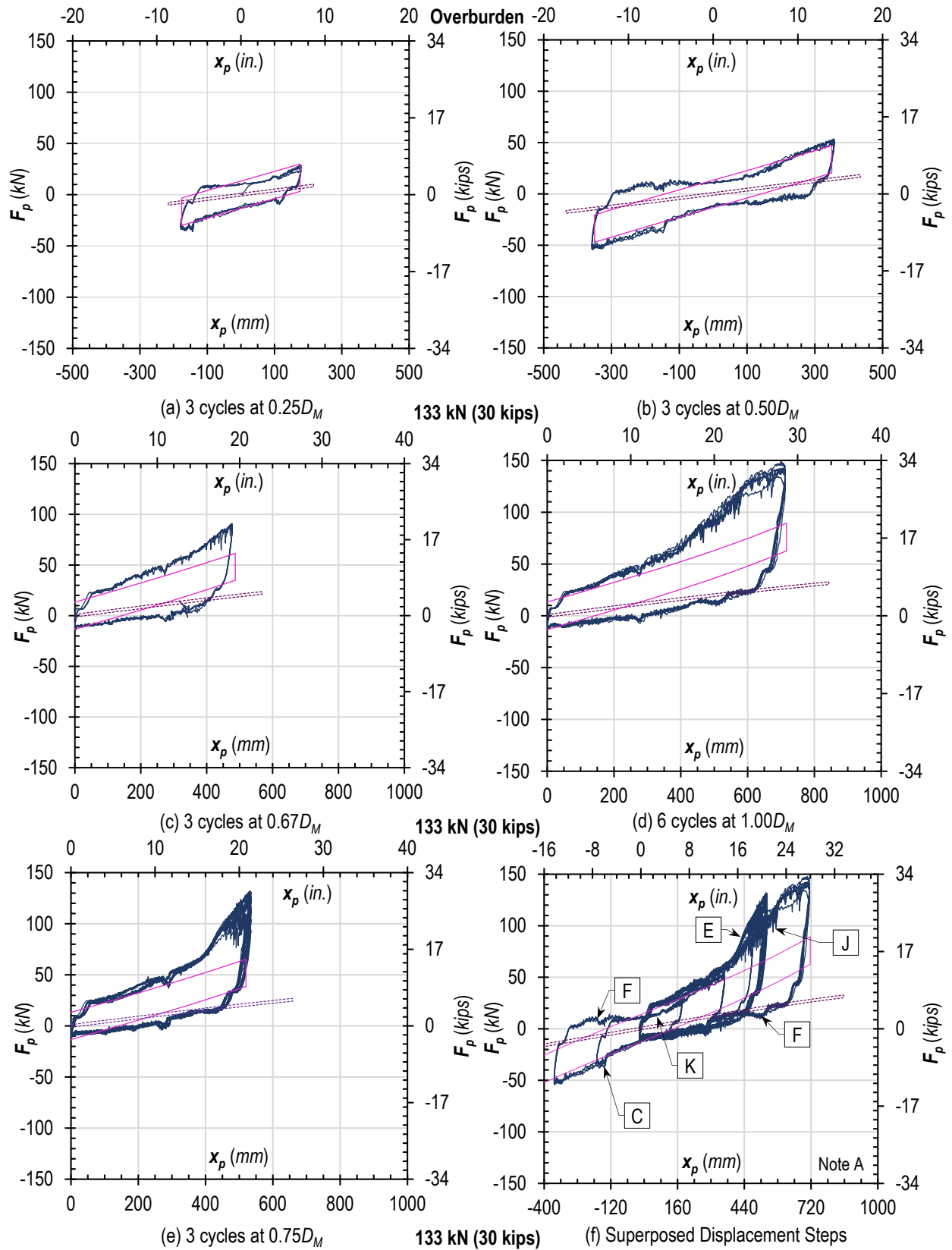


Figure 59. Slip-Friction Rocking hysteresis plots of $e = 0.73$ panel under constant low overburden through $1.00D_M$

$e = 0.82$ Panel

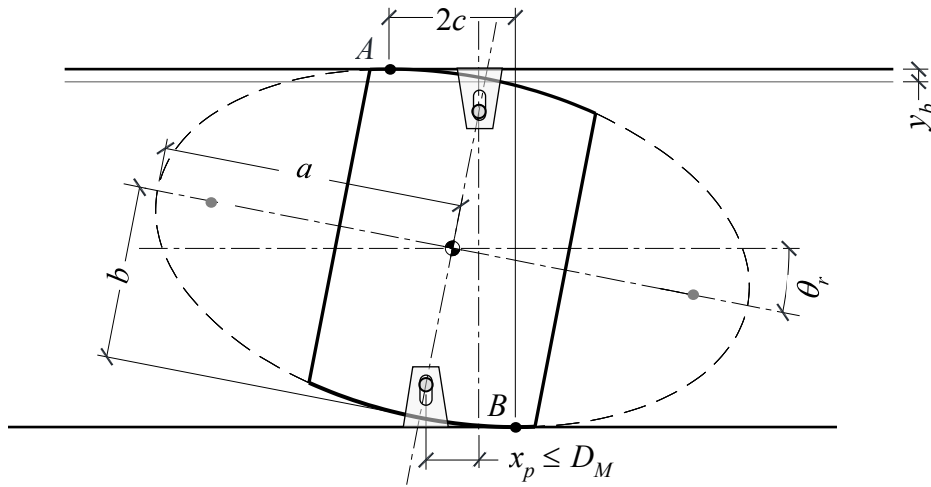


Figure 60. Slip-Friction Rocking of panel with e of 0.82 eccentricity.

Table 25. Geometric parameters for Slip-Friction Rocking of $e = 0.82$ panel

a		b		e	D_M		Max θ_r		Max y_b		Max $2c$	
(mm)	(in.)	(mm)	(in.)		(mm)	(in.)	(deg.)	(rad.)	(mm)	(in.)	(mm)	(in.)
3188	125.5	1829	72.00	0.82	563	22.17	11	0.19	133	5.25	1347	53.04

Table 26. Test protocol for Slip-Friction Rocking of $e = 0.82$ panel

Displacement step	No. of Cycles	Drift		
		(mm)	(in.)	(%)
0.0025 h_s	20	9	0.36	0.25
0.25 D_M	3	141	5.54	3.85
0.50 D_M	3	282	11.09	7.70
0.67 D_M	3	377	14.85	10.32
1.00 D_M	6	563	22.17	15.40
0.75 D_M	18	422	16.63	11.55

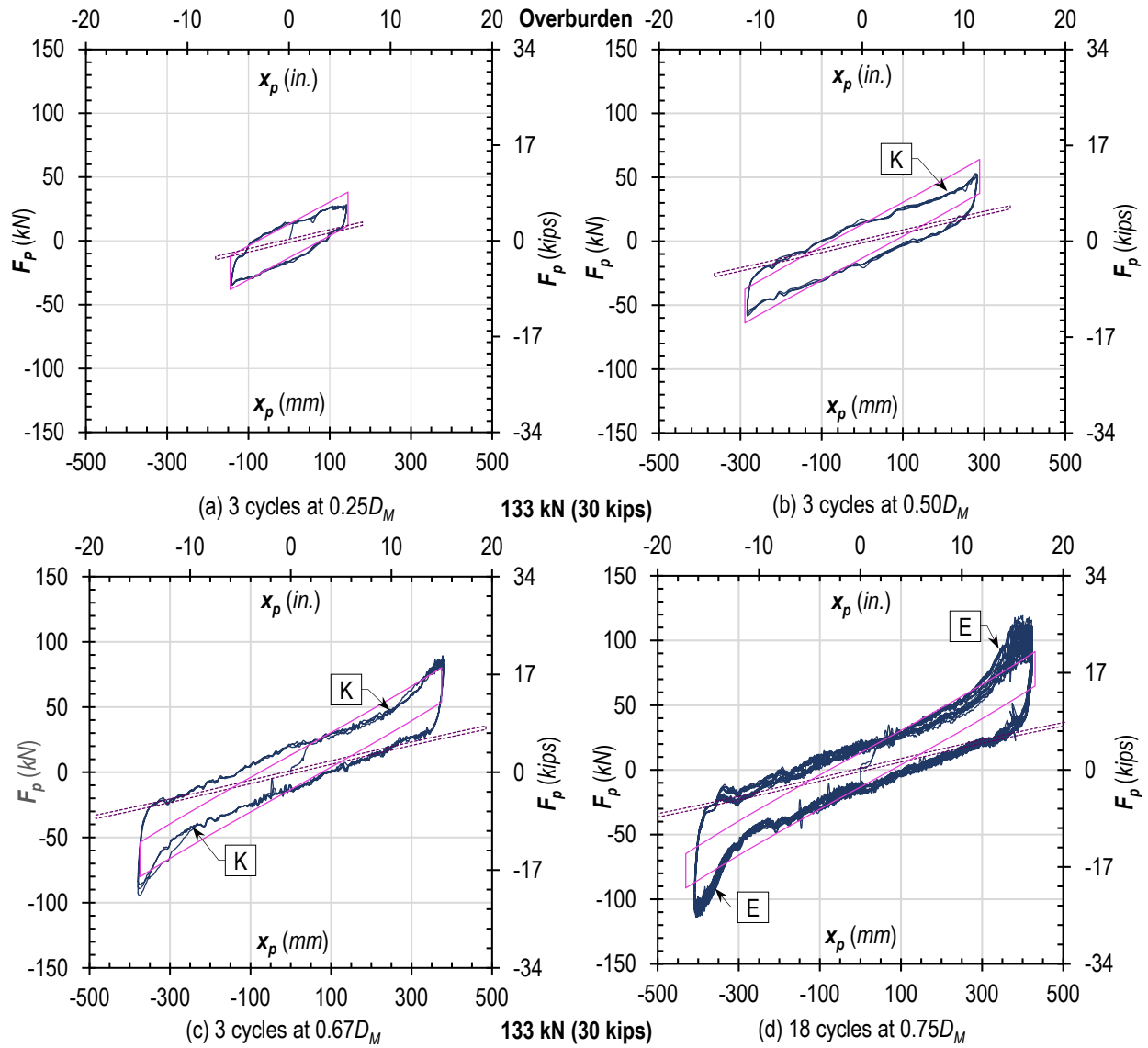


Figure 61. Slip-Friction Rocking hysteresis plots of $e = 0.82$ panel under constant low overburden through $0.75D_M$

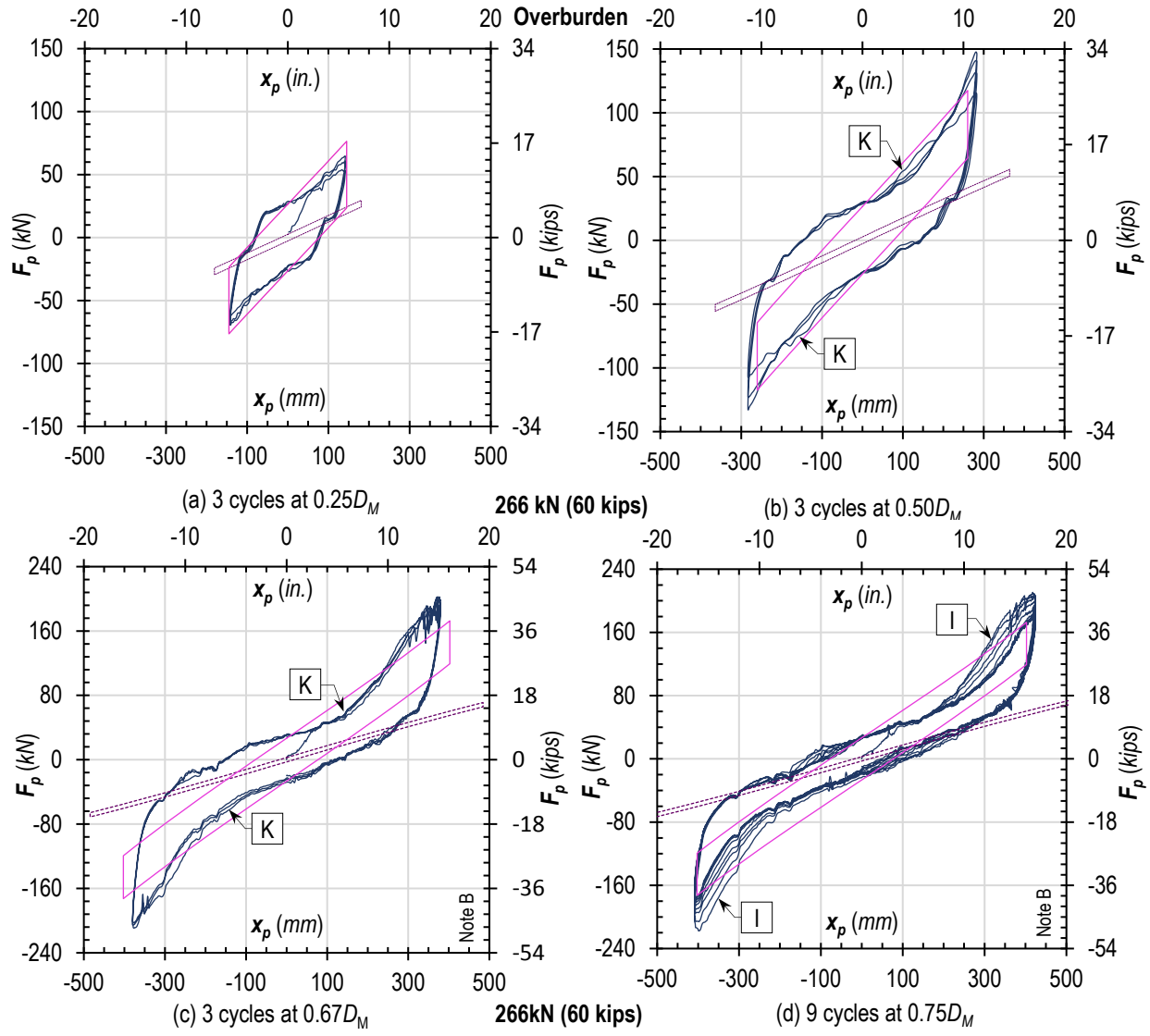


Figure 62. Slip-Friction Rocking hysteresis plots of $e = 0.82$ panel under constant medium overburden through $0.75D_M$

$e = 0.88$ Panel

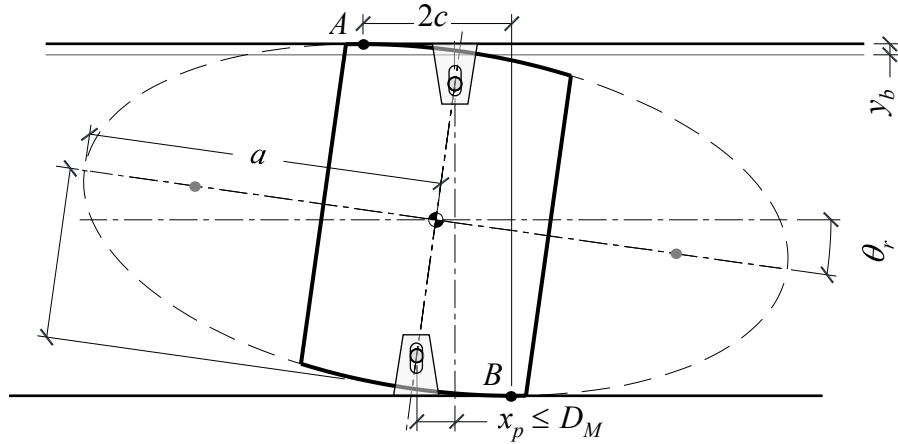


Figure 63. Slip-Friction Rocking of panel with e of 0.88 eccentricity

Table 27. Geometric parameters for Slip-Friction Rocking of $e = 0.88$ panel

a		b		e	D_M		Max θ_r		Max y_b		Max $2c$	
(mm)	(in.)	(mm)	(in.)		(mm)	(in.)	(deg.)	(rad.)	(mm)	(in.)	(mm)	(in.)
3810	150	1829	72.00	0.88	411	16.18	8	0.14	116	4.58	1632	64.25

Table 28. Test protocol for panel with e of 0.88 eccentricity in Slip-Friction Rocking

Displacement step		No. of Cycles	Drift (mm)	Drift (in.)	Drift (%)
0.0025	h_s	20	9	0.36	0.25
0.25	D_M	3	103	4.05	2.81
0.50	D_M	3	205	8.09	5.62
0.67	D_M	3	275	10.84	7.53
1.00	D_M	6	411	16.18	11.24
0.75	D_M	18	308	12.14	8.43

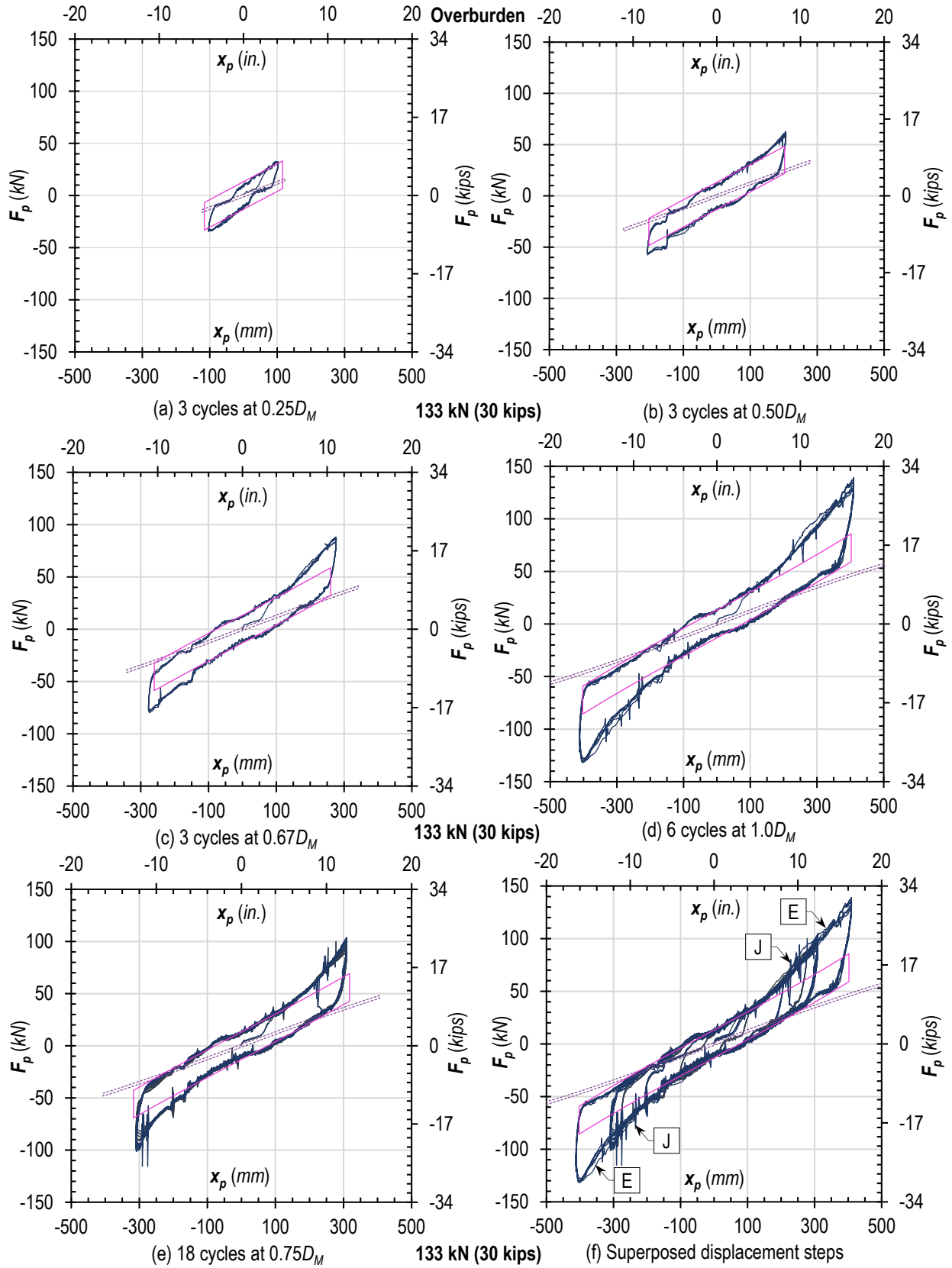


Figure 64. Slip-Friction Rocking hysteresis plots of panel $e = 0.88$ under constant low overburden through $1.00D_M$

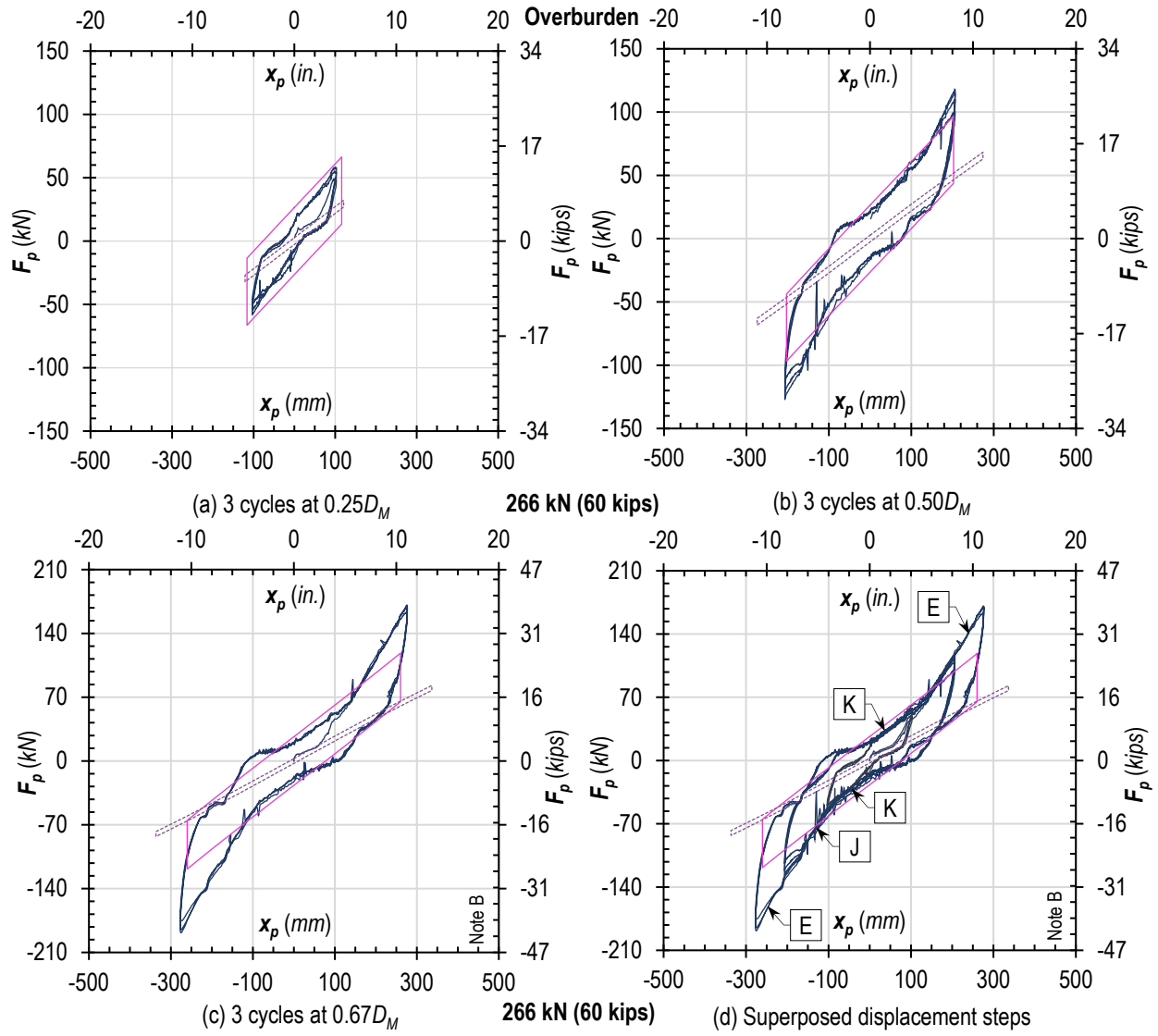


Figure 65. Slip-Friction Rocking hysteresis plots of $e = 0.88$ panel under constant medium overburden through $0.67D_M$

$e = 0.91$ Panel

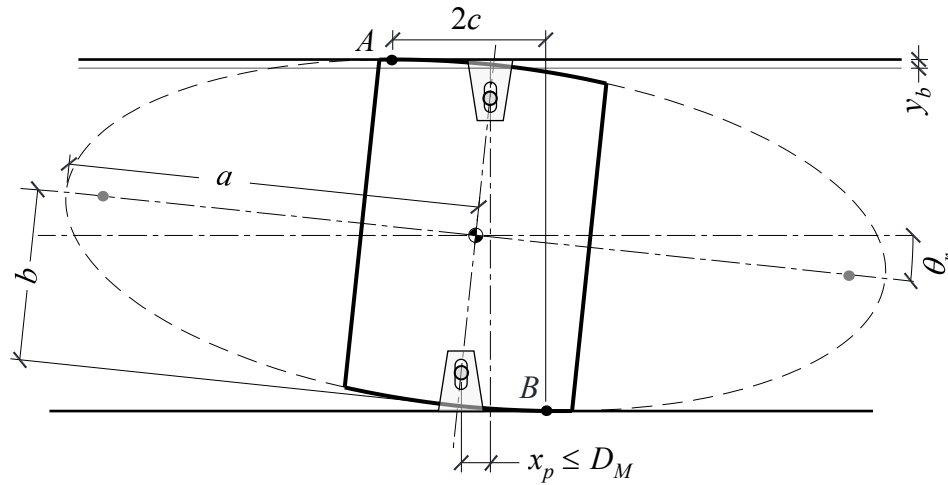


Figure 66. Slip-Friction Rocking of panel with e of 0.91 eccentricity.

Table 29. Geometric parameters for Slip-Friction Rocking of $e = 0.91$ panel

a		b		e	D_M		Max θ_r		Max y_b		Max $2c$	
(mm)	(in.)	(mm)	(in.)		(mm)	(in.)	(deg.)	(rad.)	(mm)	(in.)	(mm)	(in.)
4407	173.5	1829	72.00	0.91	307	12.09	6	0.10	95	3.73	1782	70.14

Table 30. Test protocol for Slip-Friction Rocking of $e = 0.91$ panel

Displacement step	No. of Cycles	Drift		
		(mm)	(in.)	(%)
0.0025 h_s	20	9	0.36	0.25
0.25 D_M	3	77	3.02	2.10
0.50 D_M	3	154	6.05	4.20
0.67 D_M	3	206	8.10	5.63
1.00 D_M	6	307	12.09	8.40
0.75 D_M	18	230	9.07	6.30

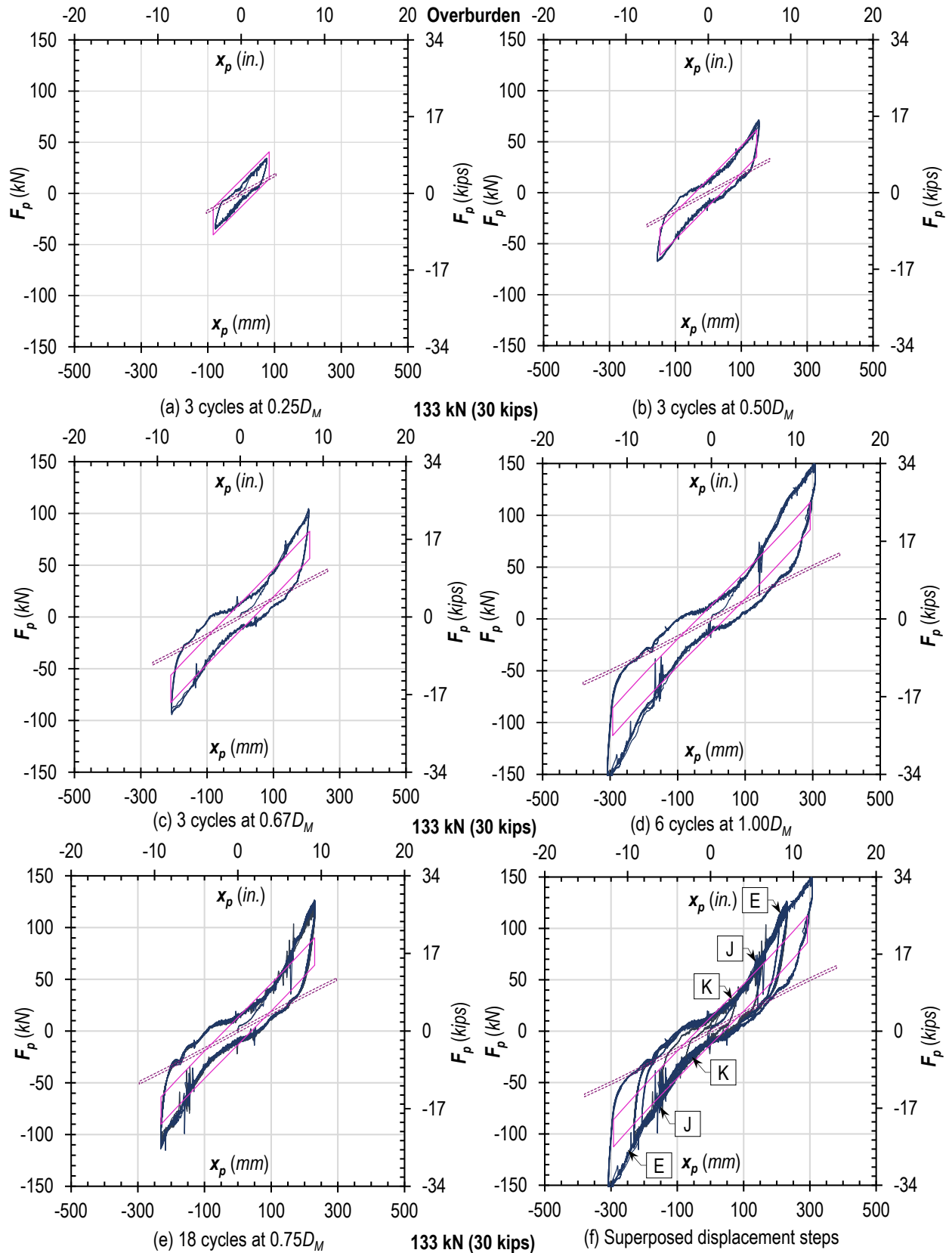


Figure 67. Slip-Friction Rocking hysteresis plots of panel $e = 0.91$ under constant low overburden through $1.00D_M$

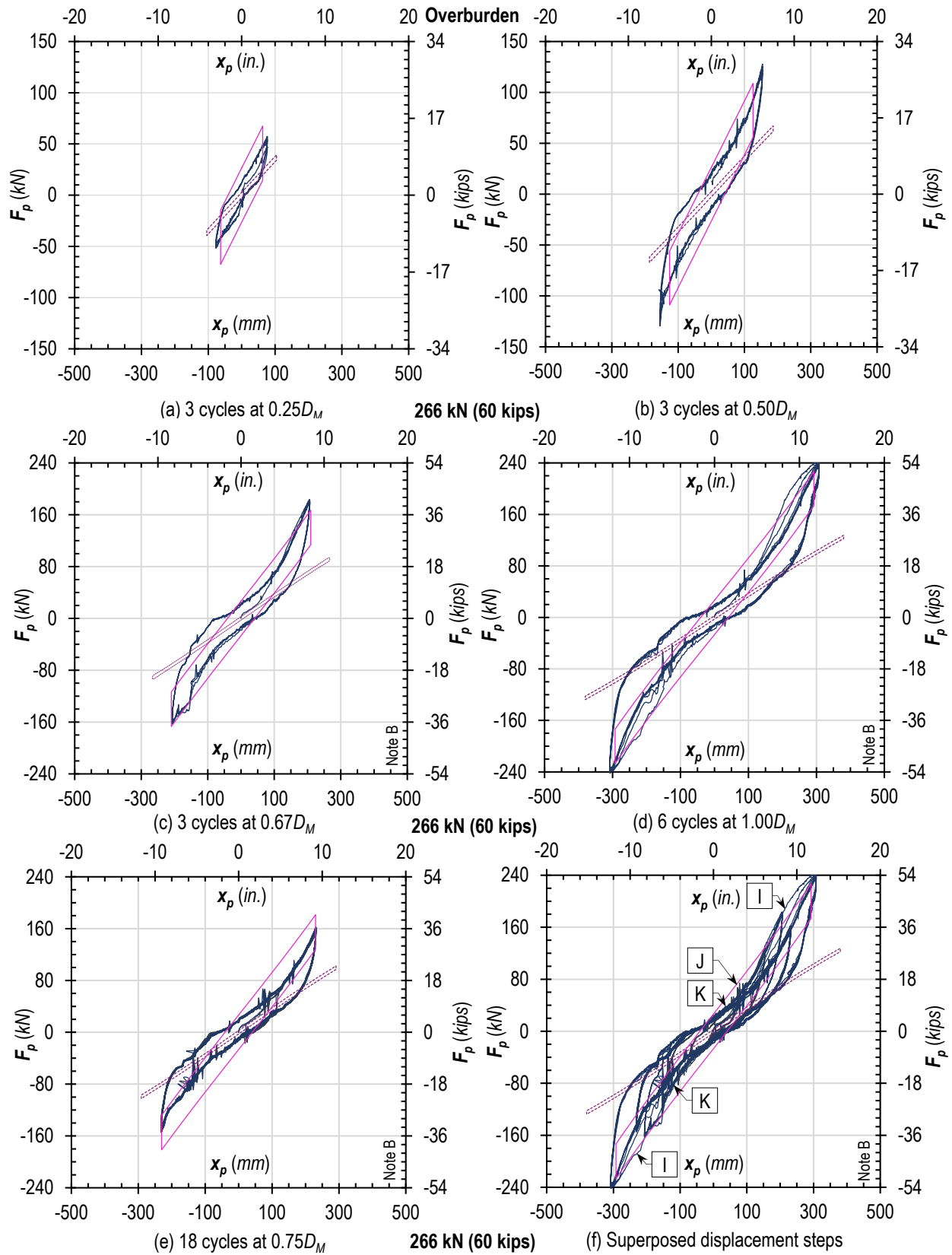


Figure 68. Slip-Friction Rocking hysteresis plots of panel $e = 0.91$ under constant medium overburden through $1.00D_M$

$e = 0.94$ Panel

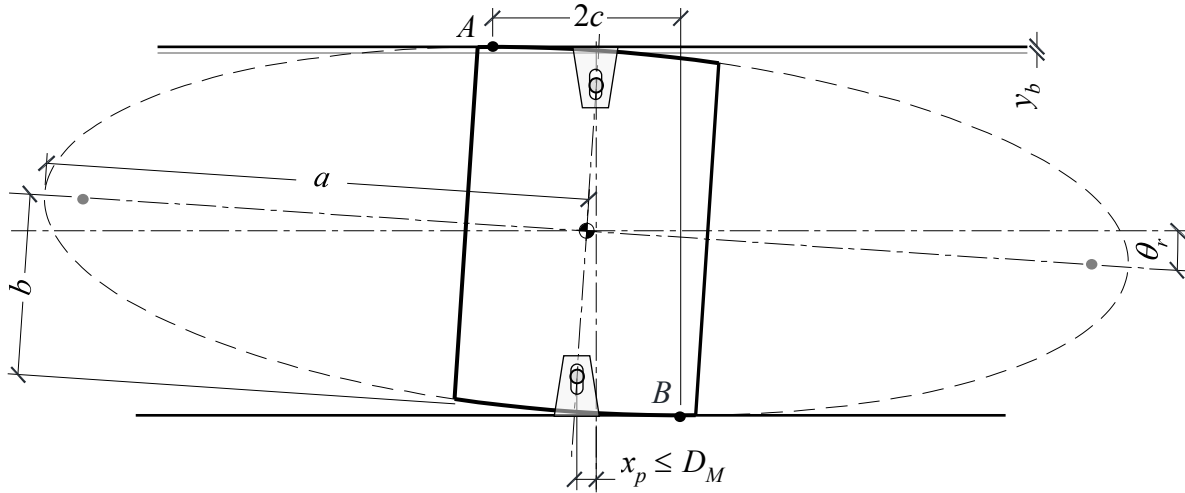


Figure 69. Slip-Friction Rocking of panel with e of 0.94 eccentricity

Table 31. Geometric parameters for Slip-Friction Rocking of $e = 0.94$ panel

a		b		e	D_M		Max θ_r		Max y_b		Max $2c$	
(mm)	(in.)	(mm)	(in.)		(mm)	(in.)	(deg.)	(rad.)	(mm)	(in.)	(mm)	(in.)
5486	216	1829	72.00	0.94	196	7.72	4	0.07	64	2.51	1903	74.92

Table 32. Test protocol for Slip-Friction Rocking of $e = 0.94$ panel

Displacement step	No. of Cycles	Drift		
		(mm)	(in.)	(%)
0.0025 h_s	20	9	0.36	0.25
0.25 D_M	3	49	1.93	1.34
0.50 D_M	3	98	3.86	2.68
0.67 D_M	3	131	5.17	3.59
1.00 D_M	6	196	7.72	5.36
0.75 D_M	18	147	5.79	4.02

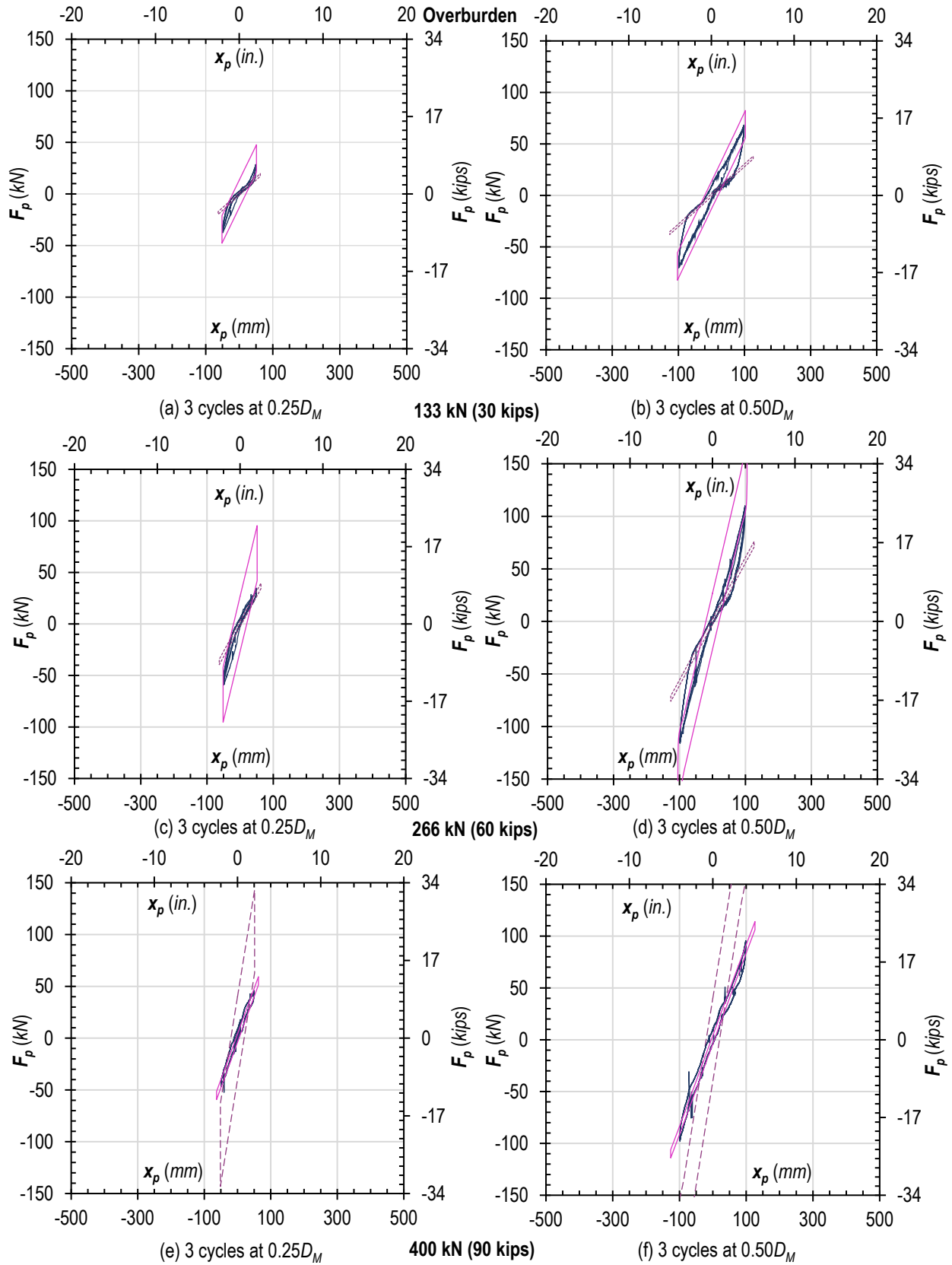


Figure 70. Slip-Friction Rocking hysteresis plots of $e = 0.94$ panel under 3 overburden levels through $0.50D_M$

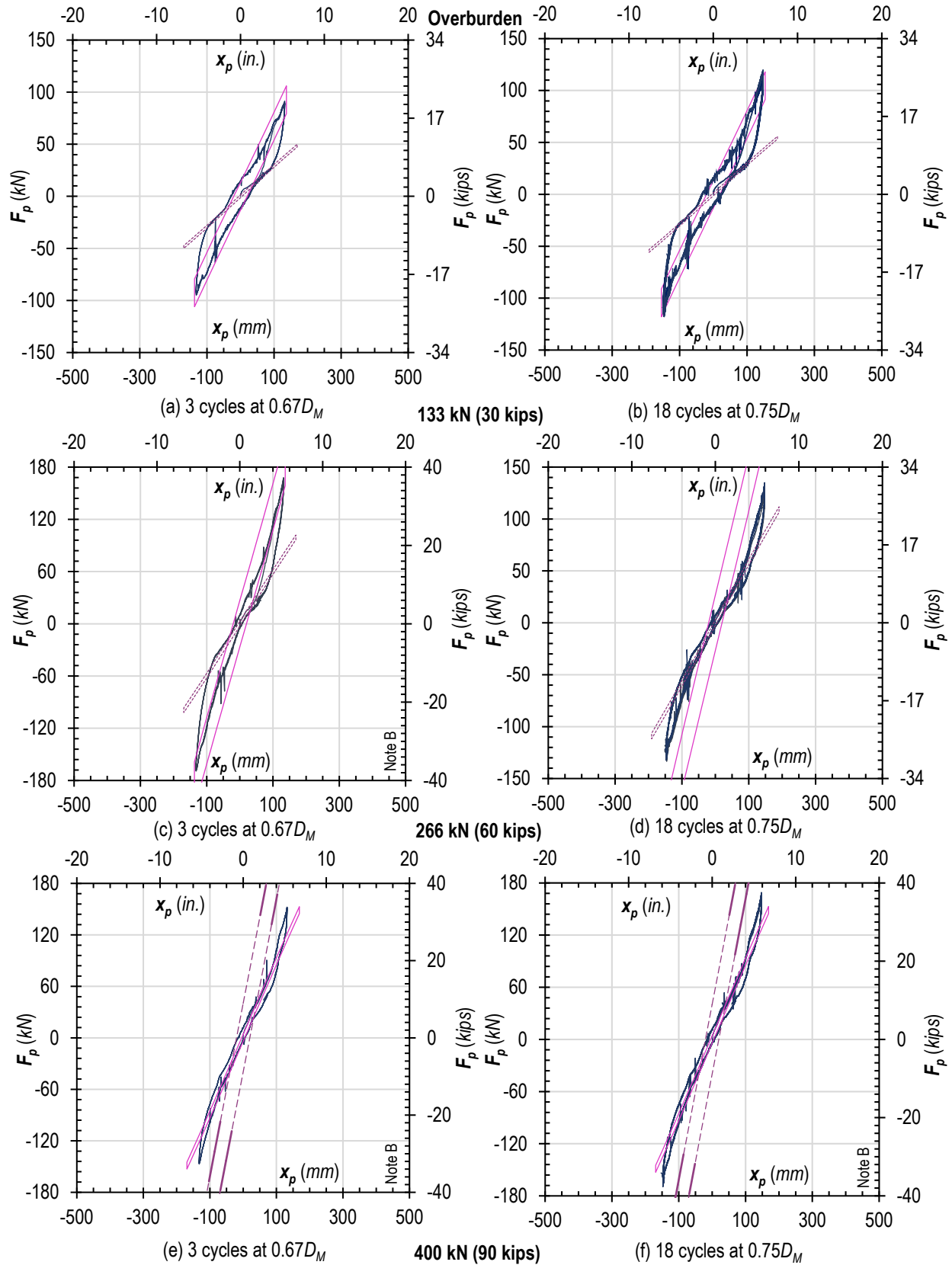


Figure 71. Slip-Friction Rocking hysteresis plots of $e = 0.94$ panel under 3 overburden levels through $0.75D_M$

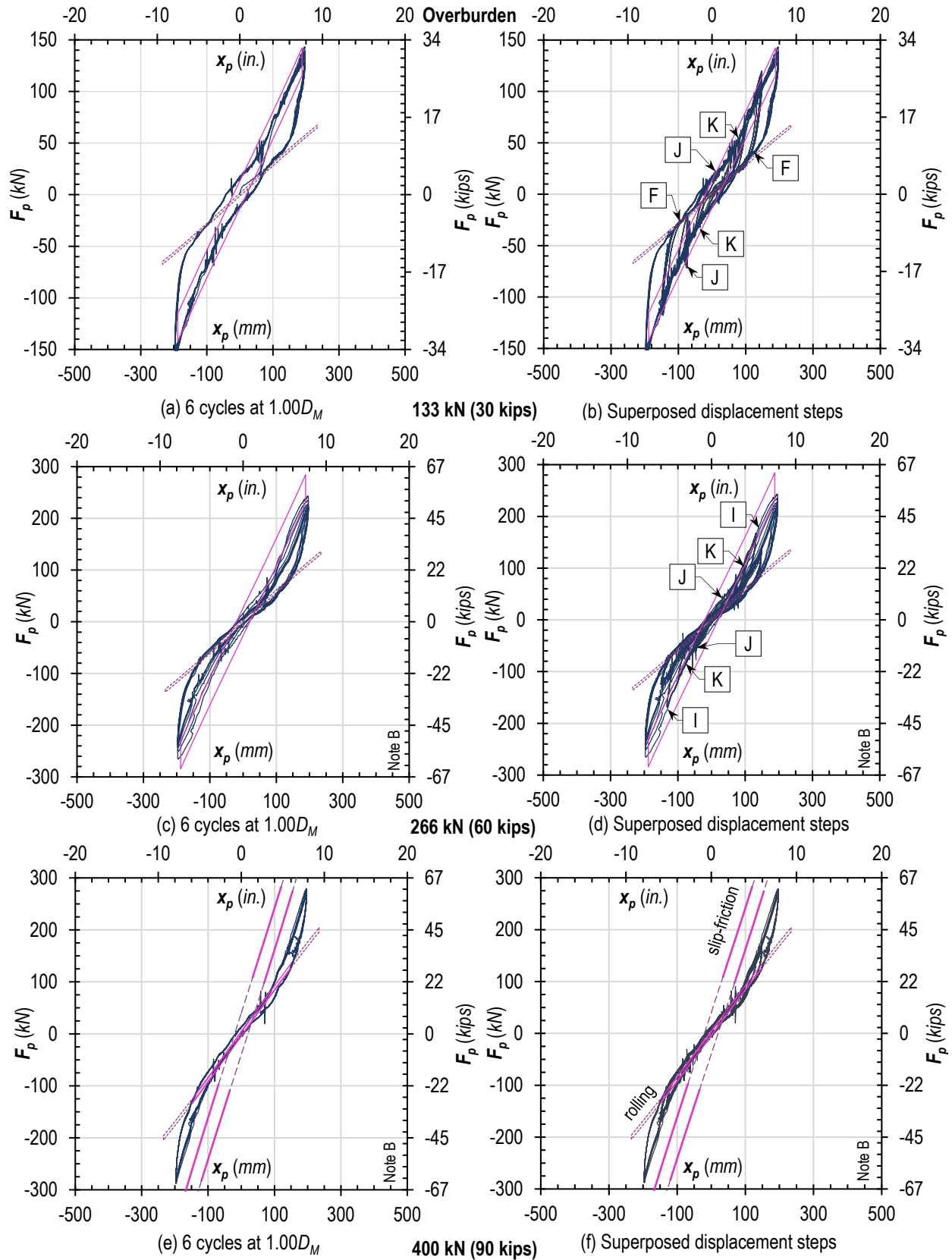


Figure 72. Slip-Friction Rocking hysteresis plots of $e = 0.94$ panel under 3 overburden levels through $1.00D_M$

Hysteresis Characteristics

Hysteresis plots of the lateral load-displacement accompany each of the tested load-displacement steps indicated in the protocol of Table 7. The preceding *Hysteresis Plots* provides the full complement of charts in Figures 35 through 72 within this chapter, organized by connection configuration, ellipse eccentricity, and displacement steps. For clarity, the plots grouped cycles in views focused on each recorded displacement step, before finally superposing displacement steps in composite views. Idealized models of *No-Slip Traction Rolling* and *Slip-Friction Rocking*, respectively derived from Equations 5 and 8, overlay the corresponding laboratory data for a visual comparison of measured results versus analytical ideals. Whenever possible, plots of equal displacement steps and varying overburden, or simulated superstructure loads, appear on the same page to facilitate comparisons. The following discussion highlights a sampling of the hysteresis plots to identify trends. Although stability, self-centering, and durability of rocking systems interrelate and describe sometimes synonymous aspects of the system, the following sections specifically address each characteristic.

Stability

Hysteresis plots alone do not reveal whether a structure is stable, but combined with other test observations, changes in the hysteresis data can signal instabilities. Generally, *No-Slip Traction Rolling* demonstrated both vertical and lateral stability across all tests, even as the vertically applied loads varied. *Slip-Friction Rocking* appeared stable at low levels of overburden but began behaving less predictably under higher simulated gravity loads. Because the prototyped systems sustained only local damage that only subtly changed hysteresis properties, identifying specimens as unstable required supplemental data and observations.

Stable Rolling through Variable Vertical Load

Hysteresis plots (a) through (f) of Figures 36, 38, 42, 44, 48, and 52 typically show that the idealized model of Equation (5) fits the lateral load-displacement data for *No-Slip Traction Rolling* specimens accurately through $0.5D_M$ cycles. Within the $0.5D_M$ displacement range, hysteresis loops retraced paths of the previous cycles, and idealized *No-Slip Traction Rolling* predicted the stiffness and damping for each level of overburden, with few exceptions. Damping significantly increases in the (f) plots of Figures 42 and 44 at the $0.5D_M$ displacement step. When multiplied by vertical load, W , the idealized hysteresis plots generally matched data at low, medium, and high levels of overburden. Varying gravity loads within the 133 to 400 kN (30 to 90 kips) tested range, therefore, had no effects on vertical or in-plane lateral stability of walls. Panels maintained stability throughout the 0.67 to $1.0D_M$ steps, despite typical damping increases exhibited by Figures 39 – 40, 45 – 46, and 49 – 50.

Prior to testing, slip posed the greatest threat to stability of *No-Slip Traction Rolling*, but only the most eccentric panel with e of 0.94 slipped during a trial under high overburden at the $1.0D_M$ maximum displacement step. The stiffest panel behaved according to the predicted lateral load-displacement model as shown in Figure 53. Plot (e) of Figure 54, however, charts abrupt declines in force at both loading segments, top right and lower left, of the hysteresis indicating where the panel slipped. The data recorded approximately 200 kN (45 kips) of force immediately prior to slip. This case of observed slip suggests a coefficient of static friction near 0.5 between timber and unpainted structural steel. One observed occasion of slip, however, cannot substantiate a frictional value for general use. After the slip event, the 18 cycles plotted in (f) of Figure 53, scaled back the displacement steps from 0.75 to $0.67D_M$ as a precaution. Later tests, plotted in Figure 73, however, repositioned the panel and cycled displacements at 0.75 and $1.00D_M$ without

incident. Tolerances measuring ± 10 mm ($\frac{3}{8}$ in.) in the V-shaped slots pictured in Figure 28 allowed up to 20 mm ($\frac{7}{8}$ in.) of slip until pins engaged the restraints and resounded with clangs.

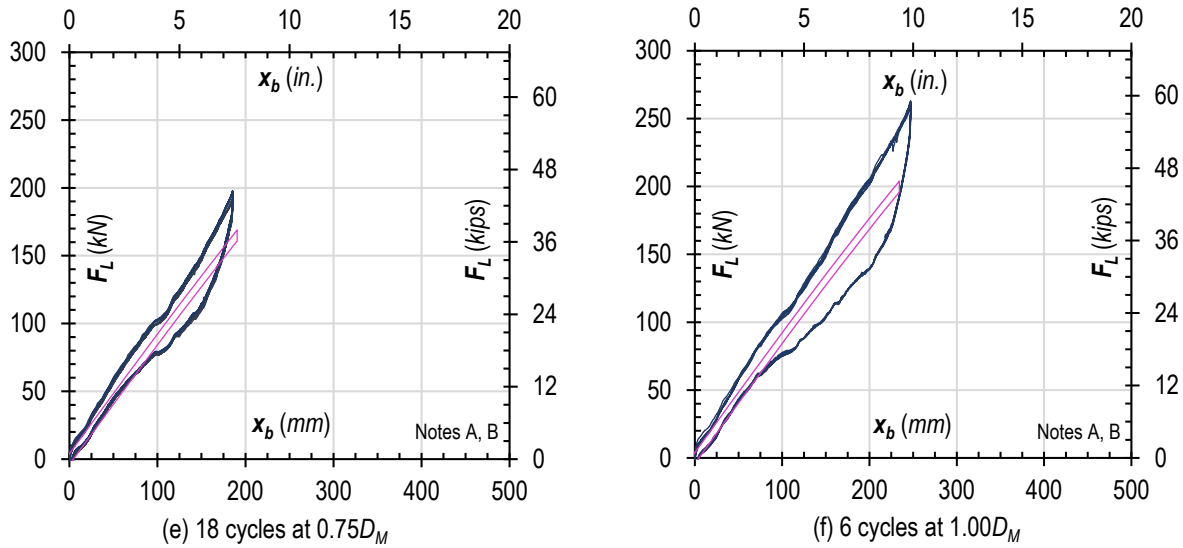


Figure 73. No-Slip Traction Rolling hysteresis plots of $e = 0.94$ panel retest under high overburden through $1.00D_M$

Slip-Friction Rocking Sensitivity to Vertical Loads

Hysteresis plots (a) and (b) of Figures 56, 58 or 59, 61, 64, 67 and 70, show that cycles of *Slip-Friction Rocking* retraced paths throughout the low overburden displacement steps, indicating stable behavior. At medium and high levels of overburden, however, plots (c) through (f) of Figures 56 and 58 showed subtle changes in *Slip-Friction Rocking*. Top right and lower left quadrants of the hysteresis loop traced distinct paths that signaled potential damage. Figure 74, for example, plots effective stiffness of the hysteresis loops of Figure 56 (f) to assess the degradation of stiffness of the $0.63e$ panel under high overburden. Over 3 cycles, the effective stiffness, k_{eff} drawn from zero to extreme points of the hysteresis loops, dropped 13.7% and 18.9% at respective right and left halves of the plot. Standards for seismic isolation deem specimens inadequate when effective stiffness drops more than 20% for repeated cycles

(ASCE/SEI 7 2017). Though degradation of effective stiffness had not yet exceeded standard thresholds, more slip-friction cycles would have diminished stiffness beyond acceptable limits.

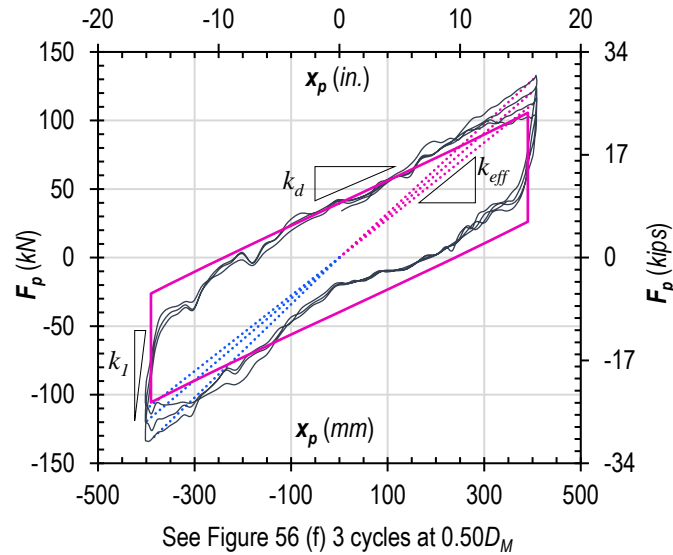
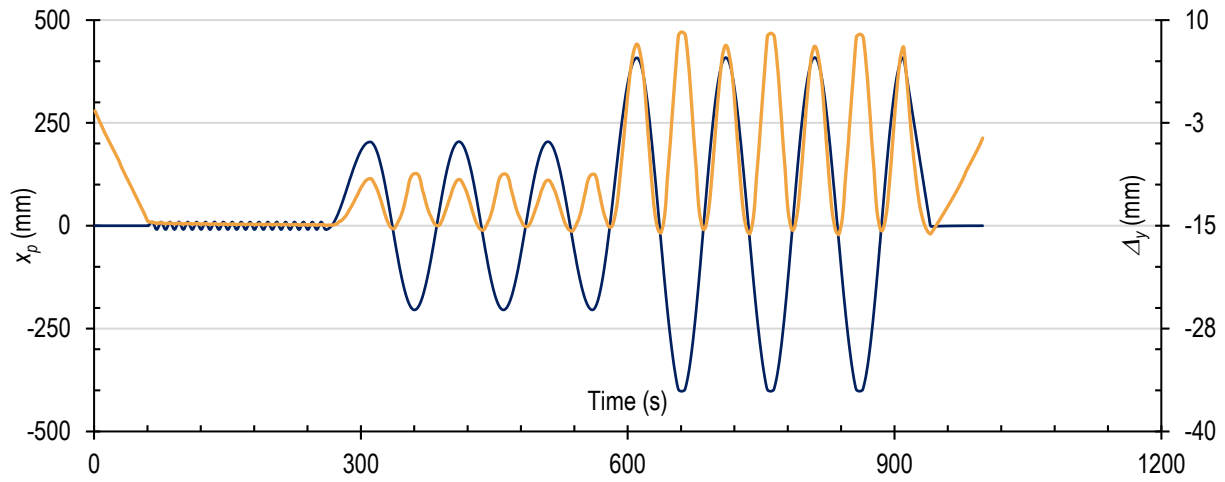


Figure 74. Effective stiffness of $e = 0.63$ panel in Slip-friction Rocking

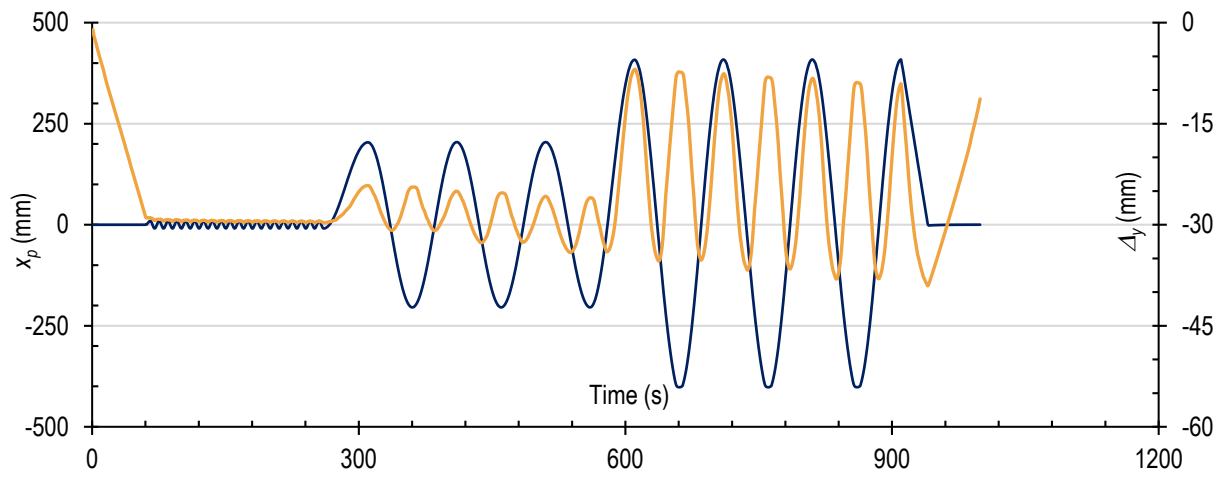
Figure 75 shows distinct changes in displacements of the top beam at medium and high overburden loads of 266 and 400 kN (60 and 90kips) for the panel of least eccentricity, which further indicated instability. Plots (a) through (c) overlay lateral displacement of the floor beam, x_p measured along the left y-axis, with vertical displacement of the ceiling beam, Δ_y measured along the right y-axis. The initial displacement of the ceiling beam supporting the overburden aligns with the zero position of the floor beam, to compare the ceiling beam displacements with the lateral displacement cycles. As expected, the initial deformation changed linearly with increased overburden, through a range of 15, 30, and 45 mm ($\approx 5/8$, $1\frac{1}{8}$, and $1\frac{3}{4}$ in.) respective to 133, 266, and 400 kN (30, 60, and 90 kips) of vertical load. In plot (a), valleys of the top beam displacement consistently returned to the initial displacement as the floor beam returned to the initial, zero position. In contrast, the valleys of plots (b) and (c) showed the top beam displaced progressively downward with each cycle.

To account for discrepancies between vertical actuator strokes and actual vertical displacements, Figure 76 diagrams sources of small beam deflections in the test setup. For most test trials, the top slotted pin connection was placed asymmetrically for practical assembly of the apparatus. To maximize lateral actuator stroke in one direction, the top slotted pin connection moved closer to center of the top beam. The bottom slotted pin connection was centered between rollers for all configurations. Vertical actuators applied P_1 and P_2 forces to maintain a constant sum of overburden that reactions R_1 and R_2 rollers ultimately transferred to the foundation. Distances L_1 and L_2 respectively measured 3.0 m (10ft) and 5.5 m (18 ft).

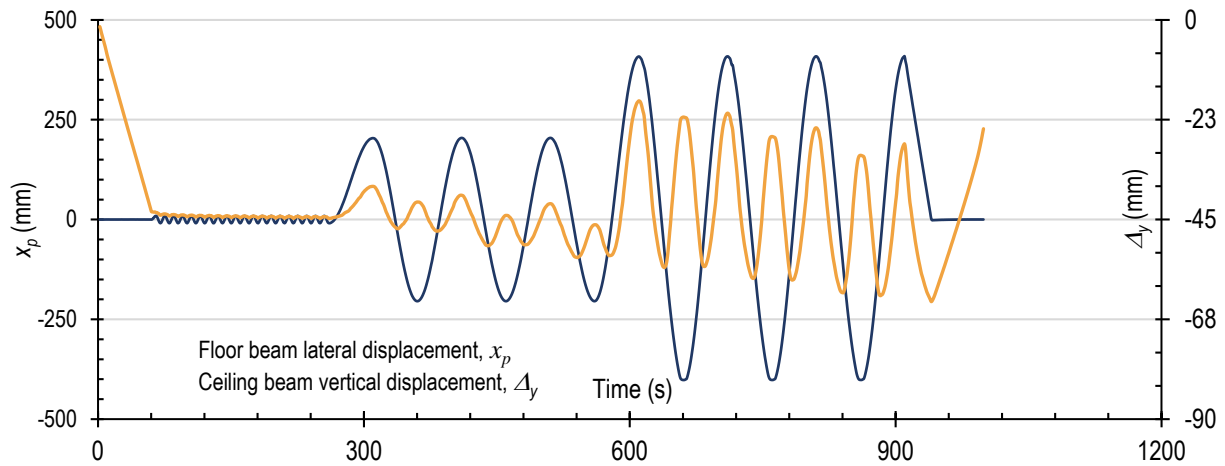
Measuring the clear distance between top and bottom beams, with a laser after unloading panels, estimated CLT shortening. The 0.91e panel shortened as much as 9 mm ($\frac{3}{8}$ in.) over several cycles beginning with plot (e) of Figure 67 and ending with plot (e) of Figure 68. The 0.94e panel shortened 4 mm ($\frac{5}{32}$ in.) over the entire range of vertically slotted connection configuration tests. Had panel shortening been noticed earlier, similar measurements would have been made throughout the test program for all specimens. Unlike *No-Slip Traction Rolling* which sustained low, medium, and high vertical loads with no notable changes, *Slip-Friction Rocking* damaged the edges and pin holes of CLT panels when simulated gravity loads increased.



(a) Low Overburden of 133 kN (30 kips)



(b) Medium Overburden of 266 kN (60 kips)



(c) High Overburden of 400 kN (90 kips)

Figure 75. Shortening of ($e = 0.63$) panel at medium and high overburden loads during Slip-Friction Rocking

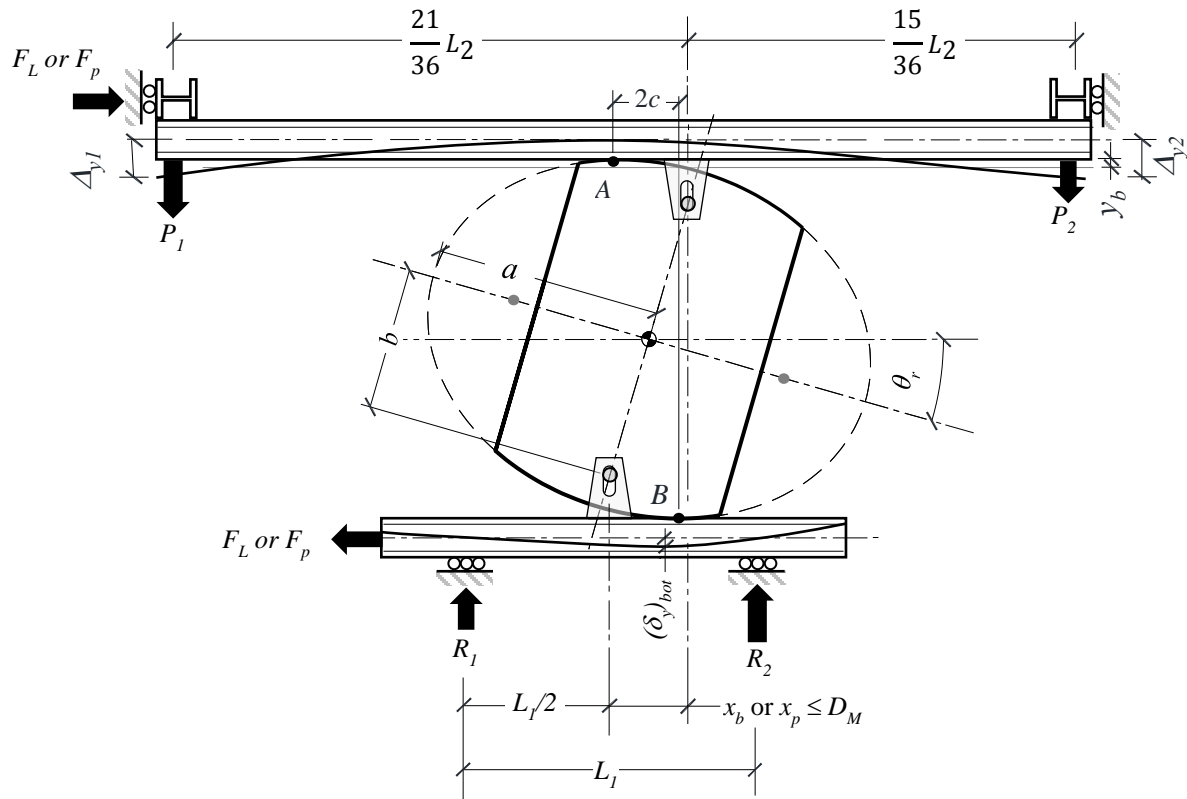


Figure 76. Free-body diagram of test setup exaggerating beam deflections

Out-of-Plane Stability

Even though the test program did not measure out-of-plane stiffness of the wall system, the observed rocking appeared stable, because precautionary out-of-plane brackets labeled (j) in Figure 30 proved unnecessary. Sizable steel plate connections, illustrated in Figures 28 and 29, sandwiched each CLT panel with enough torsional rigidity and bending strength to stabilize the walls in the out-of-plane lateral direction. Some local damage did, however, result from vertical misalignment in the out-of-plane direction that overstressed corners of laminations. Although the local damage caused by misalignment did not pose significant instabilities, adding chamfers or fillets to the edges of the CLT panels improved tolerance to out-of-plane movements.

Restoring Forces

The hysteresis plots of *No-Slip Traction Rolling* followed the behavior predicted by Equation (5) and showed no trace of residual displacements. Measurements taken between displacement step trials, however, found that panels consistently settled into vertical misalignment between the top and bottom pins measuring 6 to 16 mm ($\frac{1}{4}$ to $\frac{5}{8}$ inch) horizontally with respect to a laser level vertical plumb line. While slip could have occurred, panels typically settled in the same spot because of geometric imperfections. The misalignment typically amounted to less than 0.5% lateral drift, expressed as a ratio of story height.

Horizontal constraint of pins, within vertical connection slots illustrated in Figure 29, virtually eliminated horizontal residual displacements and exhibited distinctive self-centering features of *Slip-Friction Rocking*. At the outset, plots (a) and (b) of Figures 56 and 67 appeared to follow the idealized hysteresis of *Slip-Friction Rocking*. For most specimens, however, unloading or restoring followed a different path than loading segments of the hysteresis. Plots labeled (a) in Figures 64 – 65 , and 70, for example, appeared to follow the rolling models upon unloading. Most plots of the vertically slotted connection configurations exhibited combinations of *Slip-Friction Rocking* and *No-Slip Traction Rolling*. Plots (a) and (b) of Figure 58 or 59, for example, show slopes matched the rolling models in 3 portions of 4 segments of the hysteresis.

Meanwhile, the loading phase of the lower left quadrant followed the path predicted by slip-friction. As the same panel, of 0.73 eccentricity, reached higher lateral displacements while supporting low overburden, Figure 59 indicates that stiffness along the loading segments of the hysteresis increased beyond expectations when the specimen was pushed past half the anticipated displacement capacity. On the unloading segments, however, Figure 59 shows that rolling prevailed with slopes that match the data. Tolerances between the pins and bushings, combined

with elongation of the hole in the CLT panel, enabled the *Slip-Friction Rocking* and *No-Slip Traction Rolling* modes to interact. Constraint of the pin connection generally increases the pushover resistance of *Slip-Friction Rocking* panels, but compliance of the CLT surrounding the pin bushings enabled panels to roll for less energy intensive self-centering.

Predictability

Although most of the hysteresis plots for the vertically slotted connections configuration exhibited rolling characteristics upon unloading, not all trials followed that trend. Plots (b) through (f) of Figure 64, for example, followed the originally proposed *Slip-Friction Rocking* model more closely with little sign of rolling. Only stiffness along the loading segments of Figure 64 increased beyond expectations when lateral displacements exceeded $0.5D_M$, Plot (a) of the same panel, however, suggested mixed mode behavior happened early during the $0.25D_M$ step. Give at the pin connections, therefore, makes *Slip-Friction Rocking* more difficult to predict than pure *No-Slip Traction Rolling*. The degree of uncertainty introduced by *Slip-Friction Rocking*, however, does not disqualify the system but rather calls for analysis and design procedures that acknowledge and envelope the realm of possibilities.

Stiffness

Plots of Figures 36, 38, 39 – 40, 42, 44 – 46, and 48 – 50 show that the hysteresis model for *No-Slip Traction Rolling* model typically matched slopes of the data throughout the tested range. Plot (e) of Figure 40 shows increased slope, for the panel of 0.73 eccentricity, near the anticipated lateral displacement capacity. All plots of Figure 46 demonstrate similar stiffening of the panel with 0.88 eccentricity near lateral displacement capacity. Through most of the lateral displacement range, however, stiffness of *No-Slip Traction Rolling* behaved predictably for all specimens.

For a low level of overburden, *Slip-Friction Rocking* typically matched the slopes of the top right and lower left quadrants of the hysteresis. At greater displacements, however, loading segments of the hysteresis deviated from the predicted slopes as plot (c) of Figure 61 shows for the $0.67D_M$ displacement step of the panel with 0.82 eccentricity. When the same panel supported medium overburden, hysteresis pinching grew increasingly pronounced until reaching $0.67D_M$ lateral displacement plotted in (c) of Figure 62. For the panel of 0.88 eccentricity, comparison of Figures 64 demonstrates imperceptible pinching under low overburden that grew more conspicuously in Figure 65 under moderate vertical load. For 0.91 eccentricity, Figures 67 and 68 chart a similar progression of hysteresis pinching as overburden doubled.

The stiffest panel of 0.94 eccentricity fulfilled the entire load protocol charted in Figures 70 through 72, only because the specimen reverted to rolling after sustaining connection hole elongation during the medium overburden tests. Imprecise hysteresis caused by timber damage around the pin bushings makes estimation of *Slip-Friction Rocking* unpredictable at any given point. Overlays of idealized *Slip-Friction Rocking* and *No-Slip Traction Rolling* on each lateral load-displacement graph, however, respectively bound upper and lower stiffness of the system. Stiffness of the sliding models typically did not significantly exceed *Slip-Friction Rocking* predictions. Half of the specimens, however, presented exceptions when pushed past $0.50D_M$ as graphed by Figures 59, 65, and 67. Figures 70 through 72 portray bounds of the rolling and slip-friction stiffness models for the specimen of 0.94 eccentricity, which continued supporting full vertical loads even after sustaining connection damage. The panel of 0.94 eccentricity, therefore, demonstrated redundant and resilient potential. Elongation of holes in the CLT removed the redundant pin connection constraint and continued rocking via rolling, because damage in this case had not compromised vertical load-carrying capacity.

Track and Roller Imperfections

Blips appeared regularly in the hysteresis plots of all displacement step trials, regardless of connection configuration. Figures 36 and 38 pronounce the blips most distinctly, because the panels with least eccentric profiled charted shallower slopes. The blips grew proportionally with overburden weight. The regularity and prevalence of blips in all tests, including *Slip-Friction Rocking* trials, pointed to imperfections in the floor track and roller system of the test apparatus. Regularly spaced steel floor anchorages, labeled (k) in Figure 30, do not typically sit flush with the concrete floor surface. Wheels of the industrial movers rolled over portions of the steel channel track that spanned over the anchorages, which momentarily spiked forces but did not influence overall trends.

Frictional Damping

Regardless of variations in geometric contact bearing area along the CLT edges, the idealized models consistently assigned coefficients of friction. A rolling friction coefficient, μ_r equal to one percent, applied to both rolling and slip-friction models. The slip-friction model added a sliding friction coefficient, μ_s equal to nine percent. Increasing overburden weight, W , widened spacing between segments of the hysteresis loop, because the idealized models multiply coefficients and vertical load to express lateral frictional force effects. According to the hysteresis charts of *No-Slip Traction Rolling* and *Slip-Friction Rocking*, simple Coulomb friction models generally estimated the frictional hysteretic damping with accuracy at least through $0.5D_M$ displacement steps. At the 0.25 and $0.50D_M$ steps, *No-Slip Traction Rolling* exhibited inherently low but consistent frictional damping as shown in Figures 36, 38, 42, 44, 48, and 52. Beyond the $0.5D_M$ cycles, however, only Figure 53 for 0.94 eccentricity reasonably predicted damping of the actual test. Figures 39 – 40, 45 – 46, 49 – 50, and 54 show that damping

increased unpredictably. Though some of the damping resulted from minor slip and wear of specimens and connections, multiple components of the test apparatus likely contributed. To account for the uncertainty in damping, therefore, *No-Slip Traction Rolling* could be limited to a lateral displacement range of $0.5D_M$ or analysis procedures could bound lower and upper values of energy dissipation measured in the tests.

Slip-Friction Rocking introduced sliding that increased the inherent frictional damping as expected. Connection constraints increased stiffness, forced panels to rotate about pin centers and slide against friction. Sliding friction increased hysteretic energy dissipation and inflated hysteresis loops of *Slip-Friction Rocking*. Though enhanced energy dissipation appeared desirable at first glance, sliding increased wear on the CLT panels. Even at low overburden levels, plots (c) through (f) of Figure 59 characterized the effects of *stick-slip friction* with local peaks and valleys along the main path of the hysteresis. Though stick-slip friction traced noticeably fuzzier lines on the hysteresis plots, consequential effects on durability showed up in later test protocols.

Durability

The test protocol subjected specimens to 6 cycles at $1.0D_M$ followed by 18 cycles at $0.75D_M$ to assess durability. Specimens that completed cycles at low, medium, and high overburden levels, exceeded requirements by essentially repeating cycles several times more than the minimum number. Although a new specimen for each trial would have filtered out any possible effects of wear from previous tests, sliding would have likely produced similar results in CLT panels, whether new or preconditioned by rolling. Conversely, sliding did not maintain like-new conditions but expended two panels before rolling trials could be completed.

Rolling Protection

Among 6 total specimens tested in *No-Slip Traction Rolling*, 4 fulfilled durability cycles at 75 and 100 percent of maximum displacement. For the panel of 0.73 eccentricity, Figures 39 – 40 retraced hysteresis loops at $1.0D_M$ and $0.75D_M$ cycles, with only minor deviations along the unloading segments. For the 0.88, 0.91, and 0.94 eccentricities, Figures 45 – 46, 49 – 50, 53 – 54, respectively retraced multiple hysteresis loops without signs of degradation. Repeated cyclic trials at strokes between 0.75 and $1.00D_M$, therefore, proved rolling effective at preserving durability of the CLT panels, even when supporting the highest level of overburden.

Extrapolating from results of 4 other specimens suggests that the panels of 0.63 and 0.82 eccentricity would have fulfilled complete *No-Slip Traction Rolling* protocols, if tested in continuous sequence.

Slip-Friction Rocking and Mixed Modes

Sliding, in contrast to rolling, compromised durability, particularly at higher load levels. The hysteresis plots of Figure 56 showed only subtle signs of damage to the least eccentric panel of the test group, whereas top beam displacements of

Figure 75 revealed obvious signs of instability. The panel of 0.73 eccentricity similarly showed subtle signs of degradation in Figure 58 while supporting medium and high magnitudes of vertical loads. Views, such as hysteresis plot (d) of Figure 62 for the panel of 0.82 eccentricity, captured progressive pinching that appeared to *deflate* the hysteresis. At overburden levels of 267 kN (60 kips), *stick-slip friction* dynamically impacted connections, as explained in *Slip-Friction Rocking Effects on Laminations under Observed Damage*. The pounding elongated holes in the CLT surrounding the embedded pipe bushings, which eventually relieved pin constraint and forced panels to revert to rolling. Plots (c) and (d) of Figure 72 captured similar

“deflation” of the hysteresis. When pins could no longer force sliding, damping decreased to a rolling friction state.

Hysteresis plots of the stiffest and most eccentric panel ($e = 0.94$) captured a progression of mixed mode behavior between *No-Slip Traction Rolling* and *Slip-Friction Rocking*. Hysteresis plots (a) and (b) of Figures 70 through 72 show that slip-friction prevailed on the loading segments, while the panel typically rolled upon unloading under low overburden. Doubling the overburden pinched the hysteresis plots of each figure, until significant portions of the loading segments began rolling, as shown in the middle rows of Figures 71 and 72. After deflating during the 6 cycles at maximum lateral displacement capacity, the panel rolled for 18 cycles plotted in (d) of Figure 71. The panel continued to mostly roll under high overburden, as shown in the bottom rows of Figures 70 through 72. The bottom row of Figure 71, however, shows slopes of the data matching *Slip-Friction Rocking* at extreme lateral displacements. The trend continued in Figure 72, because pins had forced panels into sliding at the maximum reaches of the lateral displacement protocol. The mixed mode behavior demonstrates that pin connections had reserve capacity after closing the gaps produced by hole elongation. Mixed pendulum modes, furthermore, highlighted the redundancy of the connection constraints introduced by the vertically slotted connections of Figure 29.

Observed Damage

Though the hysteresis plots generally showed minimal or limited degradation at a systems level, qualitative observations clearly found that timber damage occurred. *No-Slip Traction Rolling* and *Slip-Friction Rocking* produced distinct modes of damage. The following sections explain the type of damage observed, mechanisms that produced the damage, and whether the damage

produced significant effects. Because steel components performed elastically, with only minor local yielding, the discussion focuses on timber. Observed damage prompted modifications to rigid-body assumptions of both rocking models.

No-Slip Traction Rolling Effects on Laminations

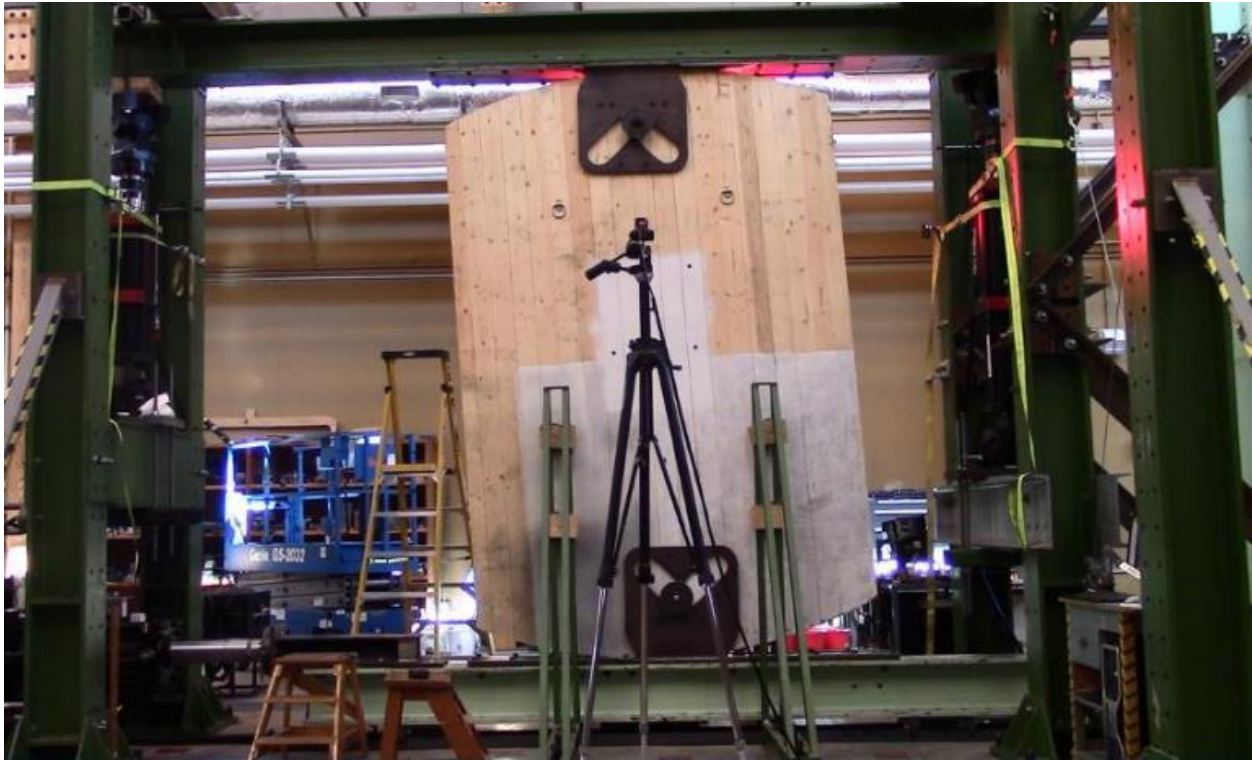


Figure 77. South elevation of panel ($e = 0.63$) in No-Slip Traction Rolling.

Figure 77 pictures an elevation view of the $0.63e$ panel tested in *No-Slip Traction Rolling*, corresponding to the hysteresis plots of Figure 36. The south elevation view shows that points of top and bottom contact remained closely spaced, as illustrated in Figure 35, even at high panel rotation. Consequently, the moment arm of the restoring force-couple remains short relative to CLT panels shaped to wider elliptical profiles. The pictured panel has much more room to laterally displace, or rotate, before contacting a corner. Stroke of the lateral actuators, however, maxed out at less than half of the theoretical displacement capacity, $0.5D_M$, of the elliptical

profile. Therefore, this panel was removed for observation and later testing, after 2 major displacement steps, or 6 complete seismic cycles, of the protocol.

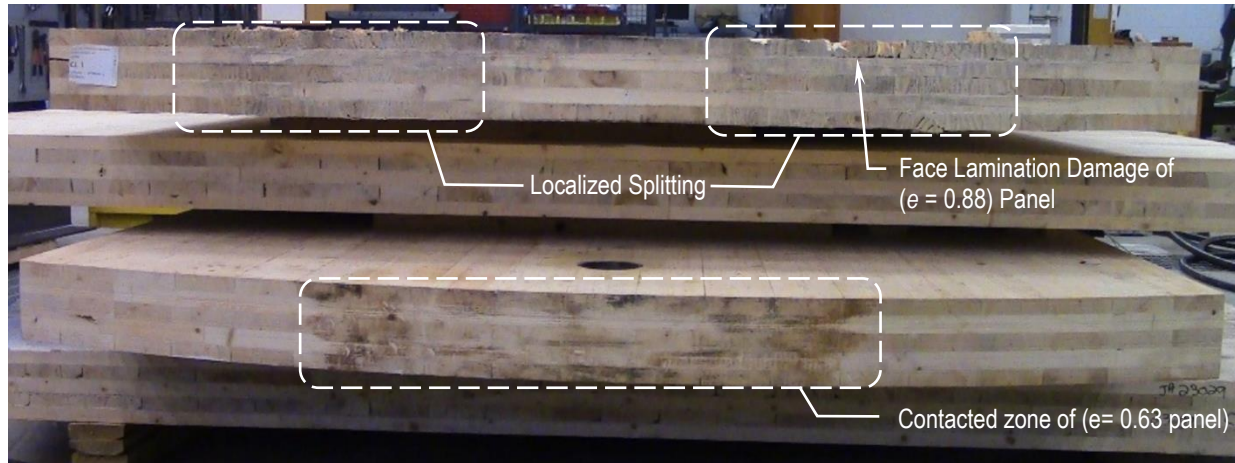


Figure 78. Top load-bearing edges after initial steps of No-Slip Traction Rolling.

Figure 78 photographed the load-bearing edges of two panels, including the 0.63e panel of least eccentricity that rolled through lateral translations of nearly ± 432 mm (17 in.) in each lateral direction. High-pressure bearing contact discolored and conditioned the region of CLT subjected to vertical loads as high as 400 kN (90 kips), but virtually no damage resulted. By comparison, the panel with e of 0.88 panel at the top of the stacked panels, pictured in Figure 78, exhibited two regions where laminations had split. The panel at the top of the stack, furthermore, sustained damage to face laminations, particularly along the pictured top face edge. Similar damage to one face lamination of the panel with eccentricity e of 0.63 had also occurred on the south elevation. After two panels had sustained incidental damage to the south face, measurements found the steel test frame out-of-plumb. Realigning the top beam apparatus and chamfering the CLT panel edges for better tolerance to misalignment out-of-plane mitigated further incidental damage.

Figure 79 revisits the free-body-diagram of Figure 20, to explain why the panel with e of 0.88 sustained damage while the panel with e of 0.63 emerged unscathed. The updated free-body

diagram considers orientation of the main longitudinal laminations with respect to contact forces on the panel. Because of grain orientation, longitudinal laminations primarily sustain nearly all the compression transferred through the top and bottom contact points. For small panel rotations, compression aligns parallel to grain well enough to prevent splitting of longitudinal laminations. Larger panel rotations, however, introduced a force component perpendicular to grain as diagrammed in (a) and (c) of Figure 79. Even though frictional traction counteracts the story shear, a tension force perpendicular to grain, $f_{t\perp}$, develops because the vertical superstructure loads, W , must be resisted by compression parallel to grain, $f_{c\parallel}$, oriented at the θ_r angle.

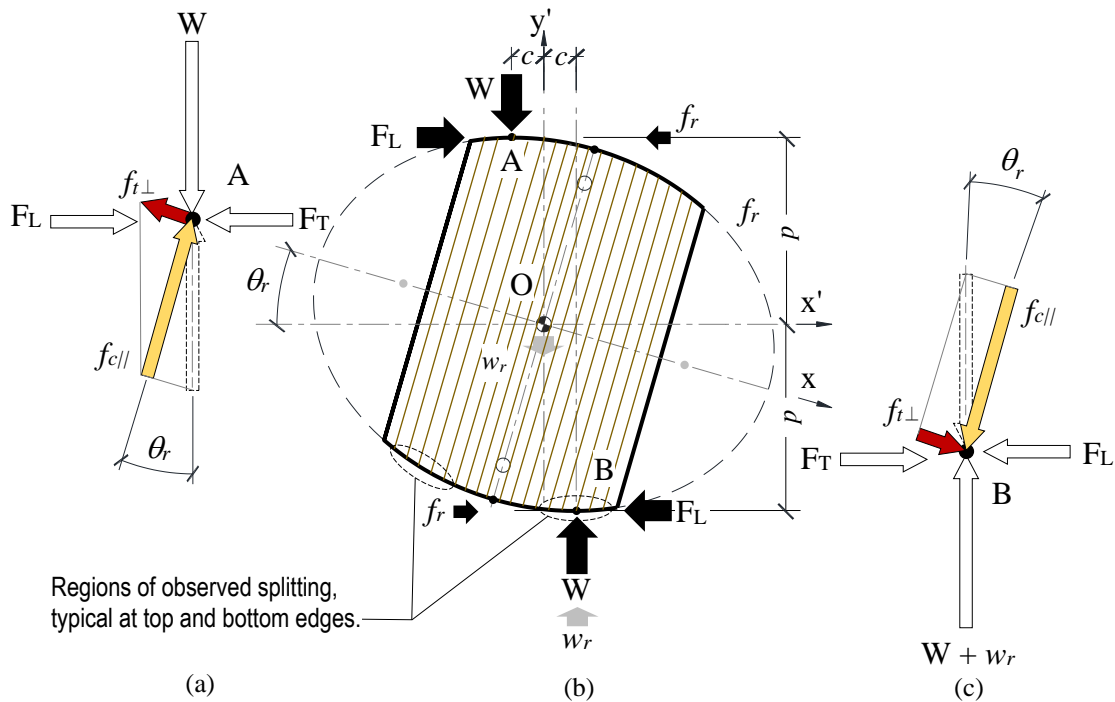


Figure 79. Free-Body-Diagrams of *No-Slip Traction Rolling* considering (a) top and (c) bottom contact points and (b) orientation of laminations

Table 1 lists allowable design capacity for tension stress perpendicular to grain of 2.76 MPa (400 psi). Limiting stresses to this value could prevent the local splitting observed in all but the least eccentric panel of *No-Slip Traction Rolling*. Allowable stress design (ASD), however, would

impose overly conservative limitations for this application, because *low* rather than *no* damage can still achieve resiliency. Adhesively bonded cross-laminations typically arrested the cracks and confined splitting damage to the very ends of the longitudinal laminations. This confinement and localization made the damage insignificant according to the hysteresis plots that showed overall stiffness had been maintained.

Slip-Friction Rocking Effects on Laminations

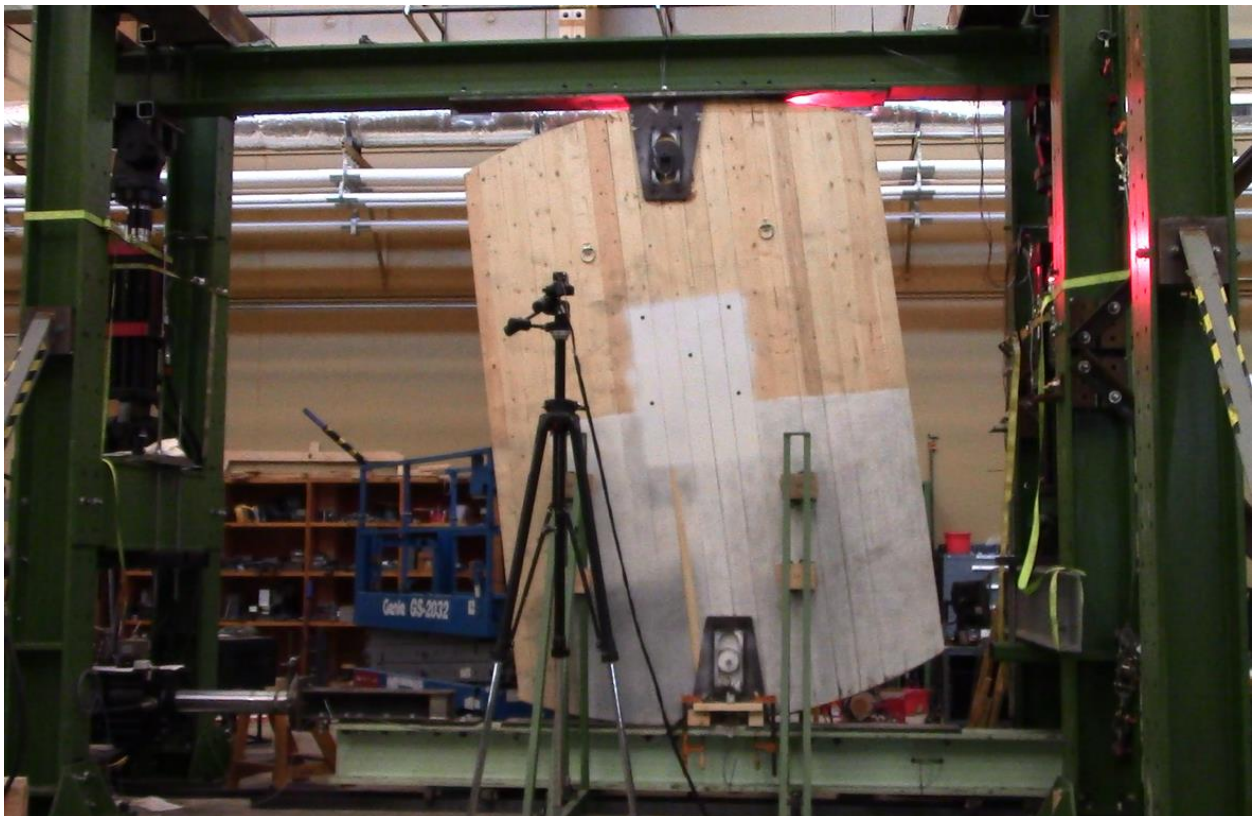


Figure 80. South elevation of panel ($e = 0.63$) in Slip-Friction Rocking

Figure 80 pictures a panel elevation in *Slip-Friction Rocking*. Visual observation might miss the differences between *No-Slip Traction Rolling* and *Slip-Friction Rocking* but sliding timber against steel under high-pressure contact generated audibly louder noise. Figures 77 and 80 picture the same specimen, respectively in each configuration. By the time the panel was loaded

into *Slip-Friction Rocking*, however, a piece of wood had already splintered from the face lamination during *No-Slip Traction Rolling*. Adding chamfers on other specimens eliminated sharp corners on the load-bearing edges of the CLT panel and improved tolerance to out-of-plane movement in subsequent tests, but not repairing the splintered wedge pictured in Figures 80 and 81 proved consequential. The shearing effect of sliding exploited the vulnerability left by the gap and damaged critical laminations, as shown in Figure 81. The split laminations around the pin connection halted further testing on this specimen. Sliding friction, furthermore, placed noticeably more wear on the edges of CLT panels, as shown in Figure 82. Longitudinal laminations split or crushed, but cross laminations felt smooth to the touch. Sliding clearly changed both color and integrity of the wood surface in the contacted regions.



Figure 81. Damage to critical laminations of south elevation of panel ($e = 0.63$) after Slip-Friction Rocking.



Figure 82. Bottom load-bearing edges after initial round of Slip-Friction Rocking

Despite the damage that sliding caused, effects remained localized and hardly influenced overall lateral load-displacement characteristics recorded by the hysteresis charts. Though energy dissipated by sliding friction drew larger and seemingly desirable hysteresis loops, the shearing that accompanied sliding exacerbated splits within laminations and gaps between laminations. Figure 83 pictures splits and gaps that triggered *stick-slip friction*. During sliding, gaps opened wide and deformations of the wood laminations bound up the sliding mechanism and created sticking phases that built up frictional energy. Upon releasing frictional energy, gaps closed, and the panel suddenly slipped. Though seemingly innocuous, alternating stick-slip phases dynamically impacted pin connections. Figure 84 pictured a typical case of pin hole elongation, and Figure 85 pictured extreme elongation that occurred with the stiffest and most eccentric panel of the test program.

Figures 84 and 85 show that the large diameter of the pinhole, relative to the lamination width, effectively severed central face boards and left behind a short segment susceptible to delamination. Because *Slip-Friction Rocking* concentrates forces around the pins, damage to these short segments of the lamination proved critical. The discontinuity of a large-diameter hole

through longitudinal laminations subjected small areas of face glue to the forces diagrammed in Figure 86. At low angles of rotation, shear forces transferred through the pin, bushing, and sliding surface produced a moment that pried loose the short segment. Figure 87 pictures a loosened lamination that measured approximately 135 mm (5¼ in.) wide by 305 mm (12 in.) long prior to splitting.

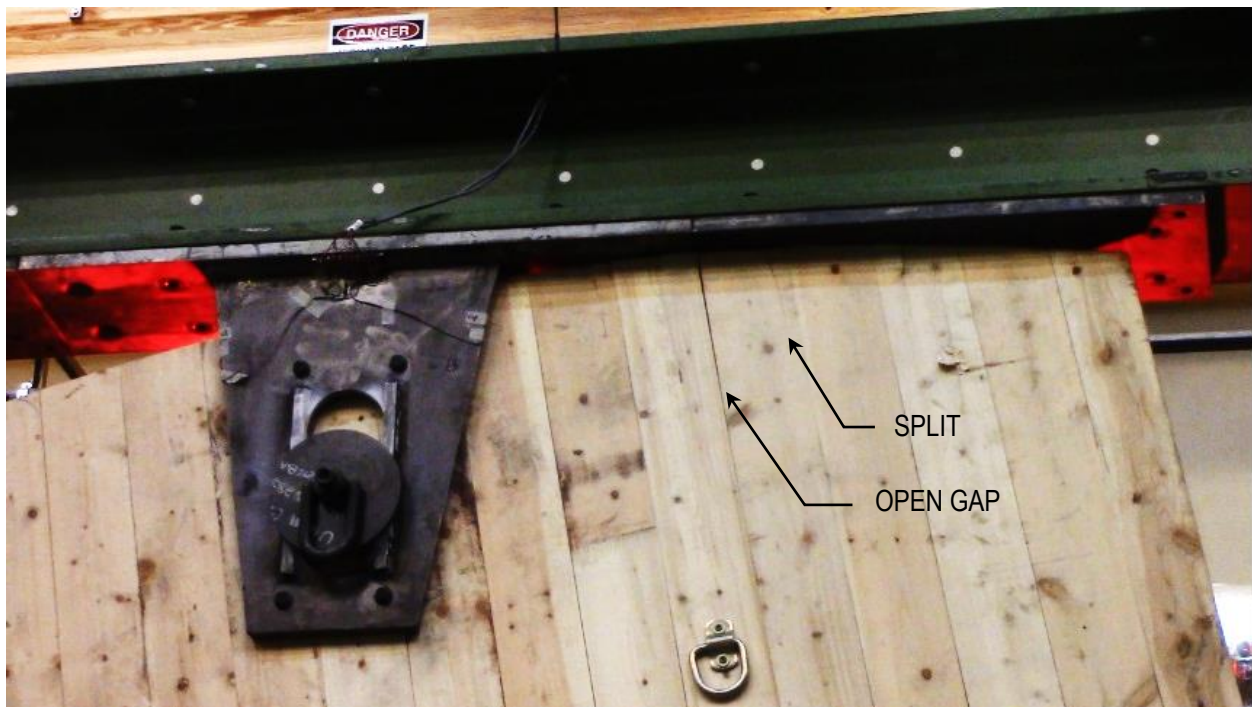


Figure 83. Top corner of panel ($e = 0.73$) with opening gaps between and splits within south face laminations.
Source: (Lo Ricco et al. 2018)

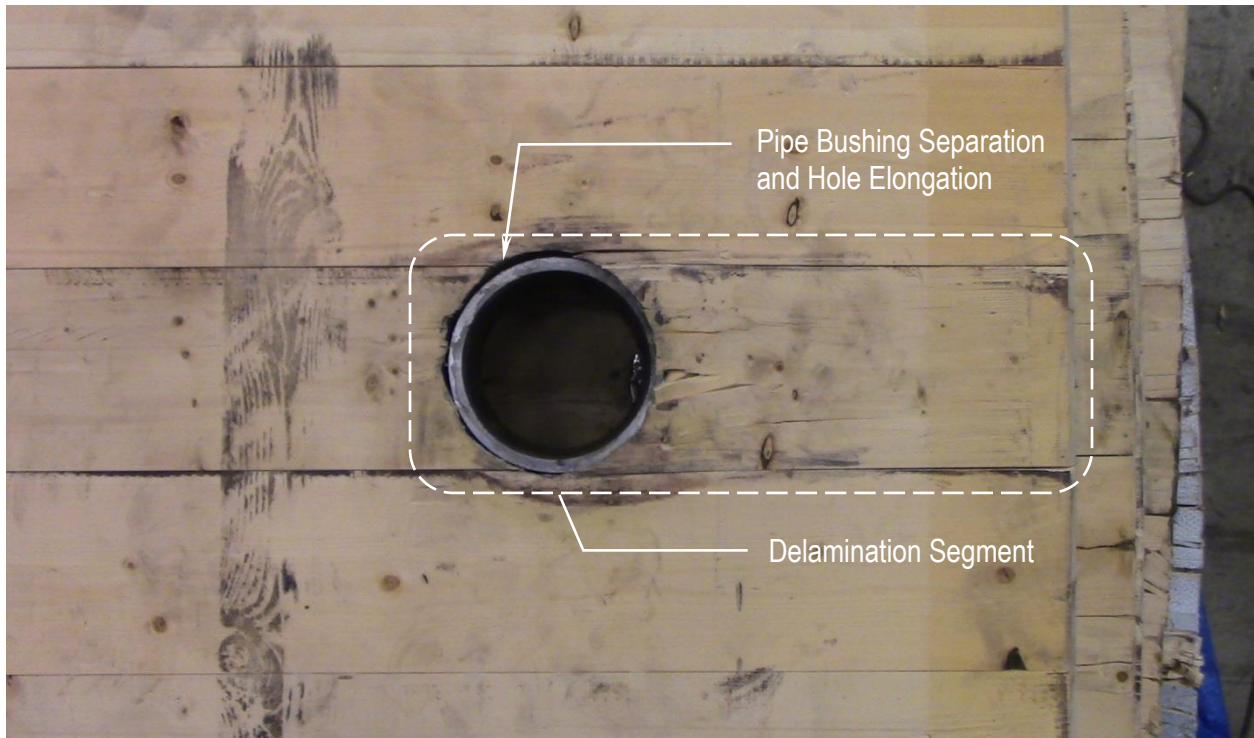


Figure 84. Typical damage in CLT face laminations surrounding pin hole.



Figure 85. Damage and elongation of hole around pipe bushing of ($e = 0.94$) panel.

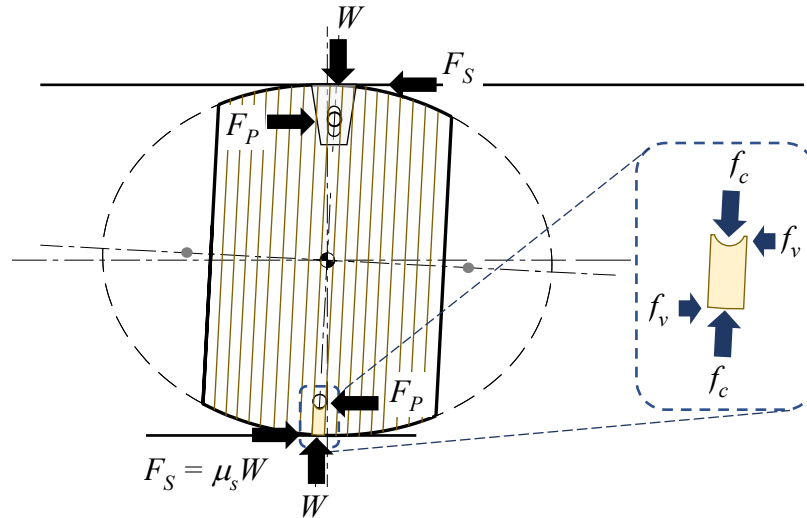


Figure 86. Free-body-diagrams of forces on panel and severed lamination in Slip-Friction Rocking

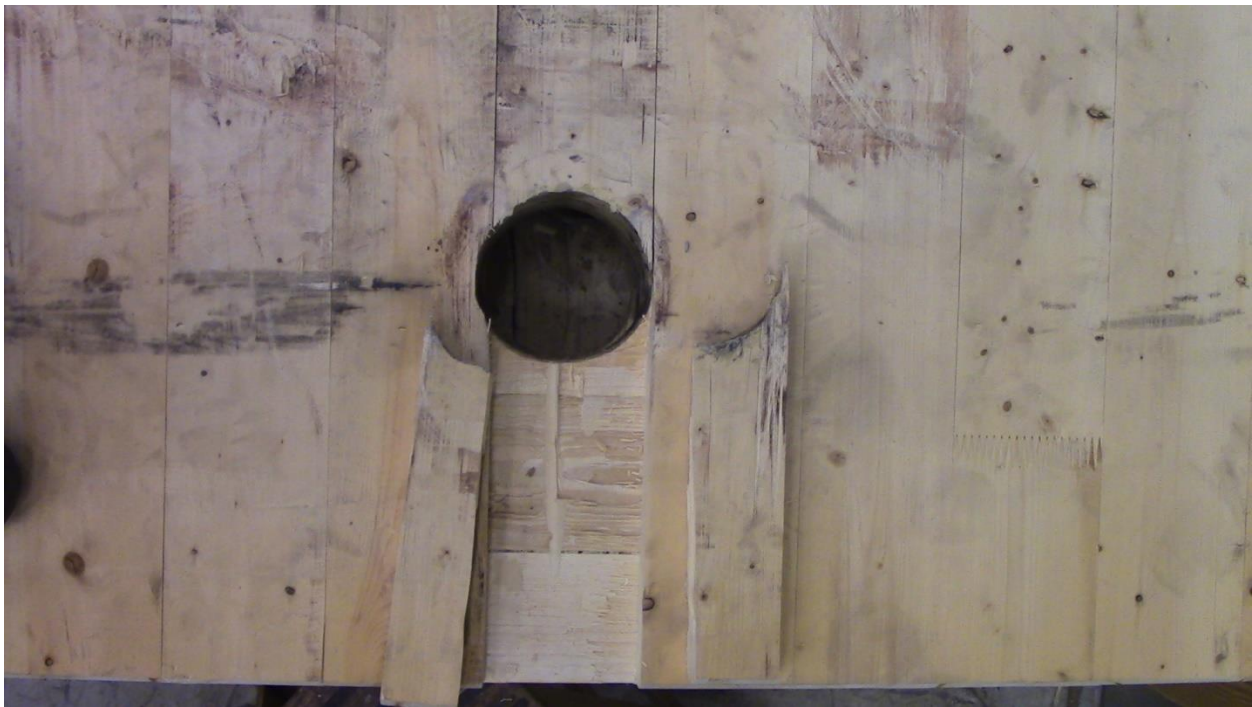


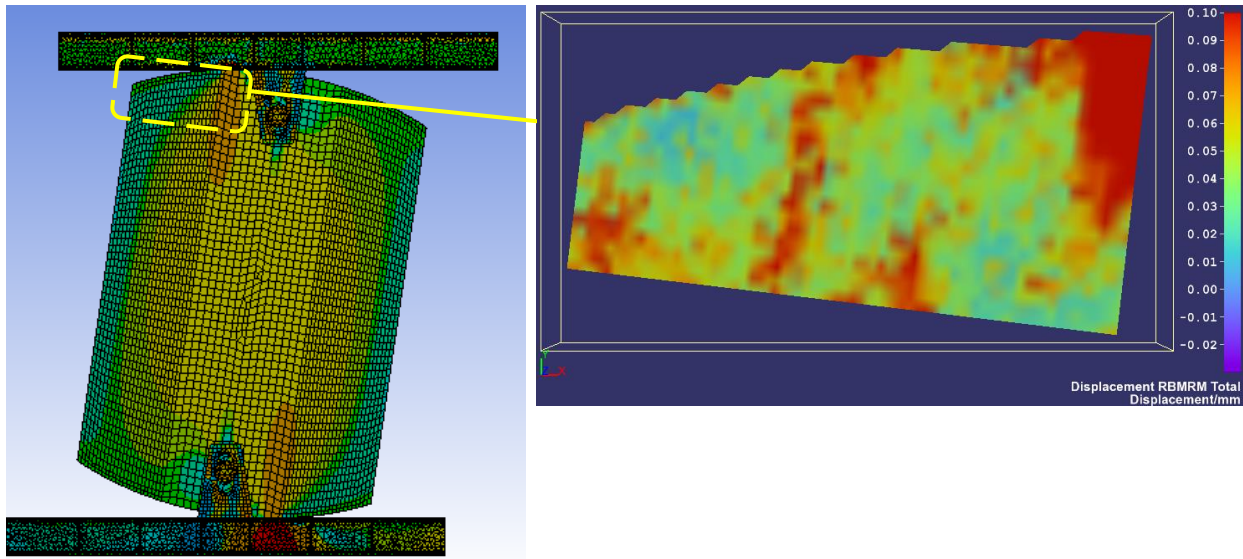
Figure 87. Delamination and splitting of face board severed by pin connection.

Slip-Friction Rocking survived low overburden loads of 133 kN (30 kips), with minimal damage. For medium and high overburden loads, greater than or equal to 266 kN (60 kips), however, *Slip-Friction Rocking* produced enough damage near the pin connections to place stability of the

pendulum mechanism at risk. All panels sustained damage around the pin hole because of *Slip-Friction Rocking*, and only 1 of the 6 panels could complete load protocols despite the damage. *No-Slip Traction Rolling*, in contrast, produced only minor damage at extreme lateral displacements. The damage observed in these first-generation prototypes can be either mitigated or avoided with design refinements, but for now, superstructure weight primarily limits the applicability of *Slip-Friction Rocking*.

Digital Image Correlation Comparisons

Full wall system tests introduced significant frictional forces along the edges of CLT panels, and DIC measurements aimed to capture the combined effects of normal and shear contact forces. Figure 88 exemplifies the primary DIC objective in the full prototype tests. Strains reported by FEA in (a) qualitatively resemble material displacements graphed by DIC in (b) using a square-root-sum-of squares (SQRSS) total of displacements measured orthogonally in 3D space of the system. DIC primarily focused on capturing the extents of damage caused by the traveling contact zone. Among secondary objectives, DIC recorded images as redundant forms of data collection. Focus on steel connections supplemented strain gage data, and overall views of the rocking panel elevations calibrated to 2D images backed up standard video.



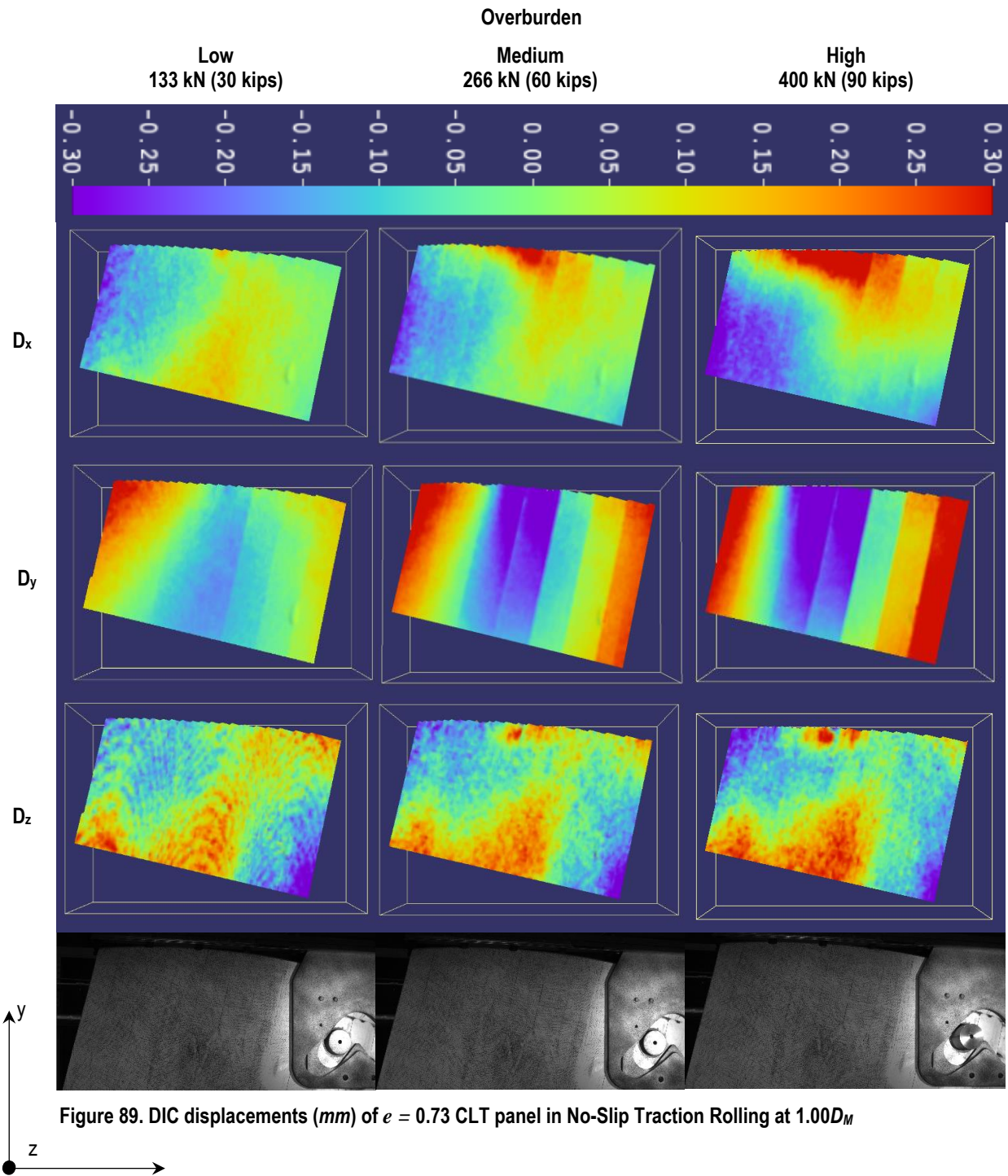
(a)

(b)

Figure 88. Slip-Friction Rocking of $e = 0.63$ panel with (a) plot of equivalent elastic strains by FEA and (b) timber material displacements reported by DIC

Timber Laminations

Representative of panels with low eccentricity, Figure 89 tracks how displacements increased within the CLT contact region proportionally with overburden loads. Under low overburden, the panel of 0.73 eccentricity exhibited barely distinguishable signs of contact. As *No-Slip Traction Rolling* continued under higher loads, however, displacements identified more distinct effects. Two or three lamination widths sustained the most extreme deformations. Plots of D_z for medium and high overburden show signs that minor splits had occurred near edges of some laminations. The images in the bottom row of the figure meanwhile show that the V-shaped slots afforded more room for lateral displacement, but actuators maxed out stroke to reach these positions. The hysteresis charts of Figure 40 correspond to the DIC plots of Figure 89 and indicated appreciable increases in damping but no changes in stiffness at maximum lateral displacement of the specimen.



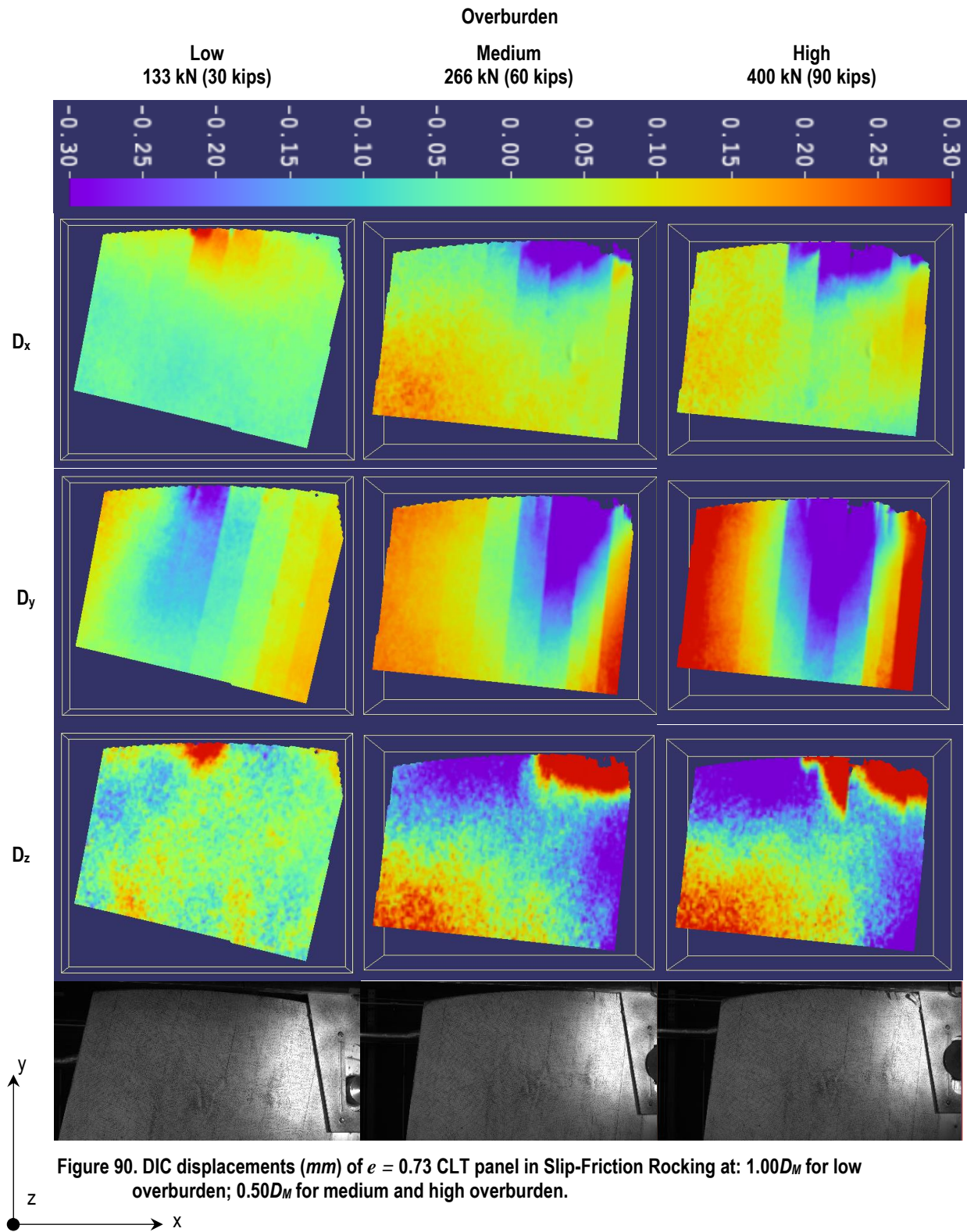


Figure 90 graphs DIC displacement fields in the same panel region under Slip-Friction Rocking. The row of displacement plots in the x -direction shows some influence of the top pin connection, coming from the right of each graph. The panel achieved $1.00D_M$ lateral displacement only under low overburden, corresponding to the hysteresis plot (d) of Figure 59. The medium and high overburden columns of Figure 90 displaced to the limits of respective hysteresis plots (d) and (f) of Figure 58, before the panel of 0.73 eccentricity had to retire. The DIC cameras recorded splits in the laminations pictured in Figure 91 that had occurred before high overburden had even been applied. The middle column of Figure 90 indicates that splits were present near the top edge at the medium overburden stage of Slip-Friction Rocking trials. The right column of Figure 90 show extents of the damage to local laminations in the D_x and D_z displacement fields. Some facets of the correlations in these regions were lost to damage, leaving blank regions in the graphs.

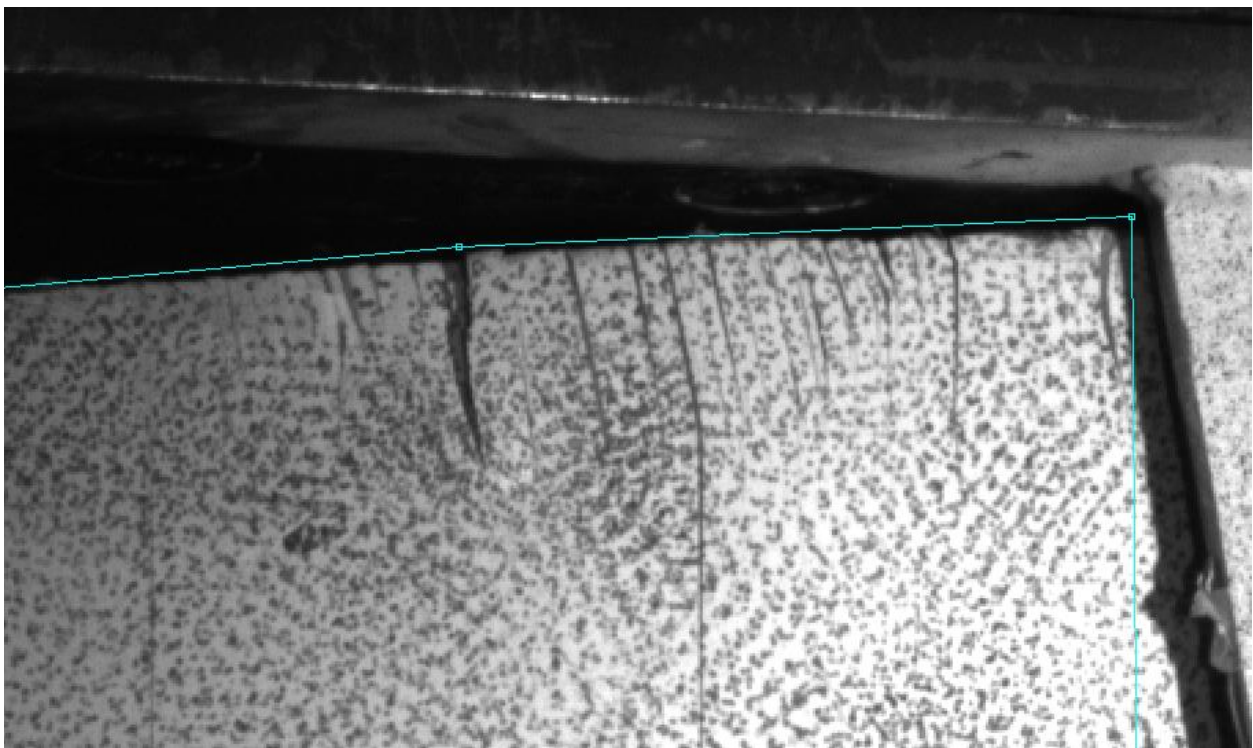
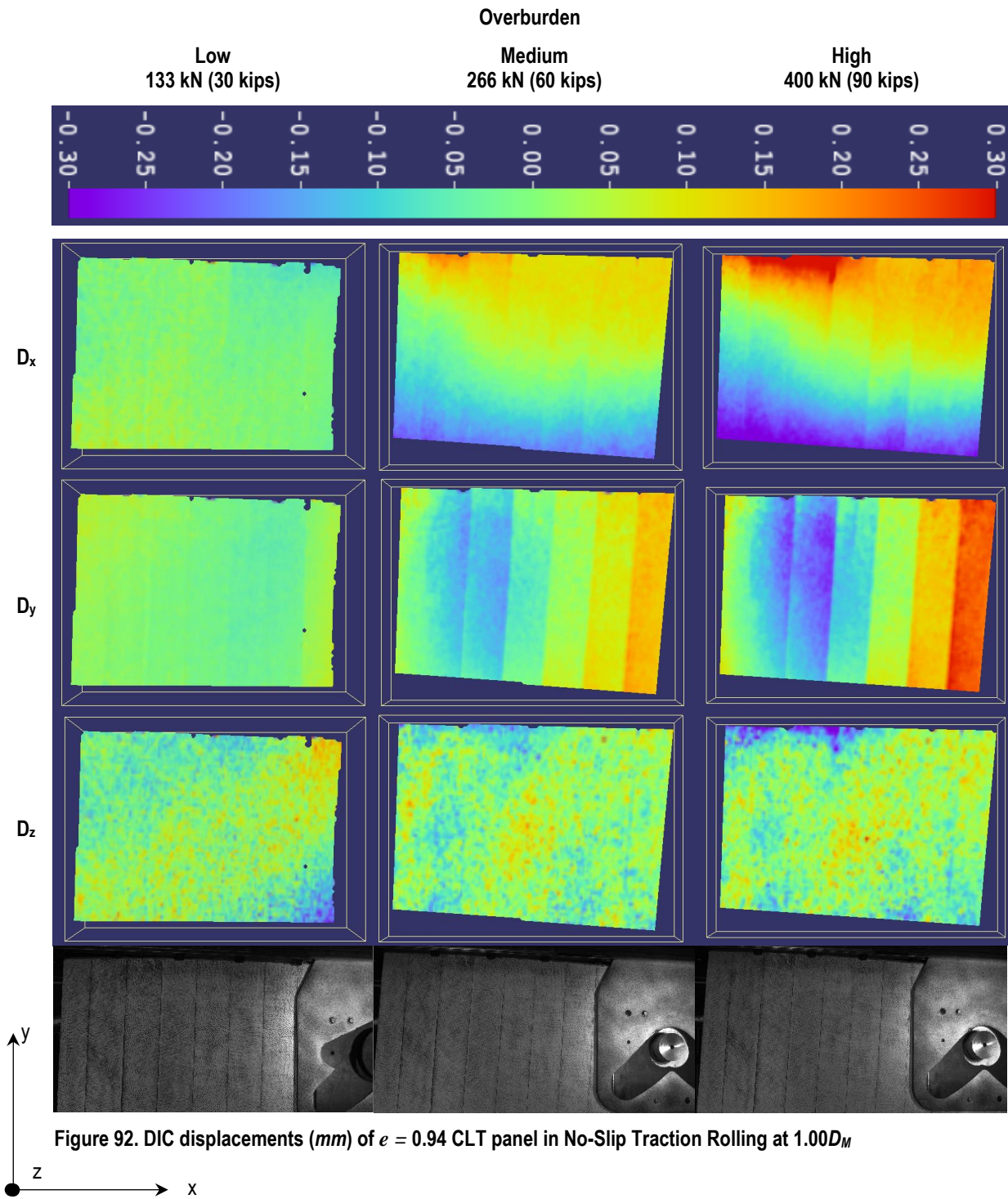


Figure 91. Splits at the tops of laminations in the $e = 0.73$ panel, adjacent to the vertically slotted connection



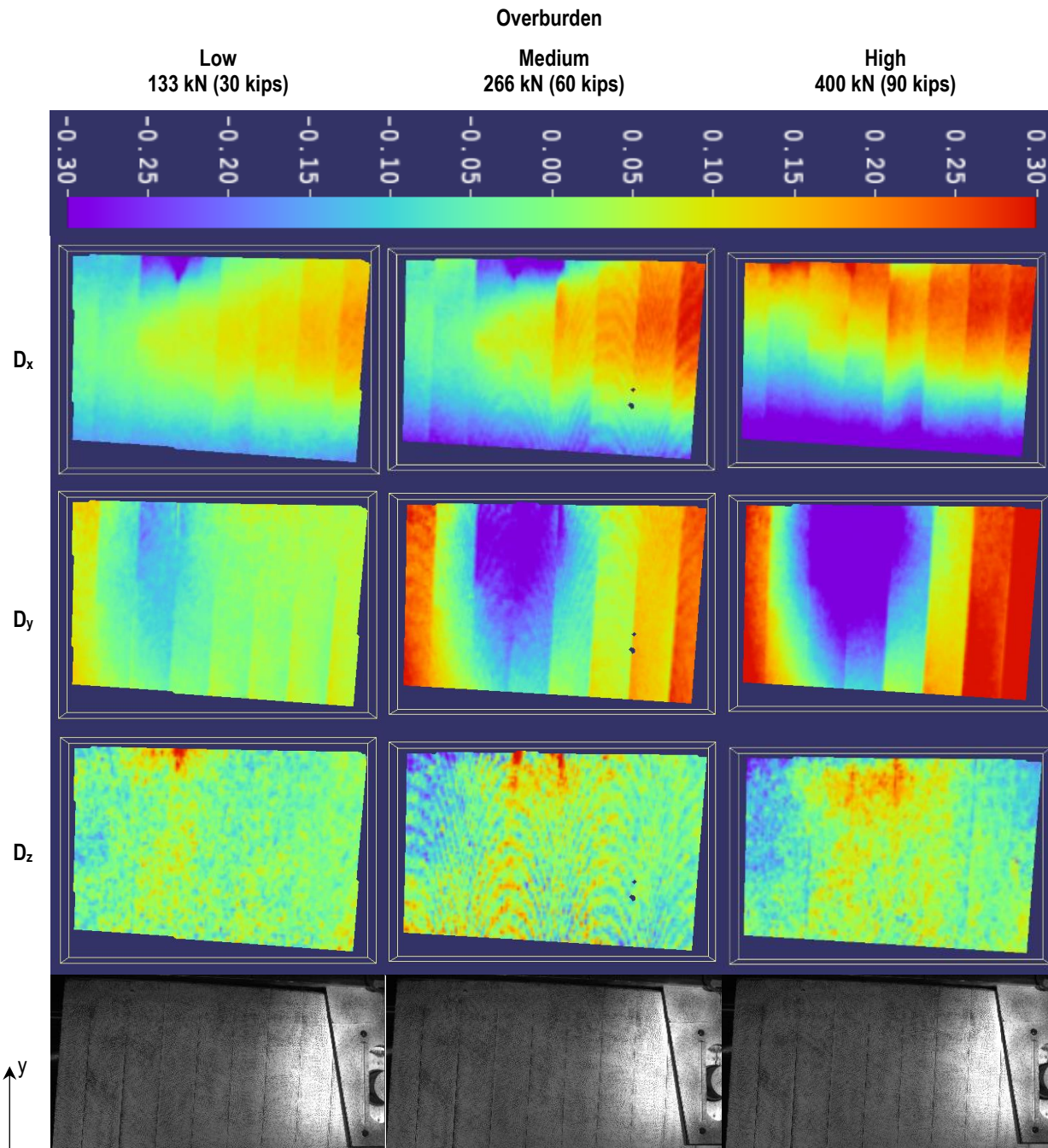


Figure 93. DIC displacements (*mm*) of $e = 0.94$ CLT panel in Slip-Friction Rocking at $1.00D_M$

Figures 92 and 93 respectively present the *No-Slip Traction Rolling* and *Slip-Friction Rocking* displacement fields of the panel with 0.94 eccentricity. Shaped to the widest elliptical profile, the panel accomplished anticipated lateral displacements of $1.00D_M$ for both connection configurations. At first glance, comparing Figures 89 and 92, or Figures 90 and 93, suggests that

the 0.94e panel fared better than the 0.73e panel, but displacement capacities of the two panels differ. The stiff 0.94e panel displaced to lateral story drifts of 6% in No-Slip Traction Rolling and 5% in Slip-Friction Rocking, compared to 23% and 19% lateral story drifts respectively traveled by the relatively softer 0.73e panel. According to hysteresis charts, lateral forces peaked at nearly 200 kN (45 kips) for the 0.73e panel and 300 kN (67 kips) for the 0.94e panel in *Slip-Friction Rocking*. Though the relatively softer panel developed lesser lateral forces, the panel sustained more damage from sliding longer distances.

Comparing the displacement fields of Figures 92 and 93 shows that *Slip-Friction Rocking* placed higher demands than *No-Slip Traction Rolling* of the same panel. Figure 93 shows greater lateral displacements influenced by the pin, more intense vertical displacements, and splits evident in the out-of-plane plots. As the only specimen to complete both anticipated loading protocols, the 0.94e panel offered one of the few direct comparisons of the material effects resulting from changing connection configurations.

Steel Connections

Because the vertically slotted connection would serve as the primary means of shear transfer in *Slip-Friction Rocking*, preliminary tests loaded the connection to a maximum horizontal proof force of 400 kN (90 kips). Figure 94 (a) shows channels applying force to a pin at the top of the vertical slot to produce maximum moment on the connection. The slotted plates exhibited minor yielding at the base corners and immediately adjacent to pin contact pictured in Figure 94 (b). Welding bars along the slot, as shown in Figure 95, provided more contact area and reinforced plates enough to prevent local yielding along the slot during full wall tests.

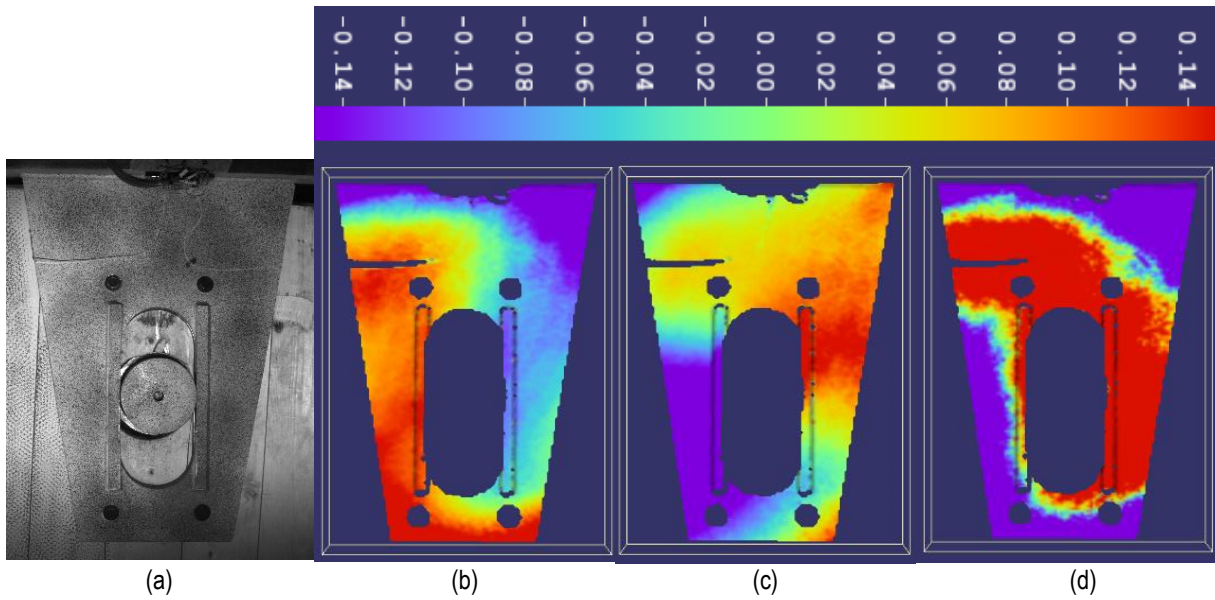


(a)



(b)

Figure 94. Preliminary proof-test of vertically slotted connection (a) loaded to max shear and moment (b) yield lines at pin contact.



(a)

(b)

(c)

(d)

Figure 95. Slip-Friction Rocking connection at 1.00DM of $e = 0.94$ panel (a) CLT hole elongation and DIC displacements (mm) of (b) D_x (c) D_y and (d) D_z

Figure 95 (a) pictures the top connection of the $0.94e$ panel with an elongated hole in the CLT and separation between the pipe bushing and timber. The photograph and DIC displacement

plots correspond to the Slip-Friction Rocking hysteresis charts (e) and (f) of Figure 72, exhibiting mixed modes of rocking and rolling. Figure 95 therefore portrays the connection sustaining peak loads, when the CLT panel supported high overburden and reached its lateral displacement capacity. DIC graphed (b), (c), and (d) of the respective displacements in the x, y, and z directions. The D_x graph of (b) captured effects of the flexural bending couple that elongated one side while shortening the other. The D_y graph of (c) captured effects of shear, including direct bearing of the pin on the right edge of the slot. The D_z graph of (d) captured incidental out-of-plane movement. For the most part, the steel performed elastically, as expected, and only load transfer to the timber needs improvement to optimize performance of *Slip-Friction Rocking*.

V-slotted connections intended only to guide *No-Slip Traction Rolling* with only incidental contact. DIC data on this connection configuration, therefore, served primarily as verification of pin positions. Although the V-slots experienced only incidental contact, the slots did not emerge unscathed. Figure 96 photographs wear on the bottom edge of the interior slotted shim. Pin contact forced the steel along the slot to flare in thickness. The local yielding may have resulted from fabrication error, slot misalignment, or specimen deformations. Slots, however, had been cut with generous tolerances of ± 10 mm ($\frac{3}{8}$ in.), and peak material deformations measured by DIC measured on the order of 0.30 mm ($< \frac{1}{64}$ in.). Partial slip, therefore, could be the predominant cause of the observed wear. Slot yielding, furthermore, could have contributed to increased exhibited in hysteresis Figures 44 and 45 corresponding to the pictured specimen.



Figure 96. Wear of slotted shim edge for $e = 0.88$ panel in No-Slip Traction Rolling

Wind Restraint

To fundamentally characterize lateral stiffness of the elliptical wall system, this project mostly excluded sacrificial wind restraints as Figure 14 had done to generalize isolator performance. Real applications of the elliptical wall system would require wind restraints to raise the threshold of rocking so that typical wind pressures do not induce nuisance vibrations. If wind restraints act integrally with the wall system, standards require prototypes to be tested with restraints installed (ASCE/SEI 7 2017). Figure 97 superposes results of the $0.73e$ panel tested under high overburden of 400 kN (90 kips) and displaced to four-hundredths of the story height for 20 cycles. The two *No-Slip Traction Rolling* trials, with and without the wind straps depicted by Figure 28, exhibited lesser stiffness than the vertical slot constraint of *Slip-Friction Rocking*. The wind strap had a minor effect on stiffness and would require more bolts to increase effectiveness.

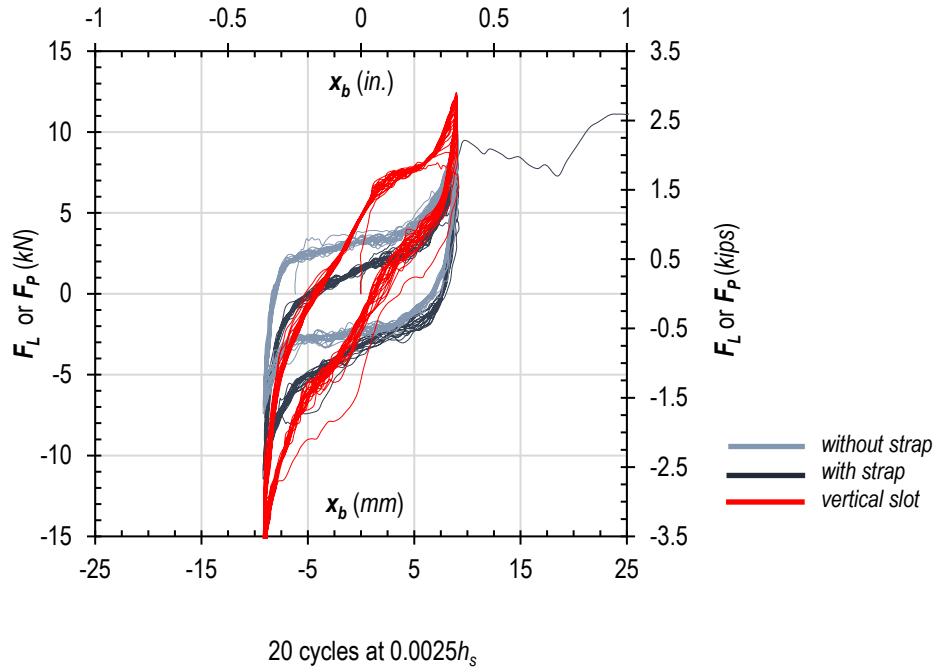


Figure 97. Effects of various pin constraints on low-amplitude displacements

Containment and subsequent replacement of sacrificial bolts, however, presents additional dilemmas. During testing, bolts traveled several meters across the room after fracturing under a minor amount of pretension. Accessing and replacing the bolts after an earthquake, moreover, would partially negate benefits of the system. Figure 97 also suggests that pin constraint offers only a partial solution to wind restraint. Effective wind restraint must also engage corners of the panels. Controlled-strength materials or hold-down connections of reliable yield strength provide sacrificial options, but resilient wind-restraint solutions need further development.

V. Summary, Conclusions, and Recommendations

Jangid and Londhe introduced the concept of elliptical rolling rod isolation decades ago with a numerical study of a 2D planar structure (1998). A recent study has revived the concept by analyzing a 3D orthogonal arrangement of elliptical rolling rods (Rawat et al. 2018). This project advances elliptical rolling past the conceptual stage with prototypes in cross-laminated timber

that scale up the elliptical pendulums for more effective self-centering. Although previous studies identified skidding as a potential vulnerability of the elliptical rolling rod system, hypothetical analysis only hinted at solutions. Story shear transfer plays a critical role in controlled rocking systems, and friction strongly influences the mechanisms of shear transfer.

The connections for *No-Slip Traction Rolling* and *Slip-Friction Rocking* prototypes approached the problem of shear transfer from divergent philosophical perspectives. The V-slotted connections of *No-Slip Traction Rolling* sought only to restrain displacements from slippage, so that frictional traction between timber and steel could drive rolling. The proactive approach of constraining pins within vertical slots guaranteed shear transfer with a redundant *slip-friction* mechanism that transformed friction into energy dissipation. Judging based on the criteria of predictability and levels of observed damage would declare *No-Slip Traction Rolling* the clear winner over *Slip-Friction Rocking* for CLT wall systems, because the intrinsic energy dissipation of the sliding system came at the cost of splitting and delaminating timber materials.

Summary Results Tables

To assess how well idealized *No-Slip Traction Rolling* and *Slip-Friction Rocking* models fit the experimental data, Table 33 compares two stiffness values. The first stiffness value $k_{d,avg}$ averages the slopes determined by linearly fitting experimental data primarily to the loading segments of the hysteresis, as illustrated in Figure 98. The second stiffness value k_{ideal} linearly approximates slope of the idealized hysteresis models, based on Equations 5 or 8 corresponding to *No-Slip Traction Rolling* (NSTR) or *Slip-Friction Rocking* (SFR). Table 33 reports percent difference between the stiffness values, using k_{ideal} as the basis. Because most test configurations laterally displaced at least $0.5D_M$, summary comparisons focus on this range.

Table 33. Stiffness comparisons of idealized model and fit to data through $0.5D_M$ of each panel configuration

<i>e</i>	Config.	$k_{d, avg}$ Fit to Data		k_{ideal} Idealized Model		Difference (%)	Pinched Hysteresis? (Yes/No)	Remarks	Referenced Hysteresis Figures	
		(kN/mm)	(kips/in.)	(kN/mm)	(kips/in.)					
Low Overburden (133 kN or 30 kips)	0.63	NSTR	0.027	0.152	0.023	0.133	14.5	N	A	36 (b)
	0.63	SFR	0.051	0.290	0.055	0.316	8.3	N	B	56 (b)
	0.73	NSTR	0.045	0.258	0.040	0.230	11.8	N	A	38 (b)
	0.73	SFR	0.098	0.558	0.096	0.545	2.4	Y	B	58 (b)
	0.82	NSTR	0.076	0.436	0.073	0.416	4.8	N		42 (b)
	0.82	SFR	0.145	0.827	0.173	0.987	16.2	N	C	61 (b)
	0.88	NSTR	0.125	0.713	0.120	0.684	4.3	N		44 (b)
	0.88	SFR	0.228	1.304	0.171	0.979	33.2	Y	C	64 (b)
	0.91	NSTR	0.184	1.052	0.173	0.991	6.2	N		48 (b)
	0.91	SFR	0.354	2.022	0.3246	1.854	9.1	N	C	67 (b)
Medium Overburden (266 kN or 60 kips)	0.63	NSTR	0.052	0.296	0.047	0.267	10.7	N	A	36 (d)
	0.63	SFR	0.111	0.631	0.111	0.632	0.1	N	B	56 (d)
	0.73	NSTR	0.087	0.497	0.081	0.461	7.9	N	A	38 (d)
	0.73	SFR	0.224	1.280	0.191	1.091	17.3	Y	B	58 (d)
	0.82	NSTR	0.150	0.858	0.146	0.832	3.1	N		42 (d)
	0.82	SFR	0.331	1.891	0.345	1.967	3.9	Y	C	62 (b)
	0.88	NSTR	0.245	1.401	0.240	1.368	2.4	N		44 (d)
	0.88	SFR	0.441	2.515	0.343	1.957	28.5	Y	C	65 (b)
	0.91	NSTR	0.361	2.062	0.347	1.981	4.1	N		48 (d)
	0.91	SFR	0.618	3.527	0.648	3.700	4.7	Y	C	68 (b)
High Overburden (400 kN or 90 kips)	0.63	NSTR	0.080	0.455	0.070	0.401	13.6	N	A	36 (f)
	0.63	SFR	0.236	1.345	0.166	0.947	42.0	Y	B	56 (f)
	0.73	NSTR	0.133	0.757	0.121	0.691	9.6	N	A	38 (f)
	0.73	SFR	0.385	2.198	0.287	1.636	34.3	Y	B	58 (f)
	0.82	NSTR	0.222	1.265	0.219	1.249	1.3	N		42 (f)
	0.82	SFR	NA	NA	NA	NA	NA	NA	C	NA
	0.88	NSTR	0.365	2.085	0.359	2.052	1.6	N		44 (f)
	0.88	SFR	NA	NA	NA	NA	NA	NA	C	NA
	0.91	NSTR	0.441	2.519	0.520	2.971	15.2	N		48 (f)
	0.91	SFR	NA	NA	NA	NA	NA	NA	C	NA
0.94	NSTR	0.889	5.073	0.805	4.598	10.3	N		52 (f)	
0.94	SFR	0.863	4.926	0.805	4.598	7.1	Y	D	70 (f)	

Abbreviations:

NSTR = No-Slip Traction Rolling

SFR = Slip-Friction Rocking

D_M = Displacement capacity; See Referenced Hysteresis Figures for limits corresponding to each panel.

$k_{d, avg}$ = average of stiffnesses k_{d1} and k_{d2} fit to loading branches of the hysteresis cycle. See example Figure 98.

k_{ideal} = stiffness of idealized model fit to either NSTR or SFR. See example Figure 98.

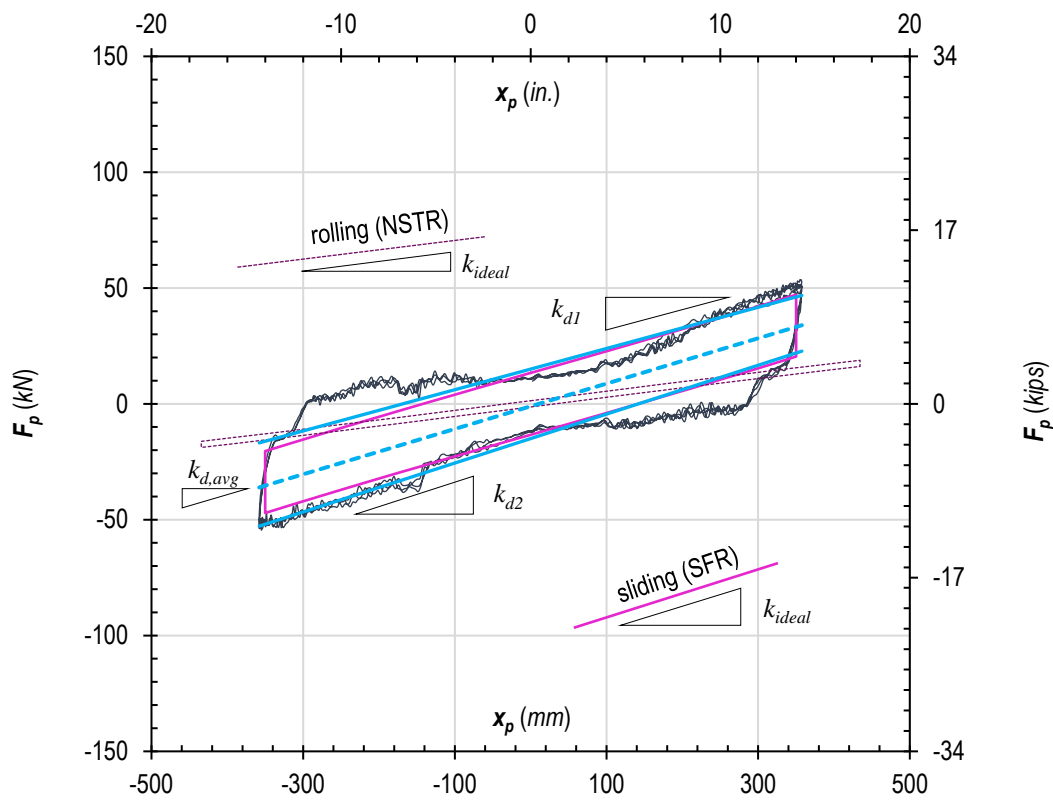
Remarks:

A = Track imperfections produced outliers included in the results, affecting the panels of least eccentricity most significantly.

B = Damage to timber around pin bushings pinched hysteresis, making bilinear slip-friction model inapplicable at either medium or high overburden levels.

C = Panel sustained damage in Slip-Friction Rocking at lower levels of overburden that prevented further testing.

D = While supporting a medium level of overburden, hole elongation around pipe bushings reverted the system to rolling, so high overburden data was fit to the NSTR model instead of SFR.



($e = 0.73$ panel): 3 cycles at $0.50D_M$

Figure 98. Stiffness comparison of idealized models to average linear fit of data

The percent difference column of Table 33 generally shows that the *No-Slip Traction Rolling* accurately applied to the corresponding test configurations. With a few exceptions for the least eccentric panels, the idealized NSTR models and fitted test data matched within 10% or less variation. For the panels with e of 0.63 and 0.73, differences between the NSTR model and fitted data modestly exceeded 10% only because track imperfections skewed results in greater proportion than panels profiled to wider ellipses. NSTR test results, did not exhibit hysteresis pinching, typically associated with damage, which made *No-Slip Traction Rolling* more predictable.

Slip-Friction Rocking models, in contrast, typically mischaracterized stiffness when the test data exhibited hysteresis pinching. According to Table 33, three of the six panels, tested under low overburden with the vertically slotted connections, charted a pinched hysteresis. At medium overburden, five of six panels showed clear hysteresis pinching, and deviations between predicted and actual stiffness generally grew more pronounced. Three of six panels could not proceed to support high overburden. Under high overburden, the three remaining panels showed clearer signs of damage. Two of the damaged panels recorded deviations from idealized stiffness exceeding 30 percent, and the third panel of greatest eccentricity reverted to rolling. Stiffness data for vertically slotted connection configurations, therefore, did not reliably follow the expected bilinear hysteresis path indicative of many slip-friction systems. While a pinched hysteresis model seems more apt to the *Slip-Friction Rocking* data, developing such a model fails to address instability of the damaged system.

In addition to stiffness, energy dissipation provides a measure of specimen adequacy. Seismic isolation standards call for no more than a 20% change in energy dissipated per hysteresis loop, E_{loop} , over repeated cycles intended to test durability (ASCE/SEI 7 2017).

Table 34. Average energy dissipated per cycle, E_{loop} , or area enclosed by hysteresis

e	Config.	0.25 D_M			0.50 D_M			Pinched Hysteresis? (Yes/No)	Remarks	Referenced Hysteresis Figures
		$\times 10^4$ (kN-mm)	(kip-in.)	CV	$\times 10^4$ (kN-mm)	(kip-in.)	CV			
Low Overburden (133 kN or 30 kips)	0.63 NSTR	0.191	16.9	11.7	0.407	36.0	4.8	N	A	36 (b)
	0.63 SFR	0.652	57.7	3.5	1.493	132.1	2.0	N	B	56 (b)
	0.73 NSTR	0.196	17.4	9.8	0.424	37.5	4.2	N	A	38 (b)
	0.73 SFR	0.826	73.1	1.4	2.436	215.6	1.8	Y	B	58 (b)
	0.82 NSTR	0.177	15.6	5.1	0.416	36.8	6.9	N		42 (b)
	0.82 SFR	0.682	60.3	1.4	1.567	138.7	1.7	N	C	61 (b)
	0.88 NSTR	0.132	11.7	5.2	0.343	30.3	4.8	N		44 (b)
	0.88 SFR	0.351	31.1	4.3	1.017	90.0	2.3	Y	C	64 (b)
	0.91 NSTR	0.080	7.1	18.5	0.227	20.1	4.0	N		48 (b)
	0.91 SFR	0.237	21.0	0.9	0.845	74.8	0.7	N	C	67 (b)
0.94 NSTR	0.051	4.5	18.0	0.141	12.4	10.0	N		52 (b)	
0.94 SFR	0.054	4.7	22.5	0.392	34.7	6.8	Y	D	70 (b)	
Medium Overburden (266 kN or 60 kips)	0.63 NSTR	0.318	28.2	16.2	0.682	60.4	10.0	N	A	36 (d)
	0.63 SFR	1.267	112.1	1.1	3.149	278.7	1.6	N	B	56 (d)
	0.73 NSTR	0.288	25.5	8.5	0.614	54.3	3.6	N	A	38 (d)
	0.73 SFR	1.481	131.0	1.7	4.577	405.1	8.5	Y	B	58 (d)
	0.82 NSTR	0.256	22.6	6.3	0.665	58.9	1.0	N		42 (d)
	0.82 SFR	1.214	107.5	2.5	3.387	299.8	1.6	Y	C	62 (b)
	0.88 NSTR	0.194	17.2	1.6	0.575	50.9	4.8	N		44 (d)
	0.88 SFR	0.458	40.5	14.9	1.847	163.4	0.9	Y	C	65 (b)
	0.91 NSTR	0.132	11.7	7.0	0.459	40.6	1.5	N		48 (d)
	0.91 SFR	0.292	25.8	6.1	1.112	113.4	2.6	Y	C	68(b)
0.94 NSTR	0.095	8.4	4.2	0.255	22.6	2.3	N		52 (d)	
0.94 SFR	0.077	6.8	32.6	0.375	33.2	11.4	Y	D	70 (d)	
High Overburden (400 kN or 90 kips)	0.63 NSTR	0.434	38.4	9.8	0.967	85.6	6.1	N	A	36 (f)
	0.63 SFR	1.990	176.1	2.4	5.546	490.9	1.4	Y	B	56 (f)
	0.73 NSTR	0.421	37.3	5.8	0.951	84.2	2.6	N	A	38 (f)
	0.73 SFR	1.984	175.6	3.0	5.508	487.5	11.7	Y	B	58 (f)
	0.82 NSTR	0.385	34.1	6.1	1.286	113.8	5.5	N		42 (f)
	0.82 SFR	NA	NA	NA	NA	NA	NA	NA	C	NA
	0.88 NSTR	0.282	25.0	2.7	0.940	83.2	0.9	N		44 (f)
	0.88 SFR	NA	NA	NA	NA	NA	NA	NA	C	NA
	0.91 NSTR	0.225	19.9	4.1	0.835	73.9	1.8	N		48 (f)
	0.91 SFR	NA	NA	NA	NA	NA	NA	NA	C	NA
0.94 NSTR	0.138	12.2	4.3	0.389	34.5	1.8	N		52 (f)	
0.94 SFR	0.093	8.3	10.2	0.203	18.0	25.6	Y	D	70(f)	

Abbreviations:

E_{loop} = Energy dissipated per cycle, or area within hysteresis, averaging test data over 3 cycles

CV = Coefficient of variation of 3 averaged E_{loop} values

The hysteresis loop “deflation” charted in Figures 62 (d), 68 (d), and 72 (c) at 0.75 and 1.00 displacement steps of D_M clearly exceeded accepted thresholds of 20% change. For displacement steps $0.25D_M$ and $0.50D_M$, however, Table 34 shows acceptable results. For each CLT specimen and test configuration, Table 34 lists the energy dissipated per cycle, or area within each hysteresis loop (summed numerically using trapezoidal rule), expressed as E_{loop} . Coefficients of Variation (CV) calculated from the mean and standard deviation of 3 cycles showed that E_{loop} remained within accepted norms of fluctuation through a range of at least $0.5D_M$. All but 3 cases of Table 34 list CVs less than 20 percent, and the exceptions correspond to the panel of greatest eccentricity, which toggled between rolling and slip-friction pendulum modes because of pin hole elongation in the CLT panel.

Comparing consecutive rows of Table 34 for each CLT panel specimen supporting the same level of overburden shows that changing connection configurations from NSTR to SFR increased energy dissipation on the order of three to five times. Similarly comparing consecutive rows of Table 33 for each CLT specimen shows an approximate twofold increase in effective stiffness going from *No-Slip Traction Rolling* to *Slip-Friction Rocking* configurations. Connection constraint increased both energy dissipation and effective stiffness. The system model of *Slip-Friction Rocking* explained how connection constraint fundamentally changing the mechanism of story shear transfer and the role of friction. In all but one case of *No-Slip Traction Rolling*, traction provided enough grip to roll panels, but rolling friction dissipated minimal energy. Sliding friction produced by horizontally constraining pins within a vertical slot enhanced energy dissipation but damaged timber laminations and produced less predictable hysteresis pinching. With improved wear of the CLT panel edges and reinforcement around the pins, the *Slip-Friction Rocking* configuration could perform more closely to the idealized SFR model.

Conclusions

The four main goals of a resilient seismic isolation system organize the conclusions of this study.

1. Horizontal and vertical stability when subjected to design displacements,
 - a. 5-ply CLT panels in the No-Slip Traction Rolling configuration supported low, medium, and high vertical loads, throughout all lateral displacement steps, with no significant damage.
 - b. Though precautionary bracing was provided in the out-of-plane direction, wall panels typically did not engage the bracing, because the steel pin connections and contact bearing points of the CLT provided enough restraint to keep the wall panel rocking in plane.
 - c. Chamfering the loadbearing edges of CLT wall panels reduced the superficial damage to face laminations, which resulted from misalignment of the test apparatus in the out-of-plane direction.
 - d. For 5-ply panels, the *Slip-Friction Rocking* configuration was stable when supporting low levels of vertical loads but began incurring damage at medium and high levels of vertical load, because of “stick-slip” frictional behavior of the wood face laminations.
 - e. Pin connection design needs to be refined to either withstand a higher concentration of load in the CLT or distribute the shear transfer forces more broadly throughout the panel for the *Slip-Friction Rocking* configuration.
 - f. Walls demonstrated stability in full-scale testing up to 432 mm (17 in.) of horizontal translation in each lateral in-plane direction (fully reversed cycles)

and 864 mm (34 in.) of horizontal translation in one direction (unidirectional cycles).

2. Inherent restoring forces that increase with increasing lateral displacement,
 - a. Visual evidence, including data from Digital Image Correlation (DIC) cameras, demonstrated that bearing contact points traveled as a function of lateral displacement, or wall rotation. As wall panels rotated more, the moment arm between the restorative force-couple proportionally increased.
 - b. Visual evidence, including DIC data, showed that the bearing contact points held up to the loads, typically only sustaining superficial damage, and that material deformations peaked at less 1 to 2 millimeters, even under the highest level of vertical load.
 - c. Residual lateral displacements, up to 12 mm ($\frac{1}{2}$ in.), occurred in the *No-Slip Traction Rolling* configuration,
 - d. Residual vertical shortening of story height, up to 12 mm ($\frac{1}{2}$ in.), occurred in panels of the *Slip-Friction Rocking* configuration that had sustained damage to the laminations surrounding the pins.
 - i. When pin connections remained intact, vertical slots succeeded in constraining residual lateral displacements,
 - ii. Surface wear to the loadbearing edges experiencing sliding friction did produce minor but residual wall shortening.
 - iii. Wall shortening only registered when outer face laminations began crushing or delaminating around the pin.
3. Durability without significant degradation under repeated cycles, and

- a. *No-Slip Traction Rolling* showed no appreciable signs of stiffness degradation in the hysteresis plots of full-scale tests.
- b. At extreme lateral translations, or rotation angles, *No-Slip Traction Rolling* showed only local and minor splitting of longitudinally oriented laminations.
 - i. Longitudinal laminations bear most of the panel loads, according to
 - 1. FEA models based on the orthotropic properties of wood,
 - 2. Piezoelectric pressure mapping of precursory test panels, and
 - 3. Observed zones of damage, which occurred only when the orientation angle of the load produced forces great enough to overcome the tension perpendicular to grain strength of wood laminations.
 - ii. Though secondary, cross-laminations critically support longitudinal laminations with bracing, load distribution, and handling shear transfer near connection boundaries.
- c. *Slip-Friction Rocking* tests of the 5-ply CLT could only reliably withstand low levels of vertical loads. *Slip-Friction Rocking* applications would require either,
 - i. Limitations of vertical loads on wall panels, or
 - ii. Improved capacity of pin connections.
- d. *No-Slip Traction Rolling* configurations can complete the displacement steps and cycles required by the prototype testing performance provisions outlined in the seismic isolation standard of *ASCE/SEI 7-16*.
 - i. 4 of 6 panels did fulfill planned test protocols.

- ii. 2 of 6 panels partially fulfilled *No-Slip Traction Rolling* protocols, with no damage, but panel specimens were damaged in *Slip-Friction Rocking* prior to completing all displacement steps.
 - 1. For logistical reasons, 2 of 6 panels were tested in *Slip-Friction Rocking* prior to completing unidirectional cycles, because achieving longer actuator strokes required reconfiguring test apparatus. These panels would have likely completed protocols without incident, had they continued in *No-Slip Traction Rolling*.
- 4. Quantifiable engineering parameters (namely stiffness and damping).
 - a. Stiffness did vary according to the geometric, rigid-body assumptions of idealized hysteresis models.
 - i. *No-Slip Traction Rolling* behavior can be accurately predicted using previously developed elliptical rolling rod calculations.
 - ii. *Slip-Friction Rocking* can be accurately predicted using the analysis developed for this project.
 - iii. Small deformations, rigid-body mechanics apply at the system level of analysis.
 - b. Damping of the system, as tested, relies primarily upon frictional energy dissipation.
 - i. Simple frictional models estimate the damping accurate enough for system level analysis of CLT contact with unpainted structural steel.

1. Rolling friction offers low damping with a frictional force that can be estimated with a coefficient $\mu_r = 0.01$,
 2. Sliding friction offers moderate damping with a frictional force that can be estimated with a coefficient $\mu_s = 0.09$,
- ii. Wood materials adapt to the boundary conditions.
1. Friction typically provided enough traction in the *No-Slip Traction Rolling* configuration.
 2. Under constraint and high pressure, timber loadbearing surfaces smoothed enough to permit *Slip-Friction Rocking*.
 3. Unpredicted frictional effects proved detrimental to Slip-Friction Rocking at medium and high overburden levels.
 - a. Gaps and splits opened and closed, between and within wood laminations, causing “stick-slip” friction.
 - b. Stick-slip friction dynamically impacted pin connections, contributing to premature demise under higher levels of load.
- iii. Frictional effects are intrinsic to rocking systems and should be harnessed for either:
1. Shear transfer, as in *No-Slip Traction Rolling*, or
 2. Energy dissipation, as in *Slip-Friction Rocking*.

Recommendations for Further Development

Despite the damage observed in this first phase of work, *Slip-Friction Rocking* should not be discounted from the repertoire of elliptical rolling isolation, because with only modest

improvements the sliding system can complement the applicability of *No-Slip Traction Rolling*. Though sliding friction placed individual laminations of the CLT at risk, the slip-friction mechanism presents several advantages. As a robust panel, CLT deserves robust connections. Many engineers, furthermore, prefer redundant means of story shear transfer that do not rely solely on traction. Using the observations of damage and contact zone behavior recorded during testing, the pin connection designs can be improved. Capacity of pin bearing on the CLT could significantly increase with several enhancements, including:

- Optimizing pin diameter to provide smaller diameter holes relative to lamination width;
- Adding cross-layers to the CLT panel faces to fully confine each longitudinal ply;
- Reinforcing exterior laminations in regions of high shearing stress with adhered fiber-reinforced polymers (FRPs) or mechanically fastened plates;
- Capping the edges of CLT panels with a wearing shoe to for predictable frictional performance and broader connection force distribution.

Despite relatively successful performance, first-generation prototypes of *No-Slip Traction Rolling* need further development with external damping devices and aforementioned wind restraints. U-shaped flexural connections and coupled wall configurations could provide energy-dissipation while raising the threshold of rocking for elliptically profiled panels, like these devices already do for rectangular systems (Andrew Buchanan et al. 2015). Other devices that could serve dual purposes of increasing both damping and wind restraint need to be developed under the overarching objective of resiliency.

With more practical development, therefore, either *No-Slip Traction Rolling* or *Slip-Friction Rocking* configurations offer viable options for supporting multistory superstructures of any

relatively rigid construction, with seismically isolating effects. Elliptically profiled walls simplify construction sequencing (within platform schemes) and connection details (with passive self-centering that does not require post-tensioning). Based on results of the current study, *No-Slip Traction Rolling* appears to be the more resilient option for taller multistory structures that typically sustain more gravity loads. *Slip-Friction Rocking* appears more suitable for shorter and more rigid superstructures that generally carry lesser gravity loads. The two options encompass a realm of possibilities conducive to versatile application of the elliptical rocking story concept.

Based on the foundations laid by this project, future prototyping should focus on optimizing connections of both configurations, coupling wall systems with external dampers and wind restraints. Though critical to actual building applications, these components might have masked the intrinsic behavior of the elliptical wall systems. Connection optimization and future testing procedures should also focus on tracking residual displacements. Tighter tolerances on the V-slots of *No-Slip Traction Rolling*, for example, could reduce residual lateral displacements. Protecting panels from wear in *Slip-Friction Rocking* could reduce residual vertical displacement. Mitigating both forms of residual displacements will maximize resiliency of the system.

Use of the Hysteresis Models

The *No-Slip Traction Rolling* and *Slip-Friction Rocking* hysteresis models developed by this project pave the way for numerical simulations of earthquake time-history analysis of tall timber buildings founded on rocking stories. Based on reasonable agreement between experimental and analytical lateral-load displacement properties, the *No-Slip Traction Rolling* model can be fashioned into a zero-length element for computer simulations with few restrictions. Although capable of reaching the $1.0D_M$ limits within the initial test program, predictability and other

practical considerations may warrant a more conservative limit less than or equal to $0.5D_M$, half the lateral displacement range tested. The *Slip-Friction Rocking* model should similarly be restricted to a lateral displacement range of $0.5D_M$. Additionally, *Slip-Friction Rocking* should be reserved for low overburden applications, until testing proves a reinforced panel system capable of supporting higher gravity loads. Analyses incorporating *Slip-Friction Rocking* models, furthermore, should compare results with *No-Slip Traction Rolling* to account for redundancy of the connection constraints. Even if expected to perform elastically through improved connection design, *Slip-Friction Rocking* connections can revert to rolling in the event of overload.

The prototyping of this project, therefore, makes building archetype development possible, through computer simulation. The six elliptical profiles provide can be tuned to optimize various multistory building schemes. Current analysis and design standards have recently evolved to require more rigorous computing to demonstrate efficacy of newly developed systems (Applied Building Technology Council 2009, ASCE/SEI 7 2017). Though previous studies of elliptical rolling rods have generally demonstrated efficacy of elliptical eccentricity, analyses conforming to current design standards represent the next logical phase of development that will advance elliptically profiled panels toward actual application.

Design Guidelines for Archetype Development

Though primarily envisioned for platform construction, the rocking walls developed for this project aimed for versatility. In fully panelized structures, as illustrated in Figure 99, the elliptically profiled walls could be designed to carry the entire gravity system of the building at the rocking story levels schematically depicted in Figure 15. Superstructure drift limits in a panelized layout should be set based on criteria considering architectural and mechanical

attachments and seismic joint limitations. Though this first phase of testing set high aims for the maximum lateral drift DM , practical applications should cut lateral drifts by at least a half for more predictable performance.

More commonly, engineers and architects would lay out elliptically profiled panels as shear walls, to be paired with structural column and beam framing. When paired with structural framing such as glulam columns and beams, the maximum lateral displacement of the system should be limited to 3% lateral story drift, to minimize the special detailing required of framing connections. More generally, the drift capacity of the gravity framing system dictates the limits of the rocking wall system, because frames must move compatibly with the rocking walls at the rocking story level. Exceeding conventional limits of the gravity framing system would require special detailing and careful consideration of P-delta effects.

Depending on elliptical profiles and layout of the walls in plan and rocking stories in elevation, elliptical rocking walls could reduce seismic base shears 25% to 50% based on conservative estimates of practical limitations. A target value of maximum lateral displacement D_M for the entire system will dictate the level of seismic force mitigation. Buildings allowed to drift only a few percent of the story height will transmit more force than a superstructure allowed to laterally displace several more percent of story height. Coupling wall panels with U-shaped flexural plates can help reduce the lateral displacements required to manage seismically induced forces by adding damping.

Sizing the CLT panel thickness should follow accepted practice outlined for compression elements (Ross et al. 2013). Bearing checks should consider unequal distributions of force and the reduced contact area resulting from the elliptical cuts to loadbearing CLT edges. This study

focused on bearing contact and frictional effects between timber and steel. Figure 99 depicts a generic beam system bounding the rocking story, because steel plates can be integrated with nearly any structural system. Bearing CLT walls directly against timber beams or slabs may be feasible but would warrant additional testing to determine frictional and other performance characteristics. The scope of study presented here provides the theoretical basis and practical guidance to further develop passively rocking pendulum systems for panelized construction in a variety of forms.

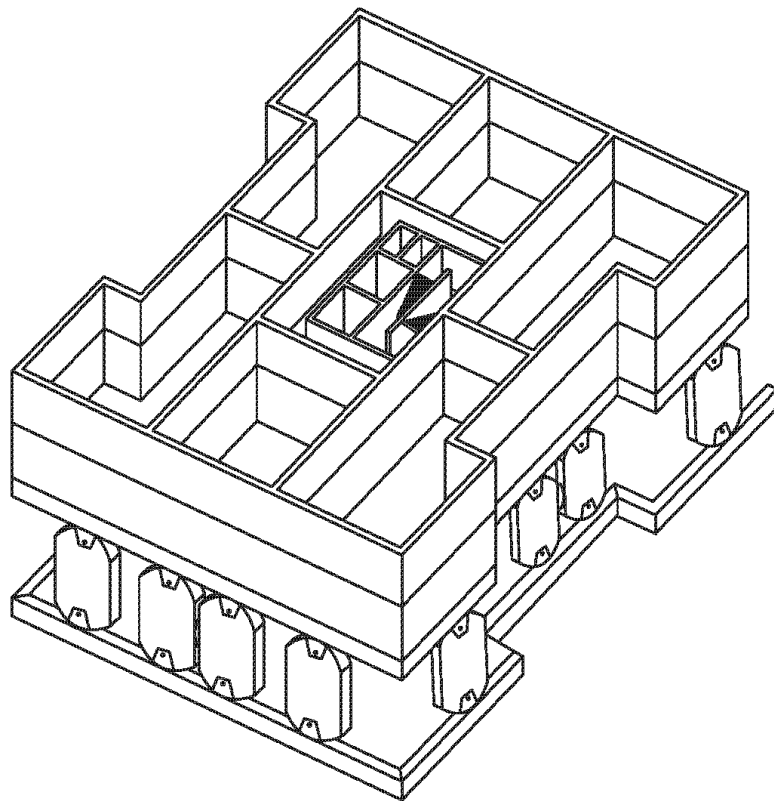


Figure 99. Sample rocking story arrangement supporting panelized superstructure

References

Abdoun, T.H., D. Ha, M.J. O’rourke, M.D. Symans, T.D. O’rourke, M.C. Palmer and H.E. Stewart (2009). Factors influencing the behavior of buried pipelines subjected to earthquake faulting. In: Soil Dynamics and Earthquake Engineering. 29(3): 415-427.

American Wood Council (2017). Chapter 10: Cross-Laminated Timber. National Design Specification Supplement (NDS) Design Values for Wood Construction 2018 Edition. American Wood Council. Leesburg, VA, American Wood Council: 1-76.

Amini, M.O., J.W. van de Lindt, S. Pei, D.R. Rammer, P. Line and M. Popovski (2014). Overview of a project to quantify seismic performance factors for cross laminated timber structures in the United States. In: Materials and joints in timber structures. S. Aicher, H.-W. Reinhardt and H. Garrecht, Springer, Stuttgart, Germany: 531-541.

Andrew Buchanan, Stefano Pampanin and Allesandro Palermo (2015). ENGINEERED WOOD CONSTRUCTION SYSTEM FOR HIGH PERFORMANCE STRUCTURES. U. S. Patent. United States, Prestressed Timber Limited, Christchurch (NZ),. US 8,935,892 B2: 1-17.

ANSI/APA PRG 320 (2012). Standard for Performance-Rated Cross-Laminated Timber. Tacoma, Washington, APA—The Engineered Wood Association: 1-23.

ANSYS Inc. (2016). ANSYS Mechanical APDL Contact Technology Guide. Online Documentation. Canonsburg, PA, SAS IP.

APA—The Engineered Wood Association (2015). Structurlam Crosslam Product Report PR-L314. Tacoma, Washington, APA: 1-4.

Applied Building Technology Council (2009). Quantification of Building Seismic Performance Factors, FEMA P695. Washington D.C., Federal Emergency Management Agency (FEMA).

Applied Technology Council (ATC), National Earthquake Hazards Reduction Program (NEHRP), United States Geological Survey (USGS), Federal Emergency Management Agency (FEMA) and A.B.E.J. Venture (2006). Next-generation performance-based seismic design guidelines : program plan for new and existing buildings. Washington, D.C. : U.S. Dept. of Homeland Security (DHS), FEMA, NEHRP.

ASCE/SEI 7 (2017). Chapter C17: Seismic Design Requirements for Seismically Isolated Structures. In: Minimum Design Loads for Buildings and Other Structures (ASCE/SEI 7-16), American Society of Civil Engineers, Reston, VA, USA: 673-692.

ASCE/SEI 7 (2017). Chapter 17: Seismic Design Requirements for Seismically Isolated Structures. In: Minimum Design Loads for Buildings and Other Structures (ASCE/SEI 7-16), American Society of Civil Engineers, Reston, VA, USA: 168-179.

ASCE/SEI 7 (2017). Chapter 12: Seismic Design Requirements for Building Structures. In: Minimum Design Loads and Associated Criteria for Buildings and Other Structures (ASCE/SEI 7-16), American Society of Civil Engineers, Reston, VA, USA: 89-119.

Bachus, K.N., A.L. Demarco, K.T. Judd, D.S. Horwitz and D.S. Brodke (2006). Measuring contact area, force, and pressure for bioengineering applications: Using Fuji Film and TekScan systems. In: Medical Engineering and Physics. 28(5): 483-488.

Beliakov, V.M.I., R.I. Kravtsova and M.G. Rappoport (1965). Tables of elliptical integrals Oxford ; New York : Pergamon Press; distributed in the Western Hemisphere by Macmillan, New York, Oxford ; New York.

Bolvardi, V., S. Pei, J.W. van de Lindt and J.D. Dolan (2018). Direct displacement design of tall cross laminated timber platform buildings with inter-story isolation. In: Engineering Structures. 167: 740-749.

Bora, C., M.G. Oliva, S.D. Nakaki and R. Becker (2007). Development of a precast concrete shear-wall system requiring special code acceptance. In: PCI Journal. 52(1): 2-15.

Brimacombe, J.M., D.R. Wilson, A.J. Hodgson, K.C. Ho and C. Anglin (2008). Effect of Calibration Method on Tekscan Sensor Accuracy. In: Journal of Biomechanical Engineering. 131(3): 034503.

Building Seismic Safety Council (2015). NEHRP Recommended Seismic Provisions for New Buildings and Other Structures (FEMA P-1050). Federal Emergency Management Agency (FEMA), Washington D.C.

Ceccotti, A. and M. Follesa (2006). Seismic Behavior of Multi-Storey XLam Buildings. International Workshop on Earthquake Engineering on Timber Structures. Coimbra, Portugal, COST E29- European Cooperation in the Field of Scientific and Technical Research: 81-95.

Ceccotti, A., C. Sandhaas, M. Okabe, M. Yasumura, C. Minowa and N. Kawai (2013). SOFIE project – 3D shaking table test on a seven-storey full-scale cross-laminated timber building. In: Earthquake Engineering & Structural Dynamics. 42(13): 2003-2021.

Dantech Dynamics (2018). DIC - Digital Image Correlation. Skovlunde, Denmark, Dantec Dynamics. 2018.

Daykin, T. (2019). Rare timber frame, 21-story downtown Milwaukee apartment tower wins Plan Commission approval. Milwaukee Journal Sentinel. Milwaukee, WI, USA Today Network.

de La Hire, P. (1685). Sectiones conicae. Apud Stephanum Michallet, via Jacobea sub signo S. Pauli, Paris.

Dujic, B., J. Pucelj and R. Zarnic (2004). Testing of racking behavior of massive wooden wall panels. Proceedings of the 37th CIB-W18 Meeting, Edinburgh, Scotland: 1-10.

Dujic, B., S. Aicher and R. Zarnic (2005). Investigations on in-plane loaded wooden elements–influence of loading and boundary conditions. In: Otto-Graf-Journal. 16: 259-272.

Dujic, B., S. Klobčar and R. Zarnic (2006). Influence of Openings on Shear Capacity of Massive Cross-Laminated Wooden Walls. International Workshop on Earthquake Engineering on Timber Structures. Coimbra, Portugal, COST E29- European Cooperation in the Field of Scientific and Technical Research: 105-118.

Dunbar, A.J.M., S. Pampanin and A.H. Buchanan (2014). Seismic performance of core-walls for multi-storey timber buildings. Towards Integrated Seismic Design: New Zealand Society for Earthquake Engineering (NZSEE) Conference. Auckland, New Zealand, NZEES: 1-9.

Fast, P. and R. Jackson (2017). Brock Commons: A Case Study In Tall Timber. STRUCTURE magazine. Reedsburg, Wisconsin, C3 Ink. 24: 50-52.

Federal Emergency Management Agency (FEMA) (2017). HAZUS® MH Estimated Annualized Earthquake Losses for the United States / FEMA 366. Washington D.C., Federal Emergency Management Agency (FEMA). FEMA 366.

Foster, R.M., T. Reynolds and M. Ramage (2016). Proposal for Defining a Tall Timber Building. In: Journal of Structural Engineering. 142(12): 02516001.

Gagnon, S., T. Bilek, L. Podesto and P. Crespell (2013). Introduction to cross-laminated timber. In: CLT handbook: cross-laminated timber, U.S. edition. E. Karacabeyli and B. Douglas. U.S. edition, United States Department of Agriculture (USDA)/U.S. Forest Service/Forest Products Laboratory and Binational Softwood Lumber Council (BSLC), Pointe-Claire, Quebec, Canada: 1-45.

Ganey, R., J. Berman, T. Akbas, S. Loftus, J. Daniel Dolan, R. Sause, J. Ricles, S. Pei, J.W. van de Lindt and H.-E. Blomgren (2017). Experimental Investigation of Self-Centering Cross-Laminated Timber Walls. In: Journal of Structural Engineering. 143(10): 04017135.

Gao, Z., X. Xu, Y. Su and Q. Zhang (2016). Experimental analysis of image noise and interpolation bias in digital image correlation. In: Optics and Lasers in Engineering. 81: 46-53.

Gavric, I., M. Fragiaco and A. Ceccotti (2015). Cyclic Behavior of CLT Wall Systems: Experimental Tests and Analytical Prediction Models. In: Journal of Structural Engineering. 141(11): 04015034.

Green, M. and E. Karsh (2012). TALL WOOD: The Case for Tall Wood Buildings. Vancouver, British Columbia, Canada, Wood Enterprise Coalition.

Grigorian, C.E., T.-S. Yang and E.P. Popov (1993). Slotted bolted connection energy dissipators. In: Earthquake Spectra. 9(3): 491-504.

Gröndahl, M. (2012). Building With Engineered Timber. The New York Times: Science. New York, The New York Times Company.

Guan, N., B. Thunell and K. Lyth (1983). On the friction between steel and some common Swedish wood species. In: Holz als Roh-und Werkstoff. 41(2): 55-60.

Harvey Jr., P.S. and K.C. Kelly (2016). A review of rolling-type seismic isolation: Historical development and future directions. In: Engineering Structures. 125: 521-531.

Hashemi, A., P. Zarnani, R. Masoudnia and P. Quenneville (2017). Seismic resilient lateral load resisting system for timber structures. In: Construction and Building Materials. 149: 432-443.

Holden, T., J. Restrepo and J.B. Mander (2003). Seismic Performance of Precast Reinforced and Prestressed Concrete Walls. In: Journal of Structural Engineering. 129(3): 286-296.

Housner, G.W. (1963). The behavior of inverted pendulum structures during earthquakes. In: Bulletin of the seismological society of America. 53(2): 403-417.

Jangid, R.S. and Y.B. Londhe (1998). Effectiveness of Elliptical Rolling Rods for Base Isolation. In: Journal of Structural Engineering. 124(4): 469-472.

Johnson, N. (2014). Forte by Lend Lease commended at 2014 Sustainability Awards. Architecture & Design. Australia. 2015.

Keegan, C.E., C. Sorenson, T.A. Morgan, S. Hayes and J. Daniels (2011). Impact of the Great Recession and Housing Collapse on the Forest Products Industry in the Western United States. In: Forest Products Journal. 61(8): 625-634.

Kretschmann, D.E. (2012). Mechanical properties of wood. In: Wood Handbook: Wood as an Engineering Material. R. J. Ross. Centennial, U.S. Department of Agriculture, Forest Service, Forest Procts Laboratory, Madison, Wisconsin: 1-46.

Kurama, Y., S. Pessiki, R. Sause and L.-W. Lu (1999). Seismic Behavior and Design of Unbonded Post-Tensioned Precast Concrete Walls Date: May-June, 1999. In: PCI Journal. 44(3): 72-89.

Kurama, Y.C. (2002). Hybrid post-tensioned precast concrete walls for use in seismic regions. In: PCI Journal. 47(5): 36-59.

Kurama, Y.C. (2005). Seismic design of partially post-tensioned precast concrete walls. In: PCI Journal. 50(4): 100-125.

Lee, C., W.A. Take and N.A. Hoult (2012). Optimum Accuracy of Two-Dimensional Strain Measurements Using Digital Image Correlation. In: Journal of Computing in Civil Engineering. 26(6): 795-803.

Lehmann, S. (2013). Low carbon construction systems using prefabricated engineered solid wood panels for urban infill to significantly reduce greenhouse gas emissions. In: Sustainable Cities and Society. 6: 57-67.

Lend Lease (2012). Forté: World's Tallest Timber Apartments, Melbourne Docklands. Melbourne, Australia, The Lend Lease Group. 2015.

Lo Ricco, M., A. Ghorbanpoor, S. Pei, D. Rammer, M. Begel, J. Bridwell and R.B. Zimmerman (2018). Prototyping a Passively Self-Centering Cross-Laminated Timber Rocking Wall System: Analytical and Experimental Investigation. In: WOOD DESIGN FOCUS. 28(2): 23-39.

Londhe, Y.B. and R.S. Jangid (1999). Dynamic response of structures supported on elliptical rolling rods. In: Doboku Gakkai Ronbunshu. 612: 11-20.

Loo, W.Y., P. Quenneville and N. Chouw (2012). Design and numerical verification of a multi-storey timber shear wall with slip-friction connectors. Auckland, New Zealand: Proc of World Conference on Timber Engineering.

Loo, W.Y., C. Kun, P. Quenneville and N. Chouw (2014). Experimental testing of a rocking timber shear wall with slip-friction connectors. In: Earthquake Engineering & Structural Dynamics. 43(11): 1621-1639.

M. Mohammad, S.G., Eng., Bradford K. Douglas, P.E., Lisa Podesto P.E. (2012). Introduction to Cross Laminated Timber. WOOD DESIGN FOCUS. 22: 3-12.

Mazzoleni, M.J., M.B. Krone and B.P. Mann (2015). Dynamics of Rocking Semicircular, Parabolic, and Semi-Elliptical Disks: Equilibria, Stability, and Natural Frequencies. In: Journal of Vibration and Acoustics. 137(4): 041017.

McKenzie, W. and H. Karpovich (1968). The frictional behaviour of wood. In: Wood Science and Technology. 2(2): 139-152.

Morgan, T.A. and S.A. Mahin (2011). The use of base isolation systems to achieve complex seismic performance objectives. Pacific Earthquake Engineering Research Center.

Murase, Y. (1984). Friction of wood sliding on various materials. In: Journal of the Faculty of Agriculture, Kyushu University. 28(4): 147-160.

Pan, B., H. Xie, Z. Wang, K. Qian and Z. Wang (2008). Study on subset size selection in digital image correlation for speckle patterns. In: Optics Express. 16(10): 7037-7048.

Pei, S., H.-E. Blomgren, A. Barbosa, J.W. van de Lindt, E. McDonnell, J. Berman and J.D. Dolan (2018). Full-Scale Shake Table Testing of a Two-Story Mass Timber Building with Resilient Rocking Wall Lateral Systems. In: WOOD DESIGN FOCUS. 28(2): 10-22.

Pei, S., J. Berman, K. Ryan, J. Ricles, R. Sause, J.D. Dolan and J.W. van de Lindt (2018). Natural Hazards Engineering Research infrastructure (NHERI) Tall Wood Project. Golden, Colorado, Colorado School of Mines. 2018.

Pei, S., J. Berman, J.D. Dolan, J.W. van de Lindt, J. Ricles, R. Sause, H.-E. Blomgren, M. Popovski and D.R. Rammer (2014). Progress on the development of seismic resilient Tall CLT Buildings in the Pacific Northwest. Proceedings of the 2014 World Conference on Timber Engineering. Quebec City, Canada.

Pei, S., J.W. van de Lindt, M. Popovski, J.W. Berman, J.D. Dolan, J. Ricles, R. Sause, H.-E. Blomgren and D.R. Rammer (2016). Cross-Laminated Timber for Seismic Regions: Progress and Challenges for Research and Implementation. In: Journal of Structural Engineering. 142(4): E2514001.

Pei, S., J.W. van de Lindt, A. Barbosa, J. Berman, E. McDonnell, J.D. Dolan, R.B. Zimmerman, R. Sause, J. Ricles and K. Ryan (2018). Full-Scale Shake Table Test Of Mass-Timber Building With Resilient Post-Tensioned Rocking Walls. World Conference on Timber Engineering. Seoul, Republic of Korea.

Pei, S., John W. van de Lindt, and Marjan Popovski. (2013). Approximate R-Factor for Cross-Laminated Timber Walls in Multistory Buildings. In: Journal of Architectural Engineering. 19(4): 245-255.

Perez, F.J., S. Pessiki and R. Sause (2004). Lateral Load Behavior of Unbonded Post-Tensioned Precast Concrete Walls with Vertical Joints. In: PCI Journal. 49(2): 48-64.

Perkins + Will (2014). SURVEY OF INTERNATIONAL TALL WOOD BUILDINGS. Vancouver, British Columbia, Canada, Forestry Innovation Investment and Binational Softwood Lumber Council.

Rawat, A., N. Ummer and V. Matsagar (2018). Performance of bi-directional elliptical rolling rods for base isolation of buildings under near-fault earthquakes. In: Advances in Structural Engineering. 21(5): 675-693.

Restrepo, J. and A. Rahman (2007). Seismic Performance of Self-Centering Structural Walls Incorporating Energy Dissipators. In: Journal of Structural Engineering. 133(11): 1560-1570.

Rinaldin, G., C. Amadio and M. Fragiaco (2013). A component approach for the hysteretic behaviour of connections in cross-laminated wooden structures. In: Earthquake Engineering & Structural Dynamics. 42(13): 2023-2042.

Risen, C. (2014). The World's Most Advanced Building Material Is...Wood and It's Going to Remake the Skyline. In: Popular Science. 284(3): 050-087.

Ritter, M.A., K. Skog and R. Bergman (2011). Science Supporting the Economic and Environmental Benefits of Using Wood and Wood Products in Green Building Construction. Madison, Wisconsin.

Ross, L.A., S. Gagnon and E. Keith (2013). Structural design of cross-laminated timber elements. In: CLT handbook: cross-laminated timber, U.S. edition. E. Karacabeyli and B. Douglas. U.S. edition, U.S. Department of Agriculture, Forest Service, Forest Products Laboratory, and Binational Softwood Lumber Council (BSLC), Pointe-Claire, Quebec, Canada: 19.

Sarti, F., A. Palermo and S. Pampanin (2015). Quasi-Static Cyclic Testing of Two-Thirds Scale Unbonded Posttensioned Rocking Dissipative Timber Walls. In: Journal of Structural Engineering. 142(4): E4015005.

Sathre, R. and J. O'Connor (2010). Meta-analysis of greenhouse gas displacement factors of wood product substitution. In: Environmental Science & Policy. 13(2): 104-114.

Schneider, J., Y. Shen, S.F. Stierner and S. Tesfamariam (2015). Assessment and comparison of experimental and numerical model studies of cross-laminated timber mechanical connections under cyclic loading. In: Construction and Building Materials. 77: 197-212.

Schneider, J., E. Karacabeyli, M. Popovski, S.F. Stierner and S. Tesfamariam (2014). Damage Assessment of Connections Used in Cross-Laminated Timber Subject to Cyclic Loads. In: Journal of Performance of Constructed Facilities. 28(6): A4014008.

Schultz, A. and R. Magaña (1996). Seismic behavior of connections in precast concrete walls. In: ACI Special Publication. 162: 274-312.

Seki, M., H. Sugimoto, T. Miki, K. Kanayama and Y. Furuta (2013). Wood friction characteristics during exposure to high pressure: influence of wood/metal tool surface finishing conditions. In: Journal of Wood Science. 59(1): 10-16.

Shen, Y.-L., J. Schneider, S. Tesfamariam, S.F. Stierner and Z.-G. Mu (2013). Hysteresis behavior of bracket connection in cross-laminated-timber shear walls. In: Construction and Building Materials. 48: 980-991.

Skidmore, Owings & Merrill, LLP (2014). Timber Tower Research Project. Chicago, Illinois, Softwood Lumber Board.

Stephens, K.F.I. (2011). Cycloid from a Rolling Ellipse, Wolfram Demonstrations Project.

Sutton, M.A. (2009). Image correlation for shape, motion and deformation measurements : basic concepts, theory and applications / Michael A. Sutton, Jean-José Ortu, Hubert W. Schreier. New York, N.Y. : Springer, New York, N.Y.

Tekscan (2017). Pressure Mapping Sensor 6300 Datasheet. Boston, Massachusetts, Tekscan.

Tekscan (2018). I-Scan System. Boston, Massachusetts, Tekscan. 2018.

van de Lindt, J.W. and Y. Jiang (2014). Empirical Selection Equation for Friction Pendulum Seismic Isolation Bearings Applied to Multistory Woodframe Buildings. In: Practice Periodical on Structural Design and Construction. 19(3): 04014010.

van de Lindt, J.W., D. Rammer, M. Popovski, P. Line, S. Pei and S.E. Pryor (2013). Lateral Design of Cross-Laminated Timber Buildings. In: CLT handbook: cross-laminated timber, U.S. edition. E. Karacabeyli and B. Douglas. U.S. edition, United States Department of Agriculture/U.S. Forest Service/Forest Products Laboratory and Binational Softwood Lumber Council (BSLC), Pointe-Claire, Quebec, Canada: 1-56.

Waugh, A., M. Wells and M. Lindegar (2010). "Tall Timber Buildings: Application of Solid Timber Constructions in Multi-Storey Buildings". International Convention of Society of Wood Science and Technology and United Nations Economic Commission for Europe. Geneva, Switzerland: 1-9.

Weiss, G. (2015). Elementary constructions for conics in Hyperbolic and Elliptic planes. In: Kog. Scient. Prof. Journal of Croatian Geom. and Graphics. 19: 24-31.

Wilharm, A., C. Hurschler, T. Dermitas and M. Bohnsack (2013). Use of Tekscan K-Scan Sensors for Retropatellar Pressure Measurement Avoiding Errors during Implantation and the

Effects of Shear Forces on the Measurement Precision. In: BioMed Research International. 2013: 1-7.

Zhang, Z. (2000). A flexible new technique for camera calibration. In: IEEE Transactions on Pattern Analysis and Machine Intelligence. 22(11): 1330-1334.

Appendix A: Principle of Virtual Work Models

The *Principle of Virtual Work* provides an alternate approach to modeling the pendulum systems with terms of energy inputs and outputs. A commonly applied form of the principle equates external work, W_{Ext} to internal work, W_{Int} , as:

$$W_{Ext} = W_{Int} \quad \text{Equation (10).}$$

For seismic design applications, effects of ground motion generally perform the external work, and plastic hinging typically performs the internal work. In the context of pendulum systems that rely primarily on potential energy to self-center, gravity and friction replace the internal work normally attributed plastic hinging. The models developed here, furthermore, organize translational and rotational work.

For *No-Slip Traction Rolling*, Figures 18 through 20 still apply. The lateral force F_L performs both translational and rotational external work on the system parameterized by:

$$W_{Ext} = F_L(x_b + 2p\theta_r) \quad \text{Equation (11).}$$

Within the parentheses the right side of Equation (11), the first term x_b represents lateral translation, and the second term represents the moment arm $2p$ and total sweep of rotation angle θ_r that factor into the rotational work of lateral force F_L . Equation (12) identifies two sources of internal work, gravity and friction inherent in the pendulum system:

$$W_{Int} = W_{gravity} + W_{friction} \quad \text{Equation (12).}$$

Superstructure load W delivered through the top contact point A in Figure 20 predominantly performs the gravitational work, and panel weight w_r typically makes small, often negligible contributions. Equation (13) considers both weights in the translational and rotational work done by gravity:

$$W_{gravity} = \overbrace{W(2y_r) + w_r y_r}^{lifting} + \overbrace{W(2c)\theta_r - w_r c\theta_r}^{rotating} \quad \text{Equation (13).}$$

When the panel lifts the superstructure, it taps into potential energy for the restoring moment that rotates the system back in place. According to Figure 18 (b), the raised height of the superstructure y_b equates to twice the raised height y_r traveled by the panel center of gravity.

In addition, both weights factor into the work done by rolling friction:

$$W_{friction} = \mu_r W (\widehat{AA''} + \widehat{BB''}) - \mu_r w_r \widehat{BB''} \quad \text{Equation (14).}$$

Equation (14) expresses the energy dissipated by rolling friction as a function of the elliptical arc distances traveled along the edges of the panel. Symmetry makes elliptical arc lengths $\widehat{AA''}$ and $\widehat{BB''}$ equal, provided that neither ceiling nor floor slips relative to the wall. Figure 18 (b), furthermore, dimensions each arc length more generally as:

$$\widehat{AA''} = \widehat{BB''} = \frac{1}{2}x_b + c \quad \text{Equation (15).}$$

The lateral force F_L must overcome gravity and friction to lift the superstructure by rotating the panel, so gravity and friction must oppose the lateral force in sign. Using the generalization of

Equation (15) and equating external work expressed by Equation (11) with the internal work expressed by Equations 12 through 14 yields:

$$F_L = \left(\frac{2W + w_r}{x_b + 2p\theta_r} \right) \left[y_r + c\theta_r + \mu_r \left(\frac{1}{2} x_b + c \right) \right] \quad \text{Equation (16).}$$

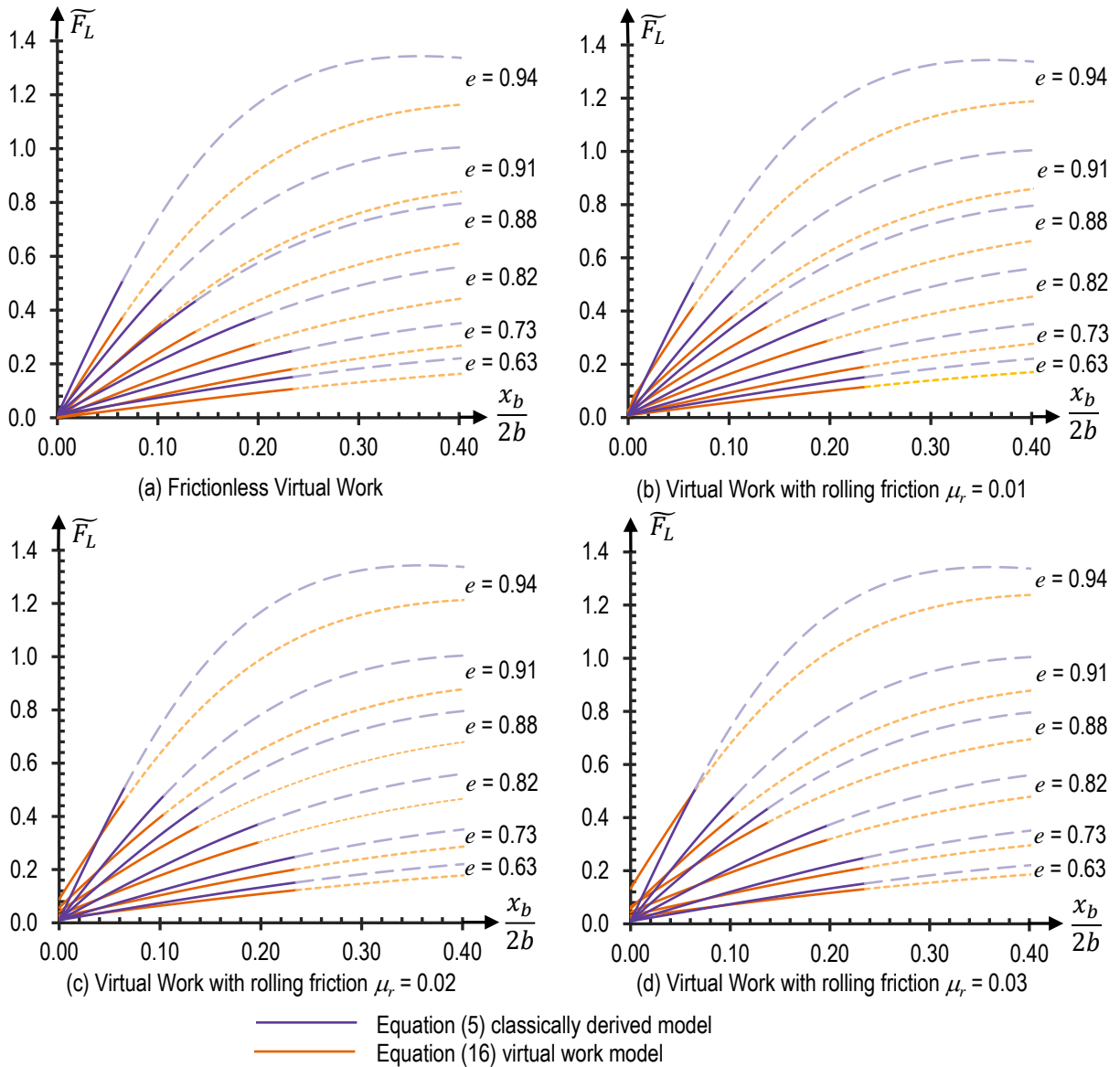


Figure 100. Normalized stiffness models for comparing Virtual Work and classical analyses of No-Slip Traction Rolling
 Virtual work models vary rolling friction assumptions, but the classical model holds a constant rolling friction coefficient of 1 percent.

Because Equation (16) includes translational and rotational terms in the denominator, the equation loses applicability near zero. A minimum threshold can be set for initial boundary conditions. Figure 100 plots values for lateral drift ratios substantially greater zero and projected y-axis intercepts with second-order polynomial trends. This technique, however, produces various values of friction at the onset of the system. Plots (a) through (d) range from assuming frictionless rolling to a rolling frictional coefficient of 3 percent to demonstrate sensitivity of the Virtual Work model to assumptions. The classically derived model based on Equation (5) assumed a rolling friction coefficient of 1 percent throughout all plots. Regardless of the level of rolling friction, Equation (16) mostly underestimate stiffness and lateral forces for *No-Slip Traction Rolling*.

Slip-Friction Rocking prompted analysis using virtual work, because the technique can examine multiple moving components. Figure 22 diagrammed potential sources of friction including pin connections, but Equation (8) aggregated frictional effects into a simplified sliding coefficient of that assumes constant frictional force. While vertical loads on panels were held constant throughout test trials, pin forces varied throughout the *Slip-Friction Rocking* cycles. Variable pin force, therefore, could lead to higher than expected lateral forces if friction on pins proved significant.

The approach to *Slip-Friction Rocking* differs from *No-Slip Traction Rolling*, because the pins introduce sliding friction. Timber-to-steel contact along load-bearing edges of the CLT panel provided a constant source of sliding friction. Steel-to-steel contact between pins and surfaces of the vertical slots and pipe bushings embedded in the CLT added to friction of the system. Equation (17) assigns external work to the lateral story-shear force transferred through pins F_P and the constrained lateral displacement x_P :

$$W_{Ext} = F_p x_p \quad \text{Equation (17).}$$

As before, the work performed by gravity includes rotational and translational components:

$$W_{gravity} = (2W + w_r)(y_r + c\theta_r) \quad \text{Equation (18) .}$$

The work performed by friction includes components of the rolling friction model with significant additions:

$$W_{friction} = (2W + w_r) \left[\mu_r \left(\frac{x_b}{2} + c \right) + \mu_s x_c \right] - 2F_p (\mu_{sp} \delta_y - \mu_{rp} r_p \theta_r) \quad \text{Equation (19),}$$

where μ_{sp} is the sliding coefficient for steel-to-steel contact of the pins, δ_y is the vertical translations of the pins in each slot, μ_{rp} is the rotational frictional coefficient for pins in steel-to-steel contact with the pipe bushings and r_p is radius of the pin. All other parameters of Equation (19) remain consistent with the classically derived models of elliptical rolling and sliding.

Lateral force F_p producing the external translation must overcome the work of gravity and friction, leading to the following expression:

$$F_p = (2W + w_r) \frac{y_r + \mu_r \widehat{AA}'' + \mu_s x_c + c\theta_r}{x_p - 2(\mu_{sp} \delta_y + \mu_{rp} r_p \theta_r)} \quad \text{Equation (20).}$$

Note that the elliptical arc length \widehat{AA}'' can be substituted with parameters x_b and c according to Equation (15). Even though the constrained system requires x_p to be less than x_b , the panel rotates through the same angle θ , by sliding and rotating at pin centers.

Figure 101 compares Equation (19) with the Equation (8) model of *Slip-Friction Rocking*. The models apply constant sliding and rolling frictional coefficients on the CLT panel, but the Virtual Work models add pin sliding and rotational friction that the classical model simplified. The resulting plots generally show reasonable match in stiffness of the two systems for low to moderate friction on the pins. When friction coefficients on the pins increase to a high value of 0.6, however, the Virtual Work models show significantly higher forces. According to plot (d) of Figure 46, therefore, pin friction could plausibly cause increased lateral force. Whether this actually occurred, however, remains uncertain. Pin bushings elongated holes in the CLT panels to the point of damage in some specimens, but pins appeared free to rotate and slide throughout the cycles. Equation (19) faces the same stability issues near zero movement as the virtual work model for *No-Slip Traction Rolling*. Equations 5 and 8 did not pose the same stability issues as the virtual work methods and established initial conditions more practically. The classically derived models, furthermore, sufficed in bounding the data within practical limits of the system.

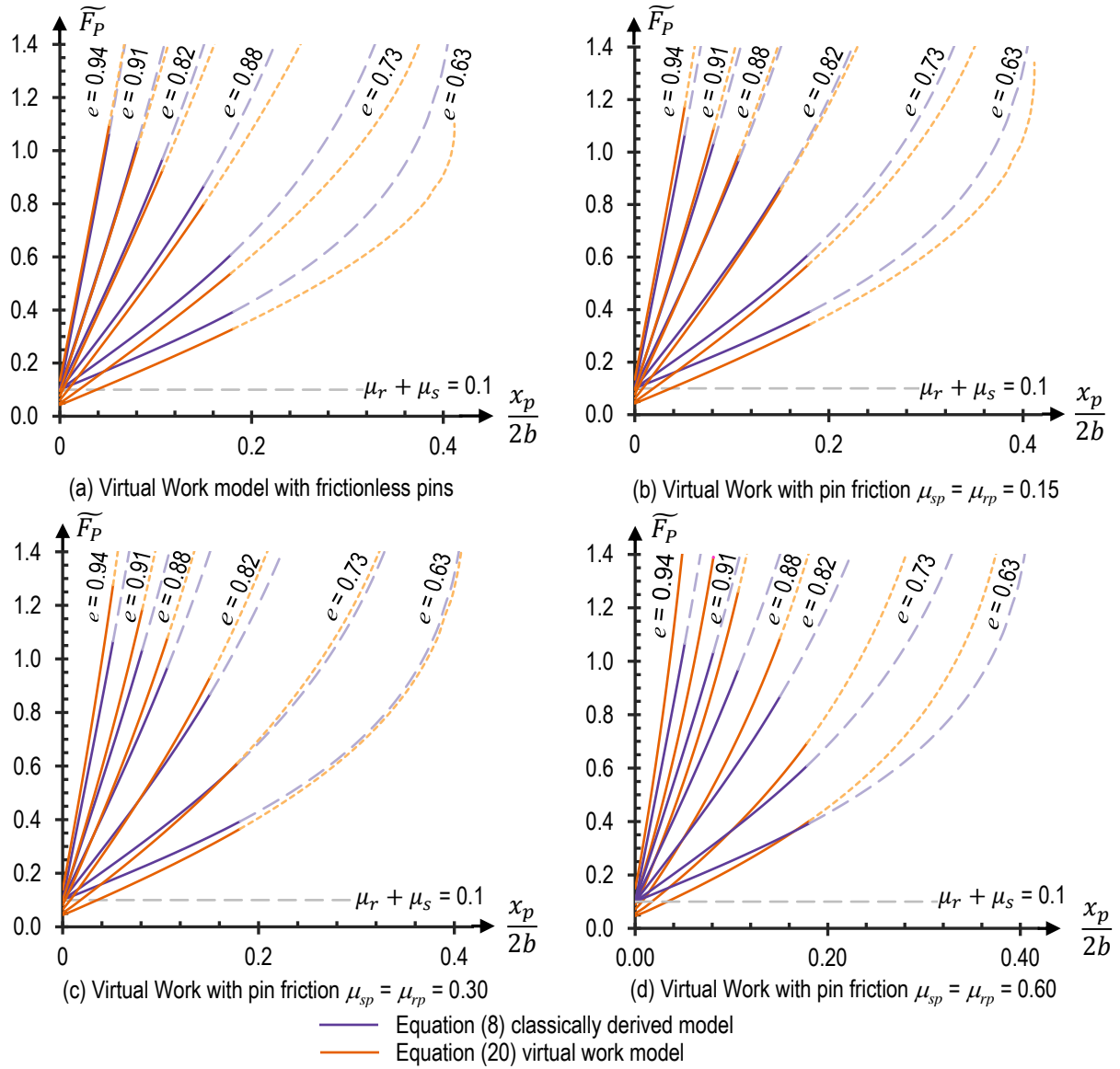


Figure 101. Normalized stiffness models for comparing Virtual Work and classical analyses of Slip-Friction Rocking
 Virtual Work models assume the same rolling and sliding friction coefficients as the classically derived model but add sliding and rotational friction of the pins.

Appendix B: Connection Details

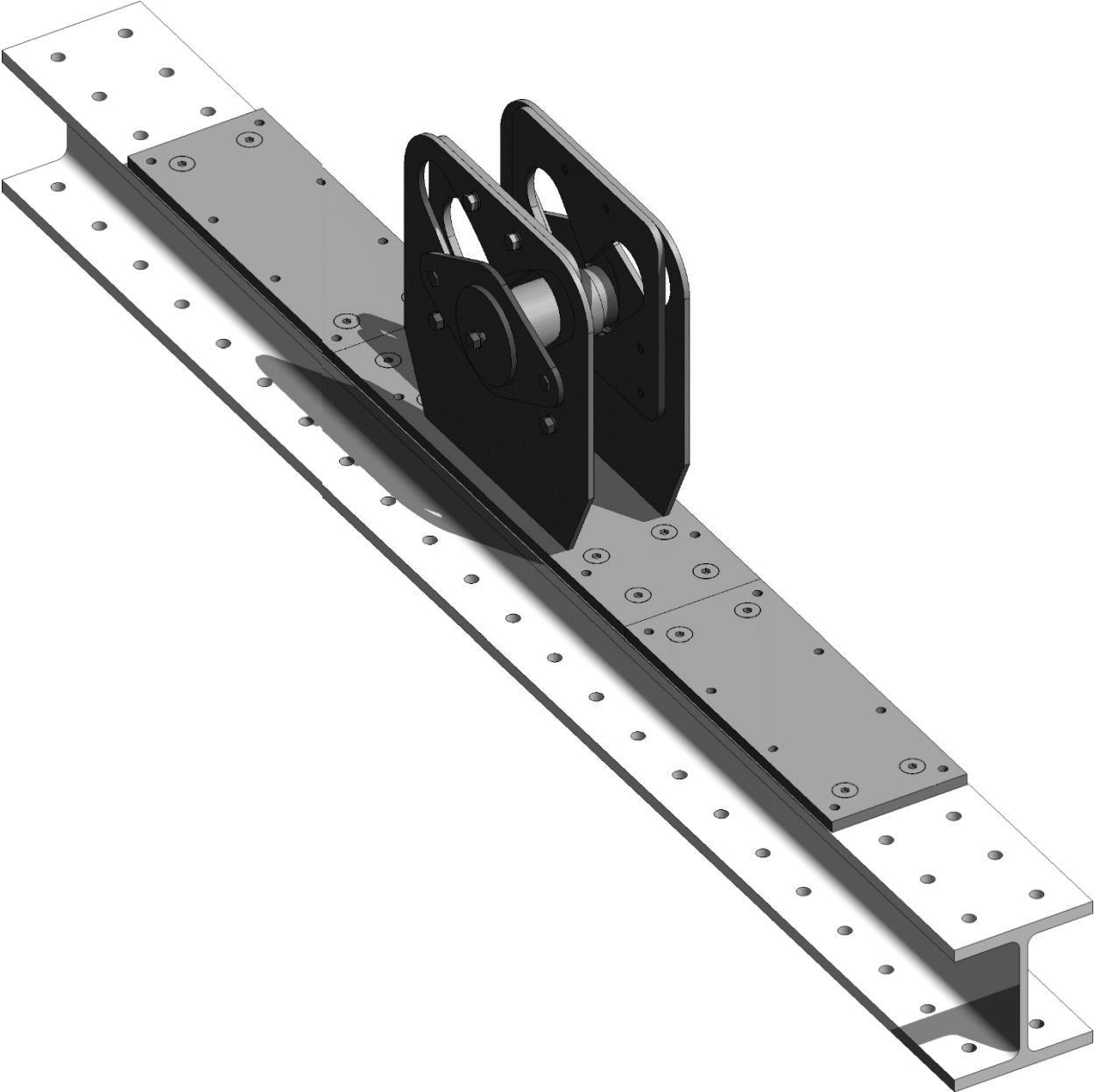


Figure 102. Orthographic view of assembled prototype connection for No-Slip Traction Rolling

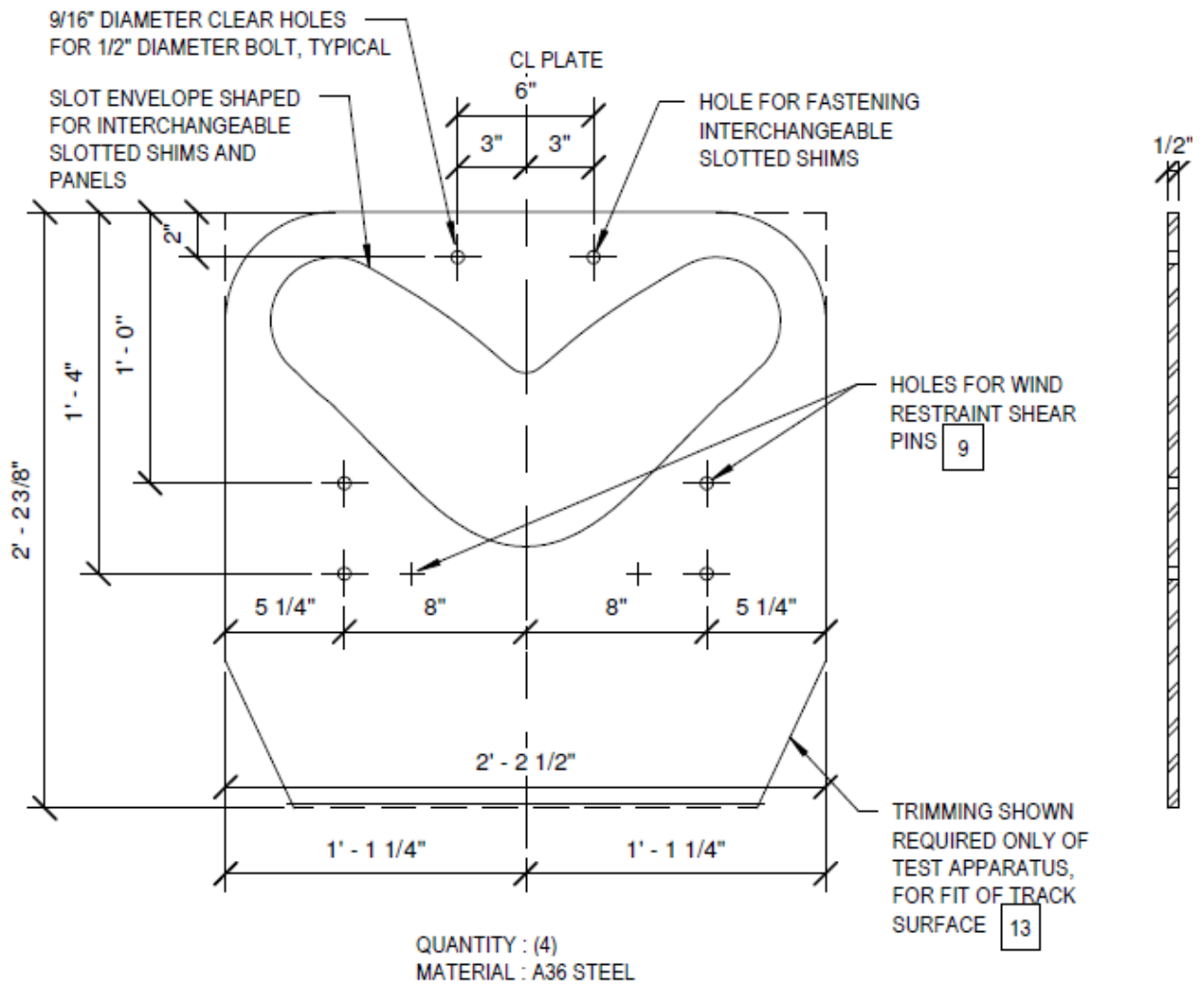


Figure 103. Main face plate enveloping slot shapes

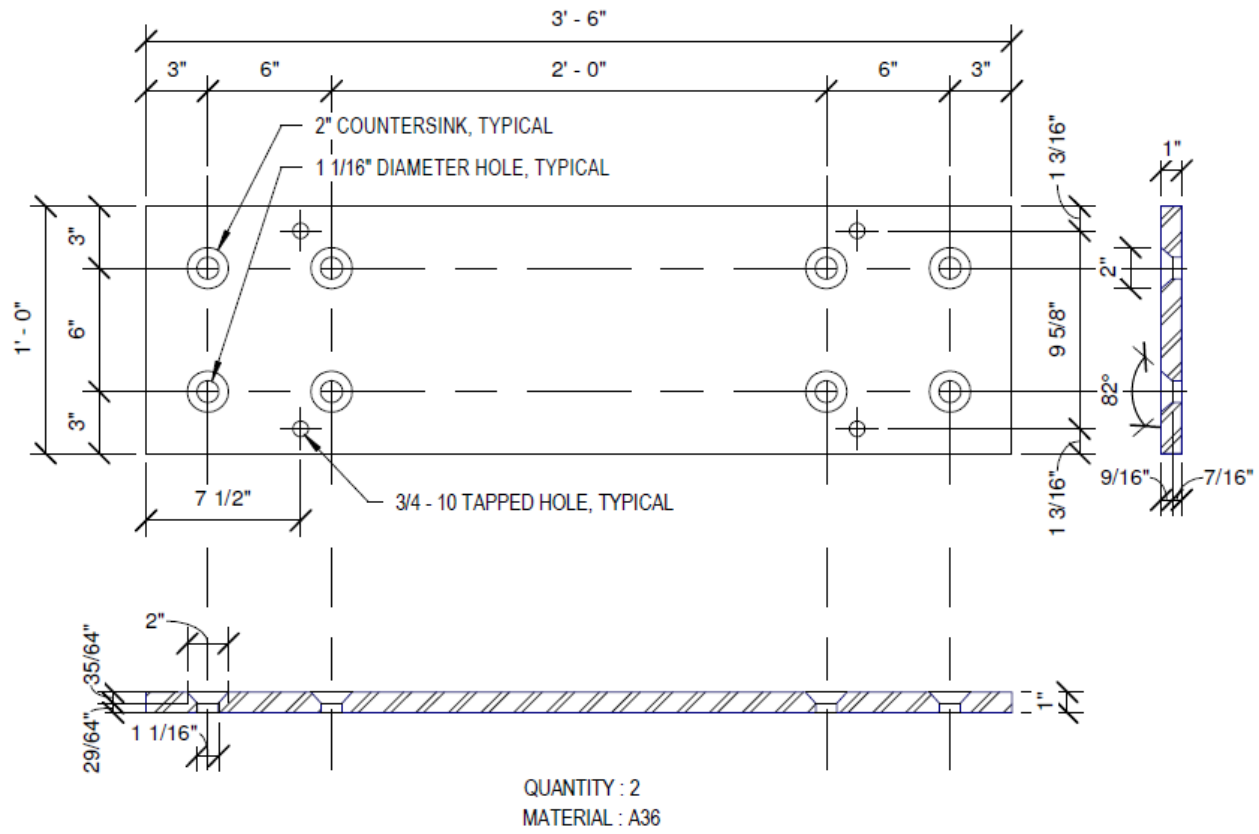


Figure 104. Main baseplate

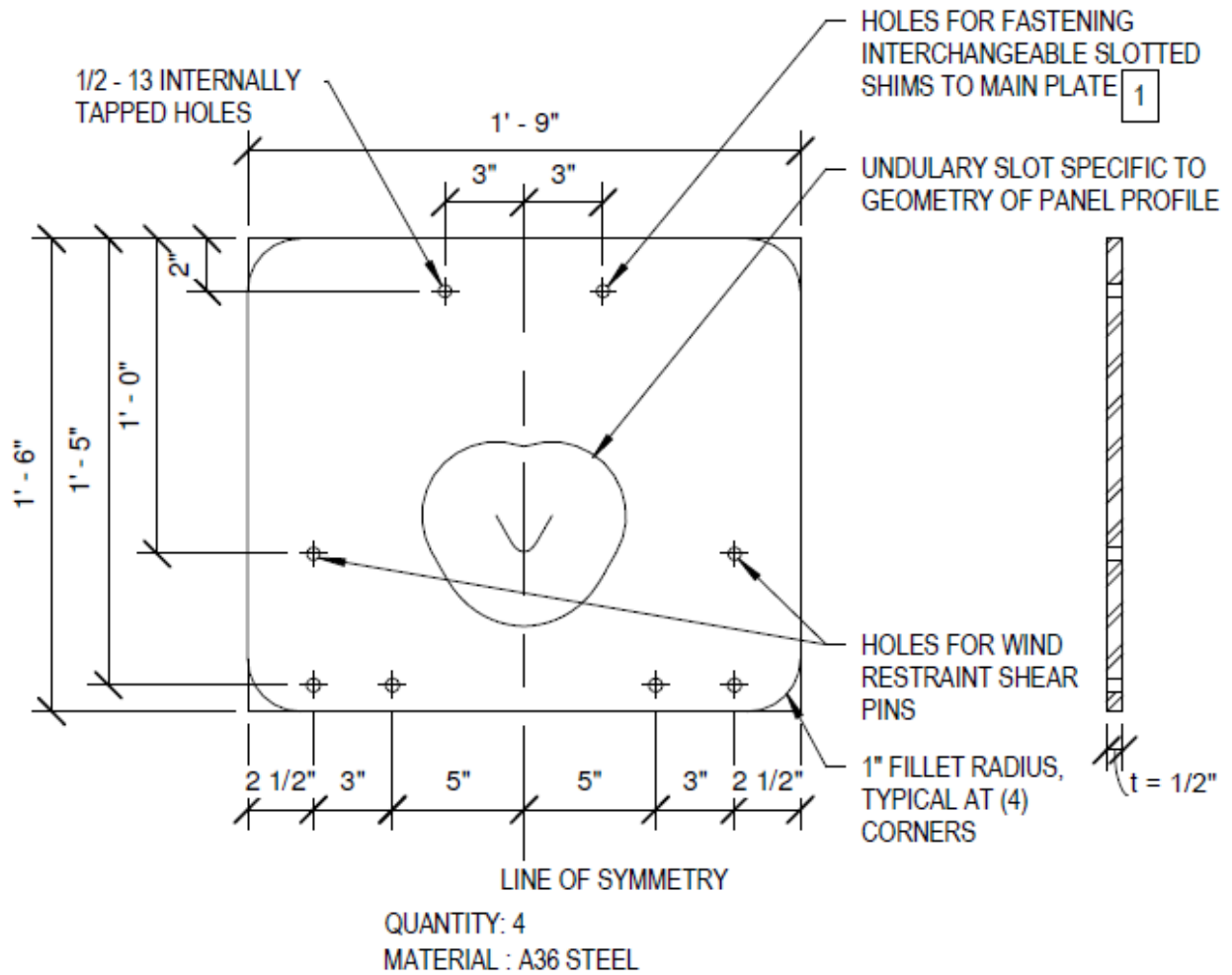


Figure 105. Slotted shim for ($e = 0.94$) panel

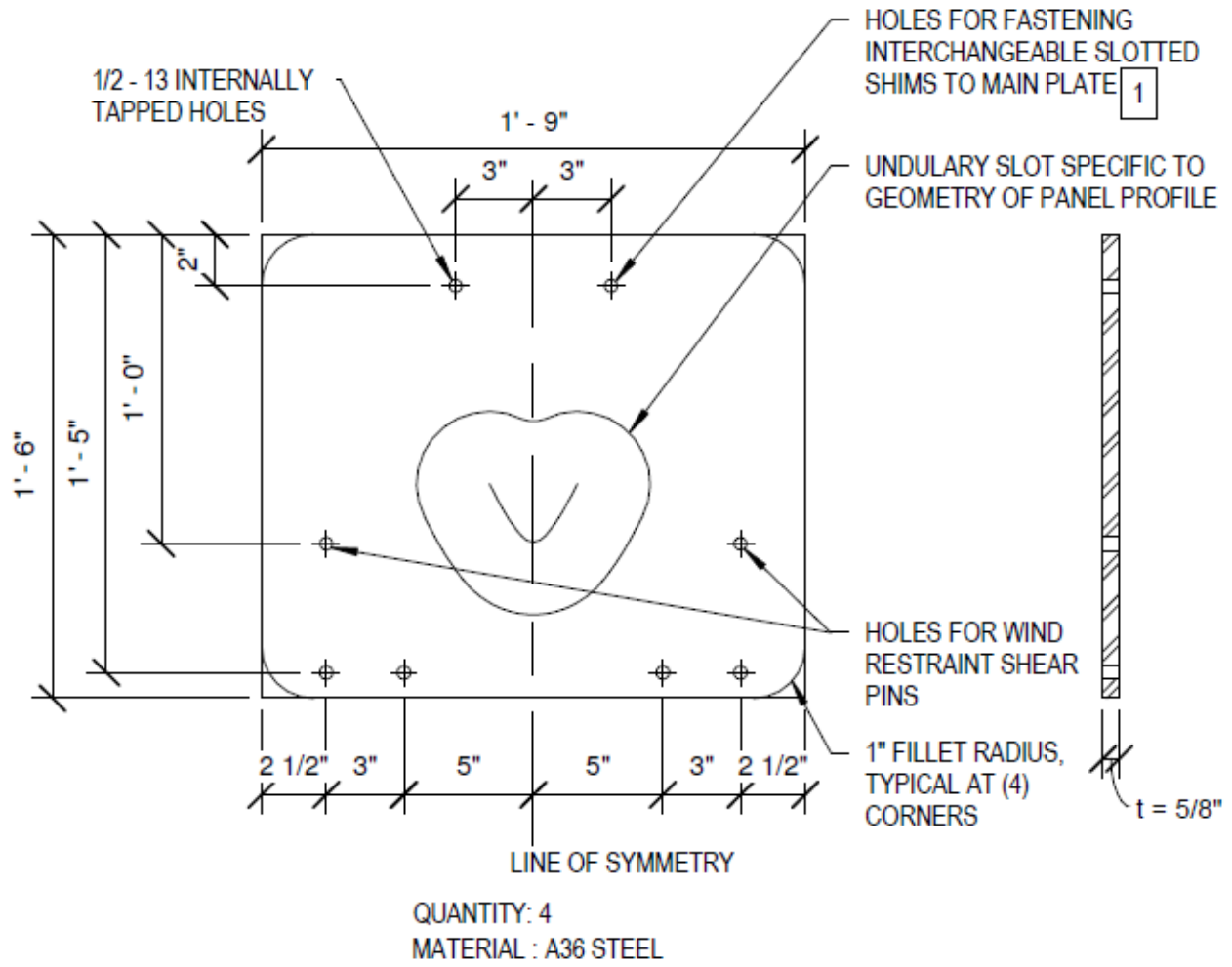


Figure 106. Slotted shim for ($e = 0.91$) panel

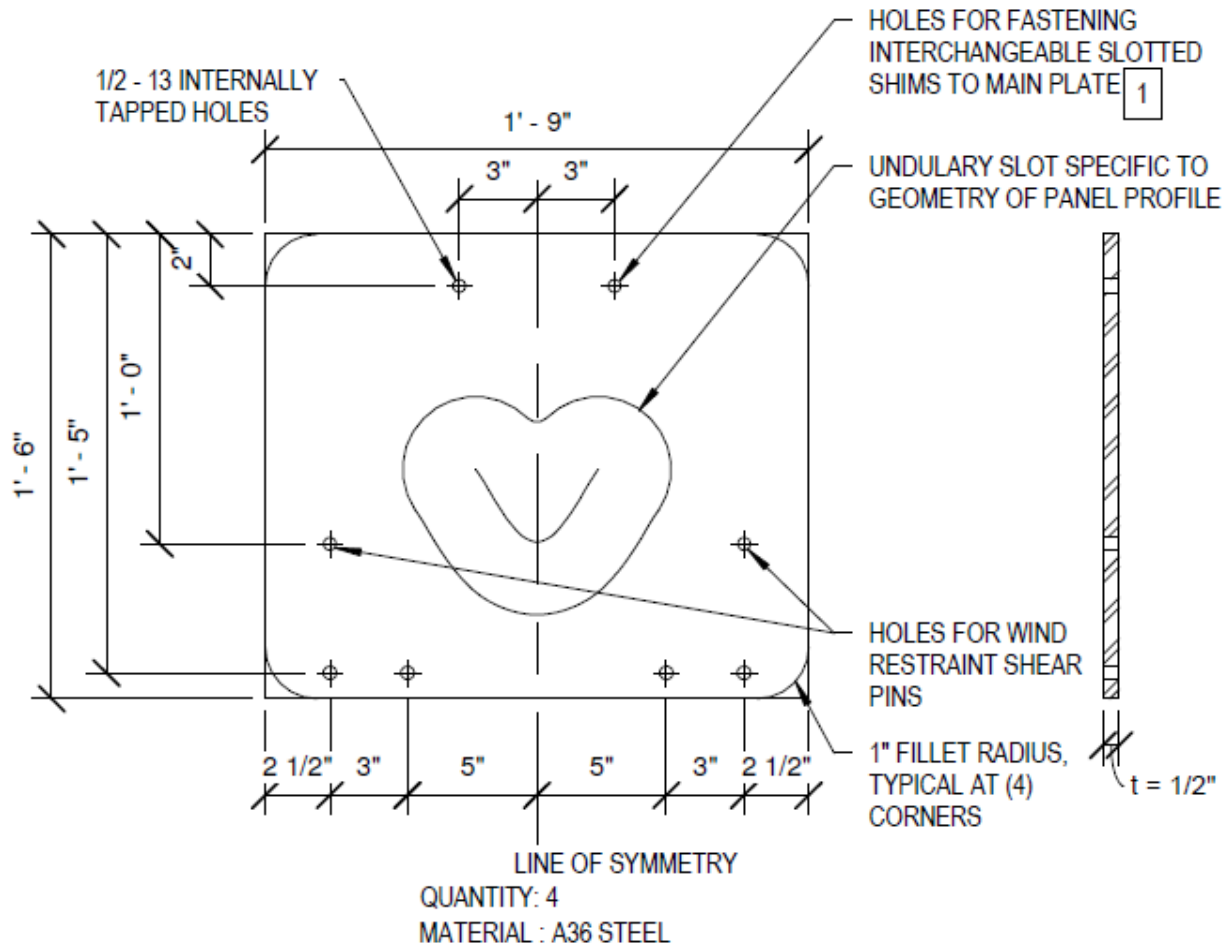


Figure 107. Slotted shim for ($e = 0.88$) panel

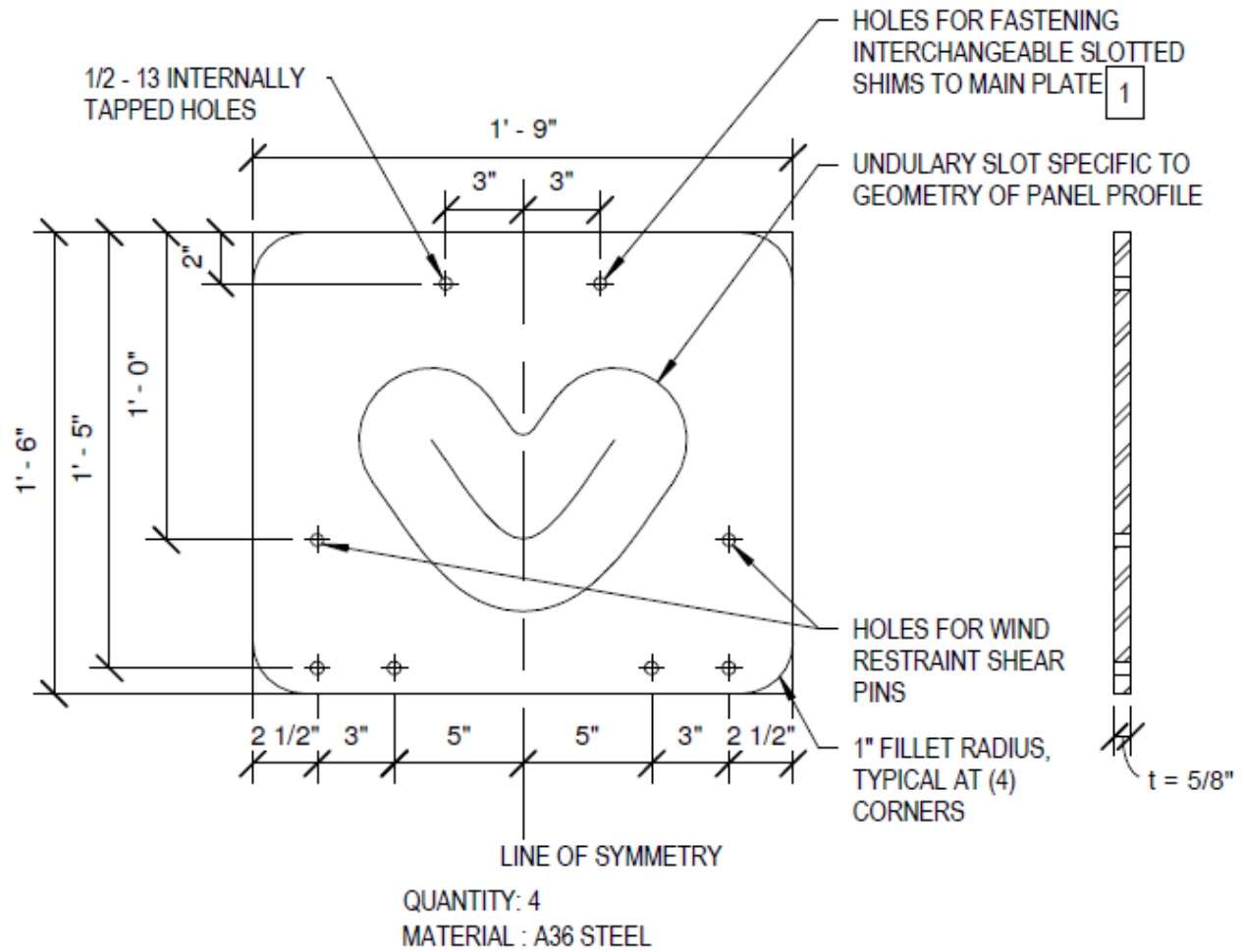


Figure 108. Slotted shim for ($e = 0.82$) panel

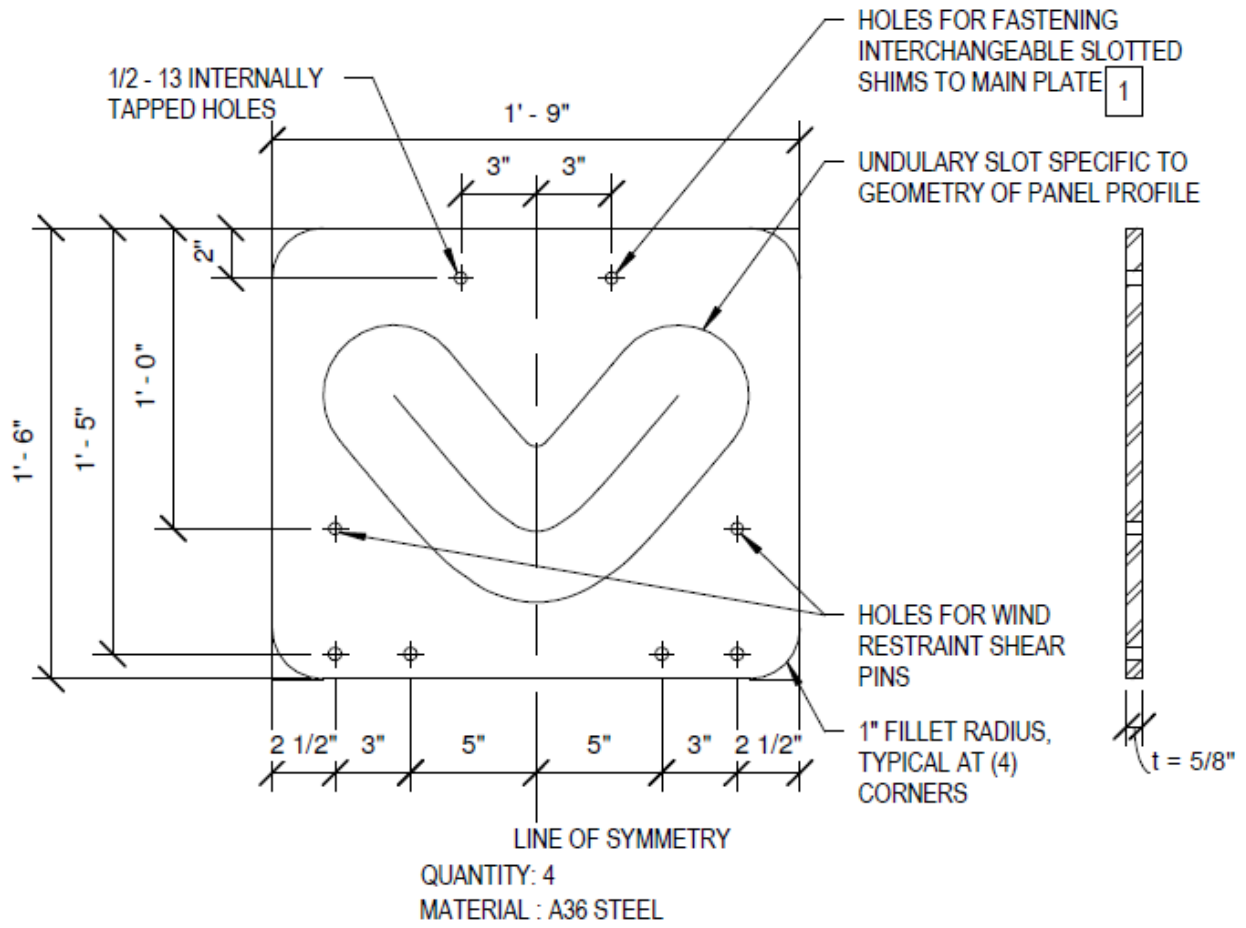


Figure 109. Slotted shim for ($e = 0.73$) panel

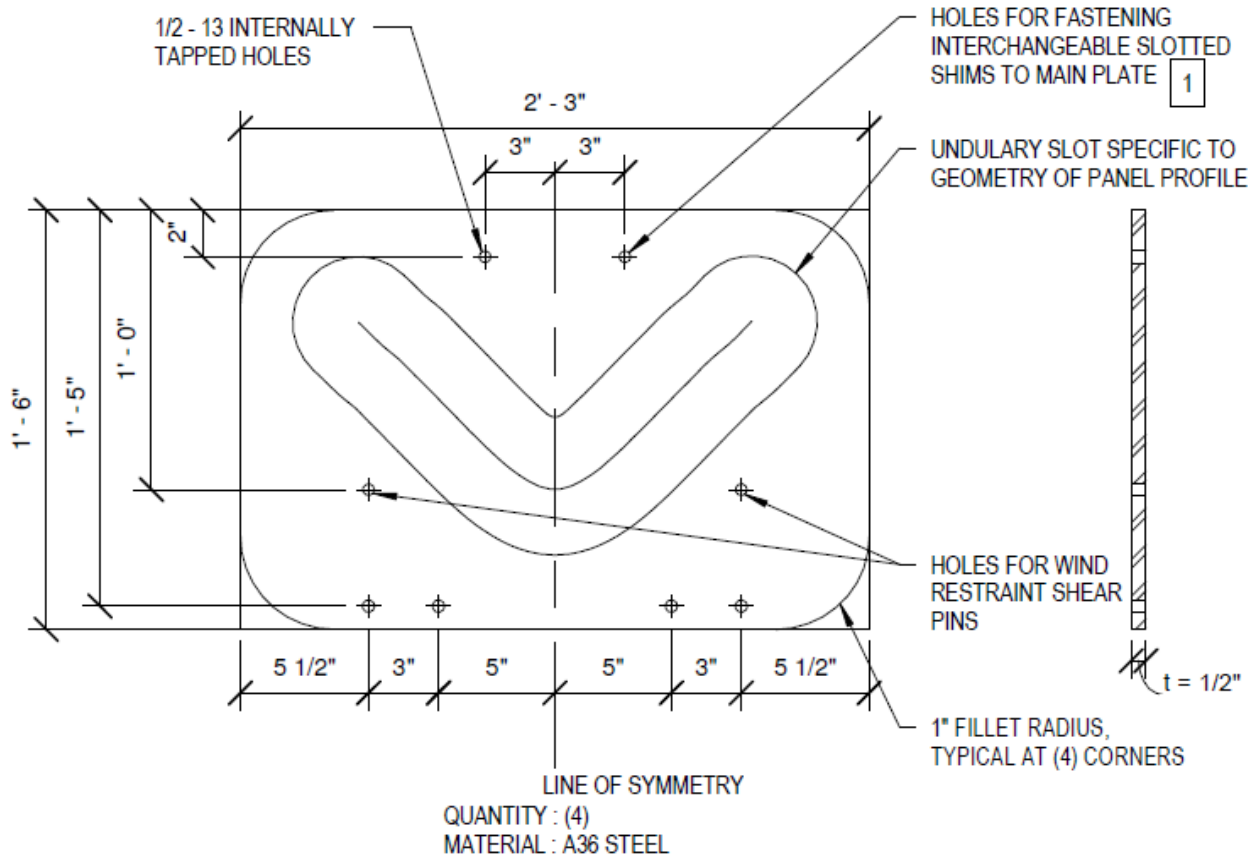


Figure 110. Slotted shim for ($e = 0.73$) panel

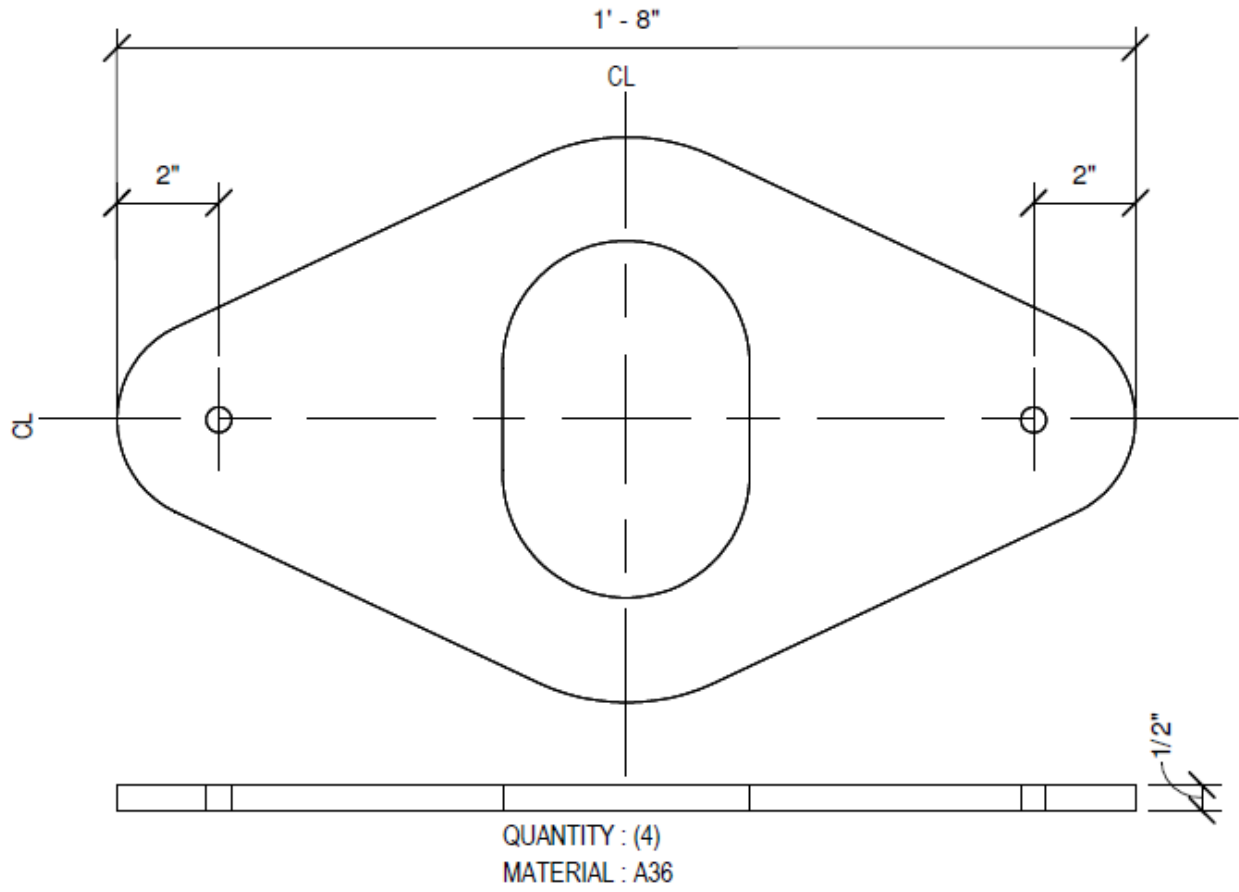
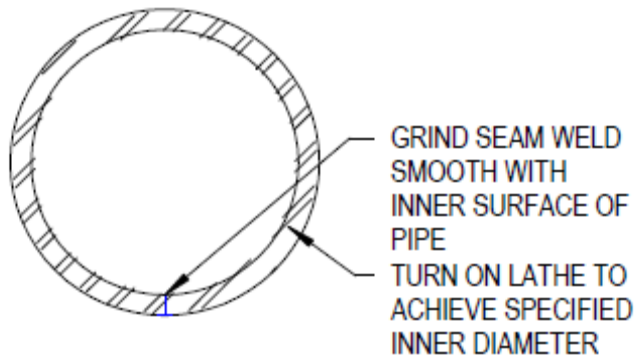
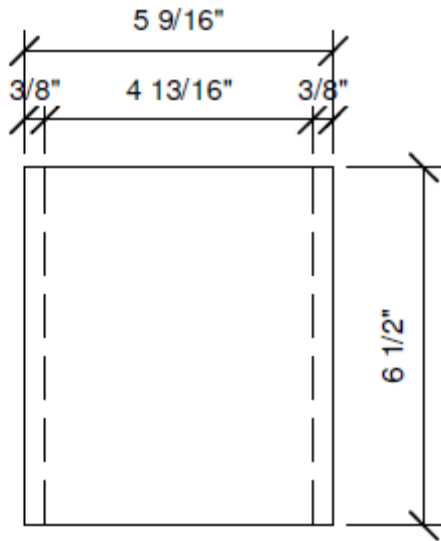


Figure 111. Wind restraint plate



QUANTITY : 12
MATERIAL : A53 GRADE B PIPE

Figure 112. Pipe bushing

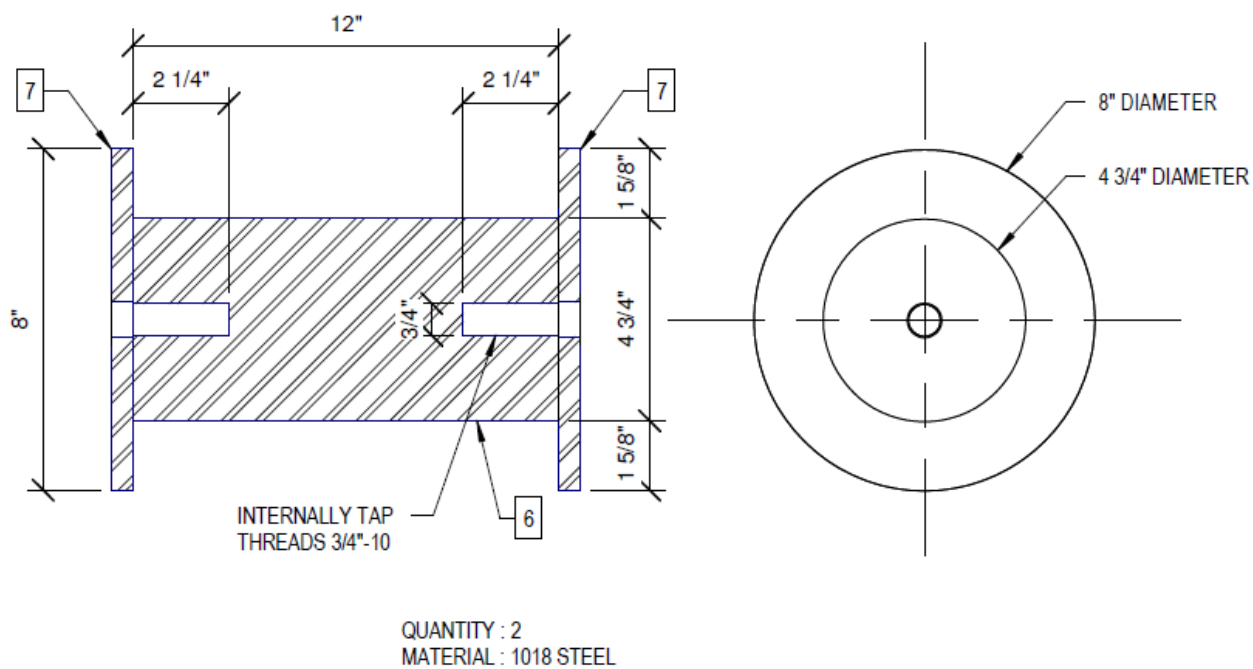
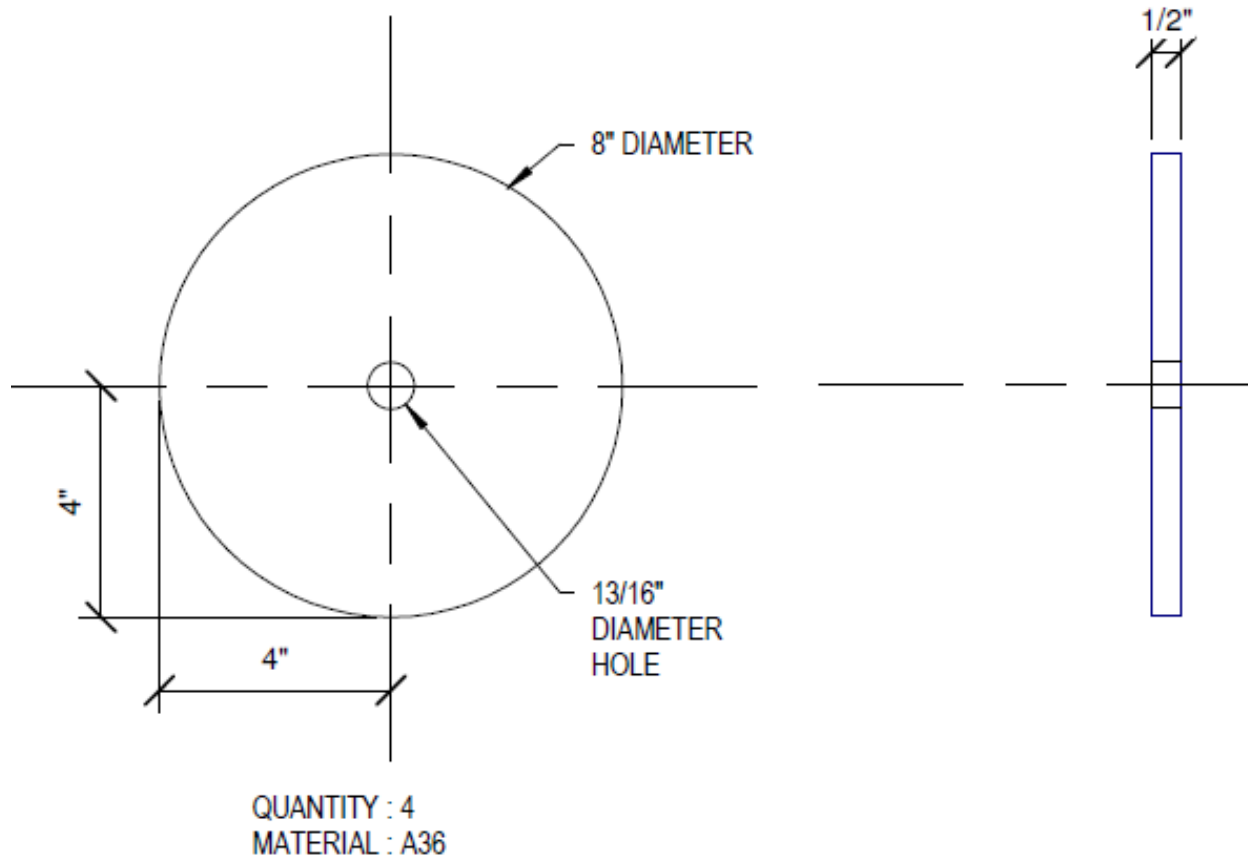


Figure 113. Pin and cap assembly

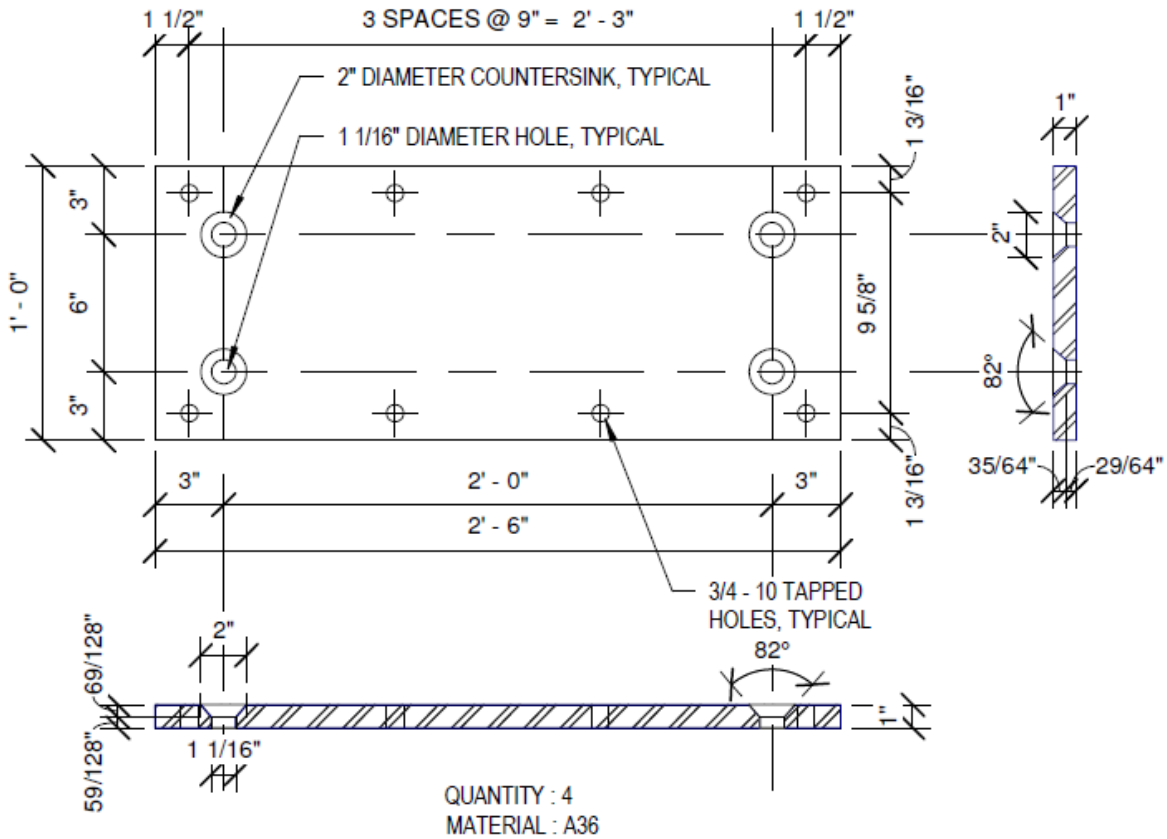


Figure 114. Track shim

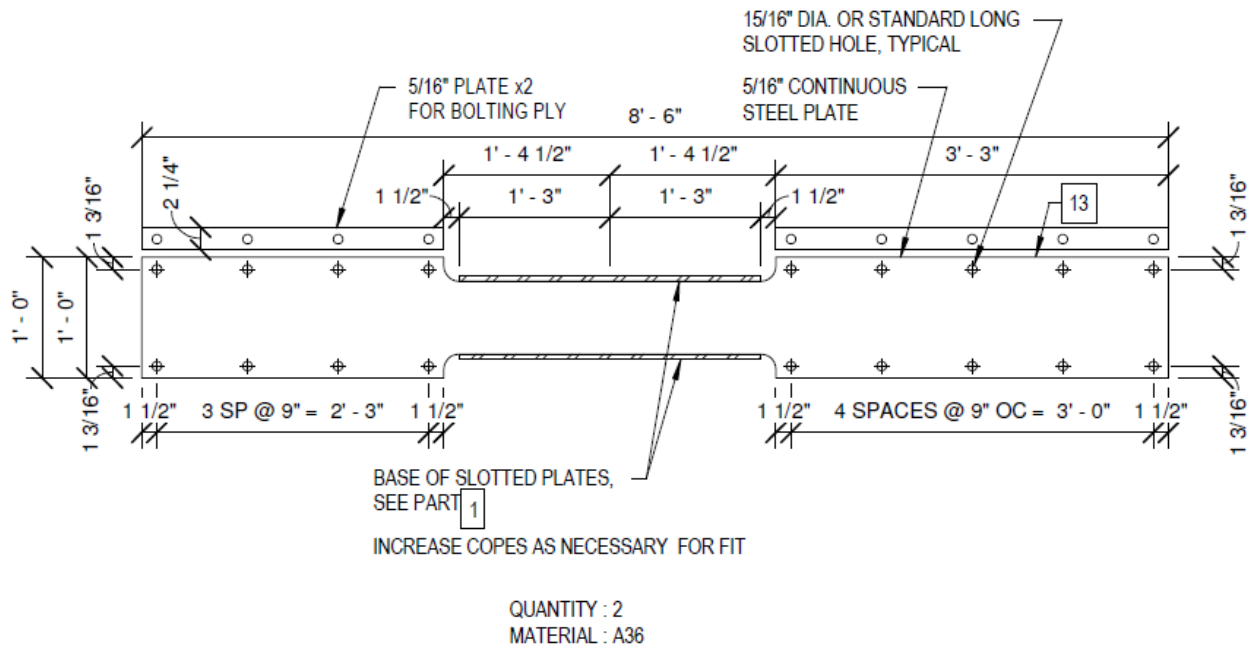


Figure 115. Continuous track surface

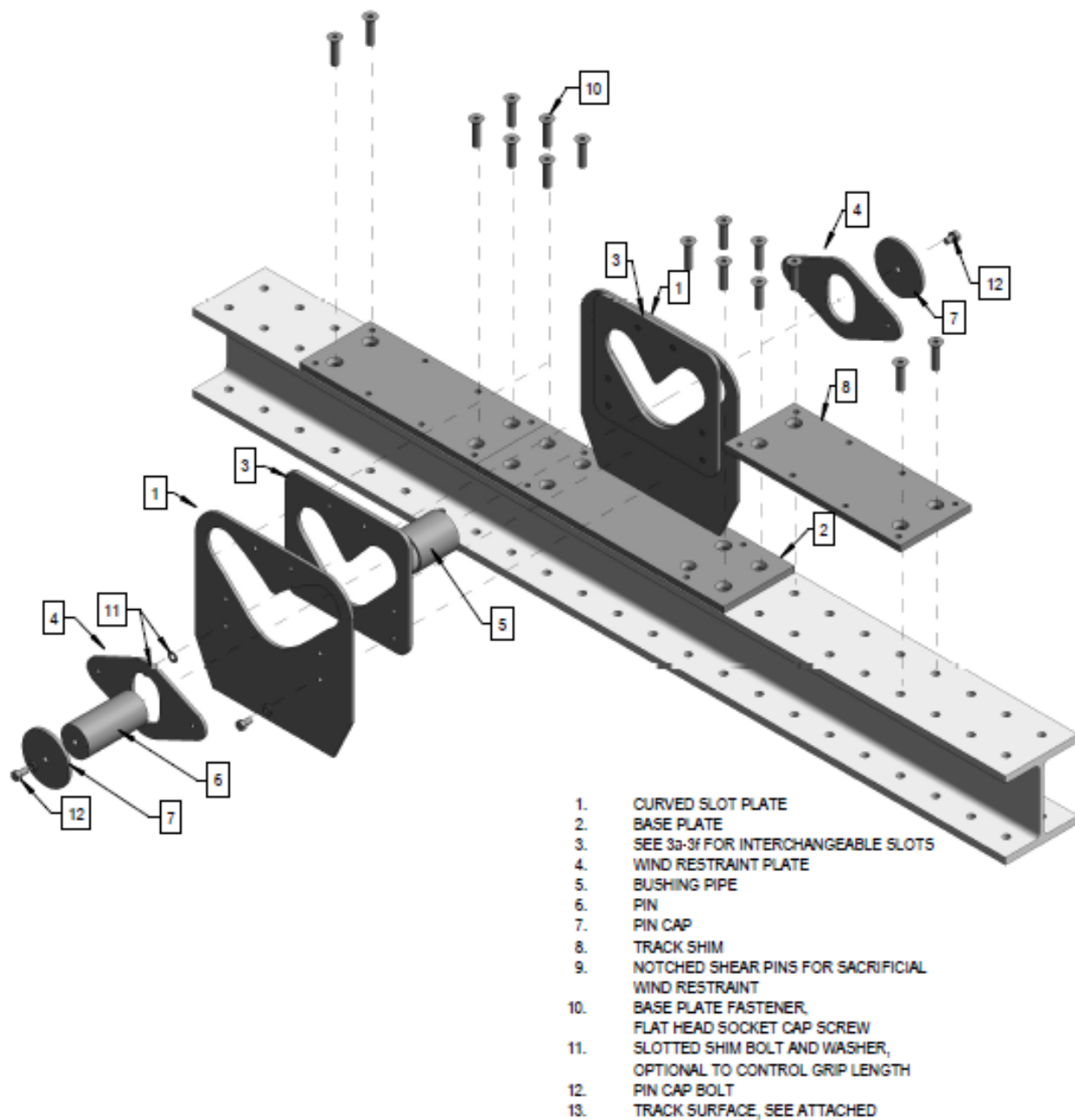


Figure 116. Exploded assembly list for No-Slip Traction Rolling steel connections

Appendix C: Precursory Characterizations of Timber-to-Steel Contact

An initial phase of study conducted in preparation of full wall testing addressed questions of force transfer including high-pressure timber-to-steel contact using Finite Element Analysis (FEA), piezoelectric pressure mapping, and Digital Image Correlation (DIC). Each method examined aspects of the orthotropic behavior intrinsic to both individual timber laminations and CLT panel layup. Collectively characterizing the contact zone, both through the thickness of the 5-ply CLT panel and from an elevation view on the panel face, visualized pressure or displacement distributions well enough to understand the mechanisms and proceed with full wall tests. The initial phase of study specifically investigated whether:

- Bearing pressure distributions along the CLT edge behaved as FEA predicted,
- Neoprene acted as a buffer between timber and steel, and
- CLT laminations could sustain quasi-statically applied pin forces up to 400 kN (90 kips) in regions concentrated around the pin.

The visualizations produced during this examination prompted some alterations to bearing and connection details, like omission of neoprene pads and reinforcement of steel slots. The visualizations, furthermore, informed the findings of *Observed Damage* in the ensuing full wall system tests.

Finite Element Analysis

The FEA rendering of Figure 117 (a) illustrates a static structural model of nearly 250,000 nodes and 65,000 elements developed in ANSYS Workbench (v. 17.1) software, as a precursor to laboratory tests. The plot of equivalent elastic strains, for the panel of 0.73 eccentricity, shows the contact zones and strain distribution within the main field of the panel. Eccentricity between

the ceiling and floor contact zones generate restoring moment, and approximately 1.5 m (5 ft) of the entire 2.44 m (8 ft) panel width appears effective in resisting axial compression in the main strain field. Figure 117 (b) provides a higher resolution plot of strains in the CLT panel by excluding steel components from view. Though the FEA model can analyze nonlinear behavior of steel, the beams and connection components operated primarily in the elastic range with minimal plasticity. Proof tests of the steel connections and behavior in the full-scale tests later confirmed assumptions of elastic behavior in the steel components.

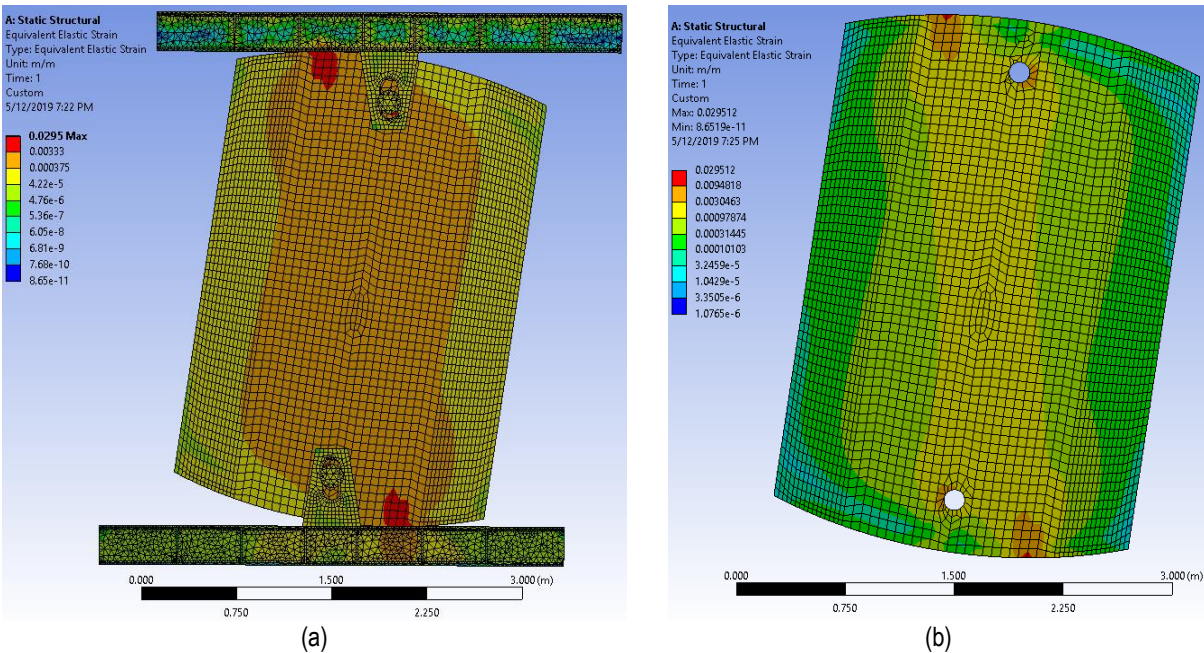


Figure 117. Equivalent elastic strain field of rotated 0.73 eccentricity panel (a) bounded by steel floor and ceiling beams and (b) viewing only CLT in elevation

Assumptions of elasticity in timber, however, proved less ascertainable. Timber deforms orthotropically and lacks the homogeneity, stiffness, and ductility of steel, so the project expected local damage in the CLT panel from high-pressure bearing contact. Extents of the contact zone damage, however, posed questions at the outset. The FEA model provided initial estimates of contact behavior by assembling a CLT panel with individual timber laminations as

shown in Figure 118. The FEA model assigned orthotropic material properties listed in Table 35 to each lamination with local axes. The modulus of elasticity in the longitudinal direction, parallel to grain, matches Table 1 and the modulus that NDS lists for Spruce-Pine-Fir (SPF) classification and No. 1/No. 2 grade (American Wood Council 2017). For more fundamental orthotropic properties, Table 35 references relationships and mechanical properties derived from testing dry (12% moisture content), clear and straight-grained subalpine fir specimens imported to the U.S. from Canada (Kretschmann 2012).

Table 35. Orthotropic elasticity of fir laminations input in FEA models

E_R		G_{LR}		G_{LT}		G_{RT}		μ_{LR}	μ_{LT}	μ_{TR}
(Mpa)	($\times 10^3$ psi)	(MPa)	($\times 10^3$ psi)	(MPa)	($\times 10^6$ psi)	(MPa)	($\times 10^3$ psi)			
887	143	609	98.0	505	81.2	52.2	8.40	0.341	0.332	0.336

E = elastic, Young's modulus

G = shear modulus

μ = Poisson's ratio

L = longitudinal to grain direction coincident with local x-axis of lamination

T = transverse to grain direction coincident with local y-axis of lamination

R = radial to grain direction coincident with local z-axis of lamination

Using laminations as a basic unit of FEA models enabled contact elements to replicate interactions between longitudinal and cross plies of boards. Capturing behavior of high-pressure bearing contact between steel and timber at the beam and pin interfaces required several types of contact pairs and at least two types of contact elements. *Fully bonded* contact elements replicated the face adhesion of cross and longitudinal laminations pictured in Figure 119. Between timber laminations, distinction between contact and target bodies bore little significance. At interfaces between dissimilar materials, however, the models identified steel as *target* and timber as *contact* bodies, because the software defaults to plotting results on the contact body surface. Figure 120 shows the contact and target body interface at elliptically profiled loadbearing edges of the CLT panel. Contact elements along CLT panel edges specified *Normal LaGrange* formulations to

establish conditions of no penetration between the nodes of the two contact bodies (ANSYS Inc. 2016).

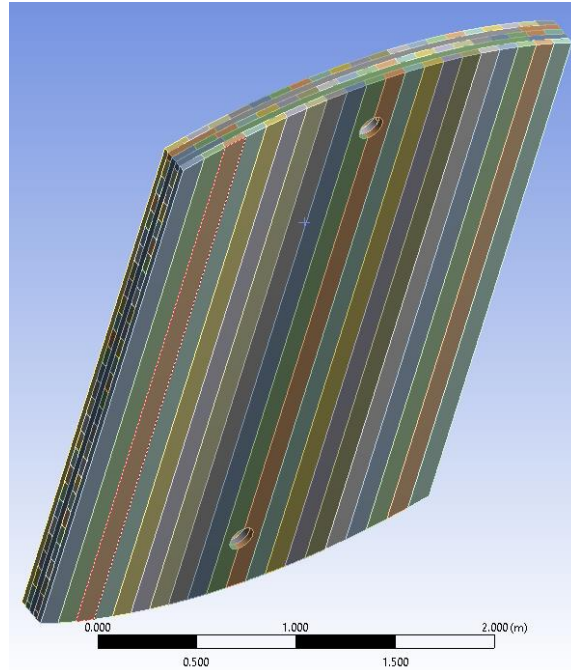


Figure 118. Geometric assembly of 5-ply CLT panel laminations in FEA model.

Because wood cannot penetrate steel, *Normal LaGrange* contact formulations theoretically matched actual material interfaces of this application. Zero-penetration constraints, however, added iterations to the computations, and solving FEA models of each panel distributed analyses across 16 computing processor cores and compiled results on a high-performance computing network (ANSYS Inc. 2016). Introducing further complexity to model damage within individual laminations and at fully bonded interfaces would require additional computing power to converge upon numerical solutions within a reasonable timeframe.

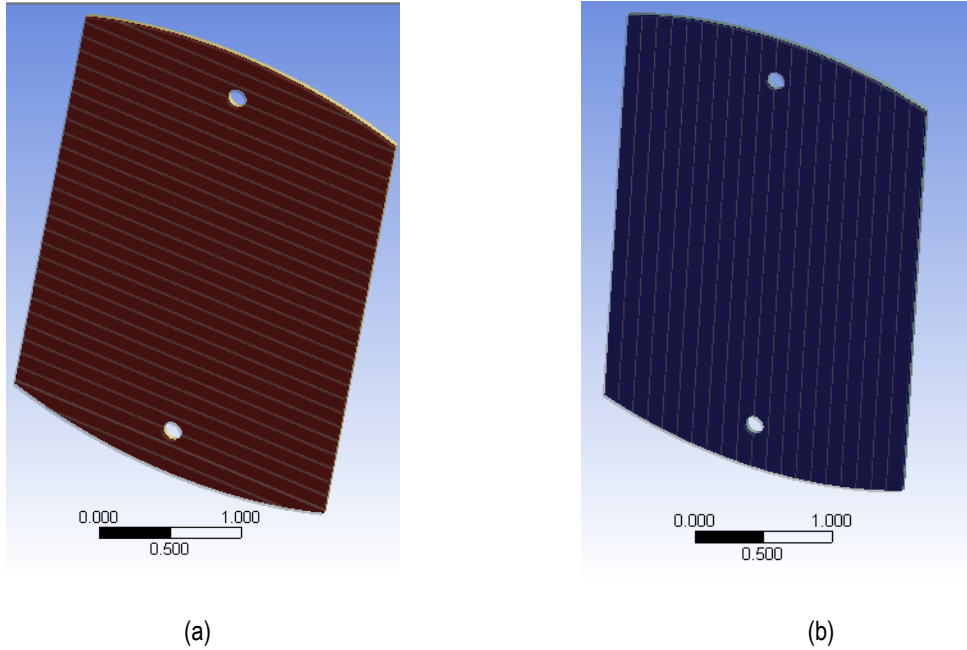


Figure 119. Laminations grouped as fully bonded (a) contact body and (b) target body of FEA model.

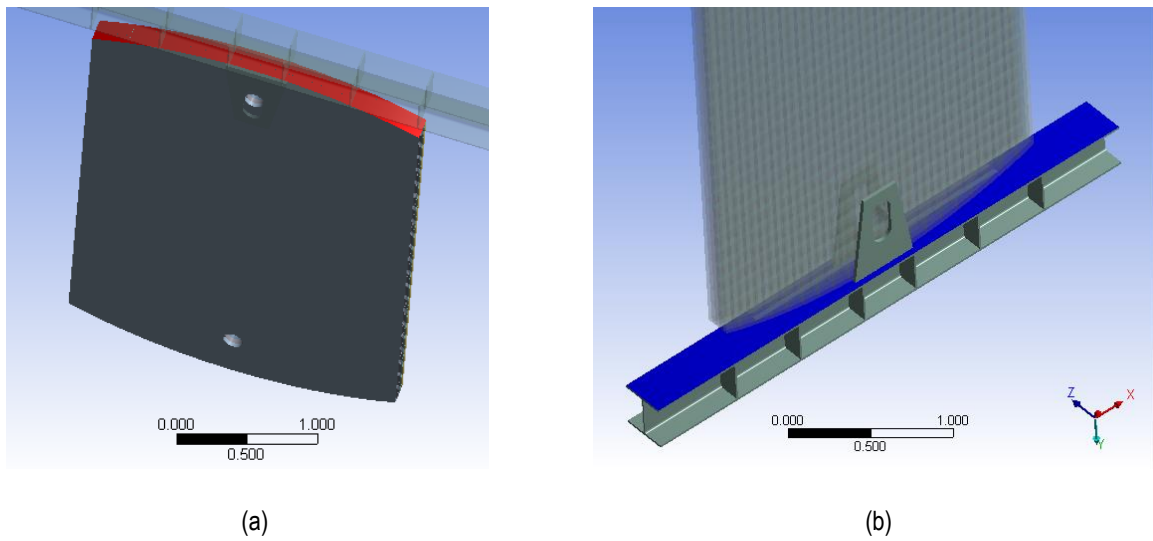


Figure 120. (a) CLT elliptically profiled edge contact and (b) beam flange target bodies of Normal LaGrange FEA

Along the loadbearing edge surfaces of the CLT panel, view (a) of Figure 121 identifies sliding as the primary contact condition and sticking near bonds between timber laminations. View (b) highlights regions of the arc that slid as much as 75 mm (3 in.) to achieve 432 mm (17 in.) of

lateral translational beam displacement. Figure 122 maps bearing contact pressures on timber in using two color-coded scales to describe the same contact region. The linear scale in view (a) shows only the longitudinal laminations bearing contact pressures. The logarithmic scale of view (b) provides higher resolution of bearing contact stresses across the 5-ply thickness, though pressures again accumulated almost exclusively in the longitudinal laminations. FEA estimated peak pressures of 43.1 MPa (6250 psi) in the middle lamination and 36.5 MPa (5300 psi) in face laminations but only 2.0 MPa (290 psi) in cross layers.

The peak stresses that FEA predicted exceeded the allowable design values of Table 1, even as stresses dissipated to 24 MPa (3500 psi) and 16 MPa (2400 psi) within the contact surface of the same lamination. Around the pin hole bushings, FEA predicted that cross laminations would bear most of the stress in end grain. Stresses around the pin bushings peaked within a range of 14 to 16 MPa (2000 to 2400 psi) for low frictional contact coefficients, generating frictional forces less than 10 percent of the normal force magnitude. Increasing the magnitude frictional contact proportionally amplified stresses around the pins. For frictional sliding coefficients up to 0.3, panels the numerical models reported stresses and strains that panels could generally tolerate if contained within the localized contact zones. Precursory computations, however, included neither fiber damage models nor subsequent dynamic impacts of stick-slip friction.

Despite the uncertainty of friction and computational limits of FEA, the results produced key takeaways. First, the models show only longitudinal laminations effective in transferring compression bearing contact forces. Second, the three longitudinal plies of a 5-ply panel do not share concentric axial loads equally, because cross layers enabled the middle lamella to carry more of the overburden by confining both faces of the interior laminations. Because face laminations contact cross layers only on one side, stresses favor the confinement near the bond

line and diminish at the free and visible panel faces. Despite lacking direct participation in compression bearing transfer, cross layers therefore proved useful in confining and increasing capacity of primary axial load carrying laminations. Figure 123 furthermore shows the middle cross plies sustained most of the story shear forces delivered by the pin connections.

Advancing the FEA models to simulate the damage observed during testing would require a number of enhancements. Adding toughness properties and modes of fracture to individual laminations could replicate some of the fiber splitting and crushing behavior. Refined friction estimates, based on the laboratory data, could improve accuracy of the force estimates. Fracture toughness of the CLT adhesives, however, presents a research gap that limits current application. Despite practical limits on the accuracy, FEA models visualized the effects of orthotropic behavior to help explain why longitudinal laminations sustained the brunt of damage.

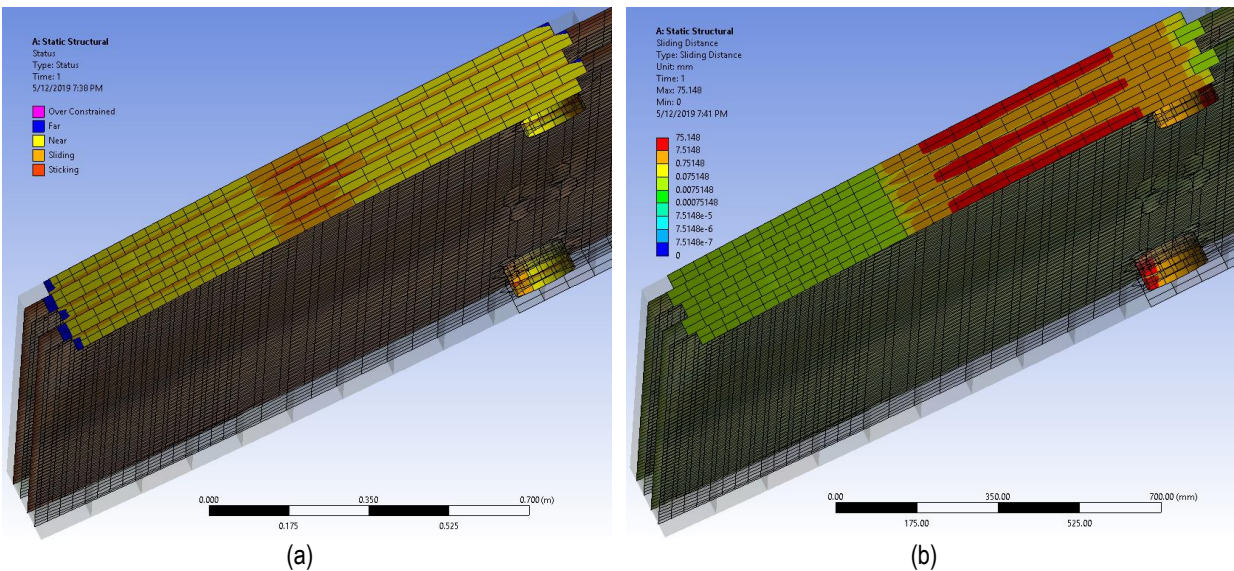


Figure 121. Results of Normal LaGrange contact FEA model showing (a) contact status and (b) sliding along arc.

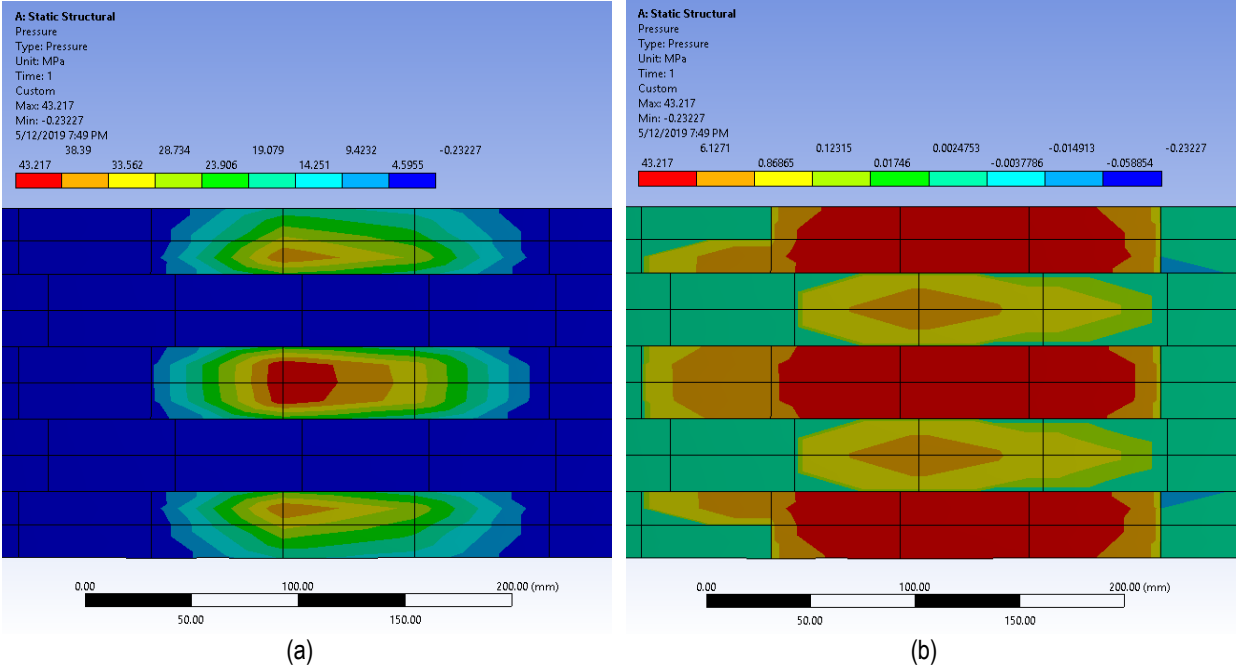


Figure 122. Bearing contact stress distribution at curved edge of CLT plotted on (a) linear and (b) log color scales.

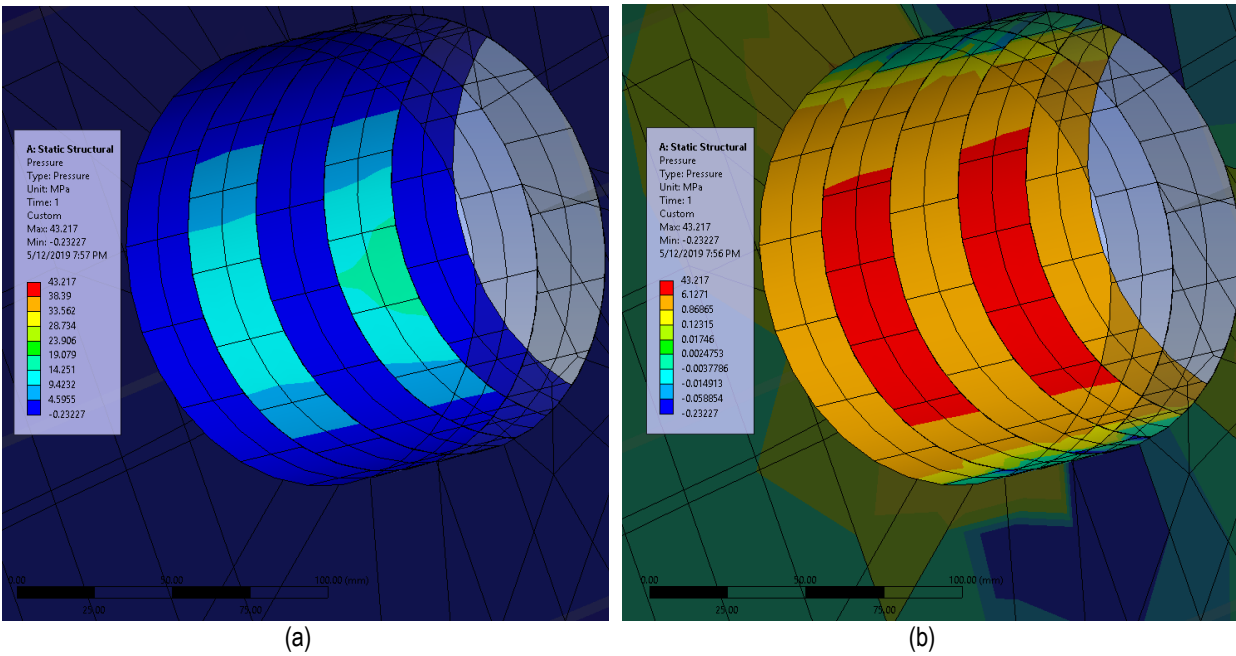


Figure 123. Bearing contact stress distribution at hole in CLT plotted on (a) linear and (b) log color scales.

Piezoelectric Pressure Mapping

Pressure mapping verified the orthotropic behavior, rendered by the FEA models, with laboratory tests. Researchers have used piezoelectric film sensors for a variety of applications that require detailed resolution of the contact area and sensitivity to various materials under pressures that range from low to high orders of magnitude (Tekscan 2018). Over the last decade, biomechanical researchers have increasingly used Tekscan piezoelectric pressure mapping systems to characterize contact interfaces within joints, mainly because film sensors maintain low profiles, flex to conform with contact surfaces, and map pressures in real-time during laboratory tests (Bachus et al. 2006). For civil engineering applications, geotechnical researchers have measured soil pressures acting on buried pipelines and other structures with Tekscan tactile sensors (Abdoun et al. 2009). Though less explored as a measurement system for interfaces between structural building materials, Tekscan sensors therefore demonstrated the versatility to map contact bearing area between timber and steel.

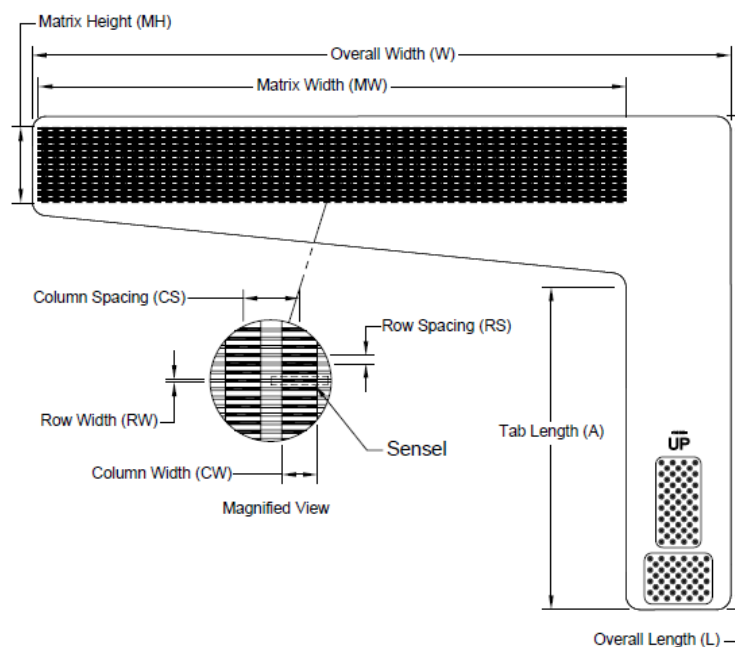


Figure 124. Pressure mapping film sensor, model 6300 by Tekscan
Source: (Tekscan 2017)

Figure 124 illustrates layout of an individual piezoelectric sensor model selected for this project (Tekscan 2017). Pressure range and sensing area primarily drove the selection criteria. For the 6300-model, sensing matrix height of 33.5 mm (1.32 in.) matched the width of CLT laminations, and the matrix width of 264.2 mm (10.40 in.) provided ample length to capture the contact zones of most curved panel edges. The 6300-model sensor, furthermore, offered adjustment to capture either a peak range of 6895 kPa (1000 psi) or 68.95 MPa (10,000 psi). The 6300-model sensor housed circuitry printed on transparent plastic films and an array of piezoelectric material adhesively laminated within a dielectrically separated assembly of layers. Compressing the “sensors” of Figure 124 generated and delivered piezoelectricity to the dots shown at the bottom of the sensor tab. A handle, pictured in Figure 125 (a), clamped the sensor tab with a pin layout matching the dots to read digital inputs of each grid point for software to interpret and graph electrical signal intensity.

Figure 125 (b) photographs the 5-sensor arrangement that captured laboratory pressure readings. Sensors overlapped to stack the sensing arrays so that each could read a layer of the 5-ply CLT. To compensate for the overlaps, laser-cut plastic film shims filled low points of the arrangement to even the contact surface and prevent artificial spikes in pressure at the sensor seams. Low-tack adhesive mounted the sensor arrangement to a Blanchard-ground steel plate. Though not representative of a hot-rolled structural steel surface, the smooth plate pictured in Figure 125 (b) prevented local asperities from puncturing the sensors and enabled transfer between the sensor calibration setup of Figure 125 (a) and the larger scale test apparatus of Figure 126. Because measuring the contact area involved multiple sensors, calibrations added extra steps to the measurement process. The custom CLT fixture of Figure 125 (a), shaped to an elliptical arc and

narrowed to one lamella width, reproduced contact conditions for individual calibrations of the sensors.

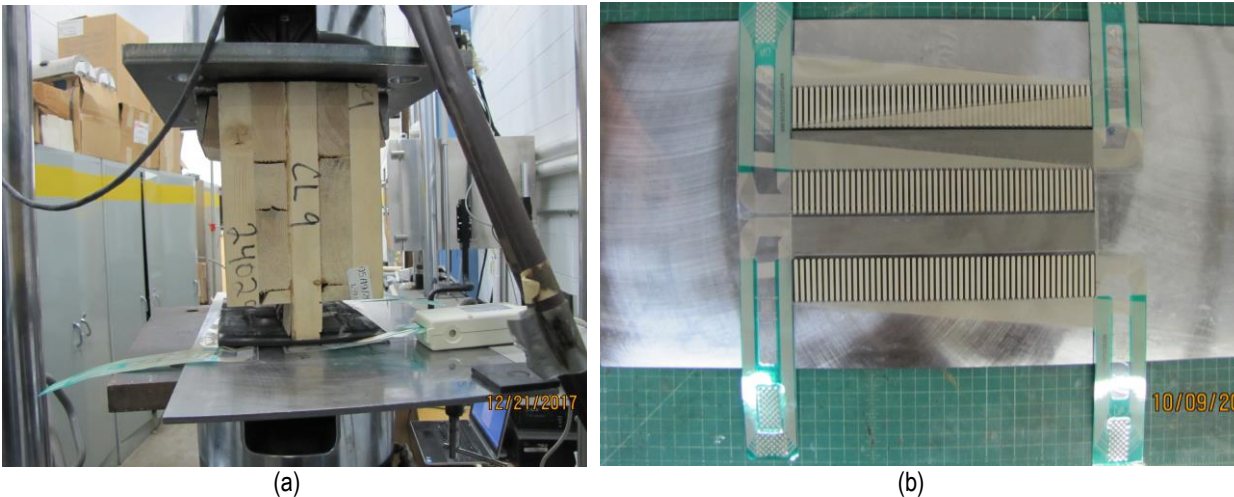


Figure 125. Piezoelectric pressure mapping (a) calibration and (b) sensor layout.

Figure 126 photographs a laboratory test of a 5-ply CLT specimen that measured 1.22 m (4 ft) square in a horizontally mounted configuration parallel to the floor. The CLT panel denoted by (a) sustained quasi-static loads at full-scale. By design, this preparatory test used truncated versions of full elliptical panels to isolate regions of critical bearing contact. C-clamps (b) affixed the 5-sensor assembly of Figure 125 (b) between the rigid steel wideflange beam and CLT panel. Two steel C15 × 40 channels sandwiched the CLT panel, top (c) and bottom, and delivered up to 400 kN (90 kips) of compression bearing on pin (d). Symmetrically placed actuators (e) initiated loading through the moveable wideflange near the top of the photo, while actuator (f) performed no work but monitored incidental loads and prevented instability transverse to the main loading direction. Additional steel bracing provided redundant precaution but never significantly contacted panel specimens. DIC hardware, mounted overhead with an adjustable swivel and extruded aluminum bar (g), aimed LED lights (h) and cameras (i) so that

surface displacements near the pin and edge contact regions could be measured simultaneously to the pressure map through panel thickness.

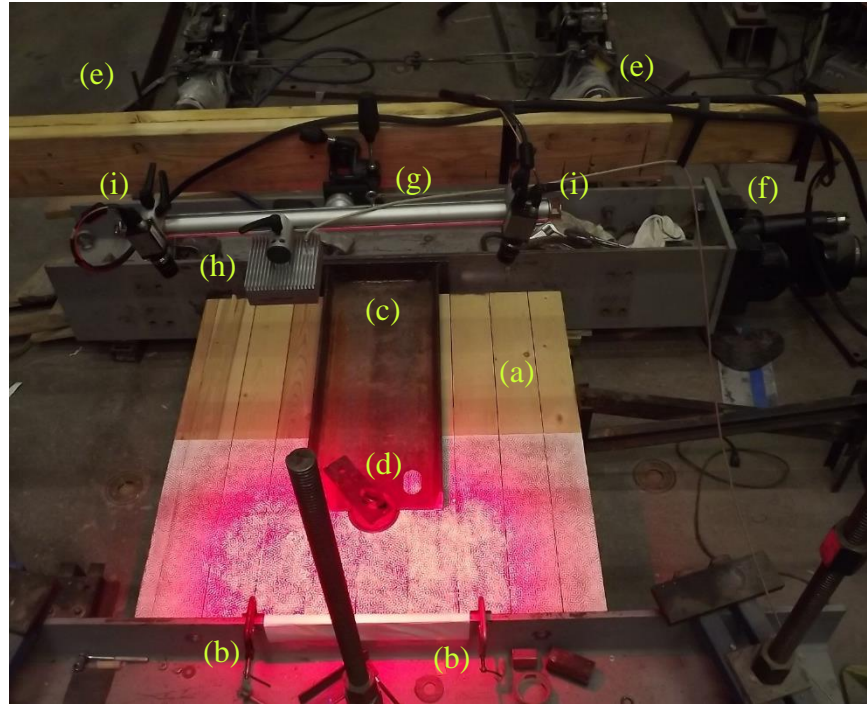


Figure 126. Precursory laboratory test of truncated panel with piezoelectric pressure mapping and DIC sensors

Face plates of Figures 28 and 29 would conceal the illuminated region of timber pictured in Figure 126, and story shear of the complete lateral load-displacement tests would damage the piezoelectric film sensors. The precursory test setup therefore presented a unique opportunity for insight into the compression bearing characteristics of CLT. Figure 127 arranges pressure maps of the 5-sensor assembly into a composite view. The middle ply sustained 201 kN (45 kips) or 47% of the cumulative axial load measured by the sensors. The face plies registered 103 kN (23 kips) and 112 kN (25 kips) or respectively 24% and 26% of the cumulative axial load measured by the sensors. Cross-laminations accounted for only 2.9 kN (0.65 kips) and 11 kN (2.5 kips) or respectively less than 1% and 2.5% of the cumulative axial load measured by the sensors. Actual

pressure readings of the piezoelectric film sensors graphed by Figure 127, therefore, generally support the FEA results given by Figure 122. The cross-layers of both images provide evidence of virtually zero compression bearing contact stress. The piezoelectric sensors, however, revealed an additional detail of the orthotropic CLT layup. Both cross plies projected curvature onto the sensors. Bond lines enforced displacement compatibility between longitudinal and cross layers, but differential shrinkage caused the cross plies to curve as Figure 128 illustrates. Figure 128 (a) simplifies the pressure distribution of Figure 127. Loading the 5-sensor assembly concentrically required normal contact between the CLT panel edge and Blanchard-ground plate. Adjustable floor jacks leveled the horizontal plane and supported the CLT on ball transfers. Non-shrink grout between the rigid wideflange beam pictured near the bottom of Figure 126 and Blanchard-ground plate leveled the vertical bearing plane. Common imperfections, however, make combinations of (a) and (b) pressure distributions of Figure 128 the likeliest loadbearing scenario, so stress-relieving chamfers were eventually added to the full-scale trials to improve out-of-plane tolerance.

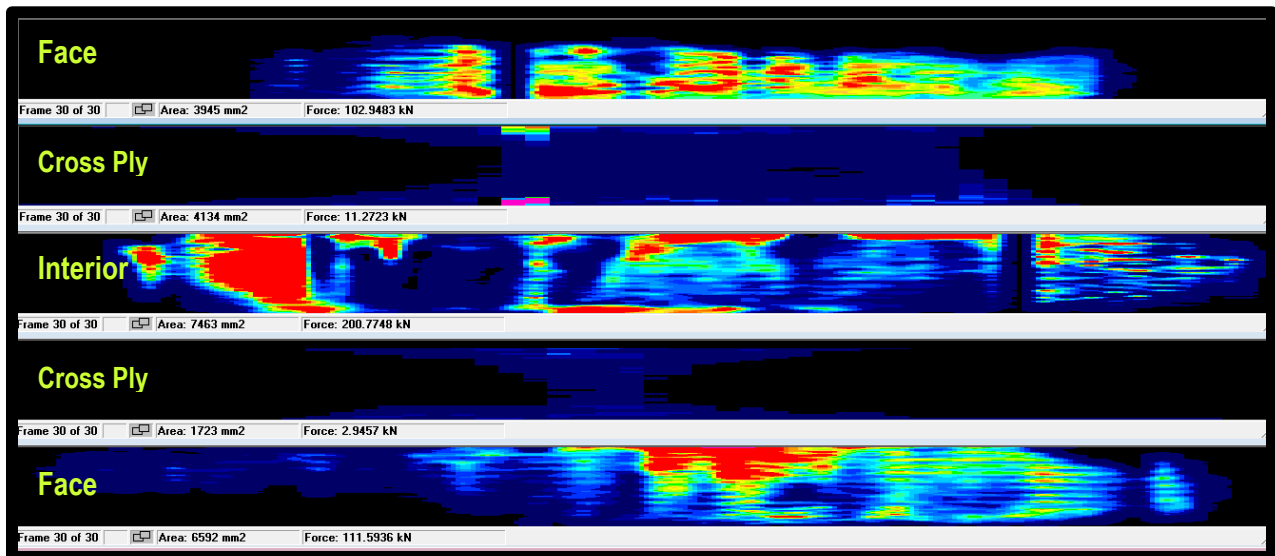


Figure 127. Contact bearing pressure map along 5-Ply CLT panel edge measured by piezoelectric sensors

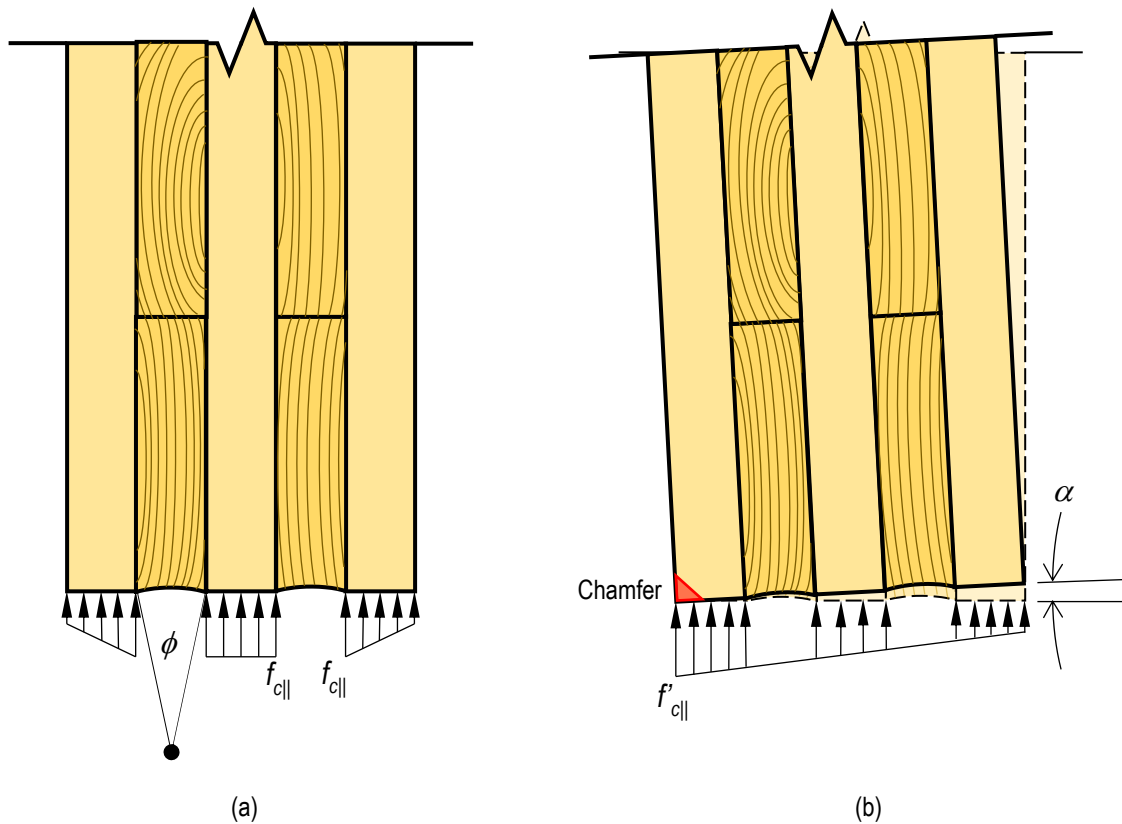


Figure 128. Simplified contact pressure distribution of 5-ply CLT panel edge (a) concentrically loaded and (b) out-of-plumb.
Internal wall forces not shown for clarity

Though the piezoelectric tactile sensors led to important insights, extrapolating quality data from additional trials was limited by several factors. Sensor creep made force calibration difficult, so calibrating took place immediately after sensors sustained the loads of the larger scale tests. Sensor calibration methods, furthermore, can vary. The project trials followed manufacturer recommendations using power law formulas fit to multiple points, but some suggest alternative methods of calibration for enhanced accuracy and repeatability (Brimacombe et al. 2008). Sensor calibration and alignment errors accumulated to an overall value of 7% for the results plotted by Figure 127. Single pressure film sensors capable of capturing the entire contact area would improve both force-calibration accuracy and error tracking but at significantly more investment in the sensors.

Fragility under shear limits usefulness of the piezoelectric tactile film sensors strictly to mapping normal compression pressures. Some applications overlay protective films and propose corrective calculations to manage minute shear forces on the sensors (Wilharm et al. 2013). Application of larger in-plane forces on the films, however, typically damages the intricate circuitry. The test configuration of Figure 126 intended to answer whether timber should be placed in direct contact with steel or on an intermediate neoprene pad that would enhance frictional traction for *No-Slip Traction Rolling*. Though vertical deformation of the neoprene proved small, accompanying lateral spreading significantly altered bearing conditions. At first glance, lateral spreading of the neoprene produced visually indiscernible effects on CLT, but tactile film sensors and the calibration fixture of Figure 125 (a) sustained irreparable damage only after neoprene entered the contact bearing interface. Though bearing on neoprene would have enhanced traction, lateral spreading risked damaging CLT laminations with out-of-plane prying.

Digital Image Correlation

Digital Image Correlation (DIC), in both precursory and ensuing full wall test phases, supplemented the visualizations achieved by FEA and pressure mapping with analysis of displacements on the faces of CLT panels. Though DIC analyzes only visible surfaces objects, image correlations have either surpassed or supplanted traditional sensor measurements in many engineering applications, because DIC requires no physical contact with specimens (Sutton 2009). DIC, furthermore, has captured broader fields of view than typically practical with traditional sensors, such as LVDTs and strain gauges (Lee et al. 2012). Because camera sensors cannot alter rocking behavior, DIC suited the highly deformable walls of this project. The capability for DIC to report full-field displacements, moreover, visualized trends of material

elasticity in the contact zones possible despite inherent local defects and orthotropic effects intrinsic to timber.

DIC Objectives

For precursory tests, DIC primarily measured timber displacements near contact of the pin connection and edge bearing. Results of the DIC measurements helped determine whether CLT should bear directly on steel or on an intermediary neoprene pad. Contact between neoprene and wood had produced high frictional coefficients, according to previous experiments performed with lightly loaded blocks (Murase 1984). Neoprene therefore promised improved traction that could help safeguard rolling against slip. Whether the contact mechanism could be scaled to the magnitude of structural building forces, however, remained uncertain. The test setup of Figure 126 minimized lateral shear transfer at the contact zone. Although neoprene was introduced to prevent lateral slip, loading primarily tested quasi-static normal bearing contact. Timber was expected to behave elastically during the precursory test, and comparisons of initial and final images, taken before loading and after unloading, served to verify that no significant damage had occurred.

DIC Methodology

DIC apparatus collected images using high-speed, 5-megapixel, grayscale cameras configured to *Q-400 DIC Standard 3D* systems distributed commercially (Dantech Dynamics 2018). For precursory tests, the DIC data acquisition module translated force and displacement from actuator signals and collected images with manually triggered snapshots at load increments of 6.67 kN (1.5 kips). Ensuing full wall tests synchronized the start of data collection with the actuator system and automatically collected images every 2 to 4 seconds depending on duration of the cyclic procedures. Calibration of the DIC cameras used planar targets and algorithms

developed by Dantec Dynamics, based on established procedures (Zhang 2000). A high-contrast target of 35-mm squares sufficiently defined a volume of space large enough to capture displacements around the pin and edge bearing contacts, pictured by Figure 126 for the precursory tests. The full rocking wall test calibrated relative camera positions with a larger target of 70-mm squares, to establish larger volumes for capturing displacements.

For acceptable accuracy in correlating images, DIC systems typically recommend high-contrast and random patterns of distinguishable points (Pan et al. 2008). Density, contrast, and size of points within patterns can factor into the accuracy of correlations, and adhesion of the pattern to the material surface can further influence correlation accuracy (Gao et al. 2016). Before collecting DIC data, therefore, Figure 129 examined two methods of applying speckle patterns over an acrylic latex base coat of low-luster white paint. One method applied black dots over the white substrate using a self-inking stencil roller made by Rollagraph. The other method speckled the white base coat using black Montana Granit Effect spray paint. Side-by-side comparison of errors reported by correlations of still images show the roller pattern produced narrower distributions of error, though both paint patterns proved acceptable. Speckling CLT specimens therefore proceeded with rolled dots. Spray paint, however, proved easier to apply over steel connections.

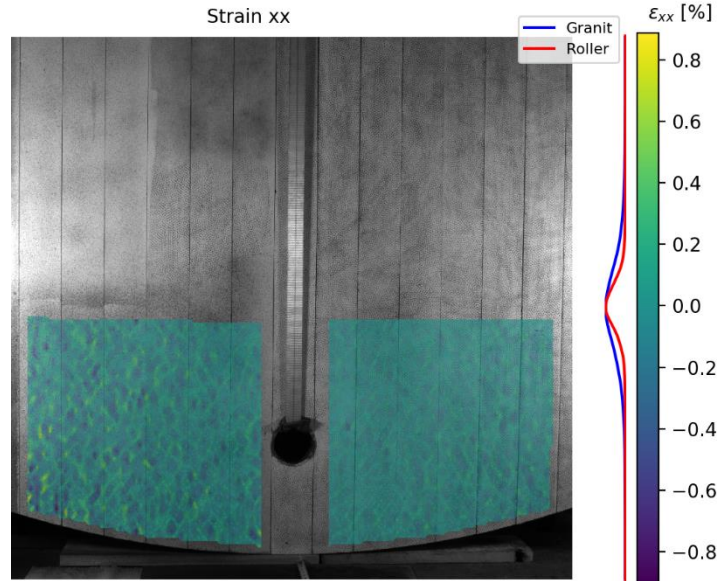


Figure 129. DIC speckle pattern comparison
Graph by Nathan Bechle

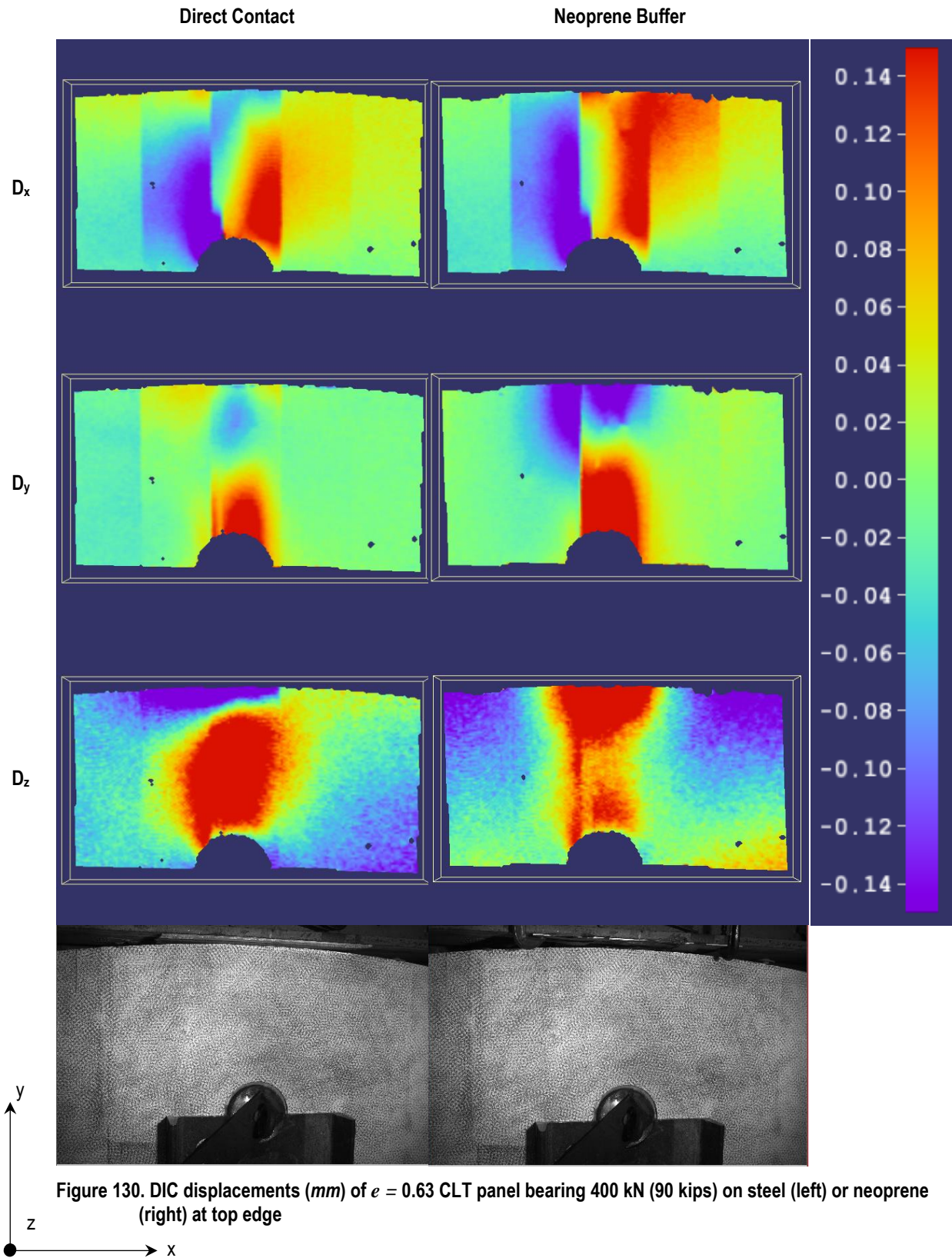
Precursory tests of five CLT panels, placed both in direct contact with steel and on an intermediary 70-durometer neoprene pad, involved a pair of DIC cameras illuminated by an array of LEDs as shown in Figure 126. A dozen setups, of six full wall panels tested in two connection configurations, involved two pairs of DIC cameras and LED illumination set on the scaffold pictured by Figure 31. The scaffold placed cameras in position to capture images where the rocking system would move least. The test apparatus of Figure 30 constrained the top beam from moving laterally, and though the top beam moved upward and downward, vertical translations of the top beam measured significantly less than horizontal translations of the bottom beam. One pair of cameras focused on the top corner of the rocking CLT panels, while the other pair focused on the top steel connection. Pairing cameras in stereovision enabled DIC to report displacements in three dimensions. On the opposite face of wall panels, an individual DIC camera captured overall elevation views throughout the displacement cycles. Though the lone camera lacked 3D vision, the camera backed up standard video, and 2D calibration images made the lone camera capable of verifying measurements in the plane of the wall panel.

DIC Results

Istra 4D software, version 4.3.1.516, correlated all images appearing in the DIC graphs, using a consistent set of parameters. The evaluations used a grid spacing of 12 pixels. Correlations used a facet size of 17 pixels and bicubic spline interpolation. Correlation accuracy set limits of 0.1 pixel. Correlation residuum set limits of 20 on a gray scale from 0 to 255 and 0.4 pixel on 3D reconstruction. According to the software developers, the default settings described above generally provide “high” accuracy, but fully user-defined settings allow for further optimization of the parameters by adjusting values. Adjusting parameters generally balances error versus resolution of the area of interest (Sutton 2009).

Timber Bearing Conditions

Figure 130 compares the x, y, and z-axis displacements of 1.22-m (4-ft) square CLT panels placed in direct bearing contact with steel versus contact with a neoprene buffer placed between timber and steel, measured with DIC. The DIC graphs filtered out rigid-body movements and plotted displacements with a color gradation of ± 0.14 mm (5.5 mils). Though the same scale effectively described the magnitudes of displacements, the right column of the figure clearly indicates more deformations within the CLT occurred when the panel pressed against neoprene. The y and z directions pronounced differences more than the x-direction, because lateral in-plane shear was absent and out-of-plane prying forces were present. To explain the increased timber displacements recorded by DIC, Figure 131 schematically depicts effects of inserting a neoprene pad at end bearing of the CLT. Neoprene tried to deliver contact bearing stresses to CLT cross laminations, but overloaded laminations crushed locally, while spreading of the neoprene pried lamination ends.



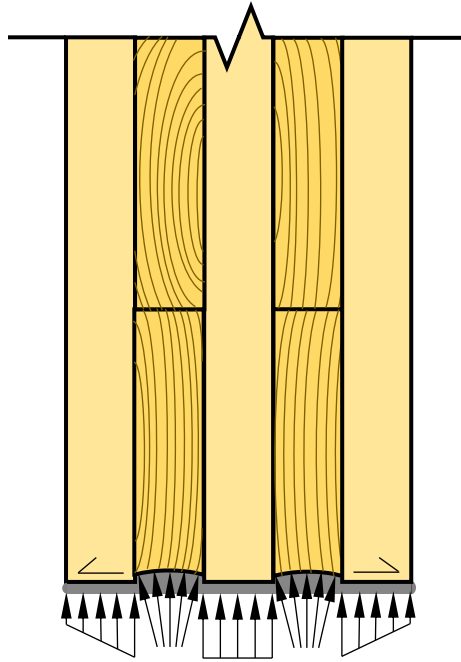


Figure 131. Qualitative distribution of contact forces generated by neoprene

Conclusions of Precursory Phase

- Longitudinally oriented laminations, middle and face layers of the 5-ply CLT panel, transfer virtually all the axial compression in bearing contact with steel;
- Though neoprene bearing contact tried to evenly distribute bearing pressures across layers, lateral spreading of the neoprene imposes more displacements on timber laminations;
- Timber around the pin bushings sustained maximum compression bearing forces of 400 kN (90 kips) applied quasi-statically without clear signs of residual displacement in the top layer analyzed by DIC.

CURRICULUM VITAE

Marco Lo Ricco

Dissertation Title: PROTOTYPING ELLIPTICALLY PROFILED INVERTED PENDULUM WALLS IN CROSS-LAMINATED TIMBER (CLT) FOR PASSIVE SELF-CENTERING AND SEISMIC RESILIENCY

About the Author

Prior to beginning a career in engineering research, Marco worked as a professional structural engineering consultant in Milwaukee, WI. With over 15 years of practical engineering experience, Marco developed a professional design portfolio that includes building and bridge structure projects constructed of concrete, steel, and timber materials. The preceding dissertation blends design experience, academic research in engineered composites, and teachings of how to shape structures for efficient performance using geometry. Marco is continuing research in advanced timber structures as a Research General Engineer at the USDA/U.S. Forest Service/Forest Products Laboratory in Madison, WI.

Objective

- Develop engineering solutions for more effective use of forest products through innovative research and creative application of proven concepts.

Education

MASTER OF SCIENCE | MAY 1999 | UNIVERSITY OF CALIFORNIA—BERKELEY

Major: Civil Engineering

Related coursework: Timber Design, Structural Dynamics, Earthquake-Resistant Design, Plastic Analysis and Design

BACHELOR OF SCIENCE | MAY 1998 | UNIVERSITY OF WISCONSIN—MILWAUKEE

Major: Civil Engineering

Minor: Spanish

Academic Honors: *Summa Cum Laude*

Related coursework: Differential and Integral Calculus, Engineering Statistics, Statics, Dynamics, Strength of Materials, Thermodynamics, Fluid Mechanics, Electrical Circuits, Steel Structures, Advanced Concrete Structures, and Prestressed Concrete Structures

Professional Experience

SENIOR STRUCTURAL ENGINEER | R.A. SMITH | MAY 2016 – JANUARY 2019

- Led bridge inspection teams providing professional services to village, town, city, and state government agencies.

STRUCTURAL ENGINEER (P4 AND PM1) | GRAEF | SEPTEMBER 1999 – MAY 2016

- Performed professional structural engineering design, analysis, inspection, and reporting services, as a consultant to various private and public sector clients;
- Managed projects ranging up to \$100,000 in design fee allocated to structural engineering;
- Worked on multi-disciplinary teams of other design professionals among the Architecture Engineering and Construction (AEC) industry;
- Applied in-depth knowledge of U.S. structural building and bridge design codes;
- Developed structural engineering details and connections, customized to applications;
- Conducted advanced computer analyses, using Finite Elements and Structural Dynamics;
 - Response Spectrum Analysis (RSA) using SAP software for earthquake engineering;
 - RSA applied to vibrational analysis of machine foundations;
 - Blast-resistant design of U.S. Department of Veterans Affairs outpatient clinics using analytical software to predict the effects of extreme impulse loadings.

Professional Licensure

PROFESSIONAL ENGINEER (P.E.) | FEBRUARY 2003 | STATE OF WISCONSIN

Discipline: Structural Engineering

License Number: 35978 - 6

Expiration: 7/31/2020

STRUCTURAL ENGINEER (S.E.) | JULY 2009 | STATE OF ILLINOIS

License Number: 081.006770

Expiration: 11/30/2020

Professional Qualifications

BRIDGE INSPECTION | INSPECTOR 9519 | STATE OF WISCONSIN DEPARTMENT OF TRANSPORTATION (WisDOT)

National Highway Institute (NHI) Safety Inspection of In-Service Bridges successfully completed in 2001

Wisconsin Bridge Inspector Refresher Training successfully completed in January 2014

WisDOT Qualified Bridge Inspection Team Leader and Member with Active Status (Inspector I.D. 9519)

Professional Publications

JOURNALS

- Lo Ricco, M., A. Ghorbanpoor, S. Pei, D. Rammer, M. Begel, J. Bridwell and R.B. Zimmerman (2018). Prototyping a Passively Self-Centering Cross-Laminated Timber Rocking Wall System: Analytical and Experimental Investigation. In: WOOD DESIGN FOCUS. 28: 23-39.
- El-Hajjar, R. F., and M. T. Lo Ricco. "Modified average stress criterion for open hole tension strength in presence of localised wrinkling." *Plastics, Rubber and Composites* 41.9 (2012): 396-406.

CONFERENCES

- Lo Ricco, Marco T., A. Ghorbanpoor, D.R. Rammer, S. Pei. "Shaping Cross-Laminated Timber Panels to Rock and Roll as Seismic Pendulum Isolators." *World Conference of Timber Engineering*. 2018.
Presented August 21st at the 2018 World Conference of Timber Engineering in Seoul, Republic of Korea.
- Lo Ricco, Marco T., and Robert J. Schumacher. "Mass Concrete Foundation Design for Precision Manufacturing of Large-Scale Equipment." *Structures Congress 2013: Bridging Your Passion with Your Profession*. ASCE, 2013.
Presented at the American Society of Civil Engineers (ASCE)/Structural Engineering Institute (SEI) 2013 Structures Congress in Pittsburgh, PA.
- Papadopoulos, Christopher M., and Marco T. Lo Ricco. "SYMMETRY-ADAPTED COMPUTATION: A CASE STUDY OF THE BUCHAREST DOME."
Presented at the 2007 Structural Stability Research Council (SSRC) conference in New Orleans, LA

POSTER PRESENTATIONS

- 2018 COLLEGE OF ENGINEERING AND APPLIED SCIENCE | UNIVERSITY OF WISCONSIN – MILWAUKEE
1st Place GRADUATE STUDENT POSTER COMPETITION for *Rock and Roll Soft-Story Seismic Isolation with Cross-Laminated Timber (CLT) Load-Bearing Wall Panels*;
- 2018 MASS TIMBER CONFERENCE | MARCH 20 – 22 | PORTLAND, OREGON
Rock and Roll Soft-Story Seismic Isolation with Cross-Laminated Timber (CLT) Load-Bearing Wall Panels;
- 2017 MASS TIMBER CONFERENCE | MARCH 28 – 30 | PORTLAND, OREGON
Shaping Cross-Laminated Timber (CLT) Wall Panels for Seismic Resiliency via Rocking and Passive Self-Centering

TECHNOLOGY TRANSFER: PATENT PENDING

- *Connector assembly for wall panel* | filed March 25, 2019 | Attorney Docket No. 020871-9148-US02 | Replaces U.S. Provisional Patent Application No. 62/734,062, filed September 20, 2018

Sponsored Research Projects

- Wood Innovations 2016-DG-11420004-170
 - Project Title: *Seismically Resilient Cross-Laminated Timber Inverted Pendulum Solutions for Tall Wood Buildings*
 - Agency Investment:
 - US Forest Service: \$241,199
 - UW – Milwaukee: \$130,475
 - Project Role (Research Assistant): Idea origination, proposal writing, prototyping, laboratory testing, structural analysis, and reporting
 - IdeAdvance Stage 1: September 2014 cohort
 - Project Title: *Biomass Builders*
 - Agency Investment:
 - UW Extension: \$25,000
 - Project Role: Proposal writing, market discovery, reporting, and convergence upon a solution to broaden applicability of CLT systems in the United States.

Teaching Experience

ASSISTANT ADJUNCT PROFESSOR | SCHOOL OF ARCHITECTURE AND URBAN PLANNING | UNIVERSITY OF WISCONSIN—MILWAUKEE | FALL 2007 – MAY 2016

- Taught ARCH 510: SURVEY OF STRUCTURES, structural design and analysis to undergraduate and graduate students of the School of Architecture and Urban Planning, in accordance with National Architectural Accrediting Board (NAAB) educational requirements;
- Synthesized architectural and structural design practice, by focusing on graphical statics to create efficient and aesthetic structural forms that take shape from the applied forces.
- Mentored 5 Master of Architecture graduates through completion of thesis projects.

ASSISTANT ADJUNCT PROFESSOR | DEPARTMENT OF CIVIL & ENVIRONMENTAL ENGINEERING | UNIVERSITY OF WISCONSIN—MILWAUKEE | SEPTEMBER 2014

- Taught CIV ENG 201: STATICS, structural design and analysis to undergraduate students of the School of College of Engineering and Applied Science, in accordance with ABET accredited educational requirements;

Professional Organizations

- American Society of Structural Engineers (ASCE)
Member (M.ASCE)
Professional Advisor of the University of Wisconsin—Milwaukee student chapter
- Structural Engineers Association of Wisconsin (SEA-WI)
Co-founder of the organization
Member organization of the National Council of Structural Engineers Associations (NCSEA)
Treasurer of organization from 2009-2011